VORTICITY SHEDDING OVER TWO-DIMENSIONAL BODIES

by

Dimitrios Mathioulakis

Dissertation submitted to the Faculty of the
Virginia Polytechnic Institute and State University
in partial fulfillment of the requirements for the degree of
DOCTOR OF PHILOSOPHY
in
Engineering Mechanics

APPROVED:

Dr. D. P. Telionis, Chairman

Dr. W. F. O'Brien

Dr. D. T. Mook

Dr. T. Herbert

Dr. C. L. Prather

Dr. S. L. Hendricks

April, 1985

Blacksburg, Virginia

VORTICITY SHEDDING OVER TWO-DIMENSIONAL BODIES

by

Dimitrios Mathioulakis

(ABSTRACT)

The vorticity shedding characteristics in attached and separated regions were investigated over three configurations, namely a backward facing circular arc, an ellipse at an angle of attack and a pitching airfoil. A fully automated data acquisition system was developed, including a two-component Laser-Velocimetry system in backscatter mode, an accurately controlled traversing mechanism and a MINK-11 minicomputer. Two-component velocity measurements were obtained over the above mentioned bodies, with steady and unsteady free streams. Emphasis was concentrated on the separation region, the free-shear layers and the wake downstream of these bodies. Two inviscid vortex models were developed to predict two different flow phenomena, namely the separated flow over a circular cylinder started impulsively from rest and propagating stall over a linear stationary cascade.

To

my parents

Στέφανο and Σοφία,

my brother Βερνάρδο and my sister Κατερίνα

ACKNOWLEDGEMENTS

I wish to express my sincere appreciation to my advisor and committee chairman, D. P. Telionis for his guidance and encouragement throughout the course of this work and especially for the spirit of optimism that he tried to transfer to me during the frustrating times of the experimental research.

My appreciation and thanks are extended to professors O'Brien, Mook, Herbert, Prather and Hendricks, for their help in reviewing the dissertation and assistance as members of my graduate committee.

I am grateful to the machine shop personnel for providing the technical support for the experimental part of this work, and especially to Mr. Maurice "Whittie" J. Hovatter, for his excellent work in constructing the elliptical cross-section cylinder.

Thanks are also extended to all members of the Greek community of Blacksburg for their moral support and fellowship. Especially I would like to express my admiration, gratitude and respect to Dr. Kriton and Maria Hatzios for their friendship and understanding during the difficult periods of my studies.

Finally, I would like to express my deepest thanks to my parents, Στέφανο and Σοφία, my brother Βερνάρδο and my sister Κατερίνα, whose love and support helped me to finish this work.

The research contained in this dissertation was sponsored by the Air Force Systems Command, USAF, under grant No. AFOSR-82-0228 and is gratefully acknowledged.

TABLE OF CONTENTS

LIST OF FIGURES

CHAPTER ONE

INTRODUCTION AND MOTIVATION

It has been more than eighty years since Prandtl (1904) discovered that the aerodynamic forces exerted on a body are greatly dependent upon the nature of a relatively thin area of the flow, close to the surface of the body, the boundary layer. Since then, theoreticians and experimentalists have been working on problems related to the flow in this region by predicting or recording its response to various free-stream conditions and body shapes.

The basic characteristic of the boundary layer is the high concentration of vorticity. Under certain conditions i.e., adverse pressure gradient, vorticity is shed into the flow, resulting generally in reduction of lift. Vorticity shedding takes place in a certain region along the surface of the body, called the separation region. This coincides with the point of zero skin friction for steady flow conditions. However, it appears that in unsteady flow there exists no criterion universally accepted by all investigators. Most prefer to define separation as the region downstream of which the flow ceases to follow the contour of the body. It is noteworthy to mention that in certain types of unsteady flow, like impulsive changes, the zero skin friction and the separation point are indeed far from each other.

The vorticity released from the separation point is convected downstream and far from the wall, forms a free shear layer or, in the framework of inviscid aerodynamics, a free vortex sheet. This layer has

the tendency to roll up further downstream and eventually clusters of vorticity are detached from it in the form of discrete vortices.

The calculation of the flowfield in the area of separation and downstream of it (wake) has been successfully performed only for relatively low Reynolds numbers (R_e). For high R_e, the numerical solution to the Navier-Stokes equations seems to be unavailable today because of limitations both in computer time and memory. A promising method, vortex dynamics, was developed by various investigators in order to fill this gap. The reader will find good literature review in Sarpkaya and Schoaff (1979) and Saffman and Schatzman (1982). Essentially, this method is based on the idea of approximating the continuous vorticity shedding process by point vortices or vortex segments in the separation region. However, this approach raises the following questions:

a) What should be the strength of the released vortices (nascent vortices)?

b) How far from the wall they should be released and at exactly which location along the surface of the body?

c) What should be their initial velocity?

Unfortunately, answers to these questions were based so far mainly on assumptions that are not rigorously justifiable.

In the past decade, considerable interest has developed in unsteady aerodynamics. Impulsive, transient and periodic disturbances imposed on the freestream on the aerodynamic surface were considered. Several articles and a book have recently been published reviewing work in this

area (Stuart, 1972; Riley, 1975; Telionis, 1975; McCroskey, 1977; Telionis, 1979; Telionis, 1981). A prominent role in the behavior of such flows is played by unsteady separation and the unsteady wake.

A large number of careful and detailed analytical studies have been devoted recently to the structure of asymptotic solutions in the neighborhood of separation and downstream, both for steady and unsteady flows. Prominent among them are the contributions of Sychev (1972) and Stewartson (1974) who introduced the ideas of triple-deck theory and essentially proved that boundary-layer theory still holds if the viscous solution is interacted with an inviscid solution. These efforts have been confined essentially to laminar flows.

Surprisingly, no detailed experimental data on the velocity field around steady or unsteady separation were available when the present investigation was launched a few years ago. It therefore appeared that no reliable data were available to the theoreticians for comparison. Since then, Varty and Currie (1984) have published their work on steady laminar separation. Moreover, the success of discrete vortex dynamics hinges critically on the proper condition at separation as discussed earlier. The present work was therefore undertaken with the purpose of studying experimentally the shedding and ultimate fate of vorticity.

Three regions of vortex shedding were identified as significant, worthy of special attention. The first is the immediate neighborhood of separation, namely the region a few boundary-layer thicknesses upstream and downstream of separation. This is the region of greatest interest for analyticians working with triple-deck theory. The second is the

region immediately downstream of separation where a free-shear layer develops in the proximity of the wall. In both these regions a significant and common feature, of course, is the development of hydrodynamic instabilities and turbulence. However, in the present study problems involving such phenomena were not considered. Finally a third region studied here is the far field vortex sheet which develops and rolls up away from the influence of the solid surface. These experimental studies have been conducted for steady and unsteady flow in a water tunnel.

The numerical work was based here on finite-difference solution of the boundary-layer equations with special emphasis on separation, and interaction of boundary layer solutions with outer flows including simulation of free-shear layers by discrete vortices.

A water tunnel was modified accordingly, so that freestream pulsations about the mean could be generated with independently controlled frequency and amplitude. An automated data-acquisition system was also developed to record the response of the flow in the regions of interest.

The calibration of the water tunnel, the Laser-Doppler-velocimetry system and the traversing mechanism are discussed, in detail, in Chapter Two. In Chapter Three, the experimental part of this work is described. Namely the experiment over a backward facing circular arc, an ellipse at an angle of attack and the flow development downstream of a pitching airfoil. A discussion of the data obtained is also included. In Chapter Four, we apply the method of vortex dynamics coupled with a boundary-layer calculation to the case of the impulsive start of a cir-

cular cylinder. Chapter Five presents another application of vortex dynamics to a complicated phenomenon occuring in axial flow compressors, called propagating stall. In the Chapter Six, conclusions and recommendations are presented. In each chapter we include a pertinent review of literature as well as comparisons of our findings with earlier experimental and analytical findings.

CHAPTER TWO

FACILITIES AND INSTRUMENTATION

2.1 Introduction

All the experimental work on this project was conducted in a water tunnel. Such a facility offers significant advantages in the study of unsteady viscous flows. By comparison to wind-tunnel work, one can conduct unsteady flow research in water at the same Reynolds and Strouhal number but at speeds and frequencies 15 times smaller. At these low frequencies, Laser-Doppler-velocimetry can generate an almost continuous signal. Moreover, flow visualization in water is more effective.

The ESM water tunnel has been constructed with Army Research Office support and its elements are described by Koromilas and Telionis (1980) and Mezaris and Telionis (1980). To conduct the experimental work of the present project, considerable modifications of the tunnel were undertaken. These involve the addition of a disturbing mechanism to generate a periodic disturbance of the mean flow and the corresponding controls. Moreover, turbulence manipulators were added to improve the quality of the flow and extensive calibrations were undertaken. This work is described in detail in the next section.

All the experimental work in the ESM Fluid Mechanics Laboratory was conducted in the past by 2 DISA LDV channels in forward scatter. At the beginning of this project, modern TSI optical equipment and one TSI counter were purchased. Soon after, the system was upgraded, with partial support of the present sponsor. In the final stages of the experimental work, a complete 2 channel TSI system in backward scatter and 2

sets of Bragg Cells were employed. Moreover, a modern data-acquisition system was integrated in the experimental rig. The entire system, the experience gathered during the optical alignment process, the electronic testing and the actual data acquisition is described in Section 2.3. In the same section, we describe the two-component traversing system which was designed and constructed especially for this project.

2.2 Tunnel Description and Calibration

In the past, work on unsteady aerodynamics was conducted in our laboratory with a steady stream (Koromilas and Telionis, 1980; Mezaris and Telionis, 1980; Jones, Barbi and Telionis, 1981). Unsteadiness was introduced by dynamic motion of the model, or part of it. The work reported here required periodic disturbances in the amplitude of the oncoming stream. This dictated a major modification of the water tunnel.

2.2.1 Disturbing Mechanism

The disturbance was generated by a rotating vane installed upstream of the settling chamber, as shown in the schematic of Fig. 2.2.1. This generates a nearly sinusoidal disturbance on the mean tunnel speed at the test section. The frequency of the tunnel speed disturbance is twice the frequency of the rotating vane. The vane is coupled to a HELLER DC motor with variable speed control. The unit automatically controls the speed to within ± 0.5% of the set value. In this way, the frequency of the flow can be varied continuously from 0 to 6 Hz.

A very significant factor in studies of unsteady aerodynamics is the amplitude of the oscillatory flow. Here the amplitude is defined as the ratio of the peak to peak value to the mean. To our knowledge, in all facilities employing some method for generating periodic disturbances in the mean flow, the amplitude is an uncontrolled quantity and depends on the frequency of the disturbance.

Special provision is necessary if one desires to control independently both the amplitude and the frequency of the oscillation. In our case this was accomplished by a bypass pipe and a bypass valve as shown in Fig. 2.2.1. In Table 2.2.1, it is shown how the amplitude ($\Delta U/U_\infty$) of oscillation is influenced by the frequency of the flow and the opening of the bypass valve. In this table we provide the speed of the rotating vane in RPM and the Doppler frequency of the mean velocity in KHz. In a separate column, under RMS, we display the root mean square of the tunnel velocity and finally the turbulence level, Tu. These measurements were obtained with a one-component L.D.V. system in forward-scatter mode. The output of a DISA photodetector was supplied to a TSI-1990 counter (signal processor). The output of the counter signal was filtered by a band pass filter set at 1 Hz (high pass filter) and 300 Hz (low pass filter) to filter any unrelated electronic noise. This filtered signal was then conditionally averaged by an HP5420A analyzer, while the RMS of its AC component was recovered by a Schlumberger time-domain analyzer (JM1860).

2.2.2 Turbulence Control

Our efforts to reduce further the free-stream turbulence level were focused on three elements of the tunnel: a) the diffuser, b) the settling chamber and the converging section.

a. The Diffuser

To distribute the flow more evenly in the multiple diffusers (space between two guide vanes), dye ports were installed at two positions for each diffuser, at the entrance and in the middle of their axial length. The distance between the separating plates which controls the cross-sectional areas at the entrance of the diffusers was then adjusted to insure uniform speed in all diffusers.

b. The Settling Chamber

A standard method for the reduction of the turbulence level of a tunnel is the installation of "tubulence manipulators" in the settling chamber. These are honeycombs or screens which, if chosen correctly, may reduce the intensity and the spectrum of the incoming turbulence. They are usually installed in the settling chamber in order to avoid excessive power losses and to permit greater travel for the dissipative decay of turbulence. The honeycombs are considered good absorbers of lateral eddies, because they eliminate large-scale vortices and swirling motions. Screens are more effective in reducing axial turbulence (Scheiman and Brooks, 1980).

Originally, there were two sets of honeycombs installed in the settling chamber of our tunnel. To further improve the quality of the flow, we installed an additional set of honeycombs at a distance of 2"

downstream of the existing honeycombs. Further downstream, we installed three fine stainless steel screens at distances of 0, 5", and 20" from the honeycombs. The wire diameter d of the screens was chosen so that $R_d = U_\infty d/\nu$ is higher than the critical Reynolds number 50, where vortex shedding takes place. This insures that the turbulence reduction is independent of the free-stream velocity (Tan-Atichat et al, 1982). Special care was also taken for the design of the screen supports so that the screens can be easily removed for cleaning and rigging the tunnel for flow visualization.

According to Dryden and Abbot (1948), three screens should reduce the turbulence level by a factor of $1/(1+k)^{3/2}$, where k is the pressure drop coefficient for one screen. However, Tan-Atichat et al (1982) found that the reduction factor is $1/(1+k)^{3/2.7}$. Moreover, in their discussion of screens and perforated plates as turbulence manipulators, they state that the turbulence decay rate is a function of the mesh size and intermanipulator separation distance. In our case, the distance between the screens was chosen arbitrarily.

At the end of the 6:1 contraction, at the entrance of test section, we installed an extra honeycomb (cell size 1/4", length 2").

Before the installation of the screen, we tried to examine how foam rubber can affect the turbulence level. We installed a 2 in. thick piece of foam rubber, covering the cross-sectional area of the settling chamber. This did not seem to result in any reduction of the turbuelnce level, though. It did generate a significant pressure loss. This idea was abandoned and the three screens were installed instead.

The performance of the tunnel is recorded in Table 2.2.1 for unsteady free stream and Tables 2.2.2 and 2.2.3 for steady stream respectively. These measurements were obtained in the test section with the DISA experimental set-up described above. Two different types and makes of signal analyzers were employed. These were a DISA tracker and a TSI counter. This phase of the tunnel calibration provided the opportunity to compare the performance of these two instruments, especially with regard to levels of turbulence.

Preliminary tests employing Bragg Cells indicated that the RMS of the velocity was strongly influenced by the shifting frequency. For this reason, it was decided to conduct the calibration work with no frequency shifting.

For the steady-flow measurements, both filters were set at 300 Hz. Unlike the measurements of the mean velocity, the turbulence intensity ($\sqrt{\overline{u'^2}}/U_\infty$) measurements proved to be very sensitive to the level of electronic noise and the type of signal processor. For a specific free-stream velocity, almost the same RMS was recorded with two different scales of the DISA tracker. This resulted in a high discrepancy of the turbulence intensity (see Table 2.2.2). Using the TSI counter, we noticed that the rms value is smaller the narrower the bandwidth of the counter band-pass filter and the lower the gain of its amplifier. It is therefore obvious that a counter is a far more reliable instrument for the measurement of turbulence level.

The basic conclusion drawn from Tables 2.2.2, 2.2.3 is that the turbulence intensity does not depend on the free-stream velocity but

rather on the bypass opening. Increasing the bypass flow results in higher values of the free-stream turbulence. In contrast to the steady case, it seems that for the unsteady flow the turbulence intensity does not change significantly with increasing the bypass flow (see Table 2.2.1).

For the steady case, in parallel to RMS measurements, we used the HP5420A analyzer to study the flow in the frequency domain. That is, we obtained autospectra of the fluctuating component u for all the cases of the pump speed and bypass opening. In Figs. 2.2.2 to 2.2.5, we display the autospectra for a driving pump speed at the 0.5 setting and 4 positions of the bypass. A similar set of spectra for the highest driving pump speed is shown in Figs. 2.2.6-2.2.9. In these figures the top spectrum corresponds to operation with the honeycomb at the entrance of the test section. In Figs. 2.2.2 to 2.2.9 we observe that the extra honeycomb at the entrance of the test section introduces some background turbulence and a few distinct spikes. From Table 2.2.2 we also deduce that the turbulence intensity actually increases when the extra test section honeycomb is employed. However, taking measurements in a region close to the upper wall of the test section, the turbulence intensity was greatly improved by this honeycomb. This is very significant for the phase of the work where data were obtained in the boundary layer developing on a false ceiling of the tunnel. It appears that this extra honeycomb does not reduce the turbulence intensity but it helps to improve the uniformity of the flow.

Figures 2.2.10 through 2.2.13 combine the effects of the bypass for different driving pump speeds. To control the pressure level in the tunnel, we installed a water trap and piping which connects the system to a vacuum pump (see Fig. 2.2.1). This was necessary because in the unsteady mode of operation, the acceleration and deceleration of large masses of water induce fluctuations of pressure that may exceed the strength of the tunnel components. It later was found that the system did not produce too large amplitudes of oscillation and the safety system of pressure reduction was not employed.

2.3 Instrumentation and Data Acquisition

In the past, the measurements of the fluid velocity in our laboratory were made by employing an one-component L.D.V. (Laser Doppler velocimetry) system in the forwardscatter mode. In the present work, the system was expanded to two-component backscatter L.D.V. The main components were designed by TSI.

2.3.1 Optical Components

a. Sending Optics

In the effort reported here, the optical components were aligned and tested in an arrangement shown schematically in Fig. 2.3.1. The variable-intensity beam splitter (TSI 9216-2) with the equal-intensity beam splitter (TSI 9115-2) split the initial laser beam into 3 beams of approximately equal intensity. The beam which is reflected from the mirror of the beam splitter (TSI 9216-2) goes through a polarization

rotator (TSI 9103-2) which changes its polarity by 45°. In this way all beams have the same polarity. Two of the three beams are led through Bragg cells which generated frequency shiftings of 40 MHz (TSI 9182-2) and 60 MHz (TSI 9282) respectively. Shifting of the beam frequencies shifts the zero velocity reading and therefore allows the instrument to identify positive or negative quantities. Moreover, frequency shifting minimizes the fringe biasing error (Seasholtz, 1977).

The three parallel beams exciting the train of optics described above are focused via a lens at a point. Actually the cross-section of the beams is finite and therefore their intersection is also a finite three-dimensional figure, commonly known as the measuring or probe volume. In order to increase the signal-to-noise ratio and reduce the dimensions of the probe volume by a factor of 2, the three beams are passed through a beam expander (TSI 9188).

The dimensions of the measuring volume are calculated via the formulas (p. 77 of TSI manual)

$$d_m = \frac{4\lambda f}{\pi D E} \text{ and } \ell_m = \frac{d_m}{\tan k}$$

where d_m is the diameter and ℓ_m the length of the probe volume, k is one half of the angle of intersection between two beams, λ is the wavelength of the laser light, D the diameter of the laser beam, f the focal length of the lens and E the expansion ratio of the beam expander. In the present experiment we worked with the following parameter values

$f = 250$ mm

$k = \tan^{-1} \frac{50(\sqrt{2}/2)}{2(250)}$, since $50\sqrt{2}/2$ is the distance between the beams

$\lambda = 0.632\ \mu m$

$D = 1\ mm$

$E = 2.27$

Using f,k,λ,D,E in the above formulas, we obtain the diameter and the length of the probe volume,

$d_m = 0.088\ mm$

$\ell_m = 1.24\ mm$

The fringe spacing d_f is

$$d_f = \frac{\lambda/2}{\sin k} ,$$

and therefore

$d_f = 4.47\ \mu m$

The focusing of the beams is shown schematically in Fig. 2.3.2. The beams meet the lens plane at 3 points which are at the corners of an isosceles orthogonal triangle. In this figure, the plane D is the plane of the lens, and P is the focal point. The midpoints of AB, BC, CA are M_1, M_3, M_2, respectively. The triangles PCA, PAB, PCB are isosceles and therefore the lines PM_2, PM_1, PM_3 are bisectors of the angles $\hat{CPA}$, $\hat{APB}$, $\hat{CPB}$ and normal to the line segments AC, AB, BC, respectively. Since the fringes generated by two beams are parallel to their bisector, there are three sets of fringes at point P parallel to PM_2, PM_1 and PM_3, respectively. The scattered light includes all the information about the local velocity of the fluid (more accurately the particles) in a direction normal to the fringes. Therefore, in this case, the scattered light will give us information about three velocity components parallel

to AB, BC and CA (see Fig. 2.3.2) respectively. Apparently only two of the three components are linearly independent.

b. Receiving Optics

The scattered light from the measuring volume is received via the receiving assembly (TSI 9140) and the photodetector (TSI 9162). These are located on the same side of the test section with the rest of the optics. This is the major advantage of the backscatter mode. It allows us to traverse the probe volume more easily and more accurately than in the case where the receiving optics are on the other side of the test section (forwardscatter mode).

Another feature of the system described here is that the train of optics has the capability to rotate about an axis parallel to the beams via two rotating mounts (TSI 9178-2 and TSI 9179). This is extremely helpful when we take measurements on a curved surface, because then we can adjust the beams so that they are tangent to the surface.

2.3.2 Signal Processing

The incoming signal is decomposed into three signals corresponding to three velocity components. This is done by virtue of the frequency shifting technique. The frequency of two light beams, i.e. CP and BP (see Fig. 2.3.2), is shifted by 40 MHz and 60 MHz respectively. Therefore, the photodetector receives three signals, with frequencies centered around 40 MHz, 20 MHz, 60 MHz, corresponding to the velocity components parallel to AC, BC, and AB, respectively.

Two band-pass filters (TSI 9185-3) with bandwidths 12-28 MHz and 32-48 MHz, allow only the signals of two velocity components to be processed. These velocity components were chosen so that they are normal to each other, or parallel to AC and BC, respectively (see Fig. 2.3.2). Next, each of these signals is fed to a different frequency mixer, namely the 20 MHz signal is fed to the TSI 9186A-20 and the 40 MHz signal to the TSI 9186. The wiring is shown schematically in Fig. 2.3.3. The mixers subtract the 20 MHz and 40 MHz respectively from the signals and they add the "zero" frequency; this is the Doppler frequency which corresponds to zero velocity of the fluid and it is adjustable. In other words, the frequency f_s of each signal is

$$f_s = f_0 + f_d$$

where f_0 is the "zero" frequency, and f_d is the frequency proportional to the fluid velocity. The output of each frequency mixer is fed to a different signal processor (TSI 1990, TSI 1980 counters) in order to be converted to voltage V_s (in the range of 0 to 10 volts) proportional to f_s. The voltage, V_d, corresponding to the fluid velocity is

$$V_d = V_s - V_0,$$

$$\text{where } f_d = XV_d,\ f_s = XV_s,\ f_0 = XV_0,$$

V_0 is the voltage proportional to f_0, and X is a constant of proportionality. The velocity of the fluid is $XV_d d_f$ where d_f is the fringe spacing. Finally, the two signals are sent to a MINK-11 minicomputer to be averaged and stored.

In conclusion, this two-component L.D.V. system, compared to other systems such as 2-color systems, has basically the following advantages:

a) It requires a relatively inexpensive, light and safe 15 mW-He-Ne laser, instead of an expensive, heavy and dangerous to operate Argon-Ion laser.

b) It requires one instead of two photodetectors.

c) It can detect positive or negative flow in both directions.

2.4 The Traversing Mechanism

A major improvement in our experimental facilities was the construction of a mechanism for traversing the measuring volume with mirrors. The design was based on the following requirements:

a) The displacements must be accurately controlled.

b) The measuring volume must be displaced in two directions parallel and perpendicular to the flow, respectively.

c) The system must be free of vibration.

d) Traversing must be controlled by the laboratory computer.

e) The beam must be able to rotate about the optical axis, facilitating measurements on any curved surface.

To meet these requirements, we designed and constructed the following traversing system. The 15 mW He-Ne laser and the entire train of optics were mounted on a sliding table, as shown in Fig. 2.4.1. The slider was mounted on a heavy table originally used and described by Mezaris (1980) and modified by Jones (1980). This table is carefully insulated from floor vibrations. The slider can be displaced in a direction parallel to the laser beams. Two mirrors reflect the three beams up and to the right and then through the focusing lens (see Fig.

2.4.2) while the lower mirror remains fixed, the upper mirror and the lens can translate in the vertical direction to move the measuring volume along the y-axis. Details of the mirror tower are shown in Fig. 2.4.2.

Both mirrors can be fine-adjusted by thumb screws. It is important to note that the lower mirror should be adjusted in such a way that the reflected beams from its surface are exactly parallel to the vertical lead screw of the mirror tower. Only under this condition will the beams hit the lens at the same points during the vertical motion of the upper mirror. Otherwise, the measuring volume does not move along a vertical line but more importantly, after relatively long vertical displacements, the beams do not cross each other at the measuring point. It is noteworthy to mention that the distance between two parallel light beams before and after the reflection from the mirors is preserved (see Appendix I). Therefore, by rotating the beams about the optical axis, the fringe spacing remains constant while their orientation changes.

Both motions (along x and y direction) are controlled by stepping motors (SLO-SYN) interphased with the MINK-11 minicomputer. One step corresponds to 1.8 degrees of shaft rotation. Displacements are triggered by pulses generated by the minicomputer. The "digital-out" module of the MINK sends a certain number of pulses to each stepping motor for a given displacement of the probe volume. For the smooth motion of the traversing mechanism we found that the pulses must be asymmetrical. In our case, the duration of the high level portion of the pulse was chosen to be one fifteenth (1/15) of that of the low level.

The two stepping motors do not move simultaneously. A pulse sent from the D/A converter of the MINK to an electronic device activates one motor at a time. The measuring volume can thus be moved along any curved or straight line with a smallest accurate displacement along the x or y axis of about 0.1 mm. Every displacement is stored on a floppy diskette, providing all the necessary information about the excursions of the probe volume in the two-dimensional space.

The axis of symmetry of the converging beams which enter the test section should not be exactly perpendicular to the tunnel window to avoid direct reflections from the window and the model. For this reason, the entire train of optics is given a small inclination, ϕ_1, with respect to the tunnel axis in the horizontal plane (see Fig. 2.4.3). Moreover, to allow the probe volume to approach as close as possible to the surface of the model, a second inclination was given to the beams entering the test section. This technique which was also employed by Koromilas and Telionis (1980), essentially inclines the large axis of the ellipsoidal shape of the measuring volume with respect to the surface of the model. In Fig. 2.4.3, this angle is denoted by the symbol ϕ_2.

The velocity components u and v along the Cartesian system aligned with the test section and the model are related to the measured quantities u_2 and u_4 via the equations (see Appendix II)

$$u = (u_4 \sin\phi_3 + u_2 \cos\phi_3)/\cos\phi,$$

$$v = (u_4 \cos\phi_3 - u_2 \sin\phi_3)/\cos\phi_2 + \tan\phi_1 \tan\phi_2 (u_4 \sin\phi_3 + u_2 \cos\phi_3) \ .$$

These formulas are based on the assumption that the flow in our test section is two-dimensional, i.e. that $w = 0$.

CHAPTER THREE

EXPERIMENTAL INVESTIGATION OF VORTICITY SHEDDING

Introduction

In this chapter we investigate experimentally the phenomenon of vorticity release from three two-dimensional bodies, namely a backward-facing circular arc, an ellipse at an angle of attack and a pitching airfoil. These are discussed in the following 3 subsections. The first body is used to examine in detail the separation region and the formation of the free-shear layer. In the case of the cylinder of elliptical cross section, we examine the suction side and pressure side shear layers as well as the front stagnation point region. Finally, in the third model we investigate the flowfield downstream of a pitching NACA 0012 airfoil which sheds vorticity in its wake. The first case is a magnification of the region where vorticity actaully detaches and starts moving away from the wall. In the second case, we study the behavior of a free vortex sheet in the neighborhood of a solid surface. This is the case of separated flow over the suction side of an airfoil. In the last case, the vortex sheet develops free of the influence of any solid boundaries. In all cases, special attention is focused on the effects of periodic unsteadiness introduced in the magnitude of the oncoming stream.

3.1 Backward-facing Circular Arc

In order to investigate experimentally the immediate neighborhood of steady and unsteady laminar separation, it is desirable to generate a thick boundary layer. This is helpful because, for a given minimum possible displacement of the traversing mechanics, we are able to take data at a large number of points across the boundary layer. To produce this condition, we chose the model shown in Fig. 3.1.1. A convergence of the test section leads the flow between two slightly diverging flat plates to account for the growth of the two boundary layers. The top surface is mounted in a manner that creates a small gap between it and the ceiling of the test section. This proved to be necessary for the reduction of the turbulence intensity on the top surface. In addition to this, the installation of an extra honeycomb at the entrance of the test section improved the quality of the flow significantly.

It is recalled that flows about symmetric bodies, i.e. a circular cylinder, are controlled by the interaction of two shear layers with opposite signs of vorticity, which eventually results in periodic shedding of large-scale vortices. However, in the case of an airfoil at an angle of attack, the separating flow over the suction side develops with little or no influence of the trailing-edge vorticity. This is the situation that is simulated by our rig. A little downstream of the convergence AB, the boundary layer is similar to the Blasius flow. Further downstream, the top surface changes into a circular arc with a radius R = 450mm to generate a region of adverse pressure gradient. To avoid symmetry, the bottom surface was continued as a flat surface downstream

of the circular arc. In this way the separated region is not affected by mirror-image separation.

The model was made out of plexiglas and extra care was taken to generate a smooth surface. The length of the flat portion of the top surface was limited to insure that the boundary layer remains laminar all the way down to the point of separation. The flow over the circular arc was the region of detailed investigation.

The two-component LDV system described earlier was employed to measure 2 orthogonal velocity components. In Fig. 3.1.2, we show the beam configuration for this particular experiment. The beams were set in space in such a way that the fluid particles intercepted as many fringes as possible and the measuring volume could reach the wall of the model.

The velocity measurements were obtained along directions normal to the curved surface of the circular arc and at 19 streamwise stations. These stations as well as the circular arc are shown in Fig. 3.1.3. The number of measuring points per station ranged between 30 and 60, while the smallest distance between two adjacent points was 0.2 mm. All the stations were located in the midspan region of the circular arc where the flowfields is two-dimensional. The smallest distance along the wall between two stations was 5 mm which corresponds to an angle of 5/450 rad. At each station measurements were obtained in sequence, starting from the free-stream and moving towards the surface of the model. The distance between two measuring points in the outer flow was about 1/10

of the boundary-layer thickness. Inside the boundary layer the measuring grid was thickened in order to capture the velocity gradient accurately.

The measurements at a particular station came to an end, when the probe volume touched the surface of the model, a fact that was accompanied by an abrupt increase of the signal noise level. In this way, we were able to define the distance of the surface from the previous measuring point with an accuracy equal to the smallest displacement, which for this sequence of measurements was 0.2 mm.

In order to study the phenomenon of unsteady separation, a well organized disturbance was introduced in the oncoming stream via a rotating vane (see Chapter 2). The freestream was oscillated with a non-vanishing mean and the period of oscillation was fixed at 4.8 sec. The mean value of the free-stream velocity U_∞ was 16.5 cm/sec. The tunnel velocity may slowly drift by approximately 5%. Based on the radius R of the circular arc, the mean Reynolds number Re_m, was 7.1×10^4, while the frequency parameter $\omega R/U_\infty$ was 3.57.

The initiation of data acquisition was triggered by a pulse sent to the laboratory computer at a fixed opening of the rotating vane. The LDV signals were then conditionally averaged. For each velocity component, 160 instantaneous values per period, T, were stored. In Fig. 3.1.4, we show time records of the velocity component parallel to the free stream, at five points along the 12th station. The continuous line connects the 160 data values, and the small circles correspond to time instants multiples of T/16. The analysis of the unsteady velocity field

was primarily based on 8 or 16 data points per period, with a time increment T/8 or T/16 respectively.

3.1.1 Experimental Results

Two coordinate systems were used: a polar (x-y) with its origin at the center of the circular arc and a Cartesian (ξ-n) where ξ was parallel to the free stream (see Fig. 3.1.3). The velocity components in the x-y system were denoted by u and v, where u was parallel to the wall, while in the ξ-η system, u_H was parallel to the free stream. The station x=0 (or ξ =0) corresponds to the beginning of the circular arc. The time dependent u_H component was analyzed by an IMSL FFT routine, namely FFTSC (see Appendix III). This routine returned the mean value u_H as well as the amplitude of each harmonic. Therefore, u_H can be written as follows

$$u_H(x,y,t) = \bar{u}_H(x,y) + \sum_{n=1}^{80} a_n(x,y)\sin\omega_n t + b_n(x,y)\cos\omega_n t \quad (3.1.1)$$

where $\omega_n = n\omega$. However, since the terms $a_n(x,y)$, $b_n(x,y)$, for $n \geq 2$ were much smaller than $a_1(x,y)$, $b_1(x,y)$, (less than 5%) the above expression can be rewritten with a small error as

$$u_H(x,y,t) = \bar{u}_H(x,y) + a(x,y)\cos(\omega t+\phi),$$

where

$$a(x,y) = \sqrt{a_1^2(x,y) + b_1^2(x,y)} \quad \text{and} \quad \phi = -\tan^{-1}(a_1/b_1). \quad (3.1.2)$$

In Fig. 3.1.5, we show contours of constant amplitude, a(x,y) being nondimensionalized by the local free-stream amplitude. The free-stream amplitude (from peak to peak) normalized by the free-stream mean

velocity was 10%. In this figure, we observe a classical feature of this type of flow, amplification of the oscillation as we penetrate the boundary layer. The amplification increases dramatically as separation is approached. This was predicted numerically by Telionis and Romaniuk (1978) and experimentally by Mezaris and Telionis (1980). In the downstream direction, the peak of the amplitude moves away from the wall in contrast to the case of oscillatory flow over a flat plate, where the amplitude overshoots approach the wall for increasing $\omega x/U_\infty$. In our case, as it is explained later (see Vorticity Contours), the amplitude overshoots downstream of the separation are located within the free-shear layer where vorticity has its maximum value.

It is also observed that the overshoots are amplified continuously in the direction of increasing x, with a maximum value of 5 times larger than the local outer flow amplitude. Mezaris and Telionis (1980) reported overshoots about 10 times larger than the amplitude of the outer flow. This difference may be attributed to the fact that their disturbance was introduced locally.

Another characteristic feature of the flow is the change of the phase angle ϕ, across the boundary layer. In Fig. 3.1.6 we plotted the variation of ϕ along y, at 16 stations (3 through 18). We notice that close to the wall and at stations 11 through 18 (where the flow is reversed), there is a large phase lead (maximum value of 100°), while in the outer part of the boundary layer there is a small phase lag (maximum value of 20°). A simple explanation of this behavior is given by the fact that the inertia effects become less important compared to the

pressure gradient as we approach the wall. Lighthill (1953), using a perturbation scheme, found a phase advance of 45° near the wall, for flat plate flow and high reduced frequencies. Tsahalis and Telionis (1974) reported a maximum phase lead of 45° and a phase lag of the order of 10°. The change of the amplitude and the phase angle across the boundary layer is depicted in Fig. 3.1.4 where the velocity waveforms at 5 different locations along the 12th station are shown.

The velocity components parallel and perpendicular to the wall were normalized by the local time mean of the outer flow $\bar{u}_{He}$. Then they were smoothed in the y-direction by the cubic spline ICSSCU (see Appendix IV). Using the same routine we were able to obtain the smoothed velocity components at equispaced locations in the y-direction $\Delta y = 0.4$ mm. The smoothed values u,v were used in our calculations for further reduction of the data. In Figs. 3.1.7-14 we show profiles of both components u and v at 19 stations and at 8 time instants t_k, where $t_k = kT/8$ and k takes values from 1 through 8. In these figures, the circles correspond to the raw data and the solid lines are the smoothed profiles. We should notice that the profiles of the v-component at stations 16 through 19 are less smooth than in the upstream locations. This is attributed to the formation of the wake, where velocity instabilities are significant.

In order to obtain a detailed picture of the unsteady phenomenon, we made a film out of the smoothed u-v unsteady data corresponding to stations 4 to 15. We plotted velocity vectors for every T/16, by vec-

torial addition of the u and v components. A 16mm animated movie was then produced based on the 16 frames thus generated.

The boundary-layer thickness $\delta(x)$ was defined as the distance from the wall where u takes the value 0.95, while the displacement thickness δ^* was defined by the equation

$$\delta^*(x,t) = \int_0^\infty (1-u(x,y,t))\Delta y \qquad (3.1.3)$$

where all lengths were nondimensionalized by the radius R of the circular arc. The above integration was performed over the smoothed profiles by using Simpson's rule. In Fig. 3.1.15 we show how δ^* changes in time at 19 stations.

The vorticity vector in two-dimensional fields is everywhere parallel to the spanwise direction, and its magnitude expressed in polar coordinates is

$$\omega = \frac{\partial u}{\partial y} + \frac{u}{1+y} - \frac{1}{1+y}\frac{\partial v}{\partial x} \qquad (3.1.4)$$

where ω was normalized by $\bar{u}_{He}/R$. Contours of constant vorticity $\omega/100$ are shown for 8 time instants in Figs. 3.1.16-19, corresponding to stations 3 to 18. The fluctuation of the free-shear layer is clearly displayed in the sequence of frames in these figures.

In Figs. 3.1.20-21 we have plotted the displacement thickness and $\left.\frac{\partial u}{\partial y}\right|_{y=0}$ versus time at stations 3-19. From these figures we notice that the position of the zero-skin-friction oscillates back and forth along the wall between the stations 10 and 13. This is also obvious from the unsteady u-velocity profiles (see Figs. 3.1.7-14). At station 13 the

skin friction is negative throughout the entire cycle of oscillation. Since this is the first downstream station where $\left.\frac{\partial u}{\partial y}\right|_{y=0} \leq 0$ throughout the period, it is considered as the separation point according to the definition of Despard and Miller (1970). Figures 3.1.20-21 also provide us with information about the skin-friction phase angle; at stations 7, 8 (attached flow) we observe a phase lag of the order of 10°, while at stations 16, 17 (reverse flow), there is a phase lead of about 45°, both with respect to δ^*. The displacement thickness seems to have, in all stations, a 180° phase difference from the outer flow. This means that the displacement thickness decreases when the outer flow accelerates and grows when it decelerates. This is also apparent in Fig. 3.1.15, where the maximum observed value of δ^* is 0.036R. This is better illustrated in Figs. 3.1.7-14, where the reversed flow region becomes thick and thin alternatively throughout the period of oscillation.

The mechanism of vorticity diffusion is shown in the unsteady vorticity contours (see Fig. 3.1.16-19). This is more obvious downstream of the zero-skin-friction area. When the flow decelerates, vorticity diffusion takes place in two opposite directions from the regions of maximum vorticity (center of shear layer), namely towards the outer flow and towards the surface of the body. At the same time the vorticity at the center of the shear layer drops. When the flow accelerates, the slopes of vorticity increase as indicated by the convergence of the contours and as a result the peak increases. From the same figure we notice also that the zero skin friction oscillates in the region $x = (0.135 \div 0.162)R$.

3.1.2 Estimate of terms of N.S. Equations

An attempt was made to evaluate the distribution of the static pressure in the flow field by using the experimental data in the Navier-Stokes equations. In polar coordinates with origin at the center of the circular arc, these are u-momentum:

$$\frac{\partial u}{\partial t} + \frac{u}{1+y}\frac{\partial u}{\partial x} + v\frac{\partial u}{\partial y} + \frac{uv}{1+y} = -\frac{\partial p/\partial x}{1+y} + \frac{1}{Re}\left[\frac{\partial^2 u}{\partial y^2} + \frac{1}{1+y}\frac{\partial u}{\partial y} + \frac{1}{(1+y)^2}\frac{\partial^2 u}{\partial x^2} + \frac{2}{(1+y)^2}\frac{\partial v}{\partial x} - \frac{u}{(1+y)^2}\right] \tag{3.1.5}$$

v-momentum

$$\frac{\partial v}{\partial t} + \frac{u}{1+y}\frac{\partial v}{\partial x} + v\frac{\partial v}{\partial y} - \frac{u^2}{1+y} = -\partial p/\partial y + \frac{1}{Re}\left[\frac{\partial^2 v}{\partial y^2} + \frac{1}{1+y}\frac{\partial v}{\partial y} + \frac{1}{(1+y)^2}\frac{\partial^2 v}{\partial x^2} - \frac{2}{(1+y)^2}\frac{\partial u}{\partial x} - \frac{v}{(1+y)^2}\right] \tag{3.1.6}$$

where $u = \frac{u^*}{\bar{u}_{He}}$, $v = \frac{v^*}{\bar{u}_{He}}$, $x = \frac{x^*}{R}$, $y = \frac{y^*}{R}$, $t = \frac{\bar{u}_{He}}{R}t^*$, $p = \frac{p^*}{\rho\bar{u}_{He}^2}$, $Re = \frac{\bar{u}_{He}R}{\nu}$ and symbols with an asterik denote dimensional quantities.

The derivatives of both components in the x and y directions have been expressed by central differences while the time derivatives by forward differences. For example $\frac{\partial u}{\partial x}$ and $\frac{\partial u}{\partial t}$ were calculated by

$$\frac{\partial u}{\partial x} = (u(i,m+1,j)-u(i,m-1,j))/(2\Delta x) \tag{3.1.7}$$

and

$$\frac{\partial u}{\partial t} = (u(i,m,j+1)-u(i,m,j))/\Delta t$$

respectively where (i,m,j) corresponds to (y,x,t). Some terms in 3.1.5,

3.1.6 were of the order $10^{-3} \div 10^{-5}$. Our measurements indicate that by dropping some terms, these equations can be simplified with great accuracy as

$$\frac{\partial u}{\partial t} + \frac{u}{1+y}\frac{\partial u}{\partial x} + v\frac{\partial u}{\partial y} + \frac{uv}{1+y} = -\frac{\partial p/\partial x}{1+y} + \frac{1}{Re}\frac{\partial^2 u}{\partial y^2} \qquad (3.1.8)$$

$$\frac{\partial v}{\partial t} + \frac{u}{1+y}\frac{\partial v}{\partial x} + v\frac{\partial v}{\partial y} - \frac{u^2}{1+y} = -\frac{\partial p}{\partial y} + \frac{1}{Re}\frac{\partial^2 v}{\partial y^2} \qquad (3.1.9)$$

The profiles of 8 terms in (3.1.8), (3.1.9) are shown in Figures 3.1.22 to 3.1.29, namely, the terms $\frac{u}{1+y}\frac{\partial u}{\partial x}$, $v\frac{\partial u}{\partial y}$, $\frac{uv}{1+y}$, $\frac{1}{Re}\frac{\partial^2 u}{\partial y^2}$, $\frac{u}{1+y}\frac{\partial v}{\partial x}$, $v\frac{\partial v}{\partial y}$, $\frac{u^2}{1+y}$, $\frac{1}{Re}\frac{\partial^2 v}{\partial y^2}$. These profiles correspond to stations 4 through 18 and at t = 8/16, t = 16/16. The displacement thickness is marked in each profile by a small vertical line.

It should be emphasized here that discrepancies easily appear in this type of calculation. For example, the quantity v is very small and very hard to measure. Moreover, x-derivatives are also small. It turned out that errors as large as 20% to 30% were found in verifing the continuity equation. Similarly, profiles of terms like $\partial u/\partial x$ appeared to be very irregular, if estimated by differences in the x-direction. In a similar attempt, Varty and Currie (1984) calculated the same terms based on experimental data for steady flow over a circular cylinder. It seems that they encountered the same difficulties, since their profiles were not smooth.

The term $\partial p/\partial y$ was then calculated from Eq. (3.1.9). Profiles of $\partial p/\partial y$ are plotted in Fig. 3.1.30. This quantity is indeed very small and as a result extremely small errors lead to erratic behavior of the profiles. We notice that $\frac{dp}{dy}$ is very small in the region $y \leq \delta^*$

upstream of the 14th station at t = 8/16 and upstream of the 12th station at t = 16/16. However, downstream of these stations (wake region) this does not hold. Concerning the $\frac{dp}{dx}$ distribution shown in Fig. 3.1.31, we cannot see any definite trend as we are approaching the separation point from upstream. This should be attributed to the $\frac{u}{1+y}\frac{\partial u}{\partial x}$ term, which does not seem to change smoothly along x. The reason is that small disturbances travelling in the flow can greatly influence quantities like $\frac{\partial u}{\partial x}$ and v. In order to make an improvement on this, we should (a) have a free stream with extremely small turbulence intensity, (b) measure the local fluid velocity and the freestream velocity simultaneously and (c) take many averages.

Evaluating Eq. 3.1.8 at y=0, we can obtain the wall pressure, gradient

$$\frac{dp_w}{dx} = \frac{1}{Re}\left.\frac{\partial^2 u}{\partial y^2}\right|_{y=0} \qquad (3.1.10)$$

Integrating this equation with respect to x yields the pressure distribution on the wall. This integration was performed between stations 4 and 18 by arbitrarily assuming that p_w at station 4 was zero. The variation of p_w along x at t = 8/16 and t = 16/16 is shown in Fig. 3.1.32 along with the variation of $\left.\frac{\partial u}{\partial y}\right|_{y=0}$. We notice that p_w starts increasing 3 or 4 stations upstream of the zero-skin-friction area.

A good parameter indicative of the validity of the boundary-layer assumption is the quantity u_m/v_m, the ratio of the two mean velocity components. Contours of this ratio are shown in Fig. 3.1.33. It is

apparent that with respect to a frame of reference aligned with the separating free-shear layer, the boundary-layer approximation is valid.

3.1.3 Discrete Vortex Simulation

The numerical prediction of the motion of a free-shear layer for high Reynolds numbers is very difficult by employing the Navier-Stokes equations. A very promising method which has been widely used recently, is discrete-vortex dynamics according to which the released vorticity is assumed to be concentrated at point vortices in two-dimensional flow fields. However, the exact positions from where these vortices are released and their initial velocities are defined by heuristic ways. It should be emphasized that these parameters significantly affect the numerical solution. A more precise method for the definition of the location and the strength of nascent vortices is needed.

If the velocity distribution in the viscous layer is known, then the discrete vortex distance from the wall y_c in the separation region and its initial velocity of convection (U_c, V_c) should be given by

$$y_c = \frac{\int_0^\delta \omega y dy}{\int_0^\delta \omega dy}, \quad U_c = \frac{\int_0^\delta \omega u dy}{\int_0^\delta \omega dy}, \quad V_c = \frac{\int_0^\delta \omega v dy}{\int_0^\delta \omega dy} \tag{3.1.11}$$

These quantities were calculated along x, from the experimental data. The quantity $y_c(x)$ which is essentially the center of gravity of vorticity at a station, is shown in Fig. 3.1.34 at 8 different times in one

cycle. This quantity does not differ significantly from the displacement thickness. This is due to the fact that vorticity can be approximated by $\omega \sim \frac{\partial u}{\partial y}$ since $\frac{\partial v}{\partial x}$ is small even in the separation region. The $\frac{\partial v}{\partial x}$ term becomes less negligible in the outer flow. Concerning the convective velocity component U_c, we found that it oscillates in time with an amplitude of 10% (as the outer flow does), while its mean value changes along x in the range $(0.50 \div 0.45)\overline{U}_{He}$.

The calculation of the circulation of the nascent vortex is based on the formula

$$\frac{D\Gamma}{Dt} = \int_c \frac{D\vec{v}}{Dt} \cdot d\vec{\tau} \qquad (3.1.12)$$

which gives the temporal change of circulation of a ring of fluid particles propagating into the flow (see Karamcheti, p. 240). Consider the x-stations m,m+1 in the separation point region. The change in time of circulation Γ referred to the loop which consists of these stations and of two circular arcs connecting the stations at the edge of the boundary layer and at the wall respectively is approximately given by

$$\frac{\Delta\Gamma}{\Delta t} \simeq \frac{1}{2}\left[\frac{DU_e}{Dt}\Big|_m + \frac{DU_e}{Dt}\Big|_{m+1}\right]\Delta x(1+\delta) + \int_0^{\delta} \frac{Dv}{Dt}\Big|_m dy - \int_0^{\delta} \frac{Dv}{Dt}\Big|_{m+1} dy \qquad (3.1.13)$$

Many investigators like Surpkaya et al (1979), Katz (1981), Kiya et al (1982), use instead the formula $\frac{\Delta\Gamma}{\Delta t} = \frac{1}{2} U_{es}^2$, where U_{es} is the outer flow velocity at separation. Using 3.1.13 we end up with the above expression only in the case that $\frac{Dv}{Dt}$ and $\frac{\partial U_{es}}{\partial t}$ are very small like it happens in our case. Sears (1975) extended Howarth's criterion to the

unsteady flow, suggesting that the change of circulation in time about a bluff two-dimensional body should be given by the formula

$$\frac{\Delta\Gamma}{\Delta t} = \left[\frac{1}{2} U_s^2 - U_{es}u_{sep}\right]_A - \left[\frac{1}{2} U_{es}^2 - U_{es}u_{sep}\right]_B$$

where A and B are two separation points and u_{sep} is their velocity.

Velocity measurements over the circular arc were also obtained with a steady free stream at the same locations as for the unsteady case in order to compare the phenomena of steady and unsteady separation. The free-stream velocity was kept at 19 cm/s and the Reynolds number was 8.2×10^4. In Fig. 3.1.35 we show the u,v components at 19 stations, where again the circles correspond to raw data. It is obvious especially for the v-component that the data scatter is much less in the steady than in the unsteady case. In Fig. 3.1.36 and 3.1.37 we show the vorticity contours, wall pressure distribution as well as $\frac{\partial u}{\partial y}\Big|_{y=0}$ distribution for both steady and time mean of the unsteady velocity field.

In Fig. 3.1.38 the streamlines are shown, obtained by integration of the equation $u = \frac{\partial \psi}{\partial y}$, where ψ is the streamfunction. From Figures 3.1.36, 3.1.37, 3.1.38, we notice that there is no significant difference between the steady and time-mean velocity fields.

However, the only noticeable difference is that the zero skin friction for the steady flow-field is located aproximately one station upstream ($\Delta x = 0.011R$) from that one for the time-mean flow field. This contrasts with the experimental findings of Despard and Miller (1971),

who observed that oscillation of the free-stream about a non-zero mean moves the separation point upstream of the steady flow separation point.

3.2 An Ellipse at an Angle of Attack

The two-dimensional flowfield about an ellipse at an angle of attack was investigated with emphasis on five sections of the flow, namely the front stagnation region, the two separation regions and the two free-shear layers emanating from the separations. Two sets of experiments were run, one with a steady and one with a periodically oscillating freestream.

The ellipse, made of aluminum, had a major axis (2a), 100.1mm and a minor axis (2b) 33.75mm, (a/b = 2.96). This ratio was employed by Schubauer, who conducted experiments about half a century ago. It was also chosen by a contemporary investigator (Ho, 1984) whose work is parallel to ours.

The model spanned the distance of 218 mm between two false tunnel walls and was free to rotate about its center, facilitating the adjustment of the angle of attack (see Fig. 3.2.1). The angle of attack, α, was defined as the angle between the major axis and the free-stream velocity. In order to adjust it accurately, we followed a trial-and-error procedure as follows. Starting from a specific point far from the surface of the model, we moved the laser beams in a direction normal to the surface until they hit it. If the distance travelled by the beams was not equal to that calculated for the specific α, then the ellipse was given a small rotation about its spanwise axis. The same procedure

was repeated, until the distances travelled by the laser beams from several reference points to the wall, were the correct ones. The angle of attack was chosen to be 14° so that the flow separated from a point close to the trailing edge.

The data acquisition system was basically the same as the one used in the experiment of the backward-facing circular arc. However, in the experiment described here, we employed an additional LDV system to record the variation of the free-stream velocity. This was an one-component LDV in the forward-scatter mode with a fringe spacing 5.6 mm. It was positioned approximately 3 chordlengths upstream of the leading edge of the ellipse, and its output signal was fed to a TSI 1995 counter to be processed. The instantaneous free-stream velocity as well as the two velocity components obtained in the region close to the ellipse by the 2-component LDV system (see Sect. 2.3) were stored in the minicomputer (MINK-11). The normalization of the velocity components by the instantaneous free-stream velocity seemed to improve the quality of the data since the variation of the time mean of U_∞ was in the range of 1-3%.

The velocity measurements were obtained in the midspan region of the elliptical cylinder in order to avoid the wall effects and its associated three-dimensional flow patterns. In the unsteady case the free-stream magnitude varied sinusoidally in time, with a period of 4.8 sec. and a peak to peak amplitude of 10% normalized by the time-mean velocity which was (14.3 ± 0.3)cm/s. Therefore, the Reynolds number $Re_m = U_\infty 2\alpha/\nu$ and the frequency parameter $\frac{\omega 2a}{U_\infty}$ were 14300 ± 300 and 0.91, respectively.

There were 16 instantaneous values per period stored for each velocity component and the free-stream. In APPENDIX V we explain the basic features of a FORTRAN program used for the acquisition of unsteady velocity data.

In the following, we discuss the velocity patterns at each of the 5 subsections of the flow around the ellipse.

3.2.1 Suction Side Separation Region

There were 8 unsteady velocity profiles taken in the separating boundary layer and on the suction side, namely at $x/a = 0.2 \div 0.55$, where x is the major axis of the ellipse. The distance $\Delta x/a$ between two adjacent stations was 0.05. In Fig. 3.2.2 we display the velocity vectors obtained by the LDV. At each station, the measuring volume was displaced normal to the model surface, with a smallest displacement of 0.125mm, while the maximum number of data per station was 33. The signals were conditionally averaged over 10 or 15 cycles. In Figs. 3.2.3 and 3.2.4 we show instantaneous velocity vectors while in Figs. 3.2.5-6 we show the corresponding u and v components parallel and normal to the wall, respectively. In the later figures, the solid line corresponds to the smoothed data obtained by the IMSL routine ICSSCU (see Appendix IV). The smoothed data were used for the calculation of the instantaneous vorticity contours of $\omega/10$, where $\omega = \frac{\partial u}{\partial y} - \frac{\partial v}{\partial x}$ shown in Figs. 3.2.7-8 has been nondimensionalized by U_∞/a. In these figures both axes have been nondimensionalized by one half the major axis' length (a).

In Fig. 3.2.9a, the amplitudes of oscillation normalized by the free-stream amplitude are shown. An FFT analysis of the time-dependent u-component did not reveal any significant phase variation across the boundary layer, while the driving frequency was clearly the most predominant frequency. The difference between the steady and unsteady flow fields is depicted in Fig. 3.2.10 where the steady and time-mean velocity vectors are shown.

The basic conclusions drawn by the analysis of the data in this region of the flow are basically the same as those for the circular arc:

(a) Deceleration of the free-stream results in a thickening of the reversed-flow region and an upstream motion of the zero-skin-friction point; the opposite happens when the flow accelerates.

(b) The amplitude of oscillation increases in the shear-layer region and in a downstream direction (maximum observed value of 5.8 times the free stream amplitude).

(c) The zero-skin-friction point for the time-mean velocity field is located downstream of that for the steady case.

3.2.2 Suction Side Free-Shear Layer

Measurements in this area of the flow were taken at 8 stations (see Fig. 3.2.11). The distance between two adjacent points in a station was 0.2mm except for stations 7 and 8 where it was 0.4mm. The unsteady motion of this layer, far and close to the model's surface, is shown in Figs. 3.2.12-13 where velocity vectors have been drawn at time intervals of T/8. The basic features of the flow were

(a) increase of the velocity amplitude in the downstream direction

(b) thickening of the reverse flow region when the freestream decelerated

(c) in the farthest downstream stations, the velocity vectors were not parallel to each other, a phenomenon, we believe, connected with the roll-up process of the shear-layer and the formation of vortices.

In Fig. 3.2.14 where the steady and unsteady time-mean vectors are shown, we notice that in the mean the shear layer is farther from the surface for the steady than the unsteady case.

3.2.3 Stagnation Point

The numerical prediction of the flow about a bluff body becomes easier if information about its stagnation point is available since the integration of the boundary layer equations starts from this point. Measurements in the stagnation-point region were taken for the steady and unsteady case. In order to approach the surface of the model as close as possible, we rotated the optical train so that the beams were located in space as shown in Fig. 3.2.15. For the steady flow, we took measurements along 8 stations normal to the surface and at points with x/a coordinates 0.001, 0.2, 0.4, 0.6, 0.8, 1., 1.2, respectively. The velocity vectors are shown in Fig. 3.2.16. We notice that the flow has been decelerated significantly since its magnitude was 60% of the free-stream at a distance of 0.25a from the wall. The u component at stations 3 to 8 appears to vary linearly with s, where s is the distance from the stagnation point along the wall. This is an indication that

the flow is potential. Apparently boundary-layer measurements were impossible in this region because of its very small thickness. For the oscillating free-stream case, velocities were obtained along 7 stations not normal to the wall, as explained in Fig. 3.2.17. In this case the stagnation point seemed to oscillate along the wall, moving downstream when the flow decelerated. The amplitude of oscillation increased when approaching the surface, with a maximum value of 2.5 times the free-stream amplitude obtained at the station closest to the x-axis (1st station).

3.2.4 Pressure Side Separation Region

In this region we took 6 steady and 7 unsteady velocity profiles normal to the wall, at x/a = 1.6, 1.7, 1.75, 1.8, 1.85, 1.90, 1.95 (for the steady case the station x/a = 1.9 is not included). The unsteady velocity vectors are shown in Figs. 3.2.18-19. Typical time records are shown in Fig. 3.2.20 (stations 2 and 6) together with time records from the suction-side separation region (station 2), for comparison. It appears that the motion of the suction-side free-shear layer disturbs the flow on the pressure side since the temporal variation of the velocity magnitude is not sinusoidal, there. In Fig. 3.2ab, we show the peak-to-peak amplitudes of the velocity normalized by the free-stream amplitude. We notice that the amplitude values are not as large as those in the suction-side separation region. In Fig. 3.2.21 we show the steady and unsteady time-mean velocity vectors.

3.2.5 The Wake

Finally, measurements were taken in the wake in order to provide information about the shear layer emanating from the pressure-side separation point (see Fig. 3.2.22). The unsteady velocity vectors are shown in Figs. 3.2.23-26, and in 3.2.27 we show the steady and time-mean vectors. Here, the sinusoidal variation in time of the velocity is completely absent because of the interaction of the two shear layers. The velocity profiles, as we expected, tend to become uniform downstream of the trailing edge. In order to have a better perspective of the measurements around the ellipse, we show the time mean velocity vectors around the ellipse in Fig. 3.2.28 except for the wake.

3.3 Experimental Investigation of Drifting Vortices

In most cases where vorticity is produced along the surface of the body, the free vortex sheets roll up. The process can be approximated by clusters of vortices or single vortices in the form of a Kármán street. This forms the far field of the vortex shedding process. A good example of such a field is the wake of a pitching airfoil. In this section we discuss the properties of such a flow field. In particular we examine how close such a region of voriticity is to the idealized situation of a Kármán vortex street.

Pitching airfoil experiments have been conducted earlier at VPI (Poling and Telionis, 1983). The wake of a NACA 0012 airfoil pitching about its quarter chord was again studied experimentally with emphasis on the far wake. The amplitude $\Delta\alpha$ and period T of the oscillation were

20° and 0.84 sec., respectively. In dimensionless form, the reduced frequency based on the half-chordlength of the airfoil was $\omega c/2U_\infty = 2.77$ where $U_\infty = 13.5$ m/s. The Reynolds number based on the chord length was 13,500.

The data acquisition system consisted of a one-component L.D.V. system in the back-scatter mode, Bragg-cells for the detection of back flow, a TSI 1985 counter as a signal processor, and a MINK-11 minicomputer. A conditional averaging technique was used; the initiation of the averaging process was triggered by a pulse sent to the minicomputer when the airfoil was passing through a 0° angle of attack in its downstroke motion. At each point in space, 53 instantaneous values of the velocity component (u) in one cycle were stored. The u-component was parallel to the free-stream.

In Fig. 3.3.1, we show schematically the measuring grid. Lengths are compared with the chord length, c. There were 8 vertical stations ($i = 1 \div 8$) covering a total downstream width of 0.7c, and 24 measuring points per station ($j = 1 \div 24$) half of which were above the axis of symmetry, namely the axis Ox in Fig. 3.3.1.

In Figs. 3.3.2-3, we show the time records of the velocity at each measuring point, while in Figs. 3.3.4-6 the instantaneous velocity profiles at nine (9) time instants of the period namely at times t_k where $t_{k+1} = t_k + 24T/210$, $k = 1$ through 8 and $t_1 = T/210$. In the latter group of figures, the solid line is a curve fit, obtained via the IMSL routine ICSSCU (see Appendix IV).

In the instantaneous profiles, we notice that at t_1 (Fig. 3.3.4) there is a minimum at i = 6,7,8 and j = 8 while at t_3 there is a maximum at i = 4,5 and j = 13, indicating the existence of a CCW (counter-clockwise) and CW (clockwise) vortex respectively. Looking at Figs. 3.3.5-6 we observe a downstream displacement of the minimum (or maximum) which is a result of the downstream drifting of the vortices.

The smoothed data of Figs. 3.3.4-6 provide essentially the horizontal velocity component in the x-direction as a function of space and time. Based on these data, we calculated first the velocity gradient $\partial u/\partial y$ for all instances t_k, k = 1,...9. The instantaneous contours of $-\partial u/\partial y$ were plotted in Figs. 3.3.7-11. In these figures, double line contours correspond to CW vortex rotation. It should be noticed that the departure from nearly circular shapes is due to the uneven scales.

The quantity $\partial u/\partial y$ was calculated and plotted here to provide some comparison with results of inviscid theory. A more appropriate quantity of course is vorticity, namely $\partial u/\partial y - \partial v/\partial x$. However, this quantity is identically zero in the analytical field, except at the center of the vortices.

In Figs. 3.3.7-11, the instantaneous location of nearly discrete vortices can be identified. Once again, the drifting of the vortices is apparent. Moreover, we can extract from these figures information about the spacing of the vortices. It was found that the horizontal and vertical spacings were approximately a = 0.6 to 0.7C and b = 0.2C respectively. Therefore the flowfield can be represented by two parallel rows of equidistant vortices of opposite sign (see Fig. 3.3.12). It is very

interesting to observe that the flow pattern differs from that of the wake of a bluff body in a sense that the vortices rotate in the opposite direction (see also Katz and Weihs, 1981).

In order to understand the phenomenon further, we attempted a few comparisons of the experimental flowfield with that generated by a Kármán street of ideal vortices. The complex velocity induced by a Kármán sreet of vortices in an unbounded fluid otherwise at rest is given by the formula (see Milne-Thomson, pg. 376)

$$u-iv = \frac{i\Gamma}{2a}\left[\frac{1}{\tan\left[\frac{\pi}{a}\left(z - \frac{a}{2} + \frac{ib}{2}\right)\right]} - \frac{1}{\tan\left[\frac{\pi}{a}\left(z - \frac{ib}{2}\right)\right]}\right] \qquad (3.3.1)$$

where a,b are shown in Fig. 3.3.12, Γ is the circulation of each vortex and u,v are the horizontal and vertical velocity components respectively.

Using the above formula, we plotted in Fig. 3.3.13 u(y) - profiles in the space between an CCW vortex and a CW vortex. In these figures, we display the dimensionless quantity $u/(\Gamma/2a)$ for a geometry, i.e. a ratio a/b which matches the experiment. The velocity scale in the figures is arbitrary and the intention here is only to provide a qualitative comparison. In each profile we observe the variations of u in the domain y = 2b to y = -2b. The first profile (top, left) corresponds to the vertical station x = a/50, while the last (down, right) corresponds to x = a/2 - a/50, with a = 1.4c and b = 0.2c. These profiles are qualitatively in good agreement with the instantaneous experimental profiles at t_5 in Fig. 3.3.5. In the profiles of the ideal flow, the velocity

increases, or drops very abruptly, in the vicinity of the center of a vortex. This does not happen in the experimental profiles because the real vortices contain a viscous core where the velocity drops to zero. The diameter of the viscous core of the vortices was estimated to be approximately 0.2c.

Another comparison between theory and experiment was made by examining time records at a fixed station in space, namely i = 3. From Fig. 3.3.7 we note that this station is located at x = a/2 + 3a/14 with a = 1.4c, at $t=t_1$. To facilitate comparison, we evaluated the variations of u in the minus x direction, starting at x = a/2 + 3/14a and covering a distance a=1.4c, at various y locations. These variations of u represent the local changes in time of the velocity at the station i = 3 and they are shown in Fig. 3.3.14. In this figure, k = 1 corresponds to y = 2b and k = 18 to y = -2b. We notice here that in the region between the vortices (k = 8,9,10,11) there are two peaks and also that a minimum is converted to a maximum when we are moving from the upper to the lower part of a CCW vortex (k = 7,8), that is when we are crossing a vortex center. The same behavior is observed in the experimental time records of Figs. 3.3.2-3 as well as in Fig. 3.3.15 where the experimental time records at j = 13,15,17 are displayed in more detail.

Another attempt was made to compare the two flow fields, the experimental and the theoretical at a specific time instant, $t = t_9$. Since the experimental u component was known everywhere, numerical integration of the continuity equation gave us the v component; v was taken to be zero at j = 1. In terms of these experimental data, we were able

to construct instantaneous vector fields of the velocity. This is shown in Fig. 3.3.16. From this data, the circulation around the vortices was calculated by integrating

$$\Gamma = \int_C \bar{v} \cdot d\bar{\ell} \qquad (3.3.2)$$

along various contours (see Fig. 3.3.17). The values of $\Gamma/U_\infty c$ decrease as smaller contours were traced, taking the values 0.952, 0.685, 0.544 and 0.441 respectively (see Fig. 3.3.17). This, of course, implies that vorticity is not concentrated at the center of the vortex. A mean value of $\bar{\Gamma}/U_\infty c = 0.58$ was obtained by integrating along numerous different paths around the vortex. This value of Γ as well as $a = 1.3C$ and $b = 0.2C$ were substituted into the formula

$$\frac{u-iv}{u_\infty} = 1 + \frac{i\Gamma}{2a}\left[\frac{1}{\tan\left[\frac{\pi}{a}\left(z - \frac{a}{2} + \frac{ib}{2}\right)\right]} - \frac{1}{\tan\left[\frac{\pi}{a}\left(z - \frac{ib}{2}\right)\right]}\right] \qquad (3.3.3)$$

which is essentially Eq. (3.3.1), modified by an extra term to account for a free-stream with speed U_∞. To match the experimental domain of information, we calculated from Eq. (3.3.3) the velocity field in the domain $-0.5C < x < 0.2C$, $-0.55C < y < 0.55C$. This is shown in Fig. 3.3.18. There seems to be good agreement between the two vector fields, except of course around the position of the vortex where the theoretical solution exhibits a singularity.

A further comparison between theory and experiment can be achieved by plotting the instantaneous u-profiles at $t = t_9$. This is shown in Fig. 3.3.19. Once again agreement is acceptable, except in the immed-

iate vicinity of the vortex center. At this point the analytical solution displays a singularity but to facilitate plotting a certain portion in the figure was cut off and replaced by a straight segment.

Finally, it remains to compare the speed of propagation, namely the rate of drifting of the vortices. It can easily be proved (see also Milne-Thompson, p. 376) that the speed of propagation u_v of each ideal vortex in a Kármán street is given by

$$\frac{u_v}{U_\infty} = 1 + \frac{\Gamma}{2aU_\infty} \tanh \frac{\pi b}{a} \qquad (3.3.4)$$

For the numerical values measured in our experiment, namely $\Gamma/U_\infty C = 0.58$, $a = 1.3C$ and $b = 0.2C$, we obtain $u_v/U_\infty = 1.10$. The velocity of drifting of vortices is a quantity which can be derived very easily from the experimental data. It is simply the ratio of $\frac{a}{TU_\infty}$ where a is the axial spacing of the vortices and T is the period of any velocity signal. This quantity was calculated to be approximately 1.14.

The above analysis shows that for this particular problem the wake can be very well represented by point vortices. This enhances the idea of representing a field with continuously distributed vorticity by ideal vortices (method of vortex dynamics), even in problems where the flow is not well organized. The advantage of using the vortex method for the theoretical prediction of a complicated flowfield is obvious if we compare it with the much harder to solve Navier-Stokes equations. The potential of the method will be demonstrated later.

CHAPTER FOUR

IMPULSIVELY STARTED CYLINDER

4.1 Introduction

The flow about an impulsively started circular cylinder has been studied by many theoreticians and experimentalists, due to both the complex nature of the velocity field and the geometrical simplicity of the body. Very useful information has been provided in the laboratory mainly through flow visualization techniques (hydrogen-buble, Aluninum-dust, electrolysis) by Taneda (1971), Nagata et al (1975, 1980), Bouard et al (1980).

The theoretical prediction of the time development of the flow has been accomplished by employing either the boundary-layer equations or the full Navier-Stokes equations. However, it is known that a finite-difference solution to the Navier-Stokes equations is satisfactory only for low Reynolds numbers (Re). At Re of practical interest, the vortical structures in the wake become so small that a very thin mesh must be used, requiring large computer memory and small time steps. Numerical solutions of the unsteady Navier-Stokes equations have been presented recently for moderate Reynolds numbers. Lin et al (1976) solved the Navier-Stokes equations for low Re and steady flow around a circular cylinder, while very recently Kawamura et al (1984) provided a numerical solution for Re of the order of 10^4. However, even today, it is of great practical importance to employ the boundary-layer approximation and inviscid-flow equations. The boundary-layer equations are solved in the region between the stagnation and separation point, while the shear

layers and the wake are often simulated by vortices. The motion of the vortices is described by the inviscid-flow equations, which do not require a grid, in contrast to the finite-difference methods. Since 1931 when Rosenhead represented for the first time a velocity-discontinuity surface by a series of point vortices, many investigators have employed the same idea with varying degrees of success (see Fink and Soh, 1973). For the case of a circular cylinder it is noteworthy to mention the works of Sarpkaya (1968, 1979), Deffenbaugh (1976), Kuwahara (1978), Spalart et al (1983). In this chapter, we treat the problem for high Re by employing the unsteady boundary-layer equations and a discrete-vortex method, which takes into account vortex shedding. Our approach is therefore an interactive process whereby the developing wake influences the inviscid flow and the evolution in time of the unsteady boundary layer.

4.2 The Boundary-Layer Equations

The non-dimensional boundary-layer equations in their stretched form read

$$\frac{\partial u}{\partial x} + \frac{\partial v'}{\partial y'} = 0 \qquad (4.2.1)$$

$$\frac{\partial u}{\partial t} + u\frac{\partial u}{\partial x} + v'\frac{\partial u}{\partial y'} = \frac{\partial U_e}{\partial t} + U_e\frac{\partial U_e}{\partial x} + \frac{\partial^2 u}{\partial y'^2} \qquad (4.2.2)$$

$$\text{with } v' = v\sqrt{Re} \text{ and } y' = y\sqrt{Re} \ ,$$

where u,v are the velocity components parallel and normal to the wall respectively, x,y are the relevant physical coordinates and Ue is the

u-component at the edge of the boundary layer. In order to facilitate the numerical integration of the above equations, we employ Görtler's transformation, modified for the unsteady case by Telionis et al (1973). The basic advantage of this transformation is that the boundary layer grows very mildly in the transformed plane and therefore the requirements for computer storage are less significant. The new independent variables ξ,η,τ are related to x,y',t through the relations

$$\xi = \int_0^s Ue(x,t)dx \tag{4.2.3}$$

$$\eta = \frac{Ue}{\sqrt{2\xi}}\, y' \tag{4.2.4}$$

$$\tau = t \tag{4.2.5}$$

while the transformed boundary-layer equations read (see Tsahalis, 1972)

$$2\xi \frac{\partial F}{\partial \xi} + F + \frac{\partial V}{\partial \eta} = 0 \tag{4.2.6}$$

$$\frac{2\xi}{U_e^3}(F-1)\frac{\partial Ue}{\partial t} + \frac{2\xi}{U_e^2}\frac{\partial F}{\partial \xi}\int_0^s \frac{\partial Ue}{\partial t}dx + \left(\frac{2\xi}{U_e^3}\frac{\partial Ue}{\partial t} - \frac{1}{U_e^2}\int_0^s \frac{\partial Ue}{\partial t}dx\right)\eta\frac{\partial F}{\partial \eta}$$

$$+ 2\xi F\frac{\partial F}{\partial \xi} + V\frac{\partial F}{\partial \eta} + \frac{2\xi}{U_e^2}\frac{\partial F}{\partial \tau} + \beta(F^2-1) = \frac{\partial^2 F}{\partial \eta^2} \tag{4.2.7}$$

where

$$\beta = \frac{2\xi}{Ue}\frac{dUe}{d\xi} \tag{4.2.8}$$

$$F = \frac{u}{Ue} \tag{4.2.9}$$

$$v' = \frac{Ue}{\sqrt{2\xi}}V - \frac{\partial \eta}{\partial x}\sqrt{2\xi}\,F \tag{4.2.10}$$

It is noteworthy to mention that for the unsteady case, points in the ξ,η plane do not have a one-to-one correspondence with points in the x,y plane. The numerical computation proceeds in the ξ,η plane. In our computational method, x is then computed in terms of ξ numerically through equation $\xi - \int_0^s U_e(x,t)dx = 0$, using Newton's method.

The $U_e(x)$ distribution is approximated by a polynomial with a maximum degree of 10 by a least-squares method (see Carnahan, Luther, Wilkes, p. 576). The boundary conditions in terms of the new independent variables are

$$F(\xi,0,t) = V(\xi,0,t) = 0, \tag{4.2.11}$$

$$F(\xi,\infty,t) \to 1. \tag{4.2.12}$$

Eq. (4.2.7) can be rewritten as follows

$$\frac{\partial^2 F}{\partial \eta^2} + a_1 \frac{\partial F}{\partial \eta} + a_2 F + a_3 + a_4 \frac{\partial F}{\partial \xi} = 0 \tag{4.2.13}$$

with

$$a_1 = -\eta\left[\frac{2\xi}{U_e^3}\frac{\partial U_e}{\partial t} - \frac{1}{U_e^2}\int_0^s \frac{\partial U_e}{\partial t}\,dx\right] - V \tag{4.2.14}$$

$$a_2 = -\frac{2\xi}{U_e^3}\frac{\partial U_e}{\partial t} - \beta F - \frac{2\xi}{U_e^2 \Delta\tau} \tag{4.2.15}$$

$$a_3 = \frac{2\xi}{U_e^3}\frac{\partial Ue}{\partial t} + \beta + \frac{2\xi}{U_e^2}\frac{F^\circ}{\Delta\tau} \tag{4.2.16}$$

$$a_4 = \mp 2\xi F - \frac{2\xi}{U_e^2}\int_0^x \frac{\partial Ue}{\partial t}\,dx \tag{4.2.17}$$

where F° is the value of F at the preceding time station at a fixed (ξ,η) location. This term was introduced in Eq. (4.2.16) via the

finite-difference form of $\frac{\partial F}{\partial \tau}$ which was assumed equal to $\frac{F-F^o}{\Delta \tau}$. In Eq. (4.2.17) the positive sign corresponds to upwind integration, i.e. marching in positive x but in a region where $F < 0$.

The system of equations (4.2.6 and 4.2.13) is solved numerically by a finite-difference method. This is essentially an iterative procedure which proceeds as follows: an approximate solution of F is obtained from Eq. (4.2.13) (by a subroutine developed by Werle and Davis, 1972) and it is substituted in Eq. (4.2.6) to obtain V. The process is repeated several times until the value of $\partial F/\partial \eta$ does not change up to the fourth decimal point between two consecutive iterations.

4.3 Small-Time Behavior

Blasius (1908) found a solution to the boundary-layer equation for the case of the impulsive start of the flow about a cylinder of arbitrary cross section. Blasius' asymptotic expansion holds for small times and reads

$$u/U_e(x) = \text{erf}(\eta') + t \frac{dU_e}{dx} f_2(\eta') \tag{4.3.1}$$

where

$$\eta' = \frac{y'}{2\sqrt{t}} \tag{4.3.2}$$

and

$$f_2(\eta') = \left(\frac{2\eta'^2-1}{2}\right) \text{erf}^2(\eta') + \frac{3}{\sqrt{\pi}} \eta' e^{-\eta'^2} \text{erf}\eta' + 1$$

$$- \frac{4}{3\pi} e^{-\eta'^2} + \frac{2}{\pi} e^{-2\eta'^2} - \left(1 + \frac{2}{3\pi}\right) (2\eta'^2 + 1) + \frac{1}{\sqrt{\pi}} \left(1 + \frac{4}{3\pi}\right)$$

$$\left[\frac{1}{2}\sqrt{\pi}\,(2\eta'^2 + 1)\,\text{erf}(\eta') + \eta' e^{-\eta'^2}\right] \tag{4.3.3}$$

The above expression evaluated at $t = t_{i\eta}$ was taken as the initial condition for F in our calculations,

$$F(\xi,\eta,t_{i\eta}) = \text{erf}(\eta') + t_{i\eta} \frac{dUe}{dx} f_2(\eta') \qquad (4.3.4)$$

and $$\eta' = \frac{\eta}{Ue} \sqrt{\xi/2t_{i\eta}} \text{ (see eqs. 4.2.4, 4.3.2)} \qquad (4.3.5)$$

and $$Ue = 2\sin x \qquad (4.3.6)$$

where t_{in} is a time instant after the start of the flow. This parameter (t_{in}) was arbitrarily chosen to be 0.05. It should be mentioned here that t_{in} should not be very small because otherwise the grid in η-direction in the rear-stagnation-point region must be extremely thin in order to include enough points inside the boundary layer. Thus, the grid in the η-direction was expressed in terms of 3 geometric progressions with the common ratio ω and the first term a as follows

$$\omega = 1.06,\ 1.2,\ 1.01$$

$$a = 0.002,\ 0.02,\ 0.64$$

where $\omega = 1.06$ and $a = 0.002$ correspond to the grid region next to the wall. Thus, at the rear stagnation point ($\phi = 178°$) and $t = t_{in}$, there were 10 points located inside the boundary layer while, for example, at $\phi = 18°$, there were 30 points. In the x direction, Δx was constant and equal to 2° (note that $\Delta\xi$ is not constant) while $\Delta\tau = 0.01$.

A very interesting feature of the flow under consideration is that the point of zero-skin-friction appears at the rear stagnation point at a finite time, t_{zs}, and then travels upstream, thus covering the rear of

the cylinder with a recirculating bubble. Because for small times this bubble is thin, the boundary layer assumptions still hold.

The present calculations indicate that t_{zs} is equal to 0.32, in agreement with the values calculated by many researchers (Collins and Dennis, 1973; Cebeci, 1979; and Wang, 1979). Telionis and Tsahalis (1974) found t_{zs} to be 0.35. We believe that this discrepancy is due to the fact that the grid they used was coarse in the η-direction for their value of $t_{in} = 0.001$. The situation becomes even more critical in the rear stagnation region, where their initial velocity profiles were essentially uniform or $u/U_e(x) = 1$. The upstream motion of the point of zero skin friction in time is shown in Table 4.3.1.

As time progresses, the boundary-layer thickness increases in the reversed-flow region and at a time $t = t_s$ a singularity appears in δ^* (displacement thickness) at $x = x_s$. In Fig. 4.3.1, $\delta^*(x)$ is shown at different times. We notice that at $t = 1.9$ δ^* increases sharply in the region $x = 104°$-$110°$ while $\frac{d\delta^*}{dx}$ becomes negative at $x = 120°$. Previously, at $t = 1.66$, $d\delta^*/dx$ becomes negative for the first time at a downstream position $x = 134°$. If we define the separation point as the location where $\frac{d\delta^*}{dx}$ becomes maximum, then according to Fig. 4.3.1, $x_s = 108°$ and $t_s = 1.9$. The same problem was solved with a Langrangian method by Van Dommelen and Shen (1981) and with an Eulerian method by Cebeci (1981). They both found that at $x_s \simeq 111°$-$114°$ and $t_s = 1.5$, the displacement thickness increases sharply. This was a verification of the claim of Sears and Telionis (1975), that the unsteady boundary layer equations can develop singularity at finite time. It should be pointed

out that despite the singular increase of δ^*, no numerical breakdown was observed. Moreover, the present calculations explain why the earlier efforts of Telionis and Tsahalis (1974) erroneously predicted the appearance of a singularity at a much earlier time, namely $t = 0.8$.

In Figs. 4.3.2-5, we show contours of $\partial u/\partial y$ at different time instants namely at $t = 0.86$, 1.26, 1.46, 1.56, respectively. We notice that the curve $\omega = 0.5$ at $t = 1.41$ and $x \approx 2$ splits into two, one attached to the surface and another far from it which in the next time steps moves downstream. Moreover, the direction of the peak line of the vorticity contour turns further away from the wall.

4.4 Vorticity Shedding

It is known that the vorticity produced on the surface of the body is shed into the flow at the separation point. An approximate method of simulating the behavior of the free-shear layers is based on discrete vortex dynamics. At each time step, a new (nascent) vortex is introduced into the flow at the separation point, and at a certain distance δ_s^* far from the wall. The strength $\Gamma(t)$ of the vortex and δ_s^* are given by (see also Chapter 3.1, p.35)

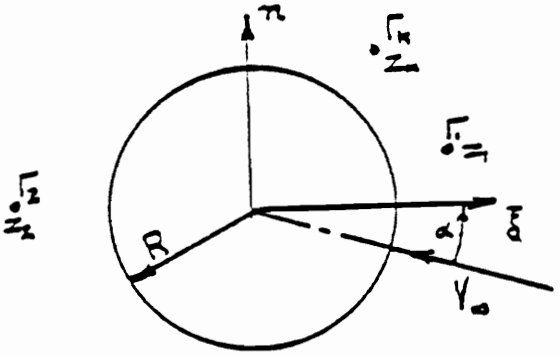

Fig. 4.4.1 Circular cylinder and ideal vortices around it.

$$\Gamma(t) = \frac{1}{2} U_e^2(x_s)\Delta t \qquad (4.4.1)$$

$$\delta_s^* = \delta^*(x_s). \qquad (4.4.2)$$

The nascent vortex is convected downstream by the local velocity which, in complex notation, is given by the formula

$$W_z = u - iv$$

$$W_z = -1 + \frac{1}{z^2} + \frac{i}{2\pi} \sum_{k=1}^{N} \Gamma_k \left[\frac{1}{z-z_k} - \frac{1}{z-1/\overline{z}_k} + \frac{1}{z}\right] \qquad (4.4.3)$$

where u,v are the components parallel and normal to the free stream (see Fig. 4.4.1), Γ_k is the strength of the kth vortex, z_k its position and $\overline{z_k}$ the conjugate of z_k. In order to avoid unrealistically high velocities when two vortices approach each other, we used a merging scheme. When two vortices (Γ_k, z_k) and (Γ_ℓ, z_ℓ) were close enough so that $|z_k - z_\ell| \leq \varepsilon$ (ε was chosen to be equal to Δt), they were replaced by one vortex $\Gamma_{k\ell}$ at $z = z_{k\ell}$ where

$$\Gamma_{k\ell} = \Gamma_k + \Gamma_\ell \qquad (4.4.4)$$

and

$$z_{k\ell} = \frac{\Gamma_k z_k + \Gamma_\ell z_\ell}{\Gamma_k + \Gamma_\ell} \qquad (4.4.5)$$

Since $x_s = 108°$ was considered to be the separation point at $t = 1.9$, the calculation of the flow field for $t > 1.9$ was as follows: first the boundary-layer was integrated in the region $0 \leq x \leq x_s$ (x_s is a function of time), then one vortex was shed at each separation point, namely at z_s and $\overline{z}_s$ (we assumed complete symmetry of the flow about the parallel to the free stream axis), where $z_s = e^{ixs}$ and these vortices were convected downstream with a velocity w_z (see Eq. 4.4.3). Finally, the $U_e(x)$ distribution was calculated taking into account the shed vortices

according to

$$U_e(x) = \left|-1 + \frac{1}{z^2} + i \sum_{i=1}^{N} \Gamma_k \left[\frac{1}{z-z_k} - \frac{1}{z-1/z_k} + \frac{1}{z}\right]\right|, \quad (4.4.6)$$

$z = e^{ix}$, where $0 \leq x \leq x_s$. The same process was repeated until the time instant that the criterion $|F(\eta_{max}) - F(\eta_{max}-\Delta\eta)| \leq 10^{-3}$ was not satisfied, indicating that the boundary-layer thickness was greater than η_{max}. In this case, the separation point was positioned one station upstream and the procedure was repeated.

In Fig. 4.4.2, we show for Re = 10^5 the vortex locations at different time instants after the first vortex was introduced. In other words, these vortices represent the shear layers which spring from the separation point. We notice that initially the vortices follow the contour of the body, but later on they move far from it. The same behavior was observed in the laboratory by Bouard et al (1980) and for a Reynolds number of about 10^4. In our calculations, the point of separation moves upstream with a mean rate of 0.5° per time step. However, it seems that, although it moves more slowly as it approaches 80° (which is generally accepted as the separation point for laminar flow), it continues to move upstream. This is a serious drawback of the method, which should be attributed to the very crude simplification of representing the actual vorticity by a point vortex. In fact, the vortices close to the separation point are responsible for causing an unrealistic deceleration of the U_e velocity. The same behavior was mentioned by Deffenbaugh and Marshall (1976), who found the final position of the separation point to be at $\phi = 67°$.

CHAPTER FIVE

MODELING PROPAGATING STALL BY VORTEX DYNAMICS

5.1. Introduction

In this section we discuss another application of the vortex dynamics method to the phenomenon of propagating (rotating) stall. It was felt that the time delay between the stall of a blade and its neighbor is due exactly to phenomena studied in this work, namely the inertia of unsteady separation and the time involved in the development and convection of a free shear layer. Both phenomena have been studied experimentally earlier and have been modeled by finite-difference boundary-layer solutions and discrete vortex dynamics, respectively.

The phenomenon of rotating stall was first discovered in 1941 by Whittle's group in England but remained unnoticed for many years. It consists of one or more stall zones, each one of which covers a number of blades in a cascade and which propagate along the blades with a speed less than the rotor speed. An explanation of rotating stall is as follows: when the cascade operates close to stalled condition an increase in angle of attack on one blade leads to separation on that blade, resulting in turn to an increase and a decrease in the angle of attack on the blades above and below the stalled blade, respectively. As a result, the blade alone stalls and the process is repeated. This unsteady phenomenon may occur when the compressor mass rate decreases, resulting in an increase of the relative angle of attack on the blades or in the starting operation of the compressor. As a result, the efficiency of the cascade drops and a fatigue failure of the blades may

occur due to the abrupt changes of the aerodynamic forces exerted on them.

Since 1950 there has been much research in this area, but still today there is a lack of basic knowledge due to the complexity of the phenomenon. For instance, it is not known yet what determines the number of stall cells and their speed of propagation in each stage of a compressor. Great efforts have been made, both via experiment and/or analysis to understand and predict the phenomenon. Most of the analytical methods have been devoted to the prediction of the onset of unsteady stall. The idea is based on the stability characteristics of a small perturbation imposed on the upstream mean flow. Such methods are based on assumptions that (i) the cascade can be represented by a linear two-dimensional sequence of blades, (ii) viscosity and compressibility are negligible and that (iii) the blade row can be represented by an actuator disc. Earlier models were linear like those of Sear's (1955) and Marble's (1955), but more recently, Nagano and Takata (1972), Adamzyk and Carta (1973) and Sexton and O'Brien (1980) demonstrated how non-linear models can be used. However, the time response of the blade characteristics to a change in inlet flow conditions was assumed to be linear.

The effectiveness of such methods hinges critically on experimental data of stall propagation. This line of thought yielded useful practical models but it did not disclose the detailed physical characteristics of the phenomenon. This is mainly due to the oversimplifying assumption of representing the blade row by an actuator disk. Modeling

the detailed flow, including separation over blades, has been attempted by Sisto and his associates (Perumal and Sisto, 1974; Tokel and Sisto, 1978). However, their interest was confined to flutter.

In this chapter we attempt to model the entire flow field about each blade and therefore capture the growth of the wakes, the blockage of a few blade passages and the propagation of stall. Eventually such a method could be used to estimate the stalling characteristics of particular blade shapes in arbitrary cascade configurations. It is intended to include eventually a viscous model for predicting the unsteady evolution of boundary layers and separation. A combination of conformal mapping and a distribution of bound vortices were used to model the flow through a cascade of blades, while free vortices allowed the simulation of rotating stall.

Some efforts have been devoted in the coupling of boundary-layer solutions with the potential flow through the cascade. However, serious difficulties were encountered in solving the equations near the leading edge, where the adverse pressure gradients grow very sharply and the curvature effects become significant. The location and time of separation is assumed. The Reynolds-number dependence is therefore part of our assumptions. The development of the vortex layers is then governed by the dynamics of vorticity.

5.2 The Transformation

The distribution of bound vorticity necessary to satisfy the no-penetration condition on an airfoil changes if a vortical wake develops

and unwinds over its surface. Therefore at every time step it is necessary to recalculate the bound vorticity. This task becomes easier if the potential solution is obtained via a conformal transformation that maps the contour of the airfoil onto a circle. In the present work, the Joukowski and Theodorsen transformations are employed, to map a linear cascade of identical blades of arbitrary shape in a cascade of closed contours, one of which is a circle. The plane of the cascade of blades is the ζ-plane and is referred to as the physical plane. The plane in which one element of the cascade is a circle is the z-plane and is called the phase plane.

Consider the transformation (Theodorsen, 1935)

$$\zeta = z' + \frac{a^2}{z'} \ , \ z' = z \exp\left(\sum_{1}^{\infty} \frac{C_n}{z^n}\right) \tag{5.2.1}$$

where $z' = \pm a$ are the singular points in the z' plane and C_n are complex constants, $C_n = A_n + iB_n$, dictated by the shape of the airfoil. The constant a is 1/4 the distance between the point midway betweeen the leading edge and the center of curvature of the leading edge and the point midway between the center of curvature of the trailing edge and the trailing edge (see Theodorsen, NACA Rep. No. 452, p. 7). The notation for real and imaginary variables as well as the notation for arguments and moduli are defined in Fig. 5.2.1.

In the physical plane the shape of the airfoil is defined parametrically in terms of the equation

$$x = 2a \cosh \psi \cos\theta \tag{5.2.2}$$

$$y = 2a \sinh \psi \sin\theta \tag{5.2.3}$$

The polar function $\psi(\theta)$ is therefore given by

$$\sinh \psi(\theta) = \pm\left[-\frac{p}{2} + \frac{1}{2}\left(p^2 + \left(\frac{y}{a}\right)^2\right)^{1/2}\right]^{1/2} \tag{5.2.4}$$

where

$$p = 1 - \left(\frac{x}{2a}\right)^2 - \left(\frac{y}{2a}\right)^2 \tag{5.2.5}$$

The real and imaginary parts of the constants C_n can then be determined (Theodersen, 1935) via

$$\frac{A_n}{R^n} = \frac{1}{\pi}\int_0^{2\pi} \psi(\phi)\cos(n\phi)d\phi \tag{5.2.6}$$

$$\frac{B_n}{R^n} = \frac{1}{\pi}\int_0^{2\pi} \psi(\phi)\sin(n\phi)d\phi \tag{5.2.7}$$

where R is the radius of the circle in the z plane

$$R = a\, e^{\psi_0} \tag{5.2.8}$$

and ψ_0 is an integral over the periodic function ψ

$$\psi_0 = \frac{1}{2\pi}\int_0^{2\pi} \psi(\phi)d\phi \tag{5.2.9}$$

The calculation of the coefficients in Eqs. (5.2.6) and (5.2.7) is not straightforward, because the funcion ψ is normally defined in the physical plane in terms of the angle θ. To determine ψ as a function of ϕ, a method of successive approximations can be employed. For airfoils with contours not far from a Joukowski airfoil usually one step in the approximation process is enough (Theodorsen, 1935). This was

verified numerically, and therefore the function $\psi(\phi)$ was determined for all the calculations reported here by displacing the argument of $\phi(\theta)$

$$\phi = \theta - \frac{1}{2\pi} \int_0^{2\pi} \psi(\theta') \cot \frac{\theta'-\theta}{2} d\theta' \qquad (5.2.10)$$

The method has been tested for a single blade. A circular-arc blade, defined in Fig. 5.2.2, was used throughout this analysis. Examples were calculated with 5 and 30 terms in the summation of Eq. (5.2.1). A difference of 0.5% in chord percentage was observed for these two cases in the vicinity of the leading and trailing edge.

The solutions discussed in the following sections were obtained in the phase plane in which one blade appears as a circle. This blade will be termed in the sequel, the "central" blade and all other blades will be termed "external". The images of infinite identical blades in a row in the physical plane do not correspond to identical blades in the phase plane. Given a certain cascade of blades, the exact shape of the configuration in the phase plane cannot be determined because it involves the inverse transformation namely the determination of z in terms of ζ.

A closer examination of the two transformations revealed that the Theodorsen transformation distorts very mildly the geometry of the blades and the flow away from the immediate neighborhood of the circle. Thus, as a first approximation for the determination of the blade geometry, it was decided simply to invert only the Joukowski transformation. By so doing the external blades define a distorted configuration in the z-plane. An estimate of the error can be obtained by employing

the complete transformation when plotting back in the ζ-plane the images of the approximate contours in the z-plane. The error involved is the difference between two ζ's, the one given by the complete transformation in Eq. (5.2.1) and the ζ given only by the Joukowski transformation. This error is

$$E = z'\exp\left(\sum_{1}^{\infty} \frac{C_n}{z'^n}\right) + \frac{a^2}{z'\exp\left(\sum_{1}^{\infty} \frac{C_n}{z'^n}\right)} - \left(z' + \frac{a^2}{z'}\right) \qquad (5.2.11)$$

It can be shown that in the limit of $z' \to \infty$, the error tends to

$$E = \lim_{z' \to \infty} \left[C_1 + \frac{2C_2}{z'} + \ldots\right] \qquad (5.2.12)$$

and therefore employing only a Joukowski instead of the complete transformation results in a uniform displacement of the blades by the complex constant C_1. In our case this constant was equal to (0.097)iR.

The proper configuration in the z-plane was thus determined as follows: All the blades in the ζ-plane except for the central blade were displaced by the complex constant $-C_1$. Their images were then calculated by the inverse Joukowski transformation. For a solidity ratio of 1 this involved an error of less than 0.1% in the position of the first external blade and the error decreased sharply for subsequent blades. This is shown in Fig. 5.2.3 for a blade spacing equal to 1/2 of the chord length.

5.2.1 Conditions Under Which the Transformation is Conformal

Theodorsen (1935) proved that the following inequality should hold

$$-\infty \leq \frac{d\varepsilon(\phi)}{d\phi} \leq 1$$

in order to have one to one correspondence between boundary points of the circle in the z plane and boundary points of the "almost" circle in the z' plane. Using the same inequality he proved that the derivative of the transformation $z' = ze^{i\sum_{1}^{\infty} \frac{c_n}{z^n}}$ does not vanish at any point of the external region of the circle (see NACA Rep. 452, p. 11). The derivative of the transformation $\zeta = z' + \frac{a^2}{z'}$, vanishes at $|z'| = a$. For points on the body (or of the "almost" circle) it vanishes if

$$y + i\theta = 0$$

since $z' = ae^{\psi+i\theta}$ for points on the almost circle. For the particular body used in our calculations, $\psi(0)$ does not vanish and therefore there are no singular points on the contour of the body. Moreover, there are no singular points in the region outside the body since $|z'| \neq a$, there.

5.3 Steady Cascade Flow

The calculation of steady incompressible attached flow through a linear cascade of arbitrary blade shape with solidity ratio $\sigma = \frac{c}{s}$ and stagger angle γ (see Fig. 5.3.1) was based on a classical formula for the flow about a single circular cylinder in the presence of discrete vortices (Milne-Thomson, p. 362). According to this formula, the complex velocity for the flow about a circular cylinder of radius R is given by

$$w(z) = -e^{i\alpha} + \frac{e^{-i\alpha}}{z^2} + \frac{i\Gamma}{z} + i \sum_{k=1}^{N} \Gamma_k \left\{ \frac{1}{z - z_k} - \frac{1}{z - \frac{1}{\bar{z}_k}} + \frac{1}{z} \right\} \qquad (5.3.1)$$

where $w(z) = u - iv$ (see sketch below).

In this equation Γ, z and w, vortex strengths complex coordinates and complex velocities were rendered dimensionless by dividing by $2\pi R U_\infty$, R and U_∞, respectively, with U_∞ the velocity of the oncoming stream.

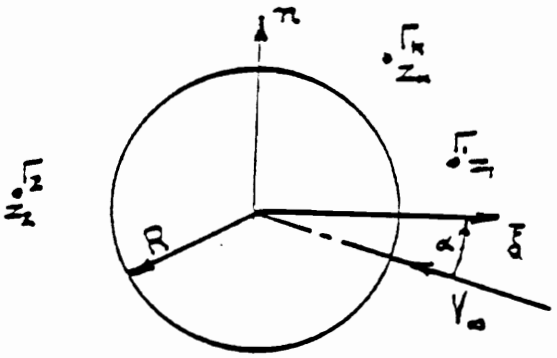

The first three terms in Eq. (5.3.1) generate the flow with circulation Γ about the circular cylinder. The first term under the summation represents a vortex of strength Γ_k located at the point z_k outside the cylinder. The other two terms are images of the k^{th} vortex inside the cylinder, necessary for preserving its shape.

Two different types of vortices Γ_k were employed in the present work: Bound vortices which were situated along the chordlines of cascade blades to satisfy the no-penetration condition on the blades and free vortices which were released from points of separation in order to simulate the development of unsteady wakes. Bound vortices will be denoted by the symbol $\tilde{\Gamma}$, whereas free vortices will be denoted by a plain Γ.

To generate the attached steady flow about a cascade, an iteration scheme was employed. To calculate the inviscid flow about the blades, an arbitrary condition is necessary to set the value of circulation. To

this end, a pseudo Kutta condition was imposed. The rear stagnation point was assumed to be at the point where the x-axis cuts the circular arc (see Fig. 5.2.1) which represents the rounding of the trailing edge of the blade. This assumption is not so crucial for the problem under consideration, since unsteady stalling flow is eventually calculated.

To generate the solution for the flow through a cascade of infinite blades the following iteration scheme was followed. Based on the pseudo Kutta condition the attached flow about a single blade was first determined. The equivalent bound vorticity distribution was then calculated at 22 equi-spaced positions along the chord by virtue of the formula

$$\tilde{\Gamma}_j(x_j,y_j) = (|w_{uj}| - |w_{\ell j}|)\Delta x_j \qquad (5.3.2)$$

where w_{uj} and $w_{\ell j}$ are the velocities at station x_j above and below the airfoil respectively and y_j is the coordinate of the chordline. This distribution of discrete vortices is then positioned along the chordline of all external blades above and below the circle in the phase plane. The flow due to this infinite number of vortices must then be calculated. It is given by formula (5.3.1) but a more practical expression can be derived simply by summing over the infinite series.

It can be proved that the summation of terms $1/(z-z_k)$ can be expressed in terms of a hyperbolic cotangent (Yocum, 1981)

$$\sum_{k=1}^{\infty} \frac{1}{z-z_k} = \frac{\pi}{\ell}\left[\cot\frac{(z-z_j)\pi}{\ell} - \frac{\ell}{(z-z_j)\pi}\right] \qquad (5.3.3)$$

We have proved that the other terms in Eq. (5.3.1) can also be grouped

in a similar way.

$$\sum_{k=1}^{\infty} \left(\frac{1}{z} - \frac{1}{z - \frac{1}{\bar{z}_k}}\right) = -\frac{\pi}{\bar{\ell} z^2}\left[\cot\frac{(z\bar{z}_j - 1)\pi}{z\bar{\ell}} - \frac{z\bar{\ell}}{(z\bar{z}_j - 1)\pi}\right] \quad (5.3.4)$$

In these formulas, ℓ is the complex distance between two adjacent blades in the physical plane, $z_j = x_j + iy_j$ and an overbar stands for a complex conjugate of a quantity.

The flowfield about a circle (representing the "central" blade) and 22 parallel rows of infinite equispaced vortices (representing the rest of the blades) is given in the z-plane by the formula

$$w(z) = -e^{i\alpha} + \frac{e^{-i\alpha}}{z^2} + \frac{i\Gamma}{z} + i\sum_{j=1}^{22} \tilde{\Gamma}_j \frac{\pi}{\ell}$$

$$\left[\cot\frac{(z-z_j)\pi}{\ell} - \frac{\ell}{(z-z_j)\pi}\right] - i\sum_{j=1}^{22} \tilde{\Gamma}_j \frac{\pi}{\bar{\ell} z^2}$$

$$\left[\cot\frac{(z\bar{z}_j - 1)\pi}{z\bar{\ell}} - \frac{z\bar{\ell}}{(z\bar{z}_j - 1)\pi}\right], \quad (5.3.5)$$

where α is the mean angle of attack, or the angle between the chord and the average flow vector U_∞ (see Fig. 5.3.2). In the same figure, V_{IN} and V_E are the velocity vectors far upstream and downstream of the cascade respectively, while a_{IN} and a_E are the angles between V_{IN}, V_E and the chord line of the blade. The vectors $D\hat{A}$ and $D\hat{E}$ are the upwash and downwash velocities respectively due to the bound vorticity of the

blades. Since AD = DE it is easily found a relationship between α, α_{IN}, α_E namely

$$2\tan(\gamma + \alpha) = \tan(\gamma + \alpha_{IN}) + \tan(\gamma + \alpha_E)$$

From the above expression we can define the angle α by an iterative procedure if γ and α_{IN} are given.

The presence of the vortices $\tilde{\Gamma}_j$ results in a change of the rear stagnation point on the circle, i.e. the image of the central blade. In effect then the Kutta condition is violated. To compensate for this the value of the bound vorticity Γ must be readjusted. The first iteration for Γ, namely Γ^1 is thus calculated. This in turn is used to calculate the velocities at 44 points on the skin of a blade and via Eq. (5.3.2) a new distribution of bound vorticity $\tilde{\Gamma}_j^1$. These values are substituted again in Eq. (5.3.5) to determine a new flow field. The process is repeated until convergence is achieved.

There is only a minor detail which should be discussed here briefly. The blade images in the z-plane are similar to each other and equally spaced within a spacial accuracy of 2% for blades beyond the fifth away from the central blade. The infinite series summations of Eqs. (5.3.3) and (5.3.4) can be used effectively only for blades beyond the fifth position from the central blade. This was achieved by subtracting the influence of five identical and equi-spaced blades from Eq. (5.3.5) and adding the same vorticity distribution on the displaced chordline as determined by the method of Section 5.2.

Results of the present method were compared with results obtained by a Douglas-Newmann code which was kindly supplied by Mr. Yokum (1981).

The pressure distribution over the suction and pressure sides obtained by the two methods are shown in Figs. 5.3.3 and 5.3.4, where p is the static pressure on the surface of the blade and p_∞, the pressure at infinity.

5.4 Unsteady Stall

The shapes of developing blade wakes were determined by releasing discrete vortices at the points of separation. In this section we briefly describe the method for a single blade.

Discrete vortices were released at small distances, 2% of chord above the wall and at the points of separation. Numerical experiments were conducted to determine the infuence of the assumption of the location of separation. The free vortices were allowed to be convected by the flow. To this end a computer program was developed and the convection process was simulated by small displacements corresponding to equal time intervals.

At each time step, three quantities are unknown. The two nascent vortices released at the points of separation $\Gamma_{\ell q}$, Γ_{tq} and the new value of the bound vorticity, Γ. Subscripts ℓ and t will be used here to denote the leading and trailing edges of the blade respectively, and q will be a counter of the time steps. Three conditions are necessary for determining these quantities and these can be the conditions that the velocity on the skin of the body at the points of separation is zero and the fact that the total amount of vorticity remains constant:

$$-e^{i\alpha} + \frac{i\Gamma^{(n)}}{z_\ell} + \frac{e^{-i\alpha}}{z_\ell^2} + i \sum_{q=1}^{2n} \Gamma_q \left(\frac{1}{z_\ell - z_q} - \frac{1}{z_\ell - \frac{1}{z_q}} + \frac{1}{z_\ell}\right) = 0 \quad (5.4.1)$$

$$-e^{i\alpha} + \frac{i\Gamma^{(n)}}{z_t} + \frac{e^{-i\alpha}}{z_t^2} + i \sum_{q=1}^{2n} \Gamma_q \left(\frac{1}{z_t - z_q} - \frac{1}{z_t - \frac{1}{z_q}} + \frac{1}{z_t}\right) = 0 \quad (5.4.2)$$

$$\Gamma^{(n)} + \sum_{q=1}^{n} (\Gamma_{\ell q} + \Gamma_{tq}) = \text{const.} \quad (5.4.3)$$

In the above equations a superscript in a parenthesis denotes the order of the time step. The assumption that the separation points are stagnation points, although not explicitly expressed in this way, was used by Sarpkaya (1979) and Deffenbaugh-Marchall (1976) in two different discrete-vortex methods for the case of separated flow past a circular cylinder. In an inviscid model Ham (1968) considers that, for a fully separated airfoil both leading and trailing edge separation points are stagnation points, while Katz (1981) using a completely different vortex method, introduces a small vertical displacement of the nascent vortex to fulfill the no slip-condition at the separation point. The new position of the qth vortex is then determined at the time step n+1 in terms of its position at the step n and the local value of the complex velocity via the equation

$$z_q(t+\Delta t) = z_q(t) + \overline{w}_q^{(n)} \Delta t \quad (5.4.4)$$

It should be emphasized that the quantity w_q does not contain the con-

tribution due to the qth vortex itself. This is a well known result for vortices that are free, i.e. vortices that "carry no force".

The paths of the corresponding vortices in the physical plane are not the mappings of the paths in the phase plane. According to Routh's theorem (Milne-Thomson, 1960), the position of the kth vortex in the ζ plane is given by

$$\zeta_q(t+\Delta t) = \zeta_q(t) + \left[\frac{\overline{w}_q(z_q,t)}{\left.\frac{d\zeta}{dz}\right|_{z=z_q}} + \overline{i\Gamma_q \frac{\partial}{\partial \zeta} \ell n \left(\frac{1}{\left.\frac{d\zeta}{dz}\right|_{z=z_q}}\right)}\right]\Delta t \qquad (5.4.5)$$

This formula reduces after some algebra to

$$\zeta_q(t+\Delta t) = z_q(t)\, e^{\sum_1^\infty \frac{c_n}{z_q^n(t)}} + \frac{a^2}{z_q(t)\, e^{\sum_1^\infty \frac{c_n}{z_q^n(t)}}}$$

$$+ \frac{1}{\frac{d\zeta}{dz}}\left[\overline{w_q(z_q,t)} - i\Gamma_q\left[\overline{\frac{d^2\zeta}{dz'^2}\frac{dz'}{dz} \Big/ \frac{d\zeta}{dz'}}\right.\right.$$

$$\left.\left. + \overline{\frac{d^2z'}{dz^2} \Big/ \frac{dz'}{dz}}\right]\right] \cdot \Delta t \qquad (5.4.6)$$

The derivatives appearing above have been calculated for the present transformation as described in the Appendix VI.

If two or more vortices approach each other, unrealistically high velocities occur leading to failure of the computational scheme. To

avoid this problem several techniques have been proposed like rediscretization of vortex sheets (Sarpkaya, 1979), or substitution of a number of vortices by a single equivalent vortex (Ham, 1968). In this work, we calculated the velocity at a point z, neglecting all the vortices Γ_q which were in a small circle of radius ε and center at z, i.e.

$$|z_q - z| \leq \varepsilon \tag{5.4.7}$$

The parameter ε was chosen to be 0.1.

The aerodynamic force exerted on each blade is calculated by integration of the presure distribution over the surface of the blade. Bernoulli's equation in its unsteady dimensionless form reads

$$p = -\frac{2}{R}\frac{\partial \phi}{\partial t} - |w_b|^2 + c_1(t) \tag{5.4.8}$$

where w_b is the complex velocity on the blade surface. The potential function ϕ takes the same value for corresponding points of the conformal transformation. This function, in the complex plane of the cylinder is given by

$$\phi = \text{Real } [F(z)] \tag{5.4.9}$$

where F(z) is the complex potential given by

$$F(z) = -z\, e^{i\alpha} - \frac{e^{-i\alpha}}{z} + i\Gamma \ln z + i \sum_{q=1}^{N} \Gamma_q \{\ln(z-z_q) - \ln(z - \frac{1}{\bar{z}_q}) + \ln z - \ln(-\bar{z}_q)\} \tag{5.4.10}$$

The derivative $\frac{\partial \phi}{\partial t}$ at a time $t = t_n$ is given approximately by

$$\left.\frac{\partial \phi}{\partial t}\right|_{t=t_n} = \frac{\phi^{(n)} - \phi^{(n-1)}}{\Delta t} \qquad (5.4.11)$$

The lift and drag was then determined by computing the integral

$$\vec{F} = \int_S p \, d\vec{s} \ , \qquad (5.4.12)$$

where S is the surface of the blade. This integral gives us the total aerodynamic force acting on the blade per unit span. This can be resolved into two components, parallel and normal to the free stream F_D (drag) and F_L (lift), respectively. The coefficients C_L and C_D were then calculated according to $C_L = \frac{F_L}{\frac{\rho}{2} U_\infty^2 C}$, $C_D = \frac{F_D}{\frac{\rho}{2} U_\infty^2 C}$. The above integration was executed numerically by computing the pressure at 180 points on the surface of the blade.

5.5 Propagating Stall

To simulate propagating stall, the flow about the central airfoil is allowed to separate. As the wake of the central blade, k = 0, grows it starts affecting the distribution of vorticity on the neighboring blade, k = 1 and induces it to stall. In principle, the presence of discrete vortices, in this case free vortices, results in violation of the boundary condition on the external blades. The bound vorticity of each blade remains constant, unless shedding occurs, but the distribution of vorticity should change to account for extraneous effects, like the shedding of vorticity from neighboring blades. However, the error

involved in keeping the vorticity distribution of all external blades fixed is negligible, except if the free vortices start approaching the neighboring blade.

To allow redistribution of the vorticity on the k = 0 blade we use at each time step 2 equations of the form of Eqs. (5.4.1) and (5.4.2) and the conservation of vorticity equation in the form

$$\Gamma_0^{(n)} + \sum_{q=1}^{n} \left(\tilde{\Gamma}_{0\ell q} + \tilde{\Gamma}_{0tq}\right) = \Gamma_{initial} \qquad (5.5.1)$$

where $\Gamma_{initial}$ is the bound vorticity of the blades for the case that the flow is attached. Once the two new nascent vortices and the new bound vorticity of the k = 0 blade are calculated, then the corresponding vorticity distribution on the central blade in the ζ-plane can be calculated by virtue of Eq. (5.3.2), taking into account all free and bound vortices in the field.

To calculate the redistribution of vorticity on the k = 1 blade, a new system of z-coordinates is defined with the k = 1 blade playing the role of the central blade and therefore appearing as a circle. The effect of all other bound and free vortices is considered by introducing once more image vortices inside the circle at the corresponding conjugate positions and the center, according to Eq. (5.3.1). Now the distribution of the vorticity on blade k = 1 is allowed to readjust. At this time the free vortices over the central blade, are convected by increments according to Eq. (5.4.4) which includes the effects of all vortices, in the field, bound and free.

When a special heuristic separation criterion is met, i.e. when vortices approach the surface of the neighboring blade, vortices are released from blade k = 1, and the distribution of vorticity on blade K = 2 is calculated as explained above. The same process described already for blade k = 0 is repeated. The only difference is that now there are free vortices developing over the preceding blade as well. The calculation of the nascent vortices over blade k = 1 and its bound strength are calculated via equations of the form of Eqs. (5.4.1) and (5.4.2) and the vorticity conservation equation in the form

$$\Gamma_1^{(n)} + \sum_{q=1}^{n} (\tilde{\Gamma}_{1\ell q} + \tilde{\Gamma}_{1tq}) = \Gamma_{initial} \qquad (5.5.2)$$

What is missing from this model is an effective method of calculating the development of the boundary layers. However, as a first attempt, we tried to capture qualitatively the different features of the phenomenon. In our laboratory a test was run on a linear cascade of the above mentioned type of blades (see Mathioulakis, 1982) providing valuable information. For instance, we noticed that propagating stall occured for an inlet angle of 20° and stagger angle of 55°, while the flow separated from the leading edge of the blades. In our calculations we considered the same case, namely a cascade of solidity ratio $\sigma = 1$, stagger angle $\gamma = 55°$ and an inlet angle $a_{IN} = 20°$. At t = 0 we assumed that the flow separated from the blade k = 0. This was simulated by releasing one vortex per time step ($\Delta t = 0.3$) at the leading edge region ($\phi = -10.13$, see Sec. 5.2) and at the trailing edge region.

The nascent vortices were released in the phase plane in a distance 0.1R from the cylinder's surface.

The pressure distribution over the next blade k = 1 is shown in Fig. 5.5.1 for two different time instants t = 0.6 and t = 6. In Fig. 5.5.2, we show the velocity field close to the leading edge and over the suction side of blade k = 1. In this figure we notice that the angle of attack locally increases with time and also accelerates in the suction side. A similar pattern was observed in the laboratory, namely the magnitude of the velocity increases before dropping (when the blade stalls) and the local angle of attack increases when the retarded mass (stall-cell) approaches the blade. At t = 6 we arbitrarily start releasing vortices from the blade k = 1 as well. The evolution of the wake development of blades k = 0 and k = 1 at t = 3, 4.5, 7.5, 9 is shown in Fig. 5.5.3. In Fig. 5.5.4, we show the velocity field in the passage between blades k = 0 and k = 1, calculated by our inviscid model. It is clearly shown how the flow has retarded in the region between the two shear layers of blade k = 0 while the angle of attack on k = 1 blade has increased.

CHAPTER SIX

CONCLUSIONS & RECOMMENDATIONS

The aim of this research has been experimental investigation and analytical modeling of the process whereby vorticity is released from a solid boundary and develops into a free-shear layer. Steady and periodic flows were considered.

With the exception of the most recent work of Varty and Currie (1984), no other detailed measurements upstream and downstream of laminar separation have been reported in literature. A considerable advantage of the present method over the one employed by Varty and Currie is that two simultaneous velocity measurements are obtained. Moreover, the investigation is extended to unsteady flows.

Our ability to carry out this type of investigation in a flow regime which involves drastic changes in the direction and magnitude of the velocity is due to the use of a 2-component Laser-Doppler Velocimetry. This technique is non-intrusive, requires no calibration and is sensitive to changes in the flow direction. A large portion of the present effort was devoted to the design of necessary components, traversing mechanisms, computer software and extensive tests to make the data acquisition process fully automatic, streamline its operation and prove the reliability of the system.

Studies of the immediate neighborhood of the separation were conducted on a backward-facing circular arc. The main contribution of this phase of the work is a body of experimental data corroborating earlier analytical findings. Most importantly, we found that in terms of a

coordinate system aligned with the displacement thickness, the boundary-layer approximation is essentially valid at and beyond separation.

The study of periodic separating flow over the circular arc provides a benchmark set of data, against which future numerical calculations can be contrasted. Moreover, our raw data were reduced and recast in combinations that reveal the character of the flow. In particular, we found that:

a) The point of zero skin friction oscillates along the wall, moving downstream when the outer flow accelerates.

b) The free shear layer emanating from the point of zero skin friction, displaces towards the wall when the outer flow accelerates, reducing the thickness of the reversed-flow region.

c) The amplitude of the velocity increases in the downstream direction, while downstream of the zero skin friction, its maximum value is located within the free shear layer.

d) The velocity phase advance with respect to the outer flow is significant in the reversed flow.

e) The velocity component normal to the wall (v) decreases when the outer flow accelerates, indicating that the flow has a tendency to become attached. In the reversed-flow region, this component is always small. However, it increases moving away from the wall and especially from the point where the u-component changes sign.

f) The motion of the free-shear layer starts becoming less organized in a distance 3 or 4 boundary-layer thicknesses downstream of

the point of zero-skin-friction. This was more pronounced in the unsteady v-profiles.

The evaluation of the static pressure distribution in the flow field over the circular arc by directly using the experimental data in the Navier-Stokes eqs., was inconclusive. This should be attributed to inaccuracies in determing extremely small terms, like v and $\frac{\partial u}{\partial x}$.

In order to improve the quality of the data further, it is suggested that

a) The digital output of the signal processor be fed directly into the computer instead of converting it to an analog signal.

b) The accuracy of the traversing mechanism be improved by using some type of feed-back mechanism.

c) The turbulence intensity of the tunnel be reduced.

It was demonstrated that the rate at which vorticity is released into the flow is very well aproximated by the formula $\frac{1}{2} U_e^2$ for the conditions of the present experiment. Unfortunately, we were not able to verify Sear's generalized criterion which involves the speed of the separation point. The reason is that the speed of separation, in our case, was very small compared to the outer-flow velocity. We believe that a good test for the above formula would be an experimental investigation of the separation region under impulsive changes of the outer flow which involves large excursions of separation.

The experimental investigation of the flow about the ellipse was undertaken in order to facilitate comparisons with theoretical solutions or models. The conclusions drawn from the investigation of the flow on

the suction side of the ellipse, including the separation region and the shear layer, seem to be very similar to those mentioned above. In the stagnation point-region, acceleration of the flow appears to force the stagnation point towards the suction side. We also notice that the velocity amplitude increases in the same direction, achieving a maximum value of 2.5 times the outer-flow amplitude.

Unsteady measurements on the pressure side of the elliptical cylinder indicated that the amplitude of the velocity is considerably smaller than that on the suction side, and the organized features of the flow quickly disappear downstream.

In the study of a free vortex sheet we were able to detect distinct vortical structures whose characteristics were investigated and found to agree well with the theory of ideal vortices. This is a very important conclusion because it demonstrates that, though the vortex sheet diffuses only a little and retains its continuity, its rolling up motion quickly resembles the field of discrete potential vortices. In fact, our findings indicate that the dynamics of such a field can be very accurately modeled by discrete vortex dynamics.

The main thrust in the experimental work was the understanding of the mechanisms of vorticity shedding from a solid surface and its subsequent interaction with the outerflow. Three regions were investigated separately, namely the immediate neighborhood of vortex-layer separation, the development of a vortex sheet in the proximity of a solid surface and the development of a vortex sheet free of any boundaries. In all cases we sought to provide detailed experimental information for

comparison with future numerical results. Moreover, the experimental findings were employed in the verification and further development of analytical modeling of free vortex sheets. It was demonstrated that with great accuracy, the strength of a nascent vortex is proportional to the square of the edge velocity (U_e) and that the speed of propagation is equal aproximately to $U_e/2$. Moreover, the development of continuous vortex sheets and its rolling up characteristics can be modeled quite accurately by discrete vortex dynamics. These findings were employed in the numerical solution of two problems involving the development of unsteady vortex sheets.

The finite-difference solutions of the unsteady boundary-layer equations for the impulsively started circular cylinder indicate abrupt growth of the displacement thickness in the region of 108°. This position is downstream of the instantaneous location of the point of zero skin friction. This is in agreement with the findings of other investigators. In subsequent times we simulated the free-shear layer via discrete vortex dynamics. The method indeed appears to provide the proper interaction which shifts direction. However, this tendency does not appear to stop and separation moves upstream of the well accepted steady state position of 80°. Apparently, the release of a point vortex in the separation region resulted in an abrupt deceleration of the outer flow and, therefore, premature separation. It seems that more attention must be given to this point. Finally, the inviscid vortex model was used for the prediction of the rotating stall in a linear cascade. The approach seems to be promising since the obtained data were qualitatively in good

agreement with the experiment. It is necessary, however, to use a more rigorous criterion for the initiation of vorticity release from the cascade blades in order to obtain more practical results.

REFERENCES

J. Adamczyk and F. O. Carter, 1973. "Unsteady fluid dynamic response of an axial-flow compressor stage with distorted inflow", Project Squid Technical Report UARL-2-PU.

H. Blasius, 1908. "The boundary layers in fluids with little friction", NACATM 1256.

R. Bouard and M. Coutanceau, 1980. "The early stage of development of the wake behind an impulsively started cylinder for $40<Re<10^4$", J. Fluid Mech., Vol. 101, pp. 583-607.

B. Carnahan, H. Luther, J. Wilkes, 1969. Applied Numerical Methods, 1969.

T. Cebeci, 1979. "The laminar boundary layer on a circular cylinder started impulsively from rest", Journal of Computational Physics, Vol. 31, No. 2, May 1979.

T. Cebeci, 1981. "Unsteady separation", in Numerical and Physical Aspects of Aerodynamic Flows, Vol. 1, edited by T. Cebeci, Springer, 1981.

W. M. Collins and S. C. R. Dennis, 1973. "Flow past an impulsively started circular cylinder", J. Fluid Mech., Vol. 60, pp. 105-127.

F. D. Deffenbaugh and F. J. Marshall, 1976. "Time-development of the flow about an impulsively started cylinder", AIAA Journal, Vol. 14, July 1976, pp. 908-913.

R. A. Despard and J. A. Miller, 1971. "Separation in oscillating laminar boundary-layer flows", J. Fluid Mech., Vol. 47, pp. 21-31.

H. L. Dryden and I. H. Abbot. "The design of low-turbulence wind tunnels", NACA TN 1755.

P. T. Fink and W. K. Soh, 1974. "Calculations of vortex sheets in unsteady flow and applications in ship hydrodynamics", Proceedings of the 10th Symposium on Naval Hydrodynamics, U.S. Office of Naval Research, 1974, pp. 463-489.

Ho Chih Ming, 1984. Private communication.

N. D. Ham, 1968. "Aerodynamic loading on a two dimensional airfoil during dynamic stall", AIAA Journal, Vol. 5, pp. 1927-1934.

G. Jones, C. Barbi and D. P. Telionis, 1981. "Separation and wake interaction of a pulsating laminar flow", AIAA-81-0053.

K. Karamcheti, 1966. Principles of Ideal-Fluid Aerodynamics, 1966.

J. Katz, 1981. "A discrete vortex method for the non-steady separated flow over an airfoil", J. Fluid Mech., Vol. 102, pp. 315-328.

J. Katz and D. Weihs, 1981. "Wake rollup and the Kutta condition for airfoils oscillating at high frequency", AIAA 81-4329.

T. Kawamura and K. Kuwahara, 1984. "Computation of high Reynolds number flow around a circular cylinder with surface roughness", AIAA-84-0340.

M. Kiya, K. Sasaki and M. Arie, 1982. "Discrete-vortex simulation of a turbulent separation bubble", J. Fluid Mech., Vol. 120, pp. 219-244.

C. A. Koromilas and d. P. Telionis, 1980. "Unsteady laminar separation; an experimental study", J. Fluid Mech., Vol. 97, pp. 347-384.

K. Kuwahara, 1978. "Study of flow past a circular cylinder by an inviscid model", Journal of the Physical Society of Japan, Vol. 45, pp. 292-297.

M. J. Lighthill, 1954. "Response of laminar skin friction and heat transfer to fluctuations in stream velocity", Proc. Roy. Soc. A224, pp. 1-23.

C. L. Lin, D. W. Pepper and S. C. Lee, 1976. "Numerical methods for separated flow solutions around a circular cylinder", AIAA Journal, Vol. 14, July 1976, pp. 900-906.

R. E. Marble, 1955. "Propagation of stall in a compressor blade row", Journal of the Aeronautical Sciences, Vol. 22, pp. 541-554.

D. Mathioulakis, 1982. "Steady and unsteady cascade measurements", M.S. Thesis, VPI & SU.

W. J. McCroskey, 1977. "Some current research in unsteady fluid dynamics - the 1976 freeman scholar lecture", J. Fluid Eng., Vol. 99, pp. 8-38.

T. B. Mezaris, 1979. "Visualization and LDV measurements of separating oscillatory laminar flows", M.S. Thesis, VPI & SU.

T. B. Mezaris and D. P. Telionis, 1980. "Separation and the near wake of a pulsating laminar flow", AIAA-80-1420.

L. M. Milne-Thomson, 1960. Theoretical Hydrodynamics, 4th Edition, 1960.

H. Nagata, Y. Kakehi, M. Tsunekawa and T. Hasegawa, 1975. "Unsteady flow past a circular cylinder started impulsively", Bulletin of the JSME, Vol. 18, No. 123, Sept. 1975.

H. Nagata, T. Matsui and H. Yasuda, 1980. "Velocity field of the flow around a circular cylinder started impulsively", Bulletin of the JSME, Vol. 23, No. 179, May 1980 (First Report).

H. Nagata, T. Matsui and M. Ichikawa, 1980. "Velocity field of the flow around a circular cylinder started impulsively", Bulletin of the JSME, Vol. 23, No. 179, May 1980 (Second Report).

P. V. K. Perumal and F. Sisto, 1974. "Lift and moment prediction for an oscillating airfoil with a moving separation point", Journal of Engineering for Power, pp. 372-378.

D. R. Poling and D. P. Telionis, 1984. "The response of airfoils to periodic disturbances; the unsteady Kutta condition", AIAA-84-0050.

N. Riley, 1975. "Unsteady laminar layers", SIAM Review, Vol. 17, pp. 274-297.

L. Rosenhead, 1931. "The formation of vortices from a surface of discontinuity", Proceedings of the Royal Society, Vol. 134, pp. 170-192.

P. G. Saffman and J. C. Schatzman, 1982. "An inviscid model for the vortex-street wake", J. Fluid Mech., Vol. 122, pp. 467-486.

T. Sarpkaya, 1968. "An analytical study of separated flow about circular cylinders", Journal of Basic Engineering, Dec. 1968.

T. Sarpkaya, R. L. Schoaff, 1979. "Inviscid model of two-dimensional vortex shedding by a circular cylinder", AIAA Journal, Vol. 17, Nov. 1979.

J. Scheiman and J. D. Brooks, 1980. "Comparison of experimental and theoretical turbulence reduction from screens, honeycomb and honeycomb-screen combinations", AIAA 80-0433R.

G. B. Schubauer. "Air flow in a separating laminar boundary layer", NACA Technical Report No. 527.

W. R. Sears, 1955. "Rotating stall in axial compressors", J. Appl. Math. Phys., Vol. 6, pp. 429-455.

W. R. Sears, 1975. "Unsteady motion of airfoils with boundary-layer separation", AIAA Journal, Vol. 14, pp. 216-220.

W. R. Sears and D. P. Telionis, 1975. "Boundary-layer separation in unsteady flow", SIAM J. Appl. Math., Vol. 28, 1975.

R. G. Seasholtz, 1977. "Laser Doppler velocimeter system for turbine stator cascade studies and analysis of statistical biasing errors", NASA TN D-8297.

M. R. Sexton, 1980. "An investigation of the dynamic stalling characteristic of rotating axial flow compressor blades", Ph.D. dissertation, VPI & SU.

P. R. Spalart, A. Leonard and D. Baganoff, 1983. "Numerical simulation of separated flows", NASA TN-84328.

K. Stewartson, 1974. "Multi-structured boundary layers on flat plates and related bodies", Advances in Mechanics, Vol. 14, pp. 145-239.

J. T. Stuart, 1972. "Unsteady boundary layers", in Recent Research of Unsteady Boundary Layers, Vol. 2, edited by E. Q. Eichelbrenner, 1972.

V. Ya. Sychev, 1972. "Concerning laminar separation", Izv. Akad. Nauk SSSR, Mekh. Zhidk. Gaza, Vol. 3, pp. 47-59.

H. Takata and S. Nagano, 1972. "Nonlinear analysis of rotating stall", ASME 1972, Paper No. 72-GT-3.

J. Tan-Atichat, H. M. Nagib and R. I. Loehrke, 1982. "Interaction of free-stream turbulence with screens and grids: a balance between turbulence scales", J. Fluid Mech., Vol. 114, pp. 501-528.

S. Taneda, 1971. "Visualization experiments on unsteady viscous flows around cylinders and plates", IUTAM Symposium on Unsteady Boundary Layers, May 1971.

D. P. Telionis, 1975. "Calculations of time-dependent boundary layers", in Unsteady Aerodynamics, Vol. 1, edited by Kinney, 1975.

D. P. Telionis, 1979. "Review - Unsteady boundary layers separated and attached", J. Fluids Eng., Vol. 101, pp. 29-43.

D. P. Telionis and M. S. Romaniuk, 1978. "Velocity and temperature streaming in oscillating boundary layers", AIAA Journal, Vol. 16, pp. 488-495.

D. P. Telionis, D. Th. Tsahalis and M. J. Werle, 1973. "Numerical investigation of unsteady boundary-layer separation", Physics of Fluids, Vol. 16, No. 7, July 1973.

D. P. Telionis, 1981. Unsteady Viscous Flow, 1981.

T. Theodorsen and I. E. Garrick, 1935. "General potential theory of arbitrary wing sections", NACA Report No. 452.

H. Tokel and F. Sisto, 1978. "Dynamic stall of an airfoil with leading edge bubble separation involving time dependent re-attachment", ASME Paper 78-GT-194.

D. Th. Tsahalis, 1972. "The boundary layer separation singularity in steady and unsteady flows", M.S. Thesis, VPI & SU.

D. Th. Tsahalis and D. P. Telionis, 1974. "Oscillating laminar boundary layers and unsteady separation", AIAA Journal, Vol. 12, pp. 1469-1476.

T. S. I. Manual, "Laser Velocimetry Systems".

L. L. VanDommelen and S. F. Shen, 1981. "The genesis of separation", in Numerical and Physical Aspects of Aerodynamic Flows, Vol. 1, edited by T. Cebeci, Springer, 1981.

R. L. Varty and I. G. Currie, 1984. "Measurements near a laminar separation point", J. Fluid Mech., Vol. 138, pp. 1-19.

C. Y. Wang, 1967. "The flow past a circular cylinder which is started impulsively from rest", J. Math. and Phys., Vol. 46, pp. 195-202.

M. J. Werle and R. T. Davis, 1972. "Incompressible laminar boudary-layers on a parabola at angle of attack; a study of the separation point", J. Appl. Mech., Vol. 39, pp. 7-12.

A. M. Yokum, 1981. "A computer program for calculating potential flow solutions for flow through linear and stationary circular cascades", Technical Memorandum, File No. TM81-130.

APPENDIX I

Let p be the surface of the flat mirror, (see Fig. below) AB, HL two parallel light beams and BD, LK the reflected ones. If CB and IL are normal to the plane p, then ABC and HLI are two parallel planes, say planes q and r respectively, normal to p. The parallel lines a_1, a_2 are the crossings of those planes with p. Now consider that LG is normal to a_1, GF is normal to AB and GE is normal to BD. Since LG is normal to a_1, this follows that LG is normal to q-plane. Therefore LF and LE are normal to AB and BD respectively. Namely, LF is the distance between the incident beams and LE is the distance between the reflected ones. Since G is located on the bisector of DBF (law of reflection), the line segments GE and GF are equal. Therefore, $\overline{LF} = \overline{LE}$, since $E\hat{G}L$ and $F\hat{G}L$ are right angles. The distance between two parallel light beams is therefore preserved after reflection from a flat mirror.

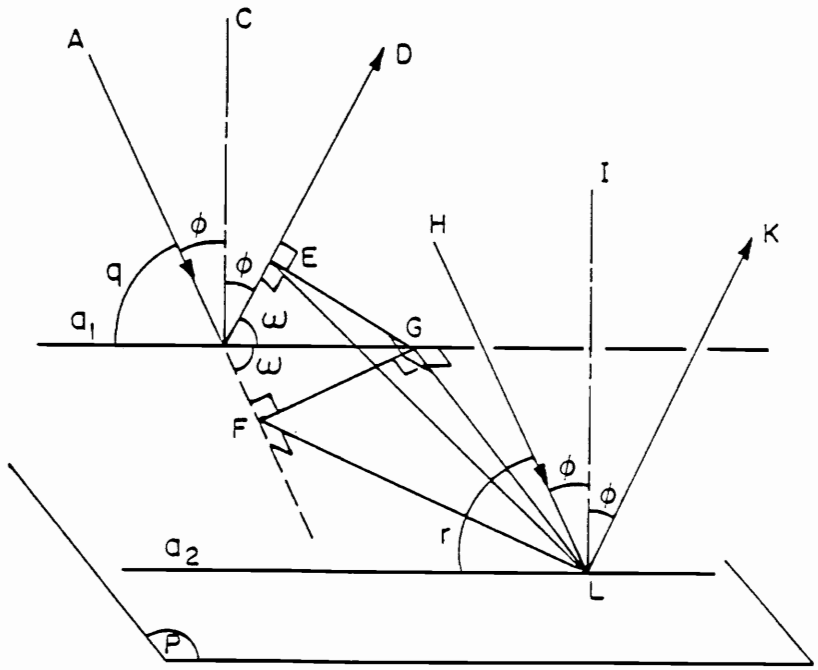

APPENDIX II

As discussed in Section 2.3, our L.D.V. system measures simultaneously two mutually perpendicular components say u_2,u_4. The velocity component u_2 is normal to the fringe formed by the 40 MHz and 60 MHz beams, while the u_4 is normal to the fringes formed by the unshifted and 40 MHz beams. The orientation of these two velocity components depends primarily on the relative position of the focusing lens and of the orientation of the parallel beams that leave the beam expander.

In this section we derive a formula that relates the components u_2, u_4 to the u,v,w components of a Cartesian coordinate system. In this system, u is parallel to the free stream, w is in the spanwise direction and v is normal to the u and w (see Fig. 1(a)).

The orientation of the surface of the focusing lens is designated by two parameters.

a) ϕ_1, which is the angle between the u,v plane (or else the surface of the window of the test section) and the axis of motion of the sliding table (see Fig. 1(b)).

b) ϕ_2, this is the angle between the vertical plane (u,v) and the surface of the lens (see Fig. 1(c)).

The first parameter (ϕ_1) takes into account the fact that the sliding table (and the lens attached to it) should not be parallel to the test section, in order to avoid reflected light from the model or the walls of the test section. Moreover when we take measurements close to the surface of a model, it is advised tha the lens is tilted a small angle (ϕ_2) with respect to the vertical plane. This permits (a) the probe

volume to touch the surface of the model, before the beams do so (see Fig. 2) and (b) the reflected from the walls light is minimized.

The orientation of the beams is defined by the angle ϕ_3 (see Fig. (d)). In this figure w_{24} is the velocity component normal to u_4 and u_2. Therefore the velocity vector $\overline{V}$ is given

$$\overline{V} = u_2\hat{k}_3 + u_4\hat{j}_3 + w_{24}\hat{i}_3, \tag{1}$$

where u_2, u_4 are measured by our L.D.V. system and also

$$\overline{V} = u\hat{k} + v\hat{j} + W\hat{i} \tag{2}$$

The coordinate system $(\hat{i},\hat{j},\hat{k})$ is transformed to $(\hat{i}_3,\hat{k}_3,\hat{j}_3)$ through three consecutive rotations (see Fig. 1).

$$\begin{Bmatrix} \hat{i}_3 \\ \hat{j}_3 \\ \hat{k}_3 \end{Bmatrix} = \begin{bmatrix} 1 & 0 & 0 \\ 0 & c\phi_3 & s\phi_3 \\ 0 & -s\phi_3 & c\phi_3 \end{bmatrix} \begin{Bmatrix} \hat{i}_2 \\ \hat{j}_2 \\ \hat{k}_2 \end{Bmatrix}$$

$$\begin{Bmatrix} \hat{i}_2 \\ \hat{j}_2 \\ \hat{k}_2 \end{Bmatrix} = \begin{bmatrix} c\phi_2 & -s\phi_2 & 0 \\ s\phi_2 & c\phi_2 & 0 \\ 0 & 0 & 1 \end{bmatrix} \begin{Bmatrix} \hat{i}_1 \\ \hat{j}_1 \\ \hat{k}_1 \end{Bmatrix}$$

$$\begin{Bmatrix} \hat{i}_1 \\ \hat{j}_1 \\ \hat{k}_1 \end{Bmatrix} = \begin{bmatrix} c\phi_1 & 0 & -s\phi_1 \\ 0 & 1 & 0 \\ s\phi_1 & 0 & c\phi_1 \end{bmatrix} \begin{Bmatrix} \hat{i} \\ \hat{j} \\ \hat{k} \end{Bmatrix}$$

where $c\phi = \cos\phi$, $s\phi = \sin\phi$. Therefore,

$$\begin{Bmatrix} \hat{i}_3 \\ \hat{j}_3 \\ \hat{k}_3 \end{Bmatrix} = \begin{bmatrix} 1 & 0 & 0 \\ 0 & c\phi_3 & s\phi_3 \\ 0 & -s\phi_3 & c\phi_3 \end{bmatrix} \begin{bmatrix} c\phi_2 & -s\phi_2 & 0 \\ s\phi_2 & c\phi_2 & 0 \\ 0 & 0 & 1 \end{bmatrix} \begin{bmatrix} c\phi_1 & 0 & -s\phi_1 \\ 0 & 1 & 0 \\ s\phi_1 & 0 & c\phi_1 \end{bmatrix} \begin{Bmatrix} \hat{i} \\ \hat{j} \\ \hat{k} \end{Bmatrix}$$

$$\hat{i}_3 = c\phi_2 c\phi_1 \hat{i} - s\phi_2 \hat{j} - c\phi_2 s\phi_1 \hat{k}$$

$$\hat{j}_3 = (c\phi_3 c\phi_1 s\phi_2 + s\phi_1 s\phi_3)i + c\phi_3 c\phi_2 \hat{j} + (s\phi_3 c\phi_1 - c\phi_3 s\phi_2 s\phi_1)\hat{k}$$

$$\hat{k}_3 = (c\phi_3 s\phi_1 - s\phi_3 s\phi_2 c\phi_1)\hat{i} - s\phi_3 c\phi_2 \hat{j} + (s\phi_3 s\phi_1 s\phi_2 + c\phi_1 c\phi_3)\hat{k} \quad (3)$$

From (1) and (3) we obtain

$$\bar{V} = u_4(c\phi_3 c\phi_1 s\phi_2 + s\phi_1 s\phi_3)\hat{i} + u_4 c\phi_3 c\phi_2 \hat{j} + u_4(s\phi_3 c\phi_1 - c\phi_3 s\phi_2 s\phi_1)\hat{k} +$$

$$+ u_2(c\phi_3 s\phi_1 - s\phi_3 s\phi_2 c\phi_1)\hat{i} - u_2 s\phi_3 c\phi_2 \hat{j} + u_2(s\phi_3 s\phi_1 s\phi_2 + c\phi_1 c\phi_3)\hat{k}$$

$$+ w_{24} c\phi_2 c\phi_1 \hat{i} - w_{24} s\phi_2 \hat{j} - w_{24} c\phi_2 s\phi_1 \hat{k} \quad (4)$$

From (4), (2) →

$$u = u_4(s\phi_3 c\phi_1 - c\phi_3 s\phi_2 s\phi_1) + u_2(s\phi_3 s\phi_1 s\phi_2 + c\phi_1 c\phi_3) - w_{24} c\phi_2 s\phi_1 \quad (5)$$

$$v = u_4 c\phi_3 c\phi_2 - u_2 s\phi_3 c\phi_2 - w_{24} s\phi_2 \tag{6}$$

$$w = u_4(c\phi_3 c\phi_1 s\phi_2 + s\phi_1 s\phi_3) + u_2(c\phi_3 s\phi_1 - s\phi_3 s\phi_2 c\phi_1) + w_{24} c\phi_2 c\phi_1 \tag{7}$$

Eliminating w_{24} from (5),(6),(7), we obtain

$$u = (u_4 s\phi_3 + u_2 c\phi_3)(c\phi_1 + tg\phi_1 s\phi_1) - wtg\phi_1 \tag{8}$$

$$v = tg\phi_1 tg\phi_2 (c\phi_3 u_2 + u_4 s\phi_3) + \frac{(u_4 c\phi_3 - u_2 s\phi_3)}{c\phi_2} - \frac{wtg\phi_2}{c\phi_1} \tag{9}$$

In the above formulas (8),(9), the unknown component w shows up. However, since ϕ_1 and ϕ_2 are small (at most five degrees), the error involved in the calculation of u and v is of the order of 5% of the w component. Since our L.D.V. system is used for the velocity measurement of two dimensional flow fields ($w \approx 0$) the above mentioned error is essentially negligible. Therefore, u and v are given by

$$u = (u_4 s\phi_3 + u_2 c\phi_3)/c\phi_1$$

$$v = (u_4 c\phi_3 - u_2 s\phi_3)/c\phi_2 + tg\phi_1 tg\phi_2 (u_4 s\phi_3 + u_2 c\phi_3) \ .$$

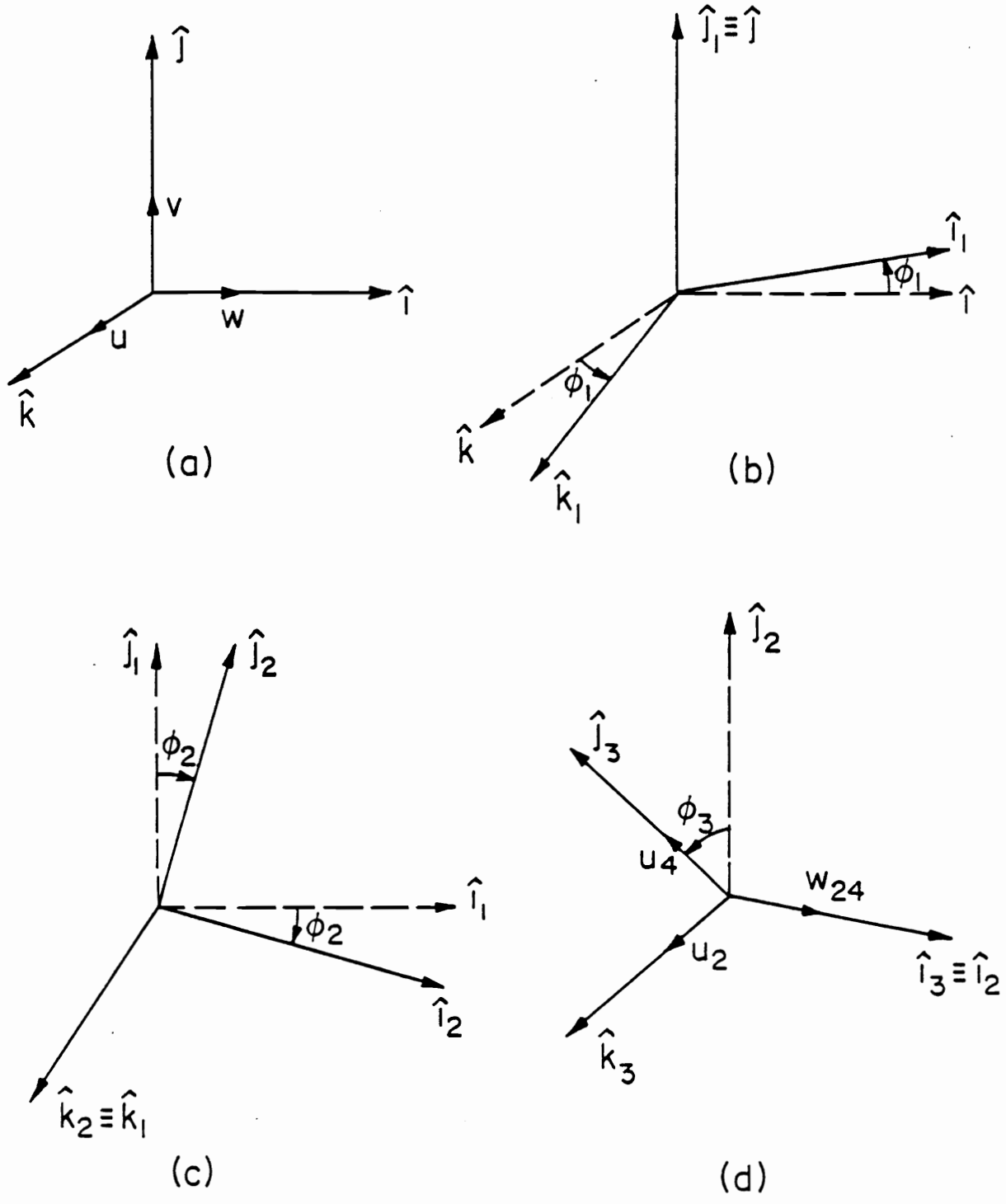
$\hat{j}$
v
$\hat{i}$
w
u
$\hat{k}$
(a)
$\hat{j}_1 \equiv \hat{j}$
$\hat{i}_1$
ϕ_1
$\hat{i}$
ϕ_1
$\hat{k}$
$\hat{k}_1$
(b)
$\hat{j}_1$
$\hat{j}_2$
ϕ_2
$\hat{i}_1$
ϕ_2
$\hat{i}_2$
$\hat{k}_2 \equiv \hat{k}_1$
(c)
$\hat{j}_2$
$\hat{j}_3$
ϕ_3
u_4
w_{24}
u_2
$\hat{i}_3 \equiv \hat{i}_2$
$\hat{k}_3$
(d)

Fig. 1

APPENDIX III

IMSL ROUTINE NAME - FFTSC

PURPOSE - COMPUTE THE SINE AND COSINE TRANSFORMS OF A REAL VALUED SEQUENCE

USAGE - CALL FFTSC (A,N,ST,CT,IWK,WK,CWK)

ARGUMENTS

- A - INPUT REAL VECTOR OF LENGTH N WHICH CONTAINS THE DATA TO BE TRANSFORMED.
- N - INPUT NUMBER OF DATA POINTS TO BE TRANSFORMED. N MUST BE A POSITIVE EVEN INTEGER.
- ST - OUTPUT REAL VECTOR OF LENGTH N/2+1 CONTAINING THE COEFFICIENTS OFTHE SINE TRANSFORM.
- CT - OUTPUT REAL VECTOR OF LENGTH N/2+1 CONTAINING THE COEFFICIENTS OF THE COSINE TRANSFORM.
- IWK - INTEGER WROK VECTOR. IF N IS A POWER OF 2, THEN IWK SHOULD BE OF LENGTH M WHERE N = 2**M. OTHERWISE, IWK SHOULD BE OF LENGTH 6*(N/2) + 150. (SEE PROGRAMMING NOTES FOR FURTHER DETAILS)
- WK - REAL WORK VECTOR OF LENGTH 6*(N/2) + 150. WK IS NOT USED IF N IS A POWER OF 2. (SEE PROGRAMMING NOTES FOR FURTHER DETAILS)
- CWK - COMPLEX WORK VECTOR OF LENGTH N/2+1.

REMARKS

1. FFTSC COMPUTES THE SINE TRANSFORM, ST, ACCORDING TO THE FOLLOWING FORMULA;

```
ST(K+1) = 2.0 * SUM FROM J = 0 TO N-1 OF
          A(J+1)*SIN(2.0*PI*J*K/N)
FOR K = 0,1,...,N/2 AND PI = 3.1415...
```

   FFTSC COMPUTES THE COSINE TRANSFORM, CT, ACCORDING TO THE FOLLOWING FORMULA;

```
CT(K+1) = 2.0 * SUM FROM J = 0 TO N-1 OF
          A(J+1)*COS(2.0*PI*J*K/N)
FOR K = 0,1,...,N/2 AND PI = 3.1415...
```

2. THE FOLLOWING RELATIONSHIP EXISTS BETWEEN THE DATA AND THE COEFFICIENTS OF THE SINE AND COSINE TRANSFORM

```
A(J+1) = CT(1)/(2*N) + CT(N/2+1)/(2*N)*(-1)**J +
         SUM FRM K = 1 TO N/2-1 OF
         (CT(K+1)/N*COS((2.0*PI*J*K)/N) +
         ST(K+1)/N*SIN((2.0*PI*J*K)/N))
FOR J = 0,1,...,N-1 AND PI = 3.1415...
```

Algorithm

FFTSC computes the sine and cosine transformations of a real vector of length N where N is any positive even integer.

Given a set of N(even) data points $A = (a_1,a_2,\ldots,a_N)^t$ where $a_1,a_2,\ldots,a_N$ are real numbers, define the cosine transformation CT and the sine transformation ST by

$$CT_{k+1} = 2 \sum_{j=0}^{N-1} a_{j+1}\cos(2\pi jk/N)$$

$$ST_{k+1} = 2 \sum_{j=0}^{N-1} a_{j+1}\sin(2\pi jk/N) \text{ for } k = 0,1,\ldots,N/2$$

FFTSC computes the vectors CT and ST.

APPENDIX IV

IMSL ROUTINE NAME - ICSSCU

PURPOSE - CUBIC SPLINE DATA SMOOTHER

USAGE - CALL ICSSCU (X,F,DF,NX,SM,Y,C,IC,WK,IER)

ARGUMENTS

- X - VECTOR OF LENGTH NX CONTAINING THE ABSCISSAE OF THE NX DATA POINTS (X(I),F(I)) I = 1,...,NX. (INPUT) X MUST BE ORDERED SO THAT X(I) .LT. X(I+1).
- F - VECTOR OF LENGTH NX CONTAINING THE ORDINATES (OR FUNCTION VALUES) OF THE NX DATA POINTS. (INPUT)
- DF - VECTOR OF LENGTH NX. (INPUT) DF(I) IS THE RELATIVE WEIGHT OF DATA POINT I (SEE PARAMETER SM BELOW).
- NX - NUMBER OF ELEMENTS IN X, F, DF, AND Y. (INPUT) NX MUST BE .GE. 2.
- SM - A NON-NEGATIVE NUMBER WHICH CONTROLS THE EXTENT OF SMOTHING. (INPUT) THE SPLINE FUNCTION S IS DETERMINED SUCH THAT THE SUM FROM 1 TO NX OF ((S(X(I))-F(I))/DF(I))**2 IS LESS THAN OR EQUAL TO SM, WHERE EQUALITY HOLDS UNLESS S DESCRIBES A STRAIGHT LINE.
- Y,C - SPLINE COEFFICIENTS. (OUTPUT) Y IS A VECTOR OF LENGTH NX. C IS AN NX-1 BY 3 MATRIX. THE VALUE OF THE SPLINE APPROXIMATION AT T IS S(T) = ((C(I,3)*D+C(I,2))*D+C(I,1))*D+Y(I) WHERE X(I) .LE. T .LT. X(I+1) AND D = T-X(I).
- IC - ROW DIMENSION OF MATRIX C EXACTLY AS SPECIFIED IN THE DIMENSION STATEMENT IN THE CALLING PROGRAM. (INPUT)
- WK - WORK AREA VECTOR OF LENGTH 7*NX+14.
- IER - ERROR PARAMETER. (OUTPUT)
  TERMINAL ERROR
  - IER = 129, IC IS LESS THAN NX-1
  - IER = 130, NX IS LESS THAN 2
  - IER = 131, INPUT ABSCISSAE ARE NOT ORDERED SO THAT X(1) .LT. X(2) ... .LT. X(NX)

REMARKS

1. THE ROUTINE PRODUCES A NATURAL CUBIC SPLINE. HENCE, THE SECOND DERIVATIVE OF THE SPLINE FUNCTION S AT X(1) AND X(NX) IS ZERO.

2. FOR EACH SET OF DATA POINTS THERE EXISTS A MAXIMUM VALUE FOR THE SMOOTHING PARAMETER. LET US CALL THIS MAXIMUM VALUE SM*. IT IS DEFINED BY THE FOLLOWING FORMULA;

   SM* = THE SUM FROM I EQUAL 1 TO NX OF

   $$((Y(I)-F(I))/DF(I))^2$$

WHERE Y IS THE SET OF FUNCTION VALUES DEFINING THE STRAGHT LINE WHICH BEST APPROXIMATES THE DATA IN THE LEAST SQUARES SENSE (WITH WEIGHTS DF).

Algorithm

ICSSCU places a smooth cubic spline along a given set of data points. Given a set of NX data points (X(I),F(I)), I = 1,2,...,NX, a set of weights DF(I), I = 1,2,...,NX where DF(I) is the relative weight of data point I, and a non-negative number SM, ICSSCU computes a cubic spline, S(X(I)), with the following properties:

i) $\sum_{I=1}^{NX} ((S(X(I)) - F(I))/DF(I))^2$ is less than or equal to SM, and equality holds unless S describes a straight line.

ii) $\int_{X(1)}^{X(NX)} [S''(x)]^2 dx$ is the minimum of all cubic splines satisfying property (i).

Upon output, the coefficients of the cubic spline are located in the vector Y (which is of length NX) and the matrix C (which is (NX-1) by 3). The value of the spline approximation at T is S(T) = ((C(I,3)*D + C(I,2)*D + C(I,1))*D + Y(I) where T is in [X(I),X(I+1)) for I = 1,2,...,NX-1 and D = T-X(I).

APPENDIX V

FORTRAN PROGRAM FOR UNSTEADY FLOW

Here we describe the functions of a FORTRAN program used with the MINK-11 minicomputer in order to obtain time-dependent velocity data in the flow about the stagnation region of the elliptical cylinder. In fact, the same program, with small variations, was used for every unsteady flow phenomenon.

The main steps followed by this program in a sequence are as follows:

a) the program reads several parameters like the number of ensembles, the time interval between two data points, the file name where the data are going to be stored

b) the A/D convertion starts whenever a pulse is sent to the computer (conditional averaging)

c) the data are averaged

d) they are stored in a file specified above (see (a))

e) they are displayed on the screen of the terminal (checking easily the quality of the data)

f) the laser system is traversed to a new location

g) steps b through f are repeated as many times as it is desirable

h) whenever we decide to stop the data acquisition, we press the "return" key of the terminal and the process is terminated.

The data stored in floppy diskettes can then be transferred to the main IBM computer system for further reduction.

Glossary

In this section we explain the most important parameters involved in the program. Namely:

DI Distance in mm between two adjacent measuring locations

IFIRST CHANNEL NUMBER. The A/D converter can support up to 64 channels, that is it can accept 64 different signals. This parameter defines the channel number of one of those signals while the rest have channel numbers IFIRST+1, IFIRST+2, etc.

PERIOD Time period between two concecutive data points in an ensemble

NE Number of points per ensemble

MS Number of ensembles

JSTH Total number of pulses sent to the horizontal stepping motor form the original location

JSTV Total number of pulses sent to the vertical stepping motor from original location

IBUF This array is used in order to temporarily store the converted (from analog to digital) data

X This array contains the values of IBUF after having been converted to voltage (0 ÷ 5.12 volts)

BA The averaged X data are stored in this array

MH It defines the direction of rotation of horizontal stepping motors (MH = 1 or 4)

MV It defines the direction of rotation of vertical stepping motor (MV = 1 or 4)

FIN Angle between the vertical and the direction along which the probe volume is moving

JSTX Number of pulses sent to the horizontal motor between two adjacent measuring locations

JSTY Number of pulses sent to the vertical motor between two adjacent measuring locations

Subroutines

Most of the subroutines, explained below, are necessary in order to achieve a communication and coordination between the software and hardware of the minicomputer.

GETSTR It specifies the name of the data file. This should be an alphanumeric string of 14 characters.

OPEN It opens the above specified file and it is ready to accept data.

XRATE,CLOCKA They activate the clock of the MINK, adjusting its frequency at 1/PERIOD (see Glossary). This clock is working along with the A/D converter, so that there is one cnvertion every PERIOD secs.

ADSWP It activates the A/D converter. However, the convertion does not start unless an external pulse is sent to the MINK. In case of more than one channel, the convertion is done for each channel at a time.

SETIBF,RLSBUF They define the buffer (array) where the converted data are stored.

IWTBUF It holds the execution of the FORTRAN program till the buffer has been filled up.

BOUNDS It calculates the maximum and minimum value of a set of numbers.

GRINIT,GRREGN,GRAPHS These routines are used to display a group of data on the screen.

VTCLR It erases the screen.

IPOKE(A",B) This routine assigns the number B to the memory location of address A. For instance the "digital-out" module of the MINK has as address the number 171262, and the "D/A" converter has as address the number 171066.

STPSWP It terminates the data acquisition process.

CLOSE It closes the data file.

Two more points from the program have to be explained. The statement IF(ITTINR( ).GE.0) GO TO 510 transfers the execution of the program

to the statement 510, when the "return" key of the terminal keyboard is pressed. Concerning the delay loop which starts after the translation of the probe volume, proved to be necessary in order to avoid erroneous data. In fact, it was observed that for a period of about 15 sec. after traversing the probe volume, data scattering was unrealistically high. We believe that is due to the slight vibration of the "mirror" tower during its motion which takes apparently some time to be absorbed.

```
      PROGRAM ELLIPSE
C
C     THIS ROUTINE makes average in time domain of 3 channels
C     USING EXTERNAL TRIGGER FOR  UNSTEADY  FLOW :
C     MOVES THE PROBE VOLUME IN A DIRECTION NORMAL TO THE SURFACE:
C     USE OF DIGITAL OUTPUT   FOR CONTROL OF TRANSLATOR :
      INTEGER*2 INFO(40),IBUF(1024,1),IGINFO(30),FNAME(15)
      REAL*4 X(510,3),Re(510,3),M11(510)
      LOGICAL*1 EFLG
C
C     PUT IN SPECIAL TT MODE SO THIS WILL WORK IN F9 (ALLOW
C     BUSY WAIT.
C
      CALL IPOKE('44,IPEEK('44),09,'100)
      TYPE 200
200   FORMAT('$INPUT X DISTANCE IN MM :')
      ACCEPT *,XX
      TYPE  232
232   FORMAT('$INPUT MAXIMUM NUMBER OF MEASUREMENTS : ')
      ACCEPT *,MMAX
      PI=3.14159
C     61 IS THE ANGLE OF ATTACK
      FI=14.*PI/180.
C     A & B ARE THE  1/2  OF THE MAJOR  &MINOR AXES
      A=50.05
      B=16.37
      PAR=A**2*SQRT(1.-(XX/A)**2)/(B*XX)
      IF(ATAN(PAR).GT.FI) GO TO 90
      MU=4
      FIN=PI/2.-FI+ATAN(PAR)
      GO TO 93
90    MU=1
      FIN=PI/2.+FI-ATAN(PAR)
93    CONTINUE
      MM=1
C     PROMPT FOR PARAMETERS
C     MPAR IS  THE INDEX OF POSITION
      TYPE 127
127   FORMAT('$INPUT STEP IN MM : ')
      ACCEPT *,DI
      JSTY=0
      JSTY=0
      type 1
1     FORMAT('$ENTER BEGINNING CHANNEL NUMBER: ')
      ACCEPT *,IFIRST
      TYPE 2
2     FORMAT('$ENTER SAMPLE PERIOD IN SECONDS: ')
      ACCEPT *,PERIOD
      type 12
 12   format('$enter number of points per sample: ')
      accept *,ne
```

```
c-------SET SA  TO ZERO--------
        do 22  i=1,ns
        DO 22  J=1,3
22      Sa(i,J)=0.
        DO 30 I=1,NE
30      X11(I)=I*PERIOD
        type 13
 13     format('$enter number of assemblies: ')
        accept *,ms
        type 3
3       FORMAT('$ENTER FILESPEC OF DATA FILE:  ')
        CALL GETSTR(5,FNAME,14,EFLG)
        OPEN (NAME=FNAME,TYPE='NEW',UNIT=10)
        TYPE 24
24      FORMAT('$INPUT INDEX OF POSITION :INITIAL=1 : ')
        ACCEPT *,MPAR
        TYPE 26
26      FORMAT('$NUMB OF PULSES IN HORIZ FROM ORIGINAL POSITION : ')
        ACCEPT *,JSTH
        TYPE 220
220     FORMAT('$NUMB OF PULSES IN VERTICAL FROM ORIG POSITION : ')
        ACCEPT *,JSTV
C       GET CLOCK RATE AND PRESET VALUE.
        CALL XRATE(PERIOD,IRATE,IPRE)
        CALL CLOCKA(IRATE,IPRE,IND)
        IF(IND.EQ.0) STOP 'CLOCKA ERROR'
C       INITIALIZE BUFFER SYSTEM.
C       DELAY LOOP
35      TYPE 35
35      FORMAT('$DELAY LOOP STARTED  ')
        DO 23 I1=1,80
        DO 23 I2=1,80
        DO 23 I3=1,80
23      CONTINUE
        TYPE 36
36      FORMAT('$DELAY LOOP FINISHED ')
        MP=I*NE
C START A/D  CONVERSION  WITH  EXTERNAL  TRIGGER
        ML=MS*NE
        PARA=1./FLOAT(ML)
        DCV=0.
        DCV2=0.
        DCV3=0
        do  15 J=1,ms
        CALL  GETIBF(INFO,IND,,IBUF,1,1)
        CALL FLSBUF(INFO,IND,0)
        CALL ADBUF(INFO,MP,1,25,,,,,IFIRST,I)
        WRITE(7,27) J
27      FORMAT(10X,I5)
C
C       WAIT FOR BUFFER OR CARRIAGE RETURN.  IF BUFFER BECOMES
C       AVAILABLE, SAVE THE DATA.
        write(7,40)  info(1)
```

```
      CALL INTBUF(INFO,IBUFN,IND)
      WRITE(7,40)  IND
      PAR1=1./FLOAT(J)
      PAR2=FLOAT(J-1)/FLOAT(J)
      IF(ITTINP().GE.0) GO TO 510
      do  16  i=1,ne
      UNUM=((IBUF(I*3-2,IBUFN+1),AND.'7777'X)-2048)*.0025
      X(I,1)=UNUM*PAR1+BA(I,1)*PAR2
      ba(i,1)=x(i,1)
      P1=((IBUF(I*3-1,IBUFN+1),AND.'7777'X)-2048)*.0025
      X(I,2)=P1*PAR1+BA(I,2)*PAR2
      BA(I,2)=X(I,2)
      P2=((IBUF(I*3,IBUFN+1),AND.'7777'X)-2048)*.0025
      X(I,3)=P2*PAR1+BA(I,3)*PAR2
      BA(I,3)=X(I,3)
      DCV=DCV+UNUM*PAR4
      DCV2=DCV2+P1*PAR4
      DCV3=DCV3+P2*PAR4
16    continue
15    continue
40    format(i5)
      JSTV=JSTV+JSTY
      JSTH=JSTH+JSTX
      CALL BOUNDS(1,BA(1,1),VMAX1,VMIN1,NE)
      CALL BOUNDS(1,BA(1,2),VMAX2,VMIN2,NE)
      CALL BOUNDS(1,BA(1,3),VMAX3,VMIN3,NE)
      DU1=VMAX1-VMIN1
      DU2=VMAX2-VMIN2
      DU3=VMAX3-VMIN3
      WRITE(10,503) DCV,DCV2,DCV3,DU1,DU2,DU3,VMAX1,VMAX2,VMAX3
      WRITE(10,502) MPAR,JSTH,JSTV,MH,MV
      WRITE(10,501) (BA(I,1),I=10,ne,10)
      WRITE(10,501) (BA(I,2),I=10,NE,10)
      WRITE(10,501) (BA(I,3),I=10,NE,10)
501   FORMAT(1X,8F9.4)
502   FORMAT(5I6)
503   FORMAT(1X,9E7.4)
C     PLOT RESULTS
      CALL GRINIT(IGINFO)
      CALL GRRESN(IGINFO,0,1)
      CALL GRAPHS(IGINFO,X1(),BA(1,1),NE,0)
      CALL GRRESN(IGINFO,1,2)
      CALL GRAPHS(IGINFO,X1(),BA(1,2),NE,1)
C     DELAY LOOP OF ABOUT 5 SECS
      DO 43 I1=1,50
      DO 43 I2=1,50
      DO 43 I3=1,50
43    CONTINUE
```

```
C       ERASE THE  SCREEN
        CALL UTCLR
C       TRAVERSE THE LASER SYSTEM
        WRITE(7,502) MPAR
        WRITE(7,501) DCV,DCV2,DCV3,DV1,DV2,DV3
        JSTY=IFIX(SIN(FIN)*DI*250.)
        JSTY=IFIX(COS(FIN)*DI*80.)
        JSTY=IABS(JSTX)
        JSTY=IABS(JSTY)
C       MOVE VERTICALLY
        CALL IPOKE('171066,4095)
        DO 90 L=1,JSTY
        CALL IPOKE ('171062,MV)
C       DELAY LOOP
        DO  95 K=1,150
95      CONTINUE
        CALL IPOKE('171062,0)
C       DELAY LOOP
        DO 90 K=1,10
90      CONTINUE
C       MOVE HORIZONTALLY
        CALL IPOKE('171066,0)
        DO 210 L=1,JSTX
        CALL IPOKE('171062,MH)
        DO 215 K=1,150
215     CONTINUE
        CALL IPOKE('171062,0)
        DO 210 K=1,10
210     CONTINUE
        MPAR=MPAR+1
        IF(MPAR.GT.MM4X) GO TO 510
        GO TO 95
510     CALL BTPSWP(INFO,,IND)
        CLOSE(UNIT=10)
        JSTH=JSTH+JSTX
        JSTV=JSTV+JSTY
        TYPE 33
33      FORMAT('$HORIZ,VERTICAL,MEASUREMENT NUMBER,DIRECTION,VERT
        WRITE(7,28) JSTH,JSTV,MPAR,MH,MV
28      FORMAT(1X,5(3X,I5))
        STOP
        END
```

APPENDIX VI

Derivation of the transformation derivative

The derivative of the transformation is the product of the following two derivatives

$$\frac{d\zeta}{dz} = \frac{dz'}{dz}\,\frac{d\zeta}{dz'} \tag{A1}$$

By virtue of Eqs. (5.2.1), (5.2.6), (5.2.7) and (5.2.8) we get

$$\frac{dz'}{dz} = e^{\sum_1^{\infty} \frac{C_n}{z^n}} + z\, e^{\sum_1^{\infty} \frac{C_n}{z^n}} \frac{d}{dz} \sum_1^{\infty} \frac{C_n}{z^n}$$

$$= z'\left[\frac{1}{z} + \frac{d}{dz} \sum_{n=1}^{\infty} [A_n + i\, B_n]\, \frac{1}{z^n}\right]$$

$$= z'\left[\frac{1}{z} - \sum_{n=1}^{\infty} \frac{R^n[C_{n1} + i\, C_{n2}]n}{z^{n+1}}\right]$$

$$= \frac{z'}{z}\left[1 - \sum_{n=1}^{\infty} \left(\frac{R}{z}\right)^n [C_{n1} + i\, C_{n2}]\right] \tag{A2}$$

where

$$A_n = C_{n1} R^n \tag{A3}$$

$$B_n = C_{n2} R^n \tag{A4}$$

$$C_{n1} = \frac{1}{\pi} \int_0^{2\pi} \psi(\phi)\, \cos(n\phi)\, d\phi \tag{A5}$$

$$C_{n2} = \frac{1}{\pi} \int_0^{2\pi} \psi(\phi)\, \sin(n\phi)\, d\phi \tag{A6}$$

Moreover,

$$\frac{d\zeta}{dz'} = 1 - \frac{a^2}{z'^2} = \frac{1}{z'}\left[z' - \frac{a^2}{z'}\right]$$

$$= \frac{1}{z'}\left[z\, e^{\sum_{n=1}^{\infty}\frac{A_n+iB_n}{z^n}} - \frac{a^2}{z\, e^{\sum_{n=1}^{\infty}\frac{A_n+iB_n}{z^n}}}\right]$$

$$= \frac{z}{z'}\left[e^{\sum_{n=1}^{\infty}\frac{[C_{n1}+iC_{n2}]R^n}{z^n}} - \frac{a^2}{z^2\, e^{\sum_{n=1}^{\infty}(\frac{R}{z})^n[C_{n1}+iC_{n2}]}}\right] \tag{A7}$$

The product of the expression given by Eqs. (A2) and (A7) finally gives

$$\frac{d\zeta}{dz} = \frac{dz'}{dz}\frac{d\zeta}{dz'} = \left[1 - \sum_{n=1}^{\infty} n\,(\frac{R}{z})^n[C_{n1} + iC_{n2}]\right] \cdot$$

$$\cdot\left[e^{\sum_{n=1}^{\infty}(\frac{R}{z})^n[C_{n1}+iC_{n2}]} - \frac{1}{e^{2\Psi_0(\frac{z}{R})^2}\, e^{\sum_{n=1}^{\infty}(\frac{R}{z})^n[C_{n1}+iC_{n2}]}}\right] \tag{A8}$$

which is needed to evaluate the right hand side of Eq. (5.4.6).

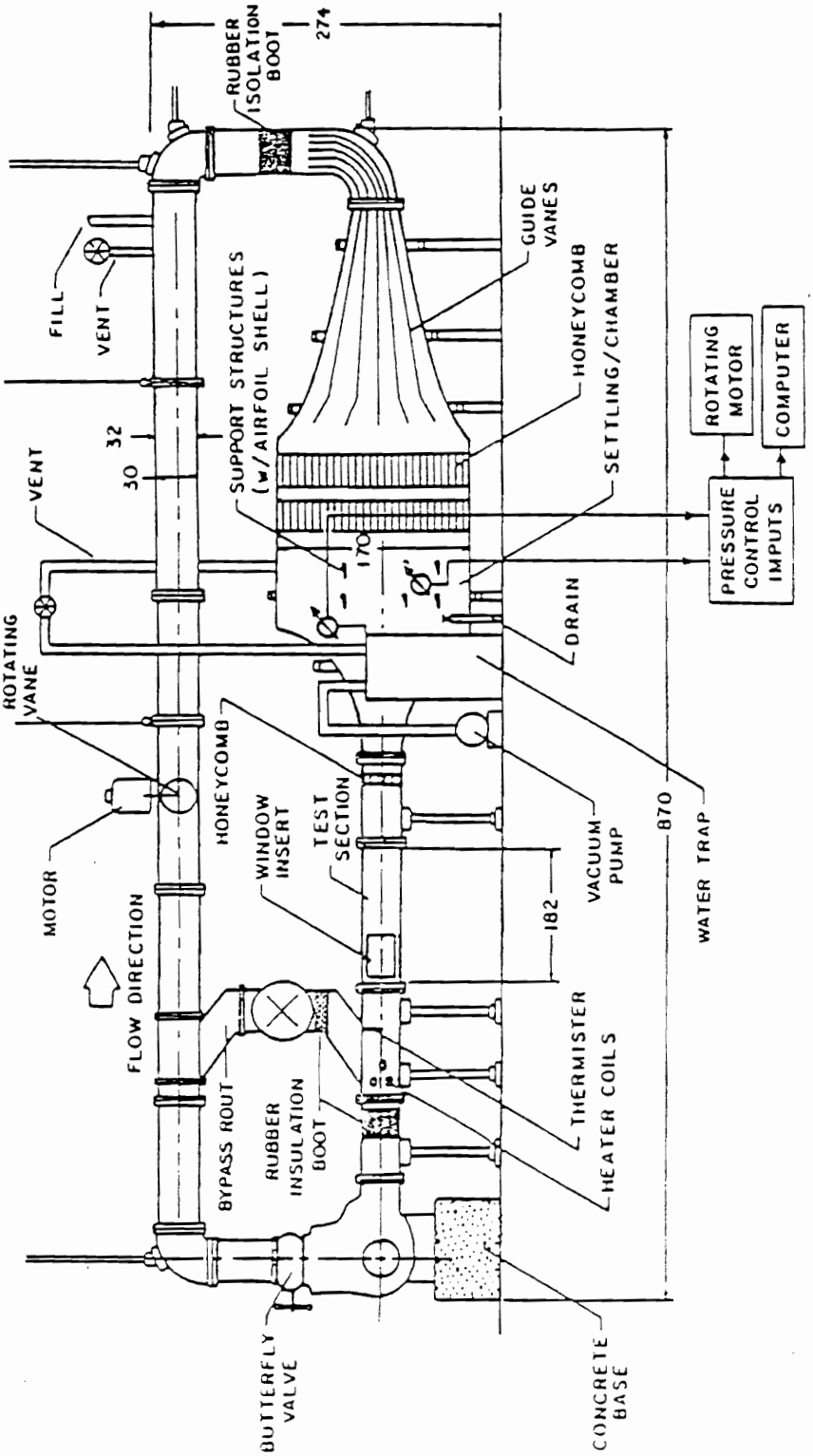

Fig. 2.2.1 The ESM water tunnel.

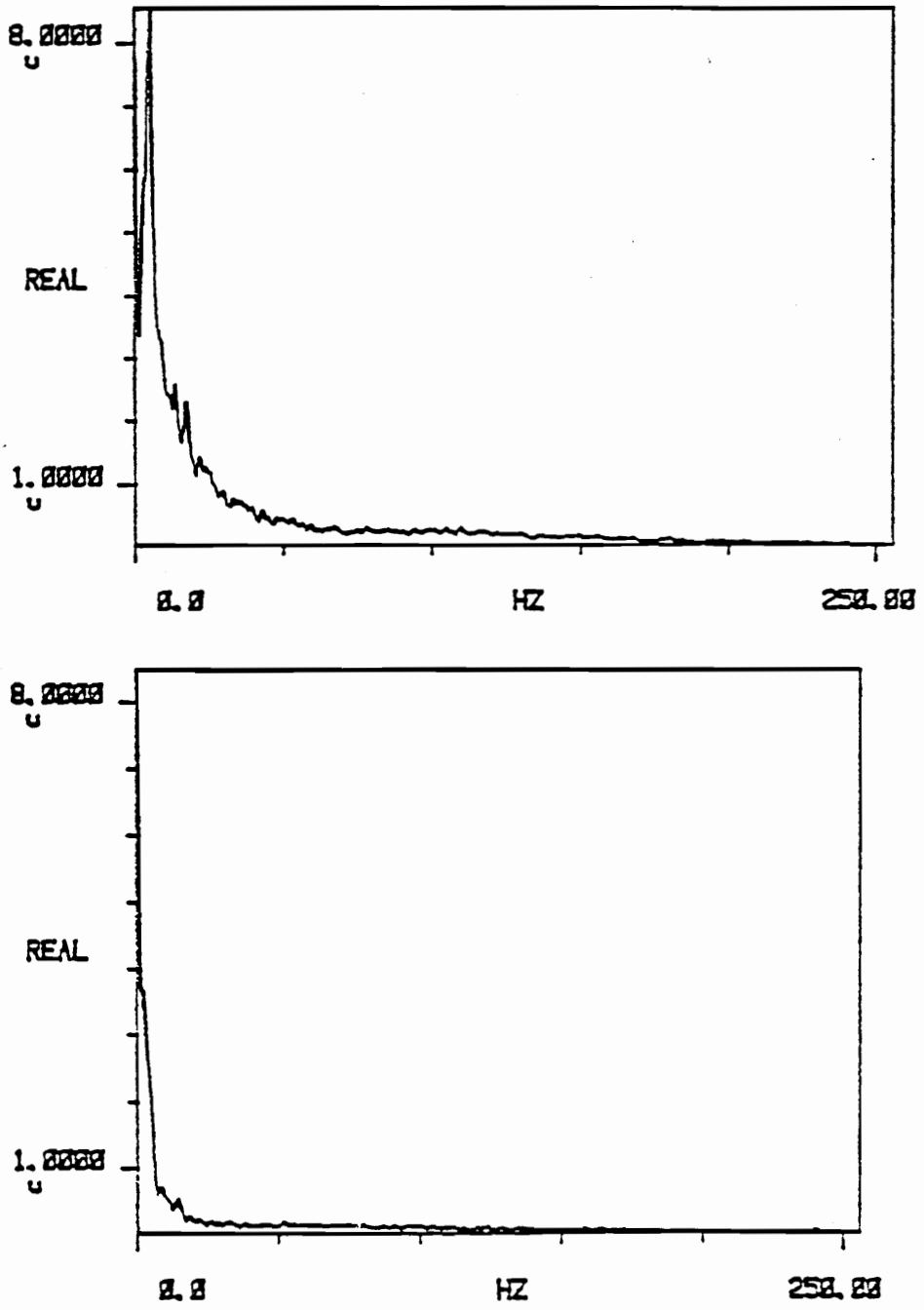

Fig. 2.2.2 Velocity autospectrum for driving pump speed = 0.5 and valve B closed. Bottom figure was obtained with no honeycomb at the entrance of the test section.

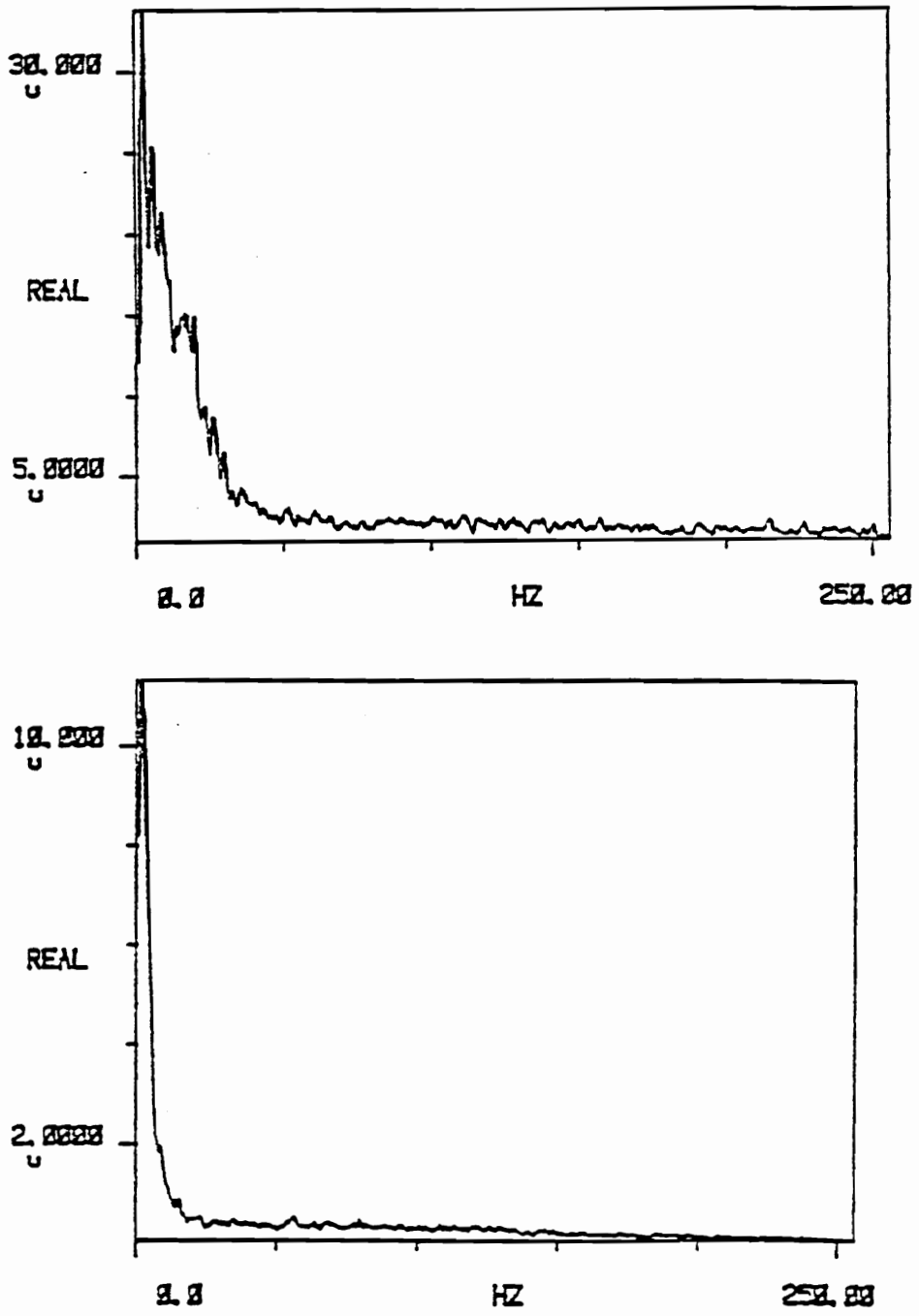

Fig. 2.2.3Velocity autospectrum for driving pump speed = 0.5 and valve 3 = setting 2. Bottom figure was obtained with no honeycomb at the entrance of the test section.

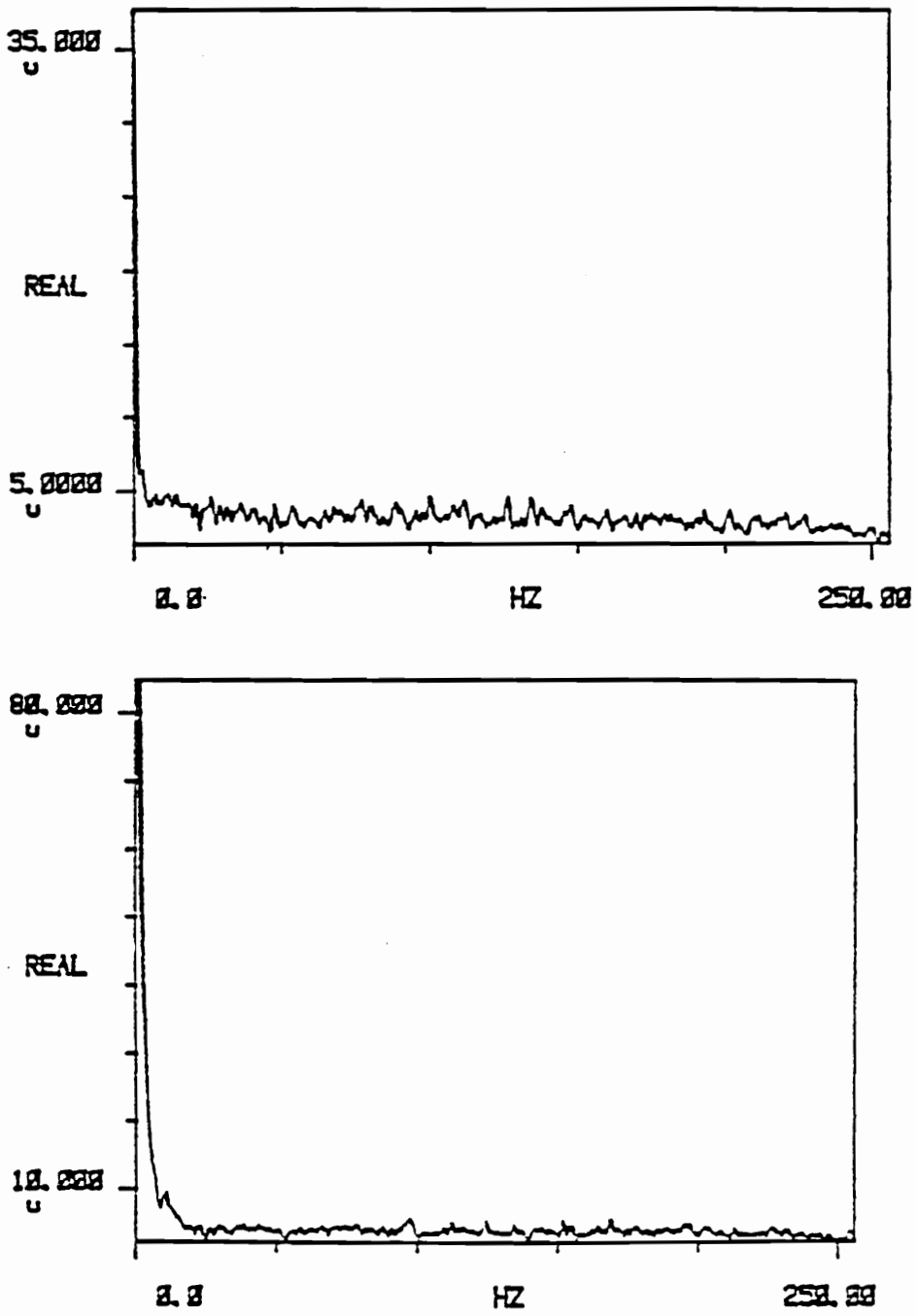

Fig. 2.2.4 Velocity autospectrum for driving pump speed = 0.5 and valve B = setting 4. Bottom figure was obtained with no honeycomb at the entrance of the test section.

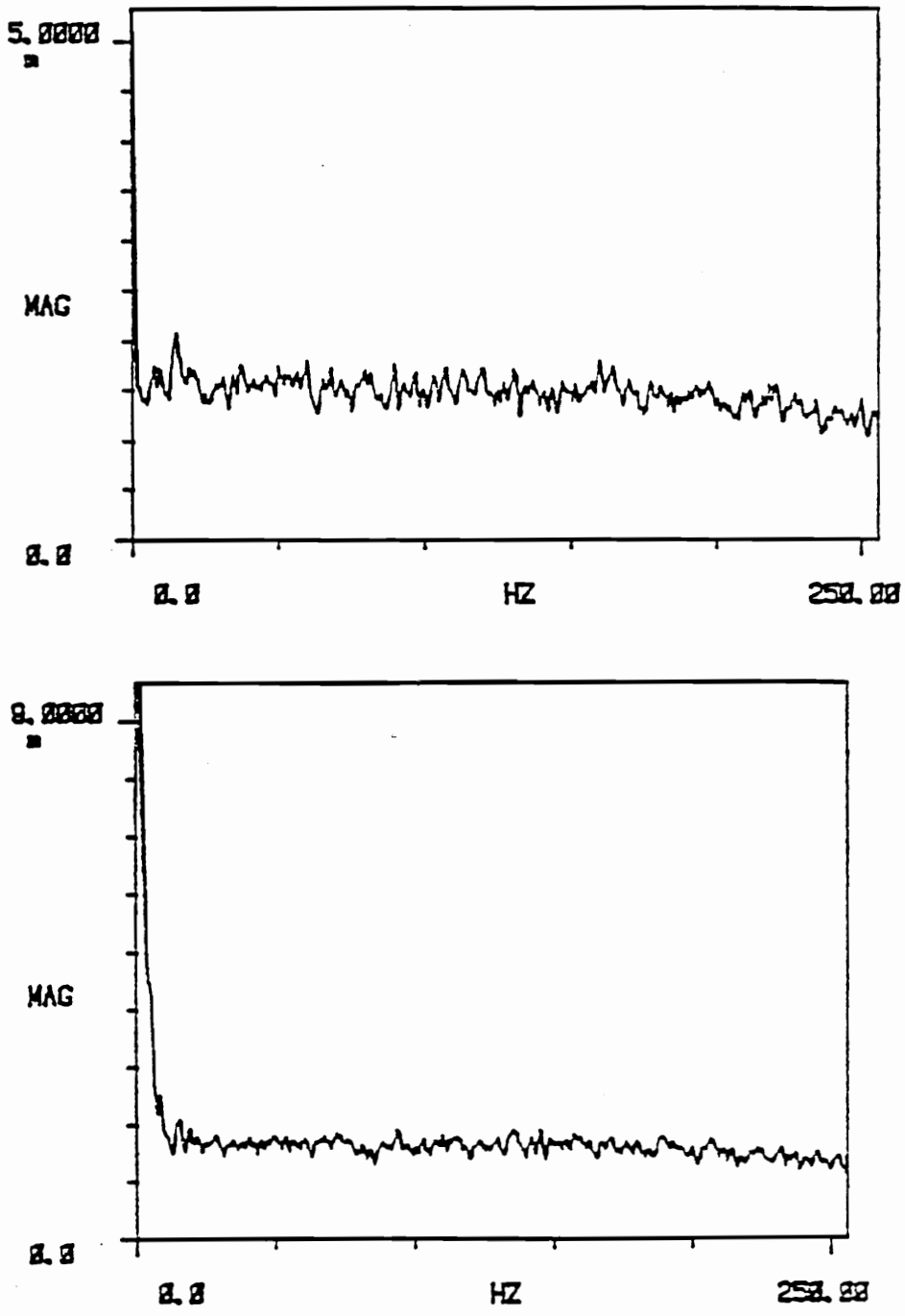

Fig. 2.2.5Velocity autospectrum for driving pump speed = 0.5 and valve 8 open. Bottom figure was obtained with no honeycomb at the entrance of the test section.

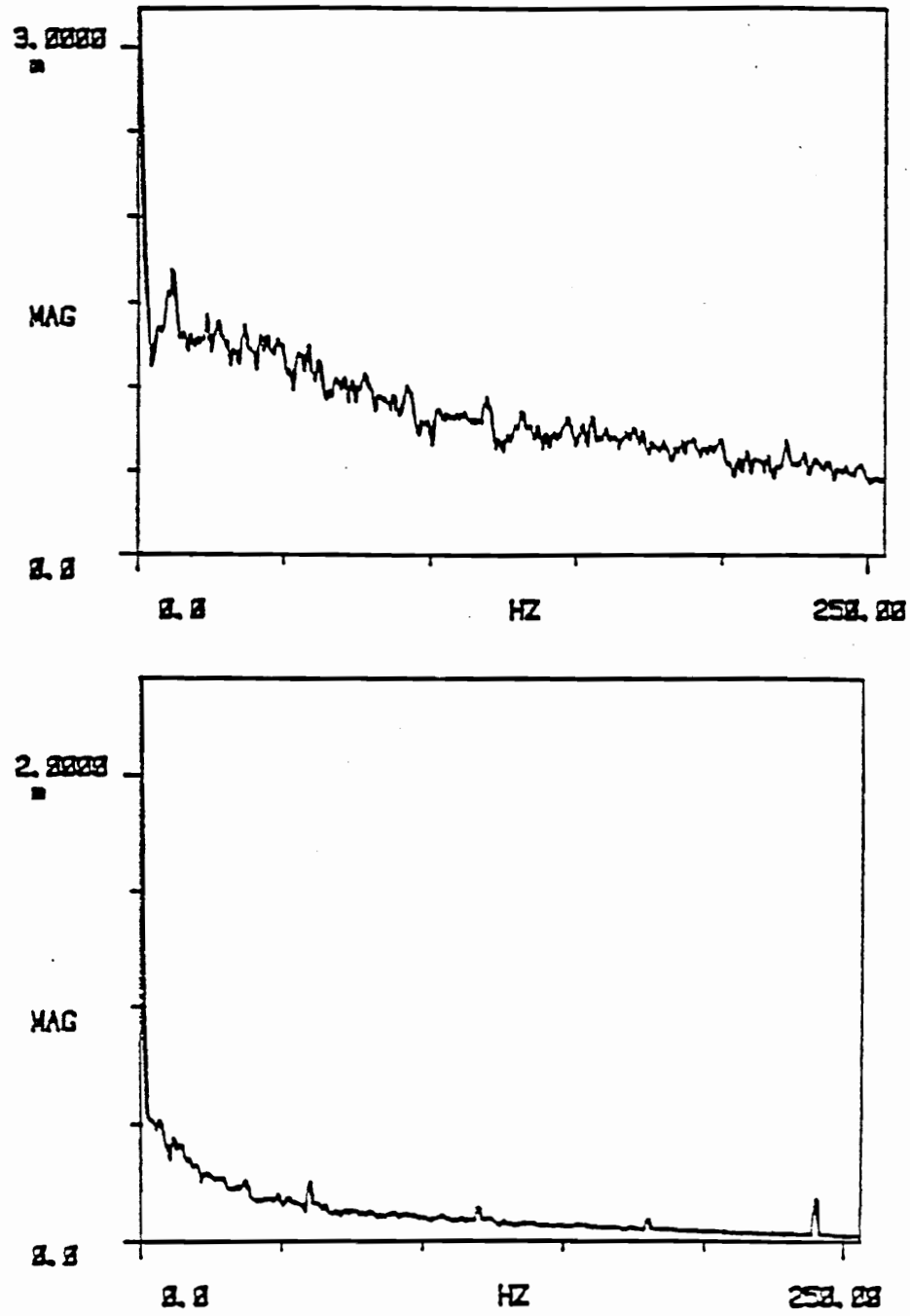

Fig.2.2.6 Velocity autospectrum for driving pump speed = 5 and valve 8 closed. Bottom figure was obtained with no honeycomb at the entrance of the test section.

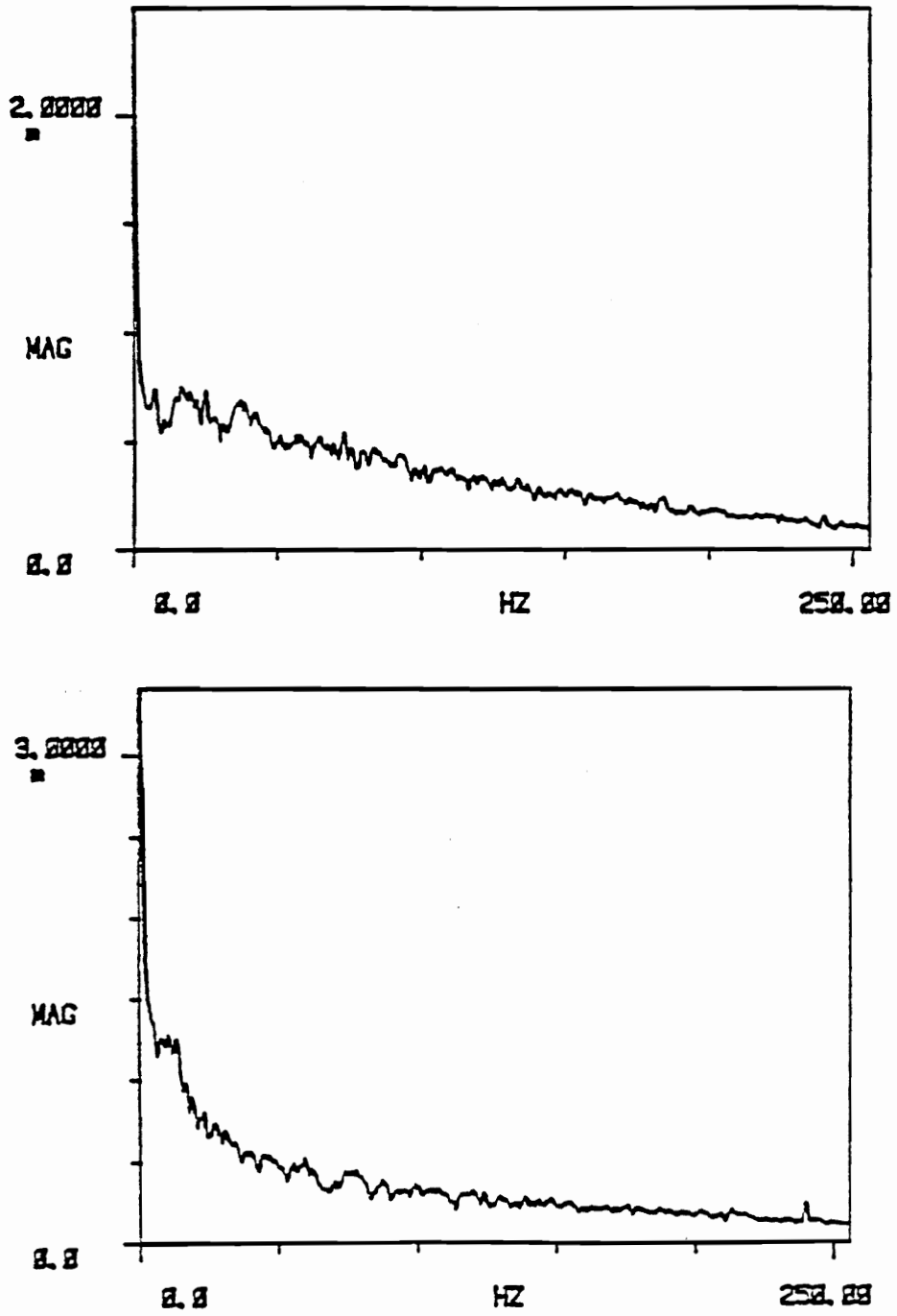

Fig. 2.2.7Velocity autospectrum for driving pump speed = 5 and valve B = setting 2. Bottom figure was obtained with no honeycomb at the entrance of the test section.

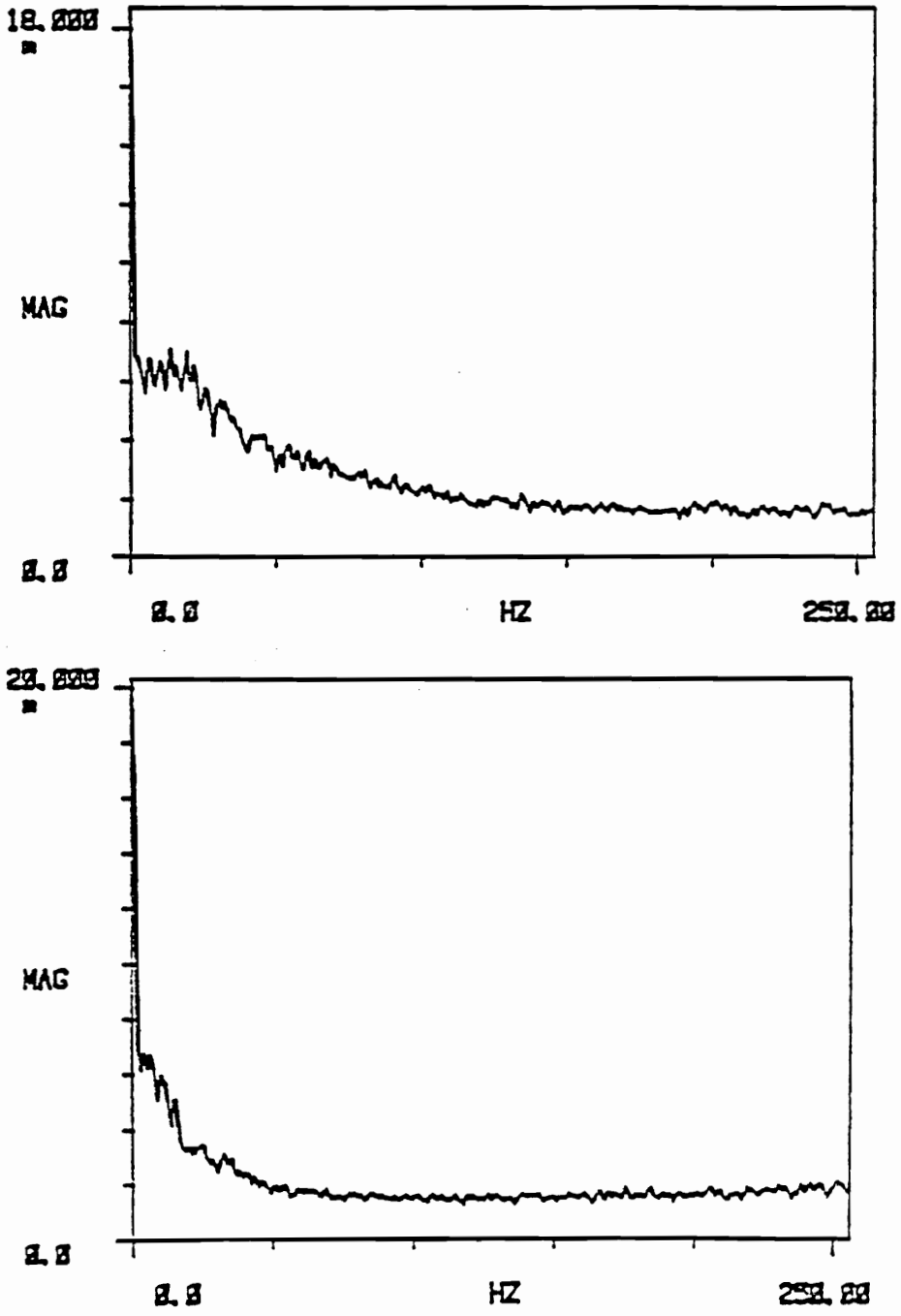

Fig. 2.2.8 Velocity autospectrum for driving pump speed = 5 and valve B = setting 4. Bottom figure was obtained with no honeycomb at the entrance of the test section.

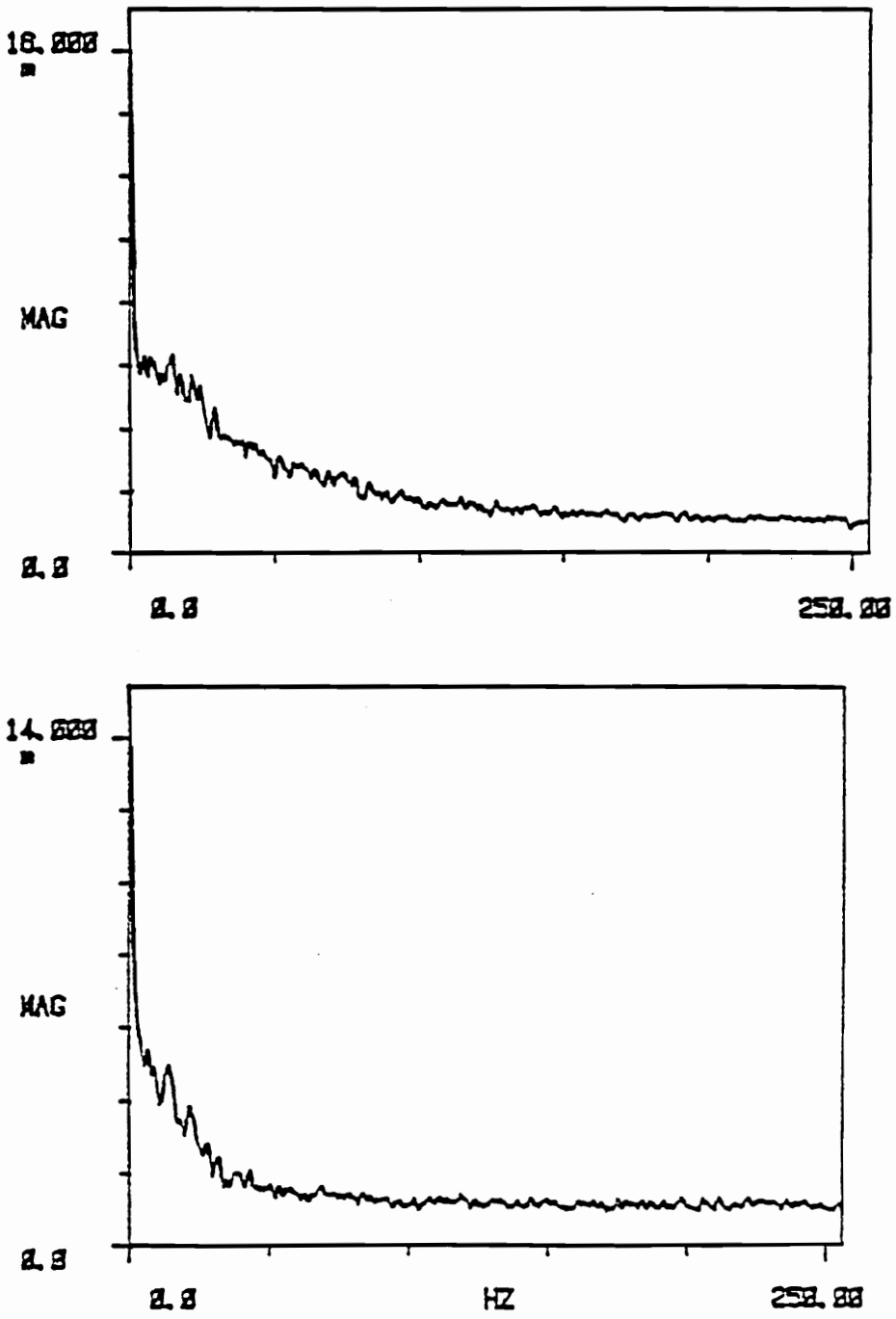

Fig. 2.2.9 Velocity autospectrum for driving pump speed = 5 and valve B open. Bottom figure was obtained with no honeycomb at the entrance of the test section.

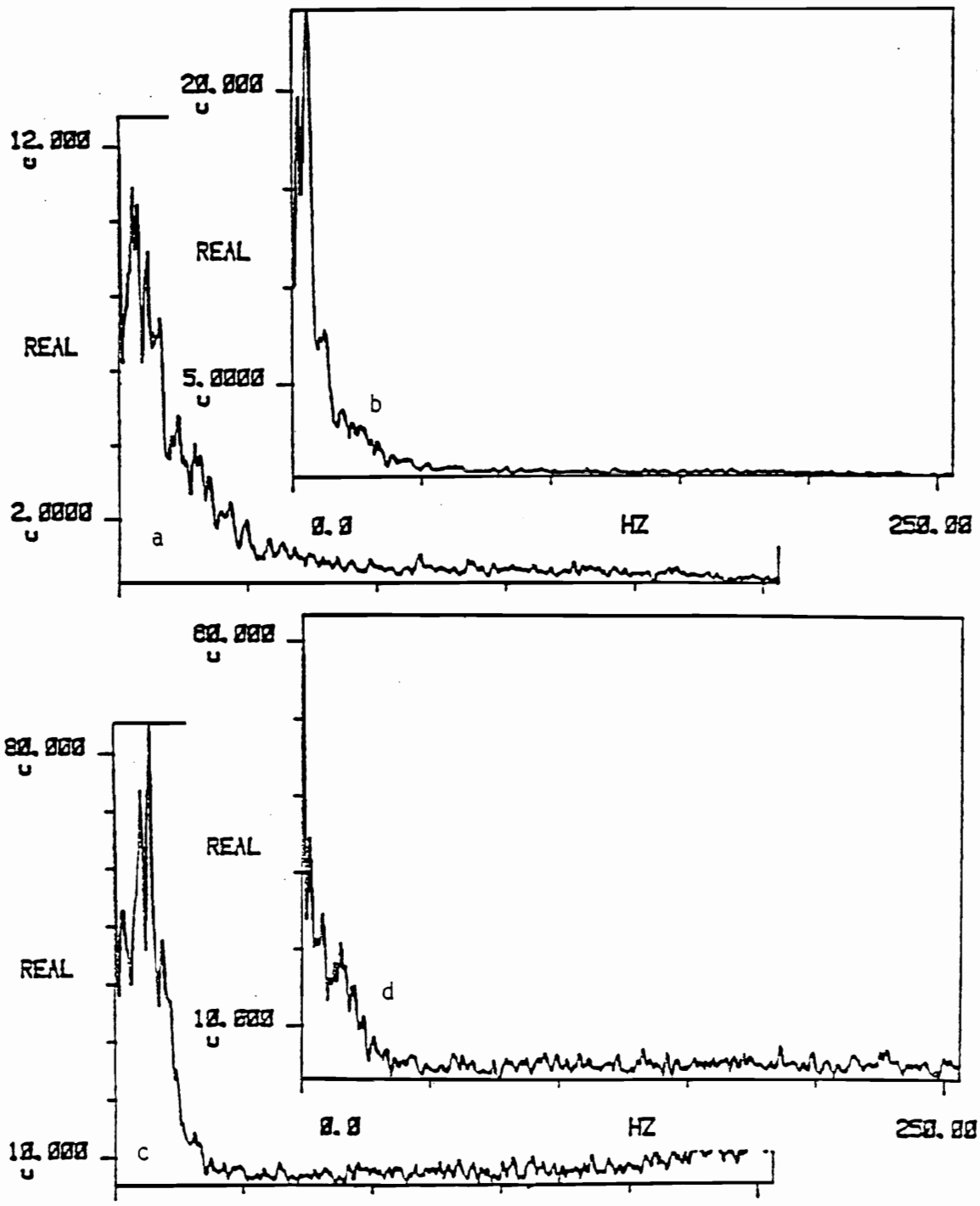

Fig. 2.2.10Velocity spectra for driving pump speed = 1 and varying positions of valve B. a) valve B closed; b) valve B = 2; c) valve B = 4; d) valve B open.

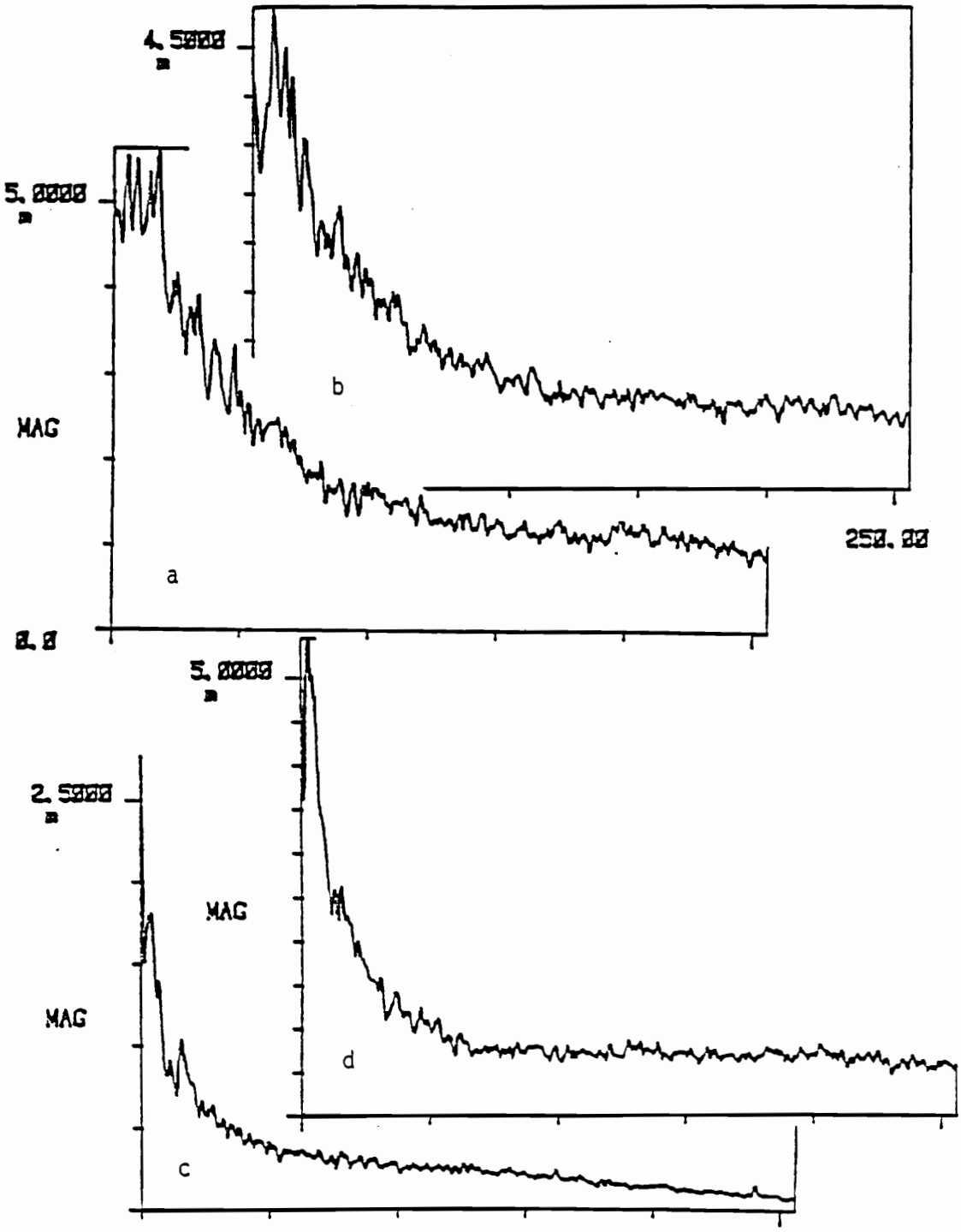

Fig. 2.2.11 Velocity spectra for driving pump speed = 2 and varying positions of valve B. a) valve B closed; b) valve B = 2; c) valve B = 4; d) valve B open.

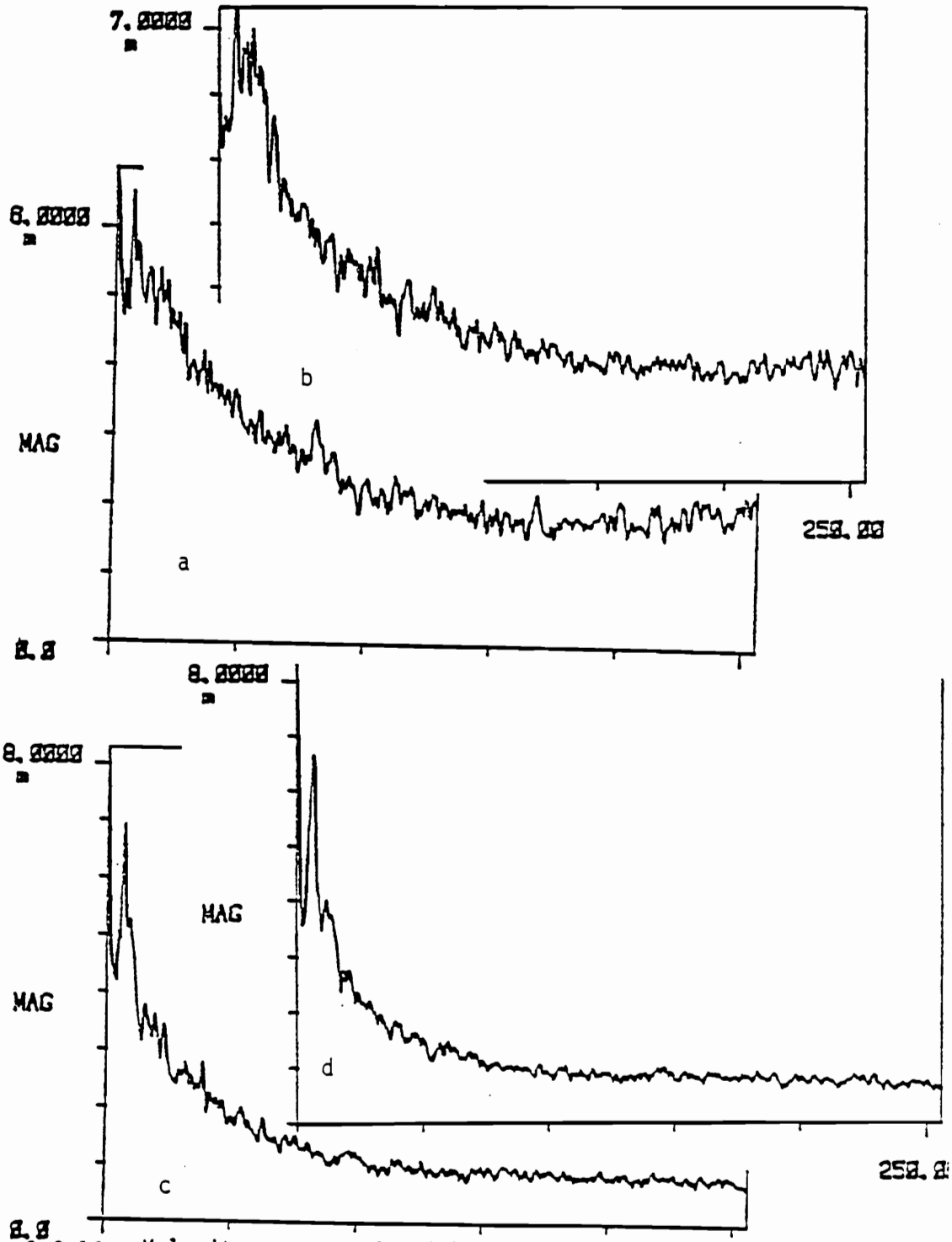

Fig. 2.2.12 Velocity spectra for driving pump speed = 3 and varying positions of valve B. a) valve B closed; b) valve B = 2; c) valve B = 4; d) valve B open.

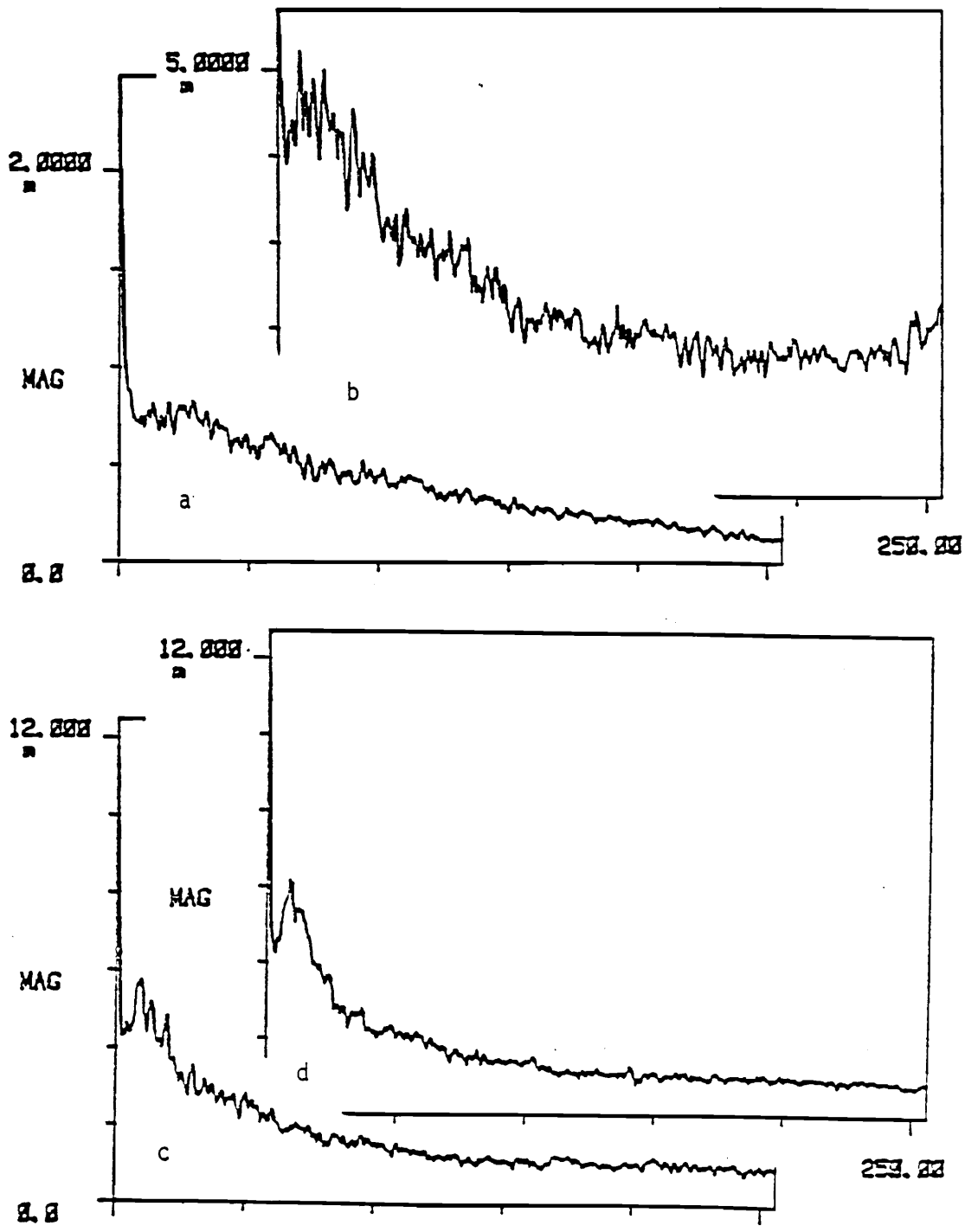

Fig. 2.2.13 Velocity spectra for driving pump speed = 4 and varying positions of valve B. a) valve B closed; b) valve B = 2; c) valve B = 4; d) valve B open.

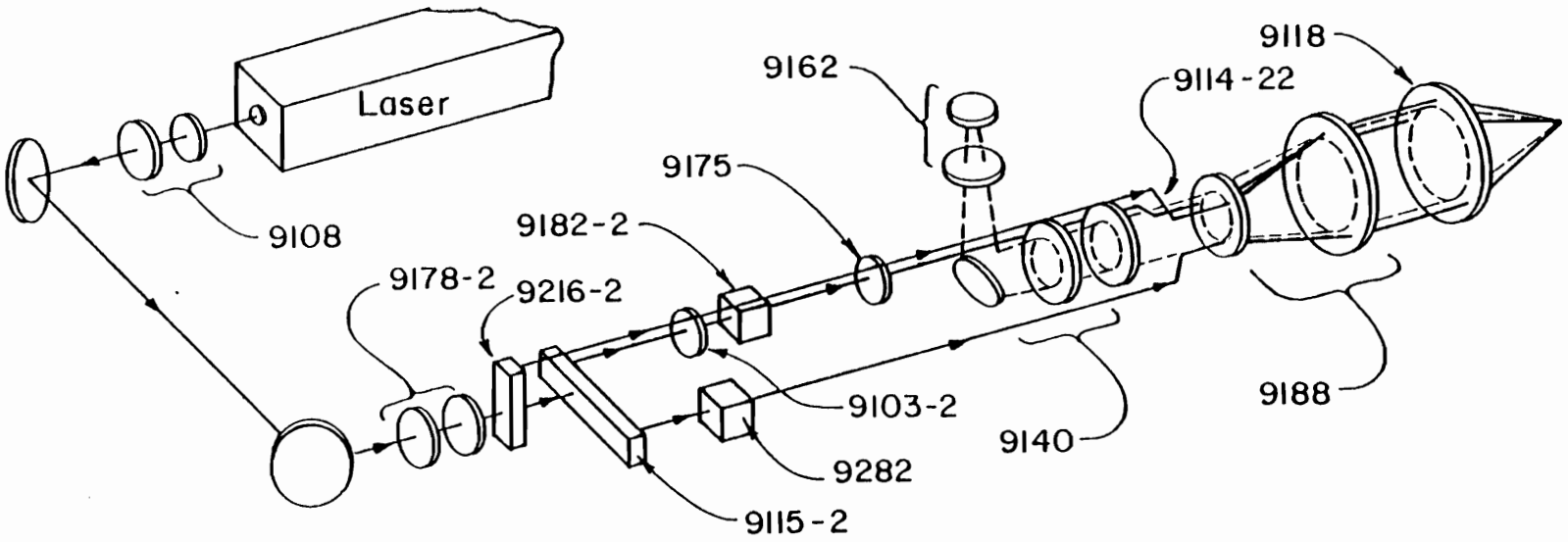

9118 Achromatic lens with focal length 250 mm
9188 Beam expander
9114-22 Beam spacer
9140 Receiving assembly
9162 Photodetector
9175 Beam Steering module
9182-2 Bragg-cell of 40 MHz
9282 Bragg-cell of 60 MHz
9103-2 Polarization rotator
9115-2 Beam splitter of equal intensity
9216-2 Beam splitter of variable intensity
9178-2 Rotating mount
9108 Collimator

Fig. 2.3.1 The Optical Train

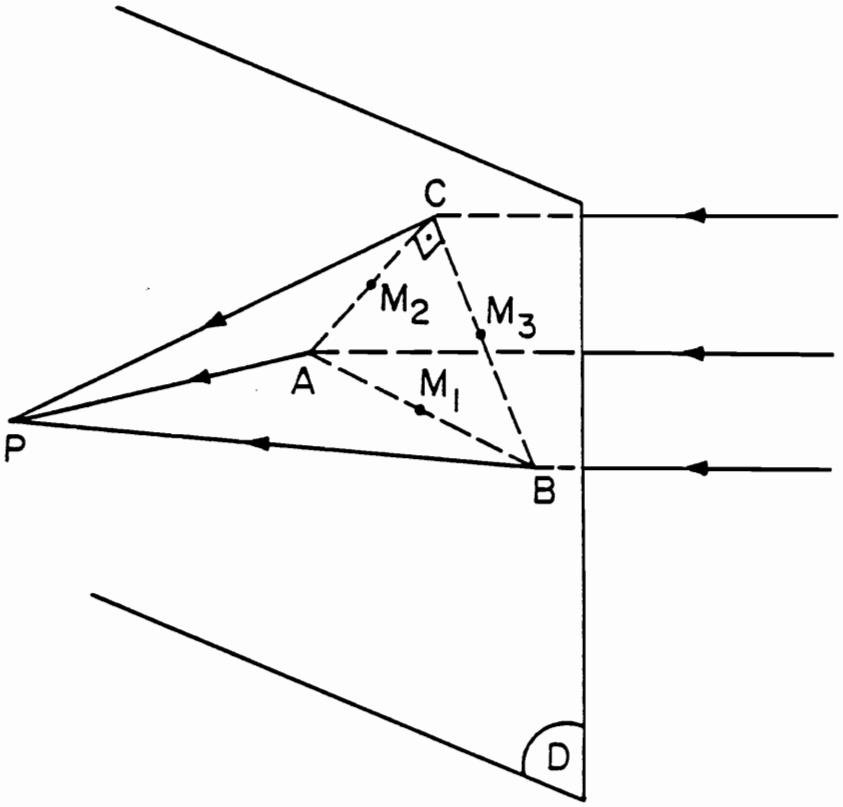

Fig. 2.3.2 Schematic of the 3 intersected laser beams

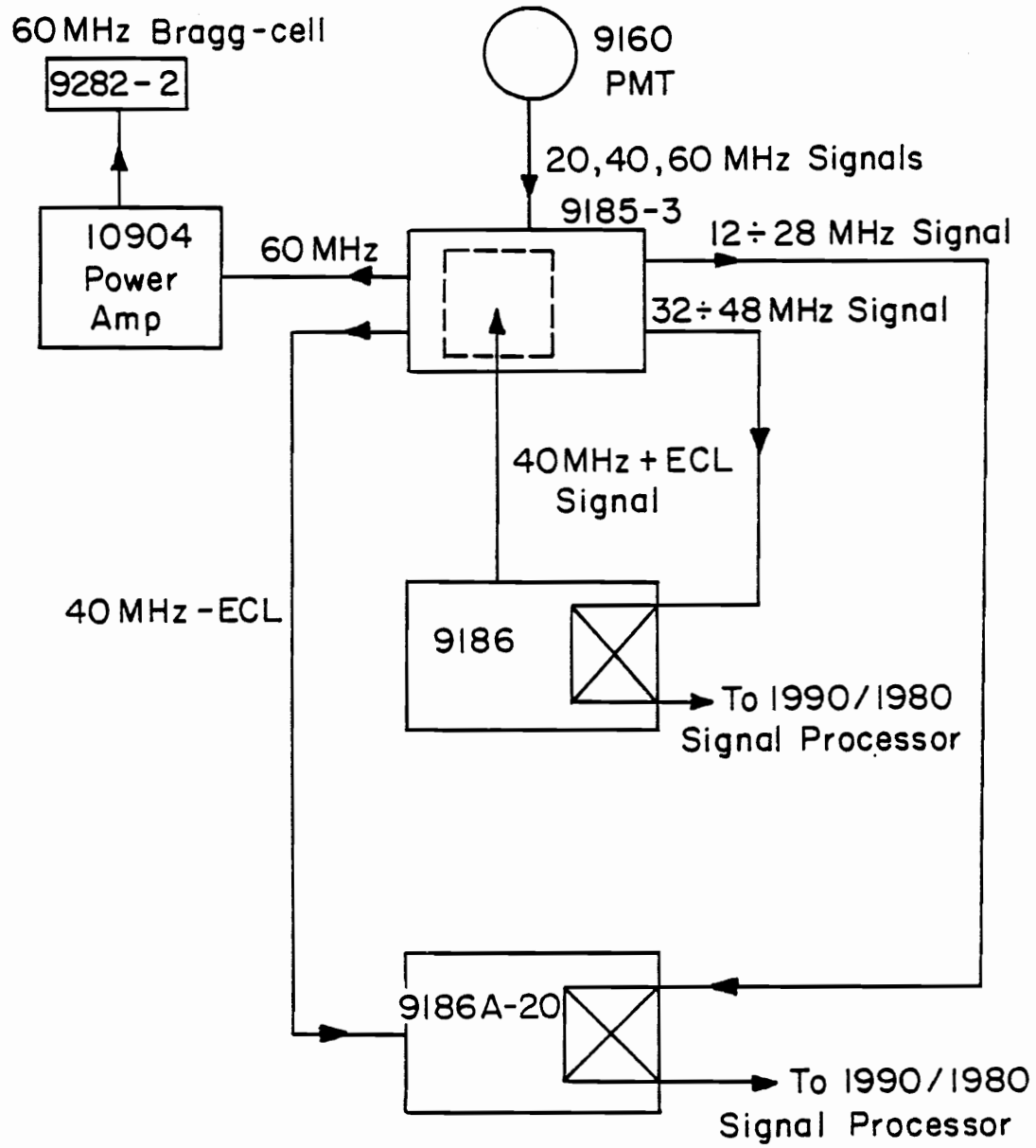

Fig. 2.3.3 Sketch of the electronics layout for the 3 beam frequency separation system.

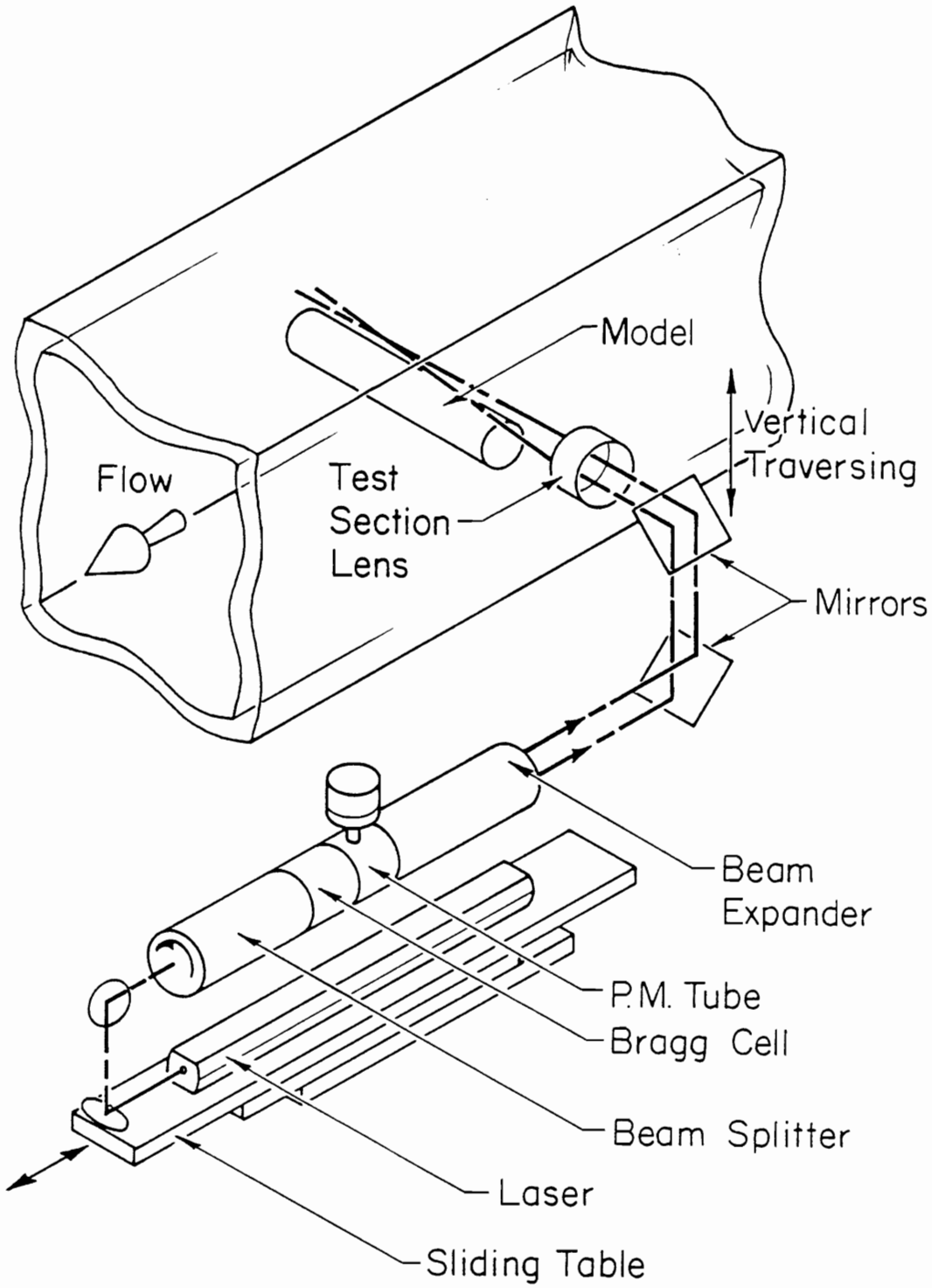

Fig. 2.4.1 Sliding table and traversing mechanism

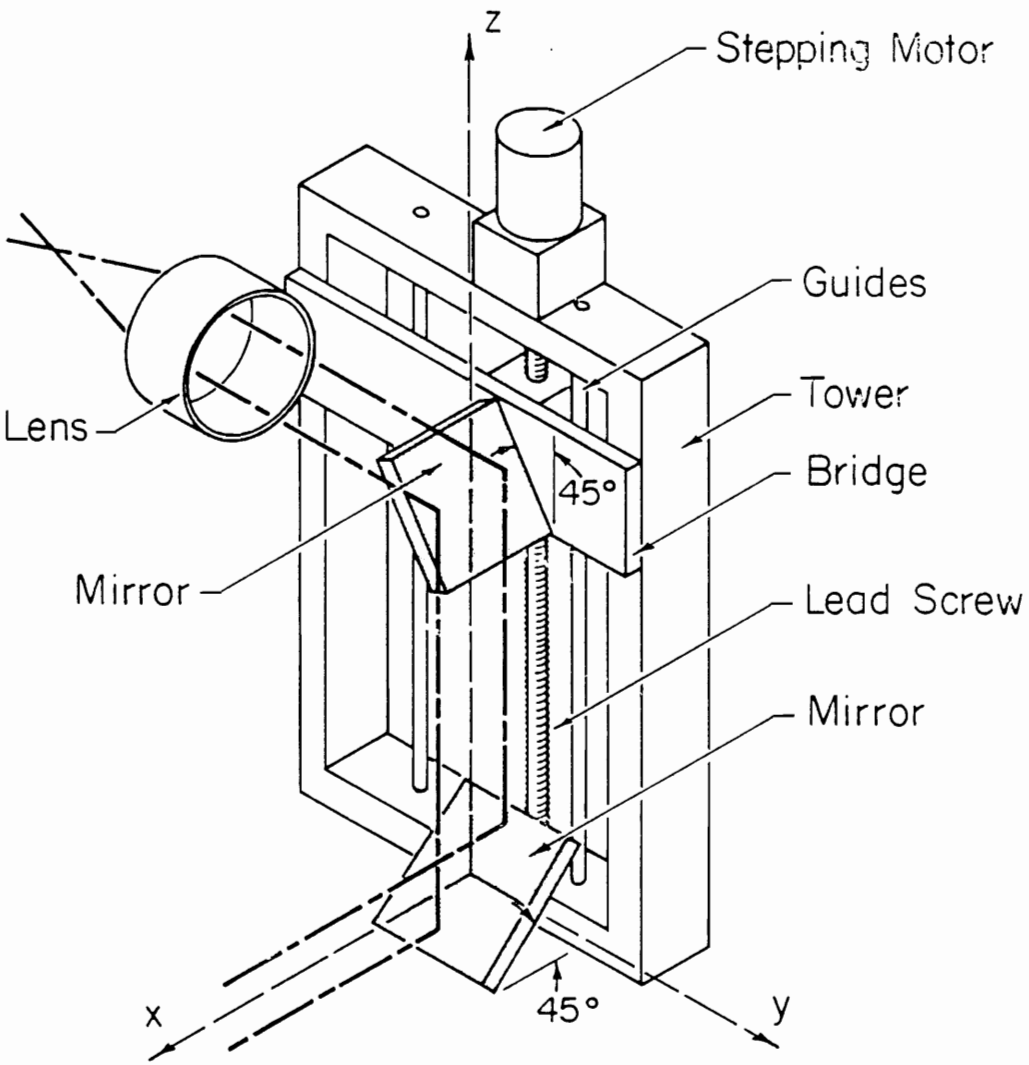

Fig. 2.4.2 Mirror tower

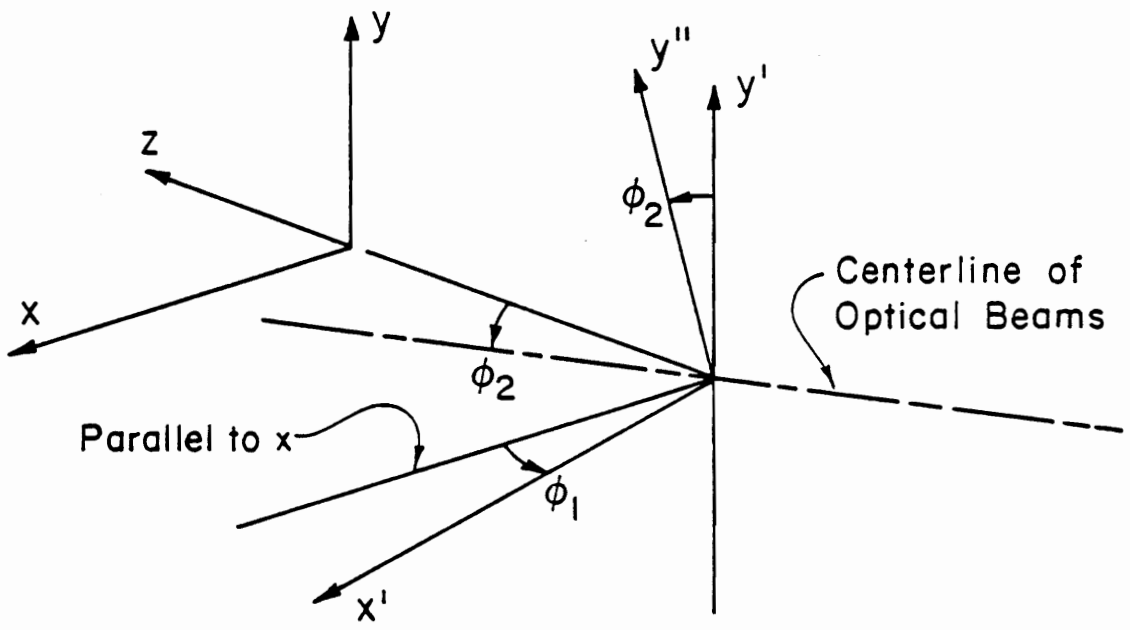

Fig. 2.4.3 Inclinations of beams

The axis x' is horizaontal and aligned with the train of optics. The axes y' and y are vertical. The axis x is aligned with the axis of symmetry of the test section. The plane x'y" is the plane of the focusing lens and is inclined with respect to the vertical by the angle ϕ_2. The plane of the lens is also turned about the vertical axis y' to form an angle ϕ_1 with the axis of the test section.

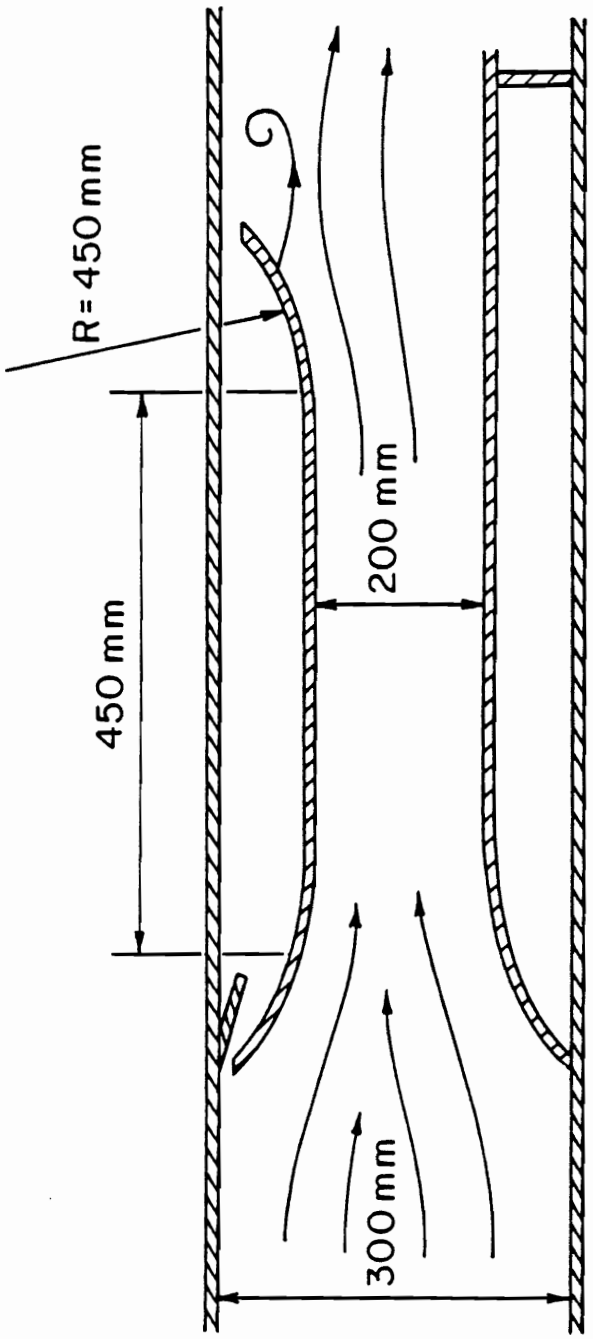

Fig. 3.1.1 Schematic of the model (circular arc) mounted in the test section.

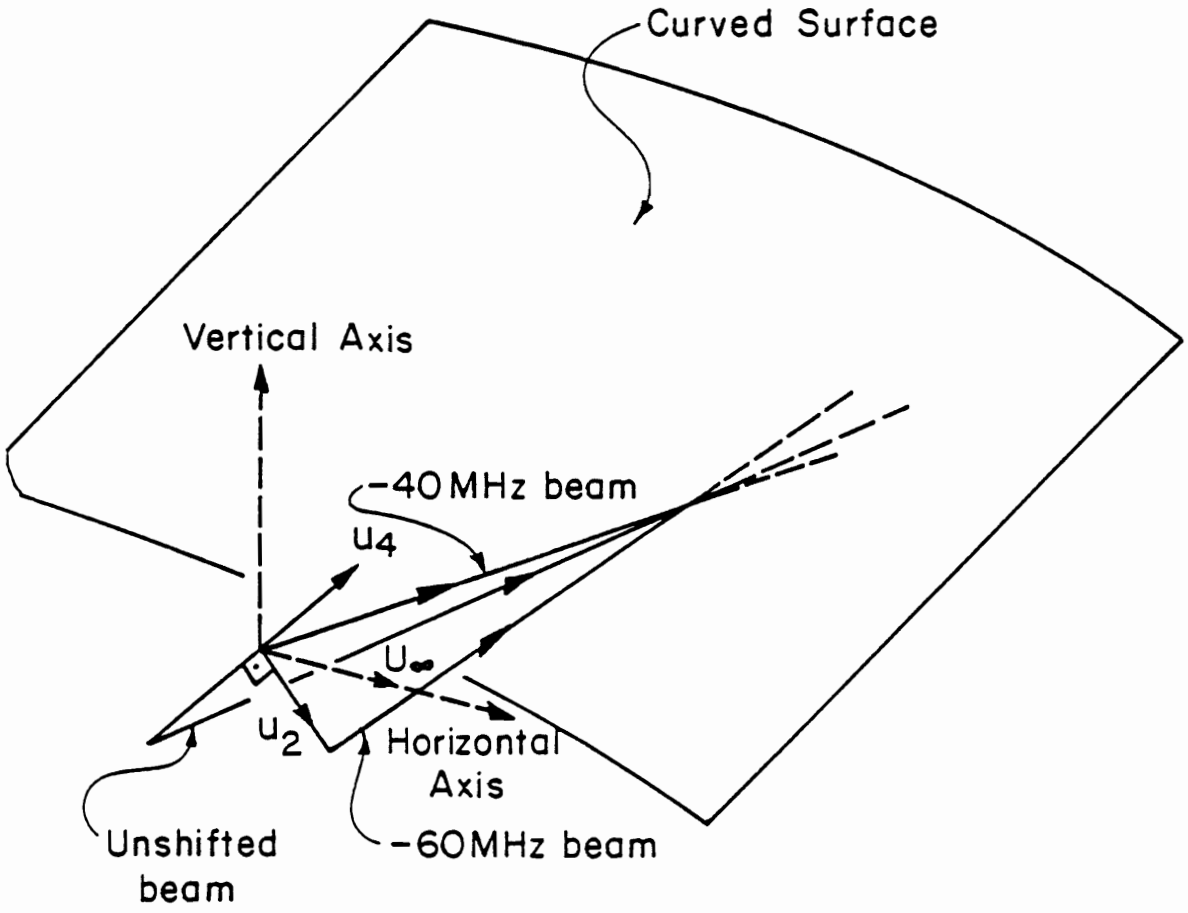

Fig. 3.1.2 Schematic of the 3 laser beams over the circular arc and the velocity components obtained by them (u_2, u_4).

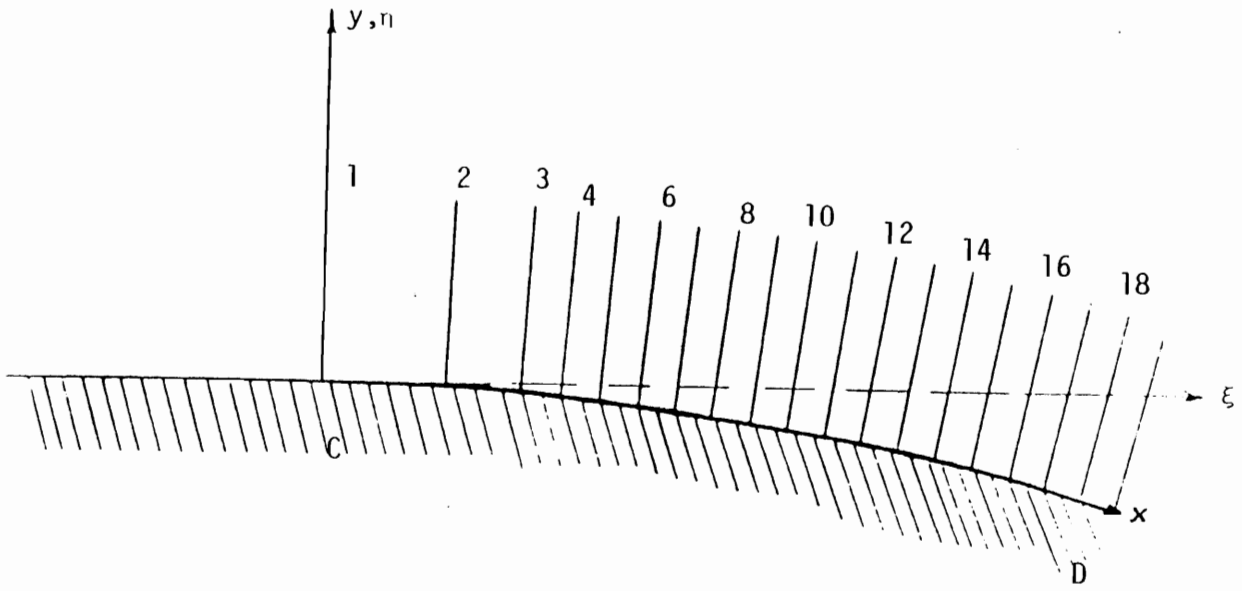

Fig. 3.1.3 The circular arc with the two coordinate systems and 19 measuring stations. The distance between two stations on the wall from No. 3 and on is 5 mm. The radius of the circular arc is 450 mm. This is a detail of the portion CD as indicated in Fig. 3.1.1.

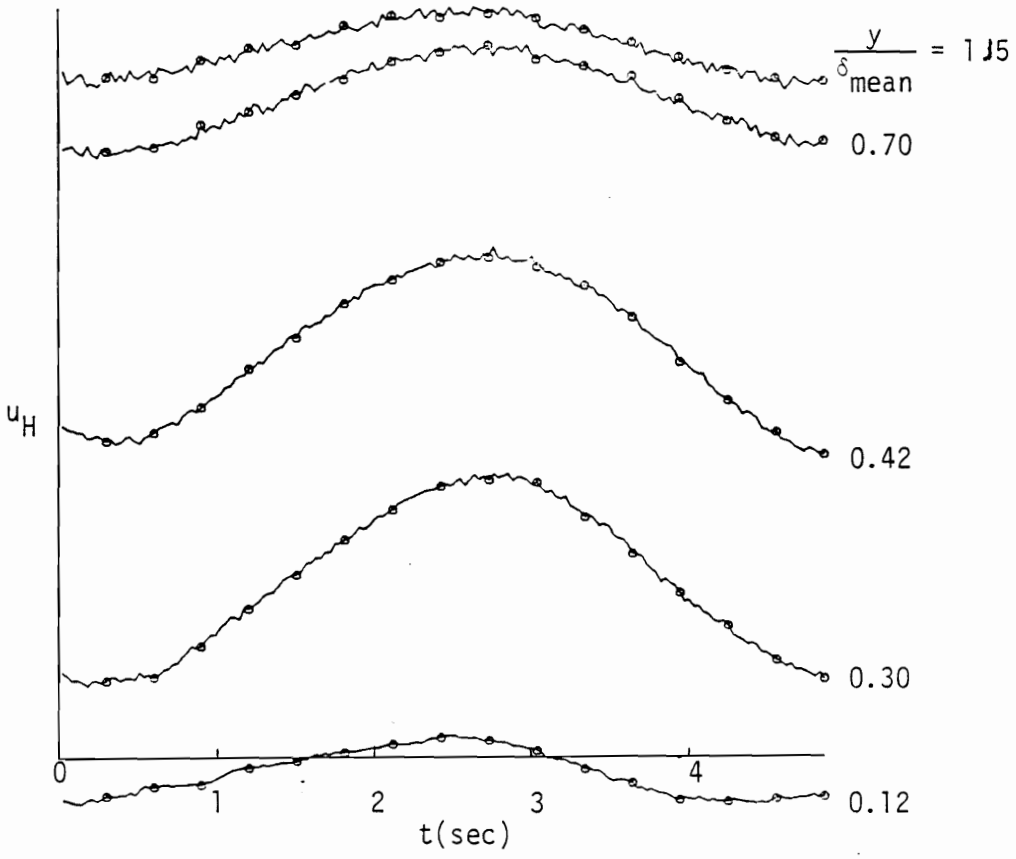

Fig. 3.1.4 Time records of u_H at 12th station. This is the output in Volts of the signal processor, after 15 averages.

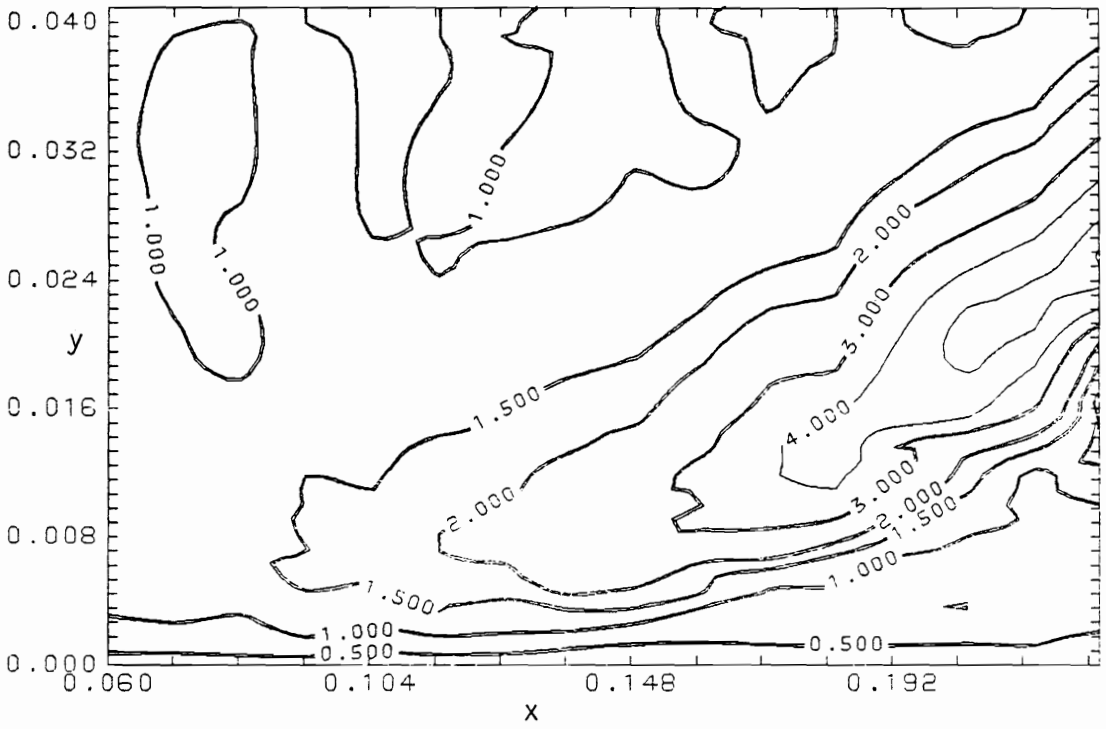

Fig. 3.1.5 Contours of velocity amplitude normalized by local free-stream amplitude

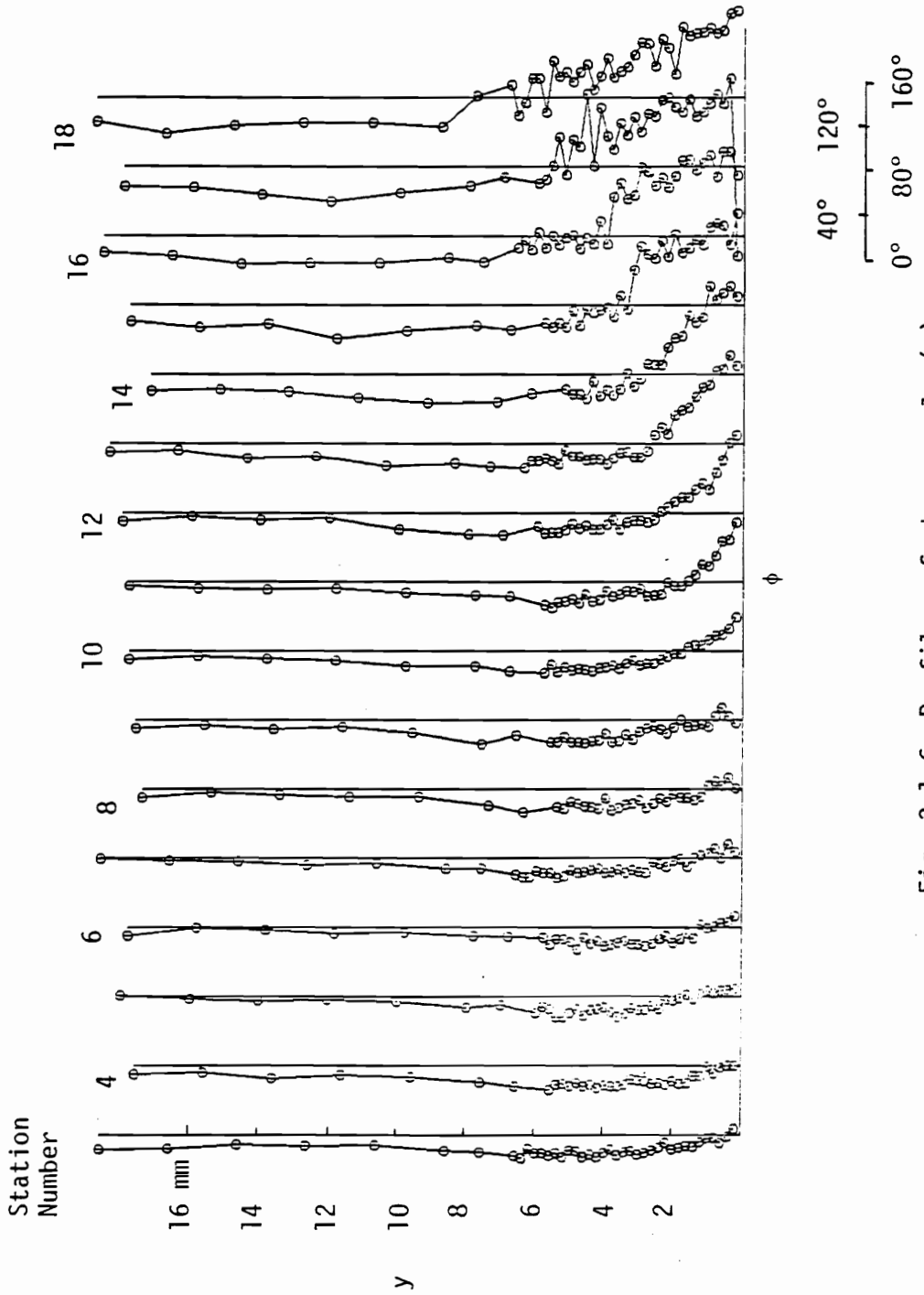

Fig. 3.1.6 Profiles of phase angle (ϕ)

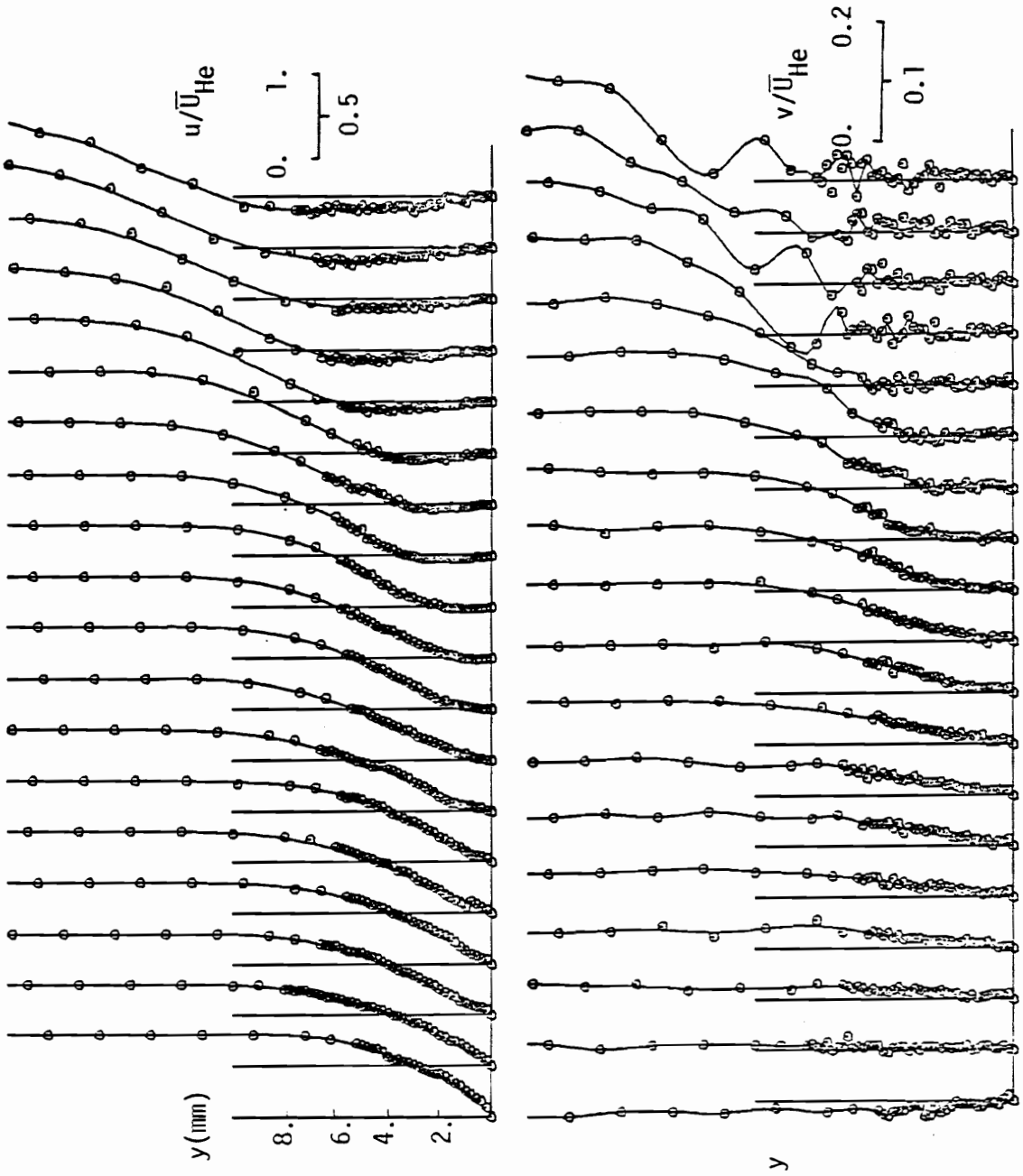

Fig. 3.1.7 Velocity profiles, t = 1/8

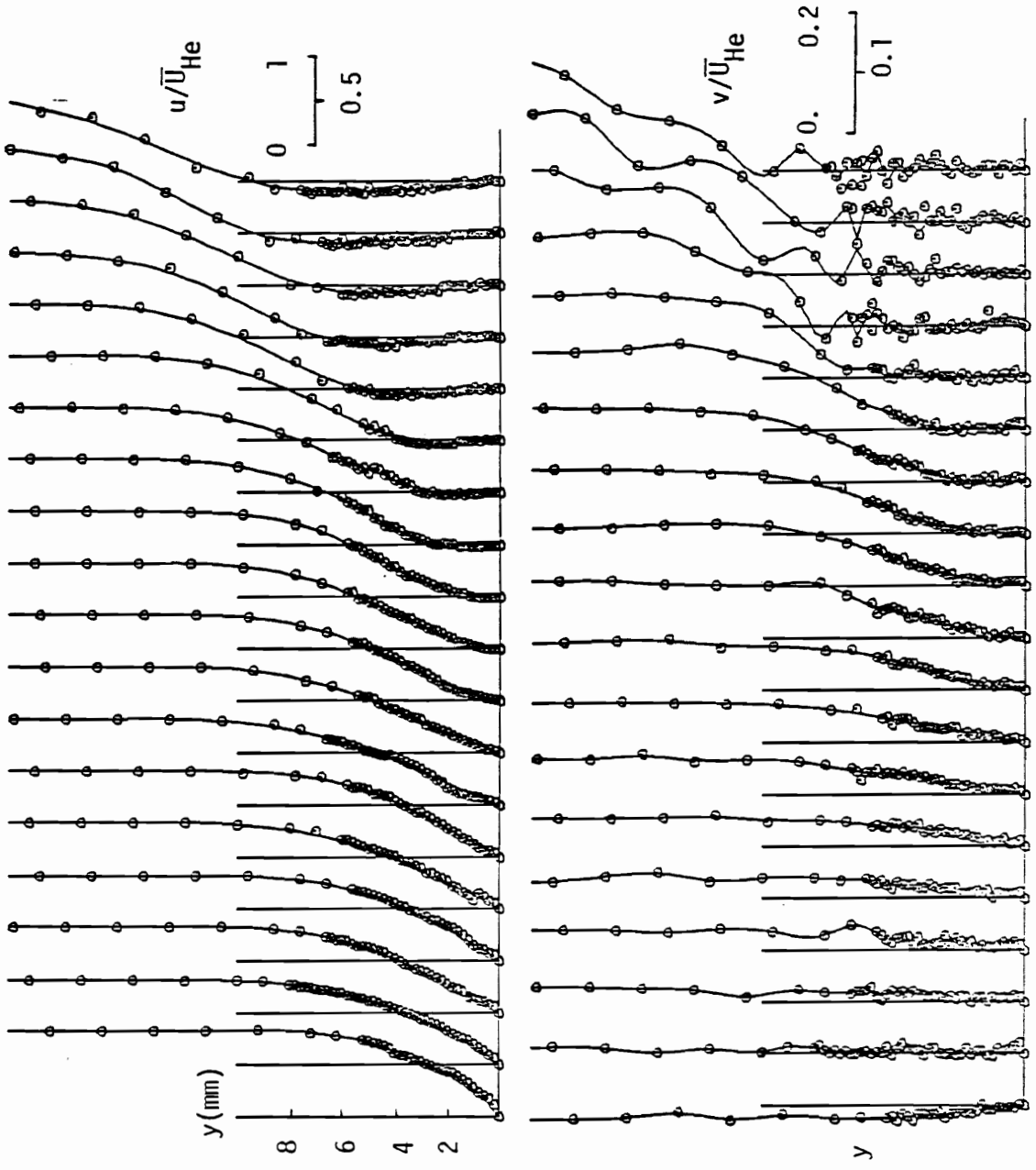

Fig. 3.1.8 Velocity profiles, t = 2/8

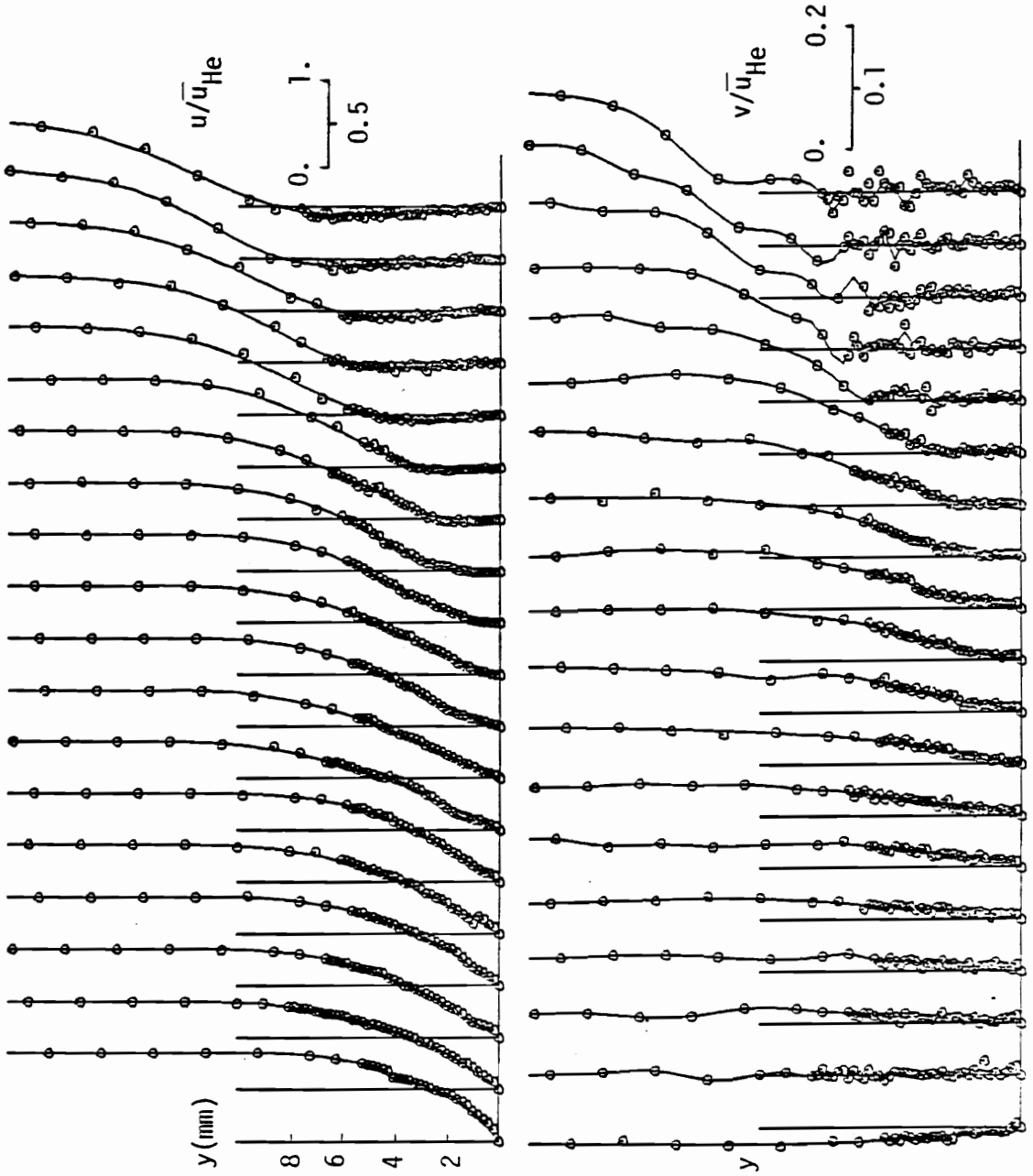

Fig. 3.1.9 Velocity profiles, t = 3/8

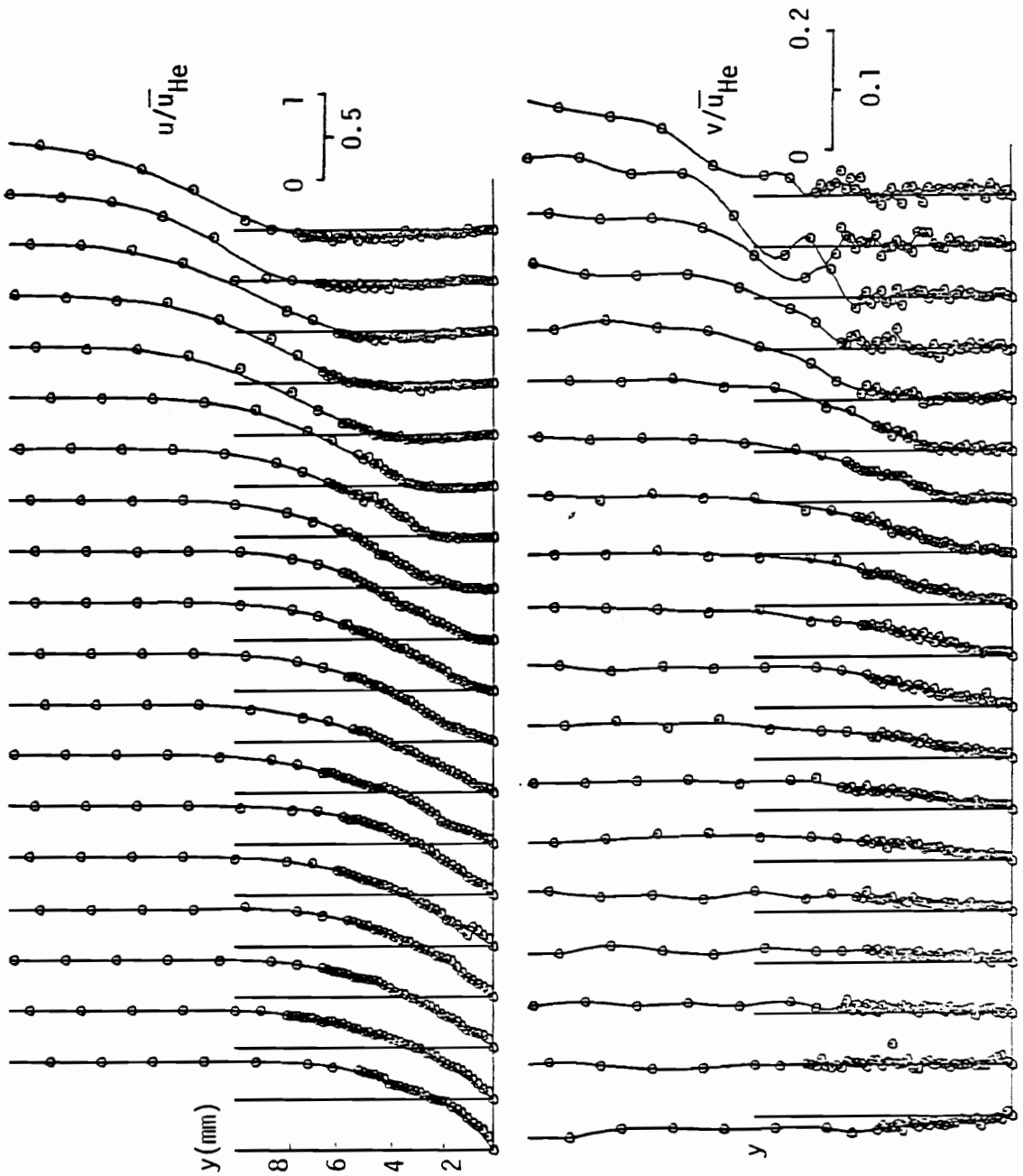

Fig. 3.1.10 Velocity profiles, t = 4/8.

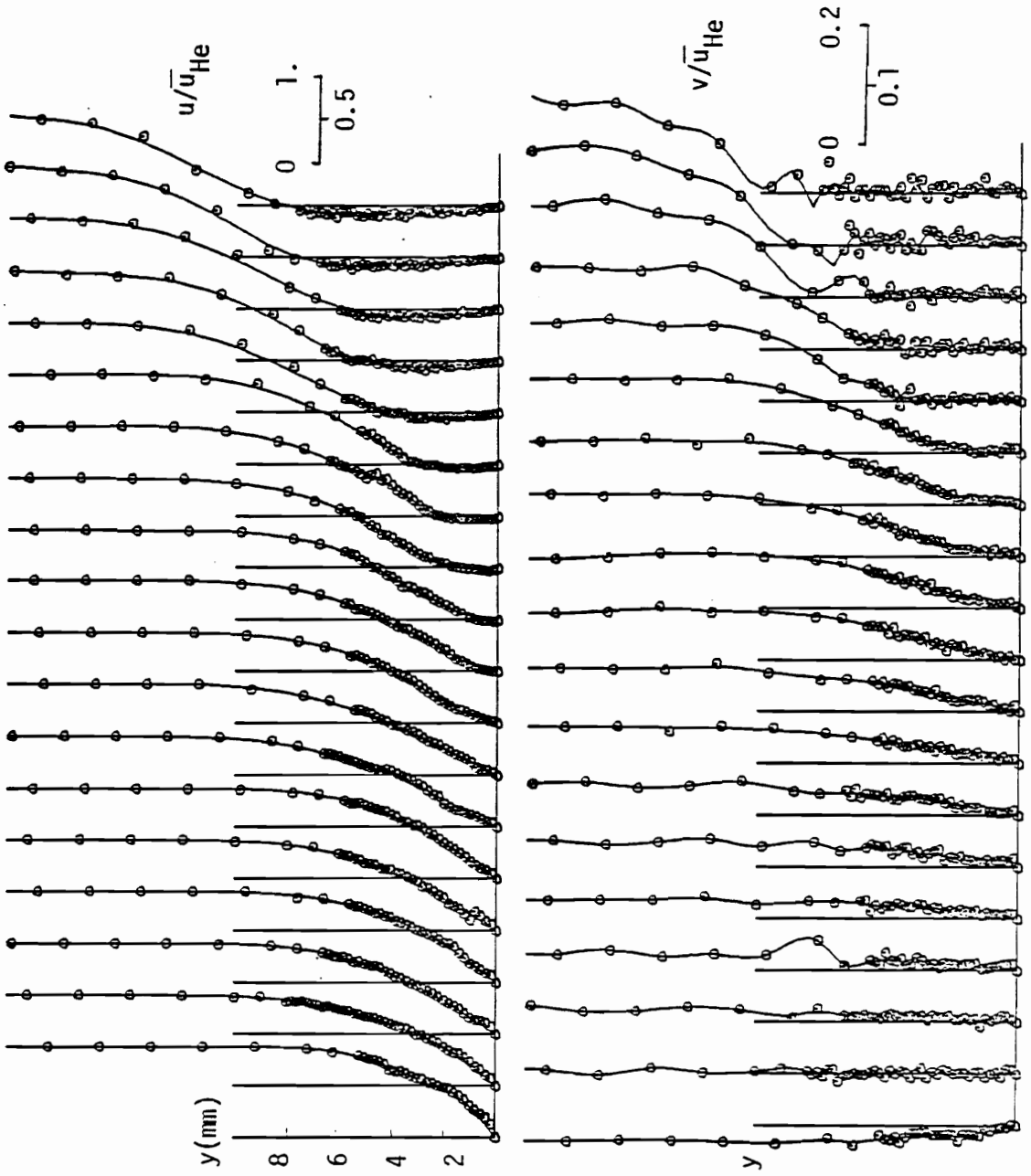

Fig. 3.1.11 Velocity profiles, t = 5/8.

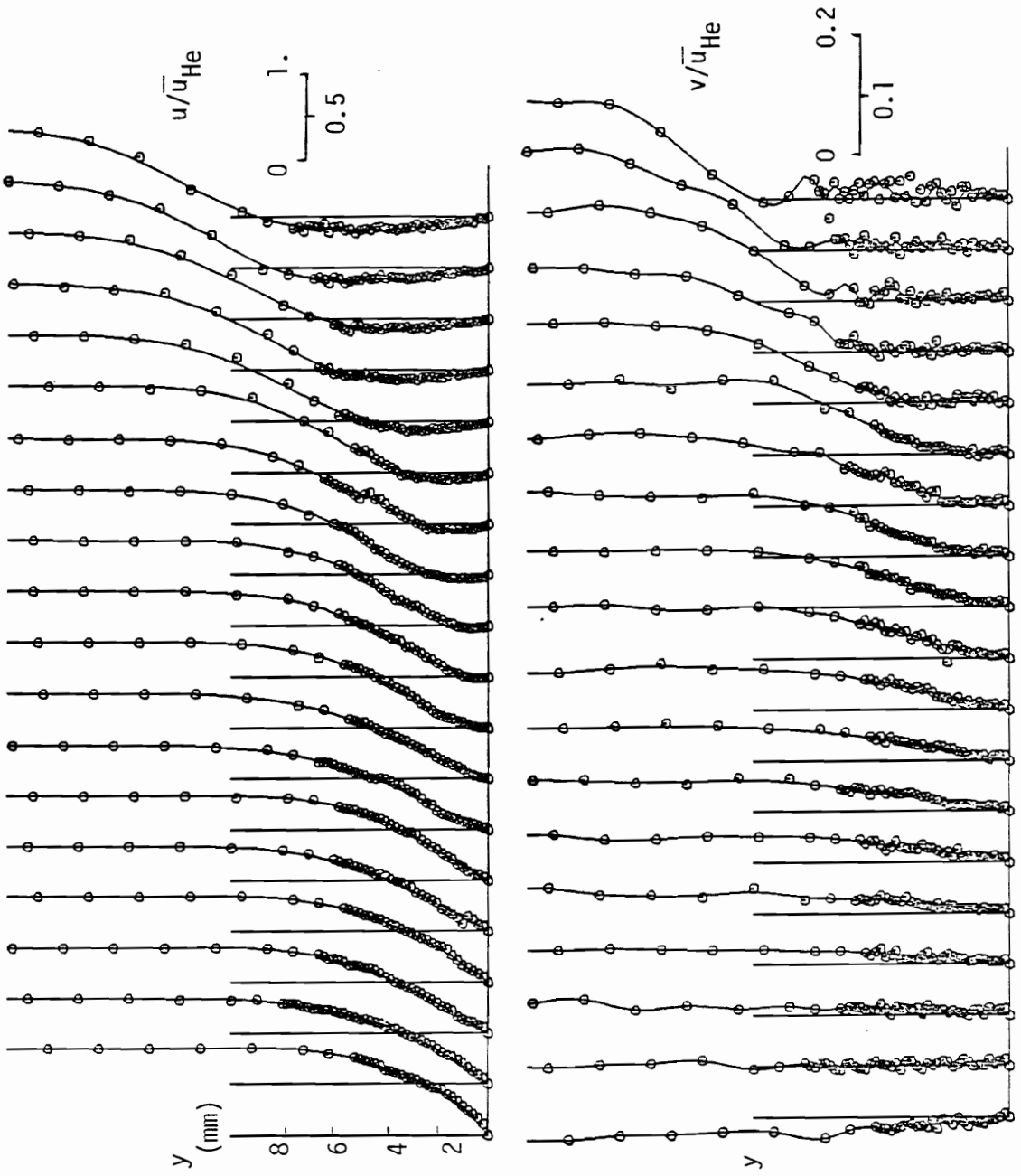

Fig. 3.1.12 Velocity profiles, t = 6/8.

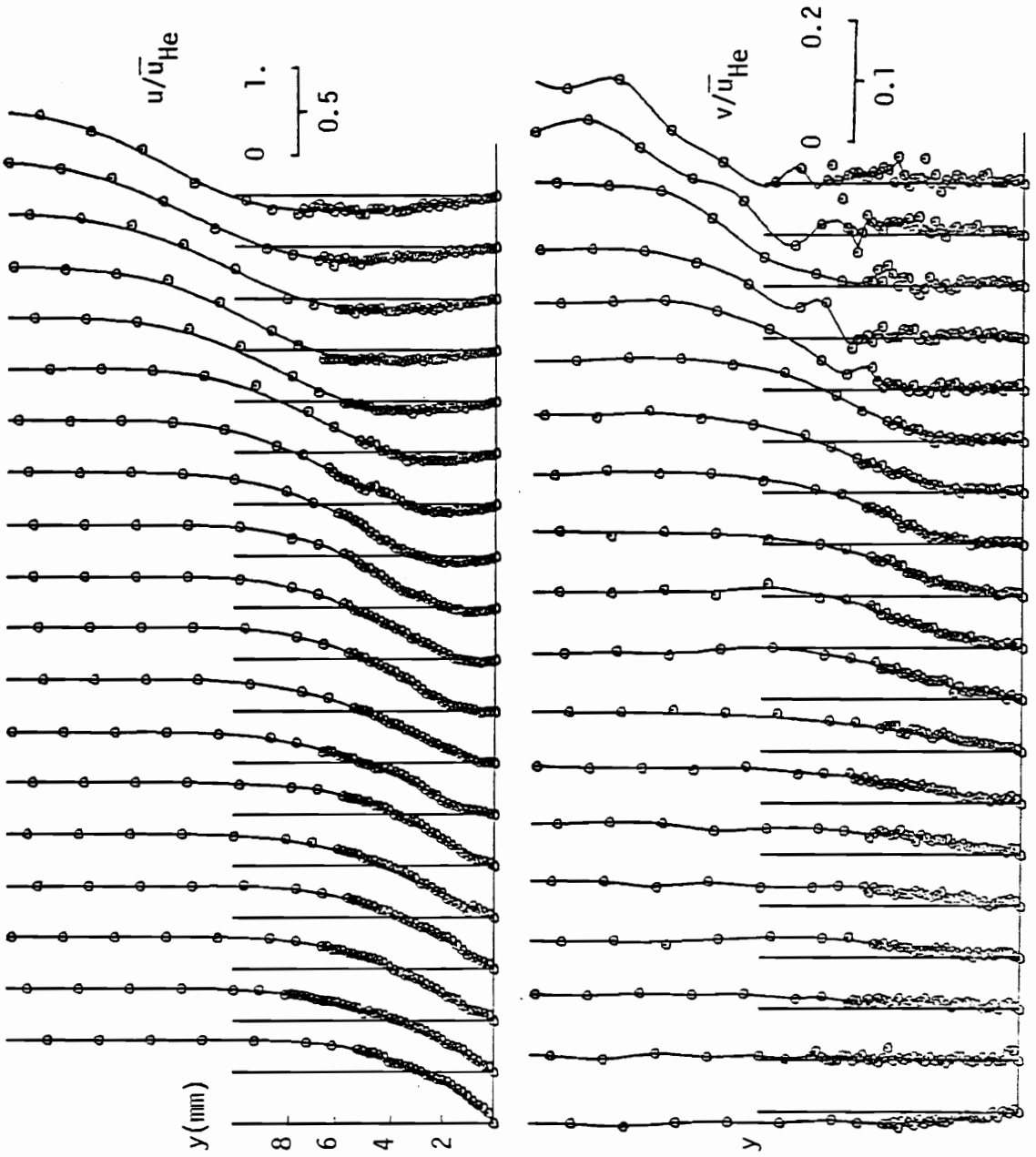

Fig. 3.1.13 Velocity profiles, t = 7/8.

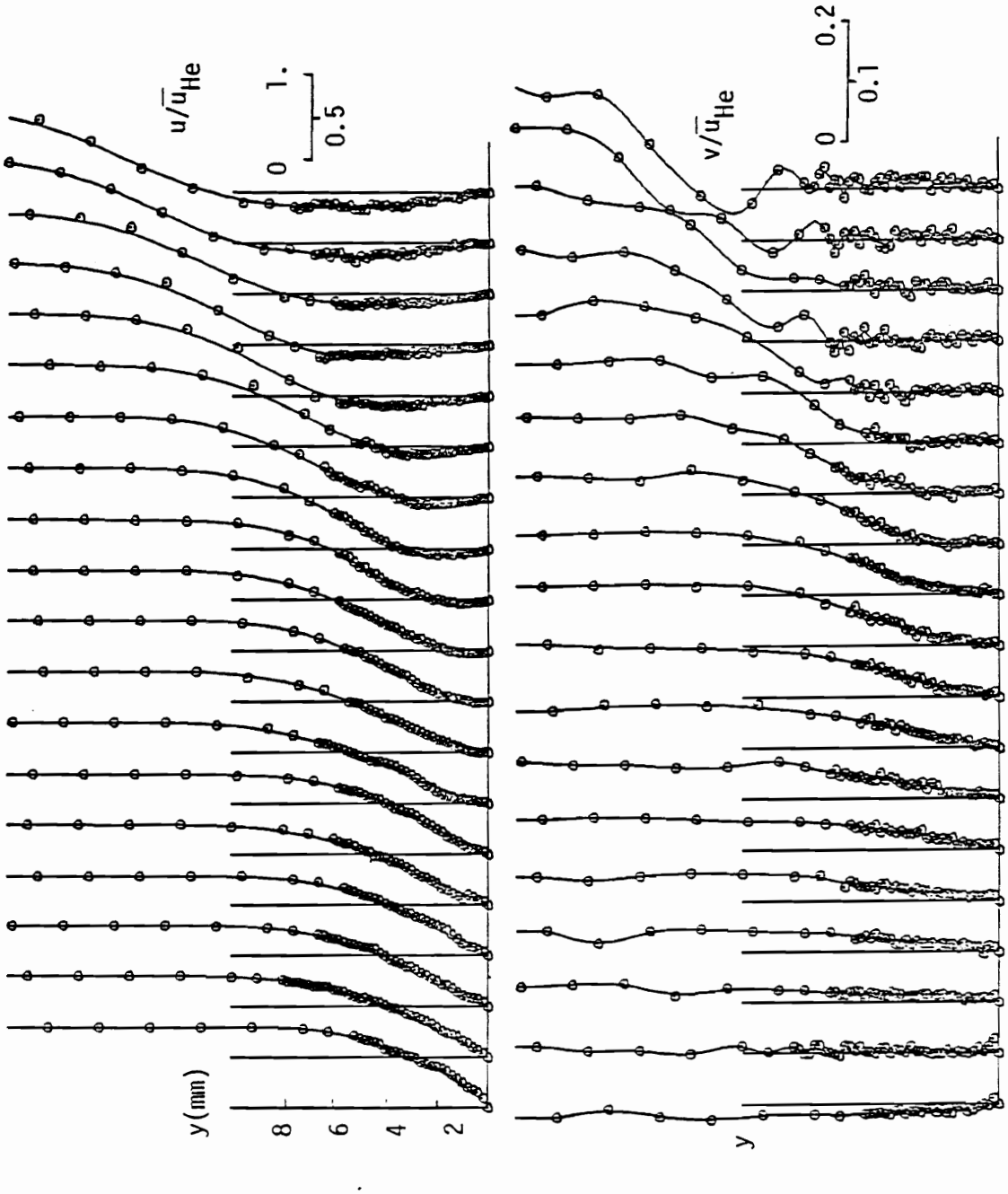

Fig. 3.1.14 Velocity profiles, t = 8/8.

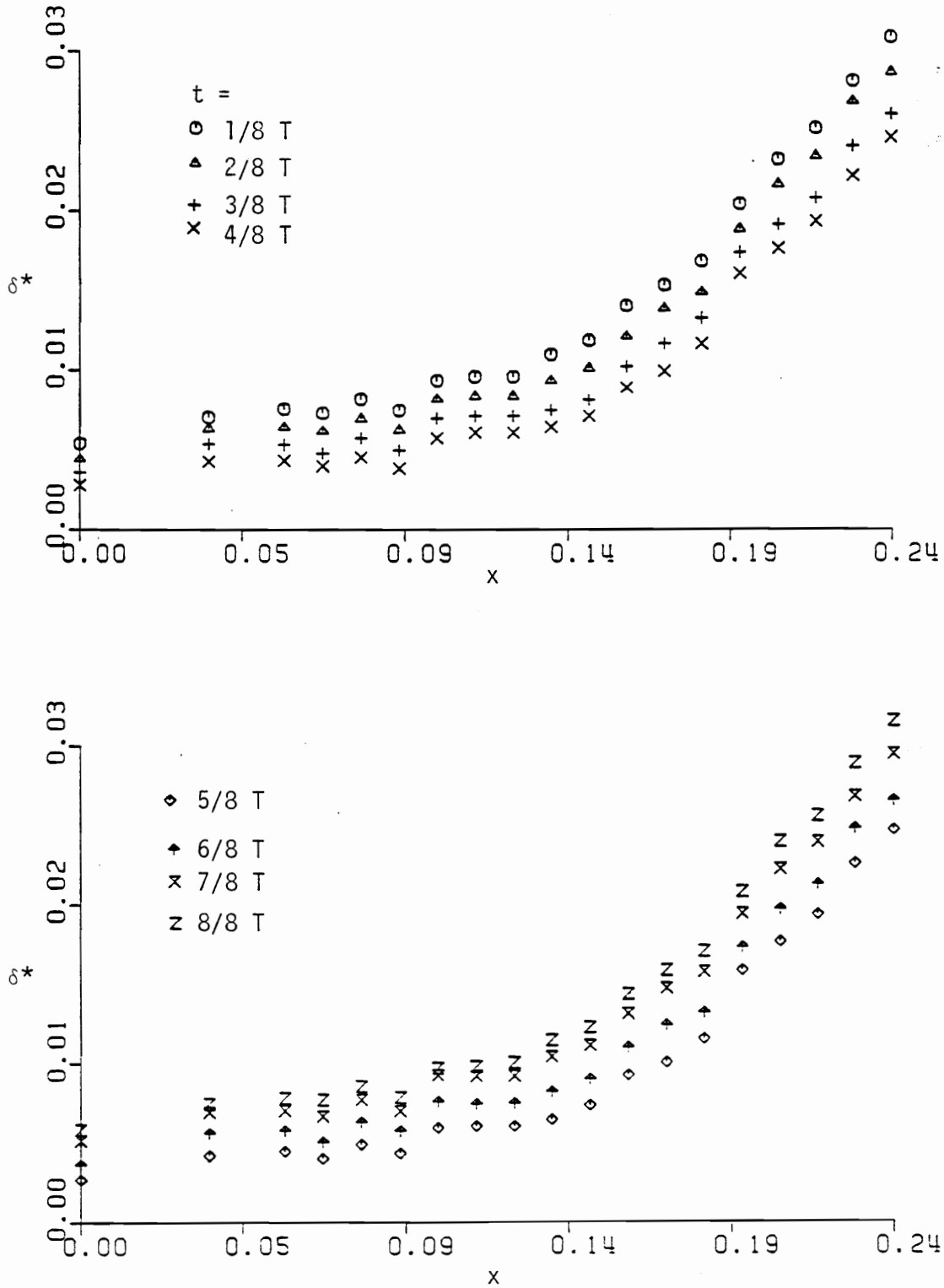

Fig. 3.1.15 Displacement thickness as function of x,t.

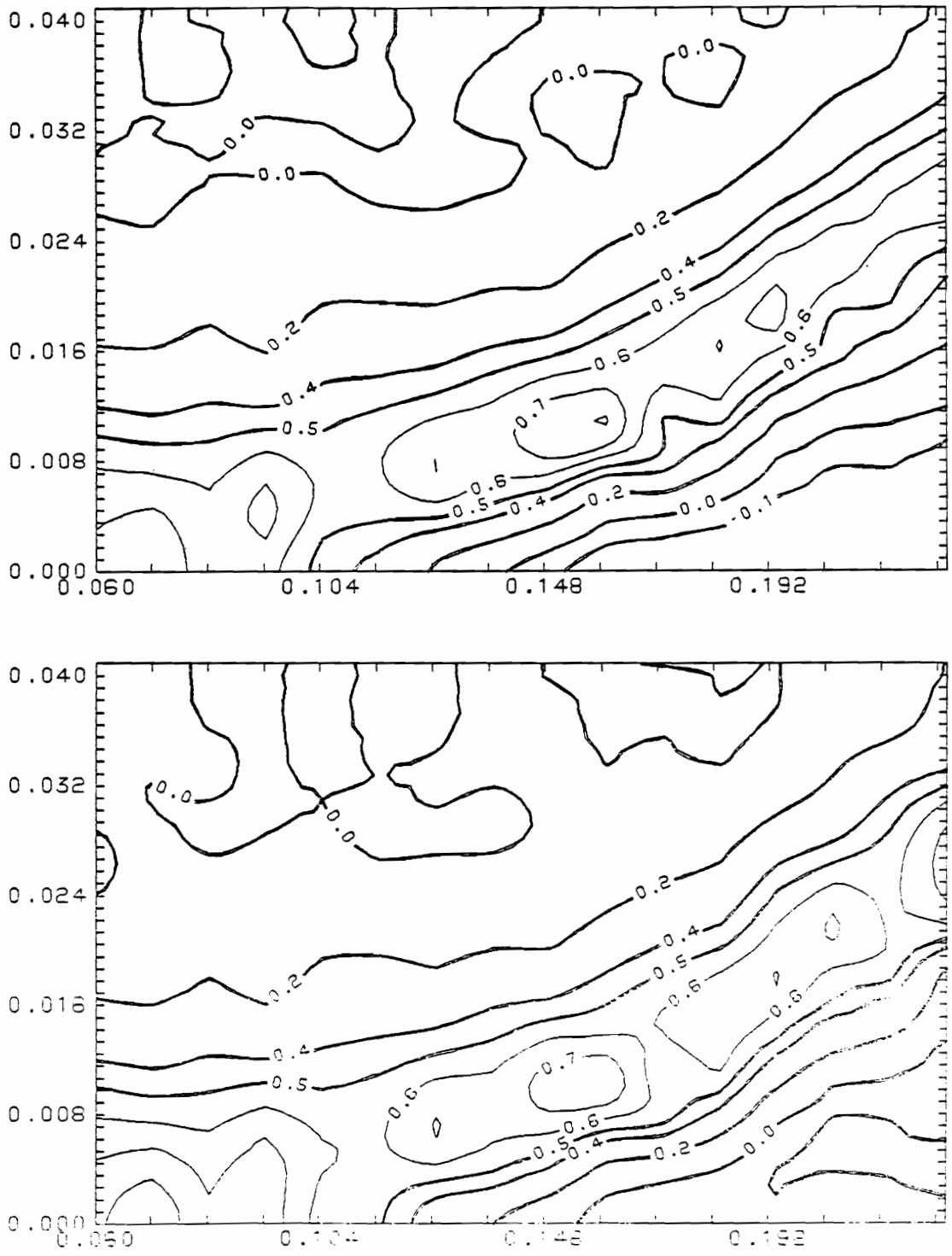

Fig. 3.1.16Vorticity contours at t = 1/8, 2/8 (from top to bottom). The horizontal and vertical scales are x/R and y/R respectively.

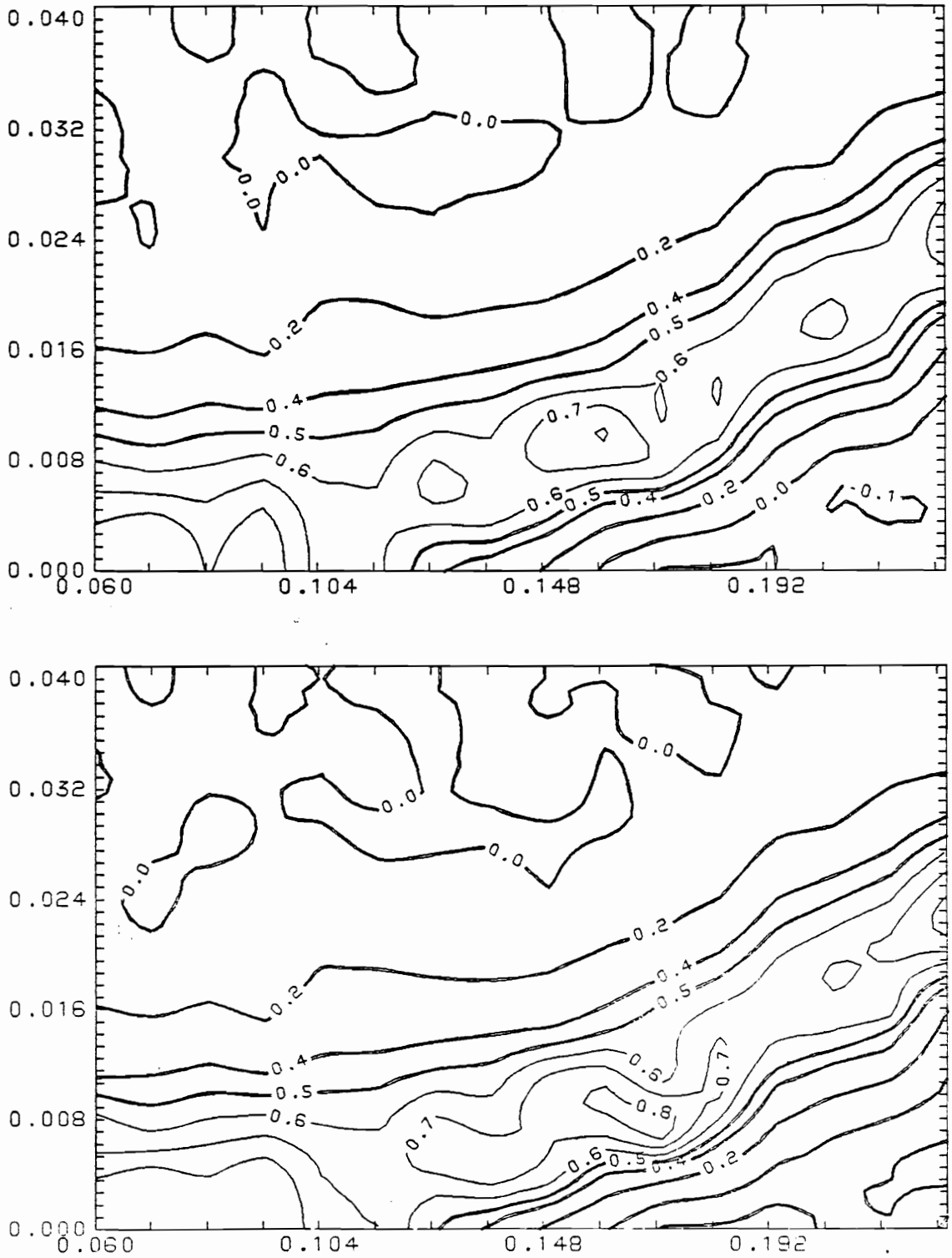

Fig. 3.1.17 Vorticity contours at t = 3/8, 4/8 (from top to bottom)

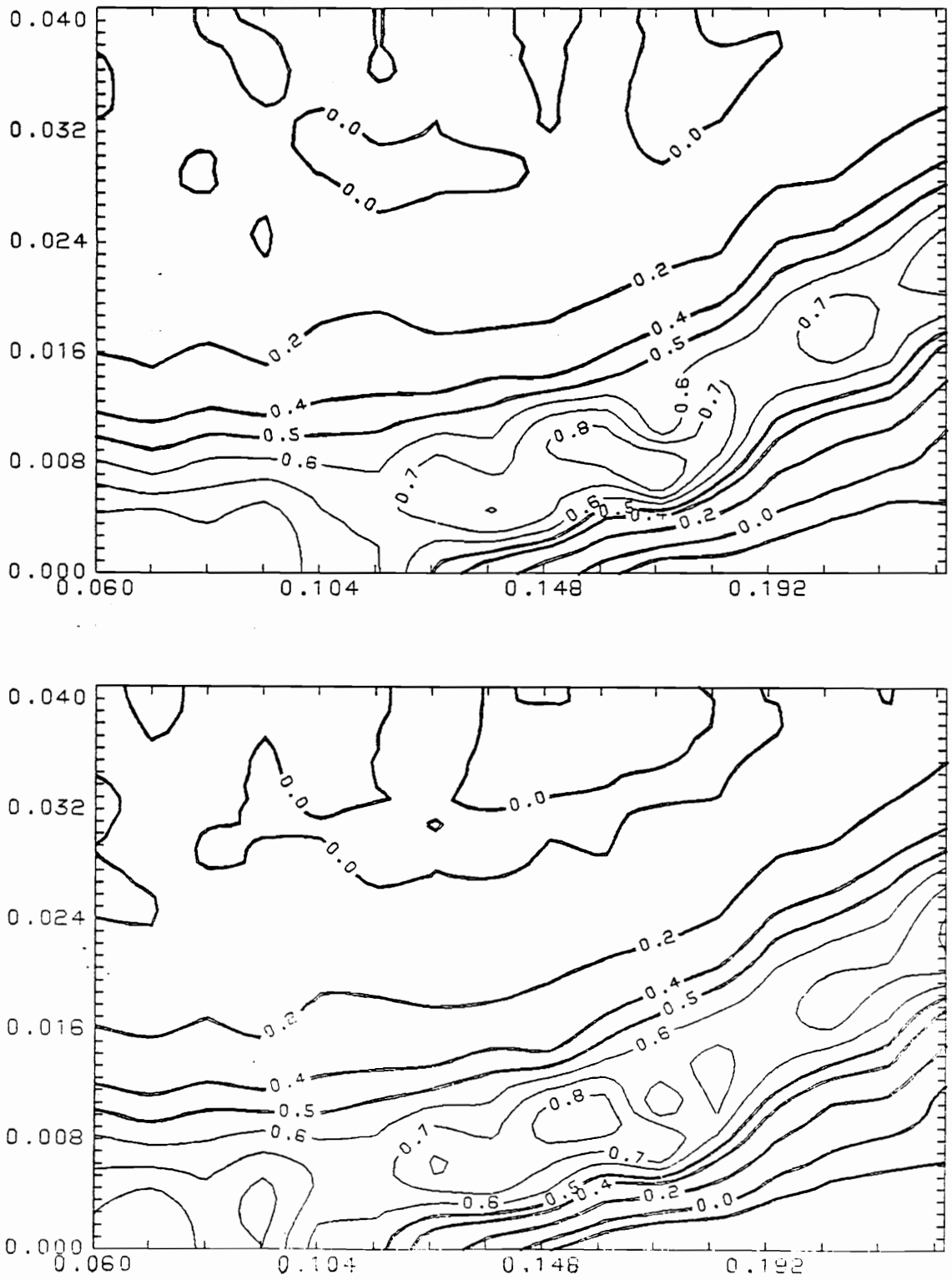

Fig. 3.1.18 Vorticity contours at t = 5/8, 6/8 (from top to bottom)

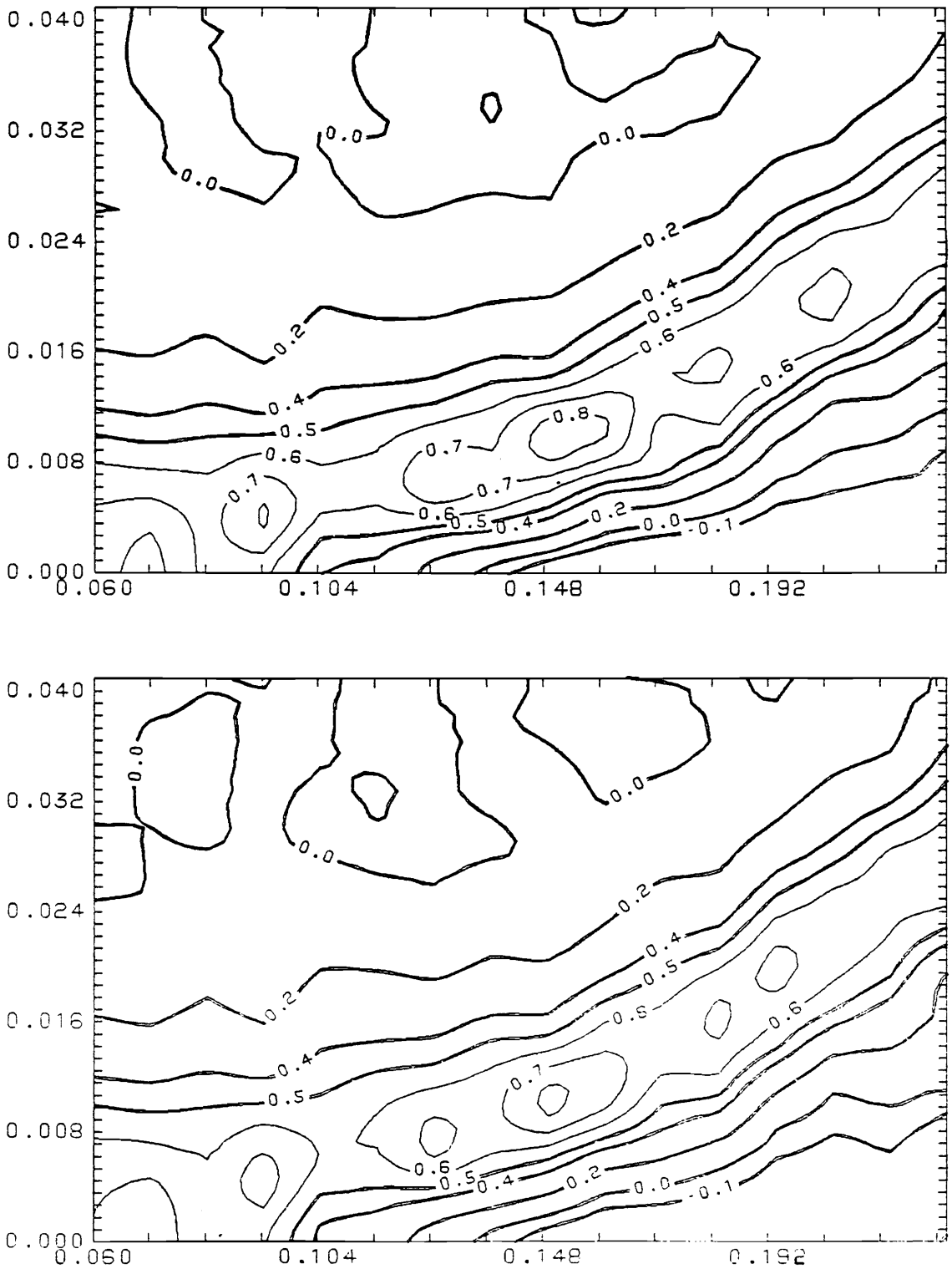

Fig. 3.1.19 Vorticity contours at t = 7/8, 8/8 (from top to bottom)

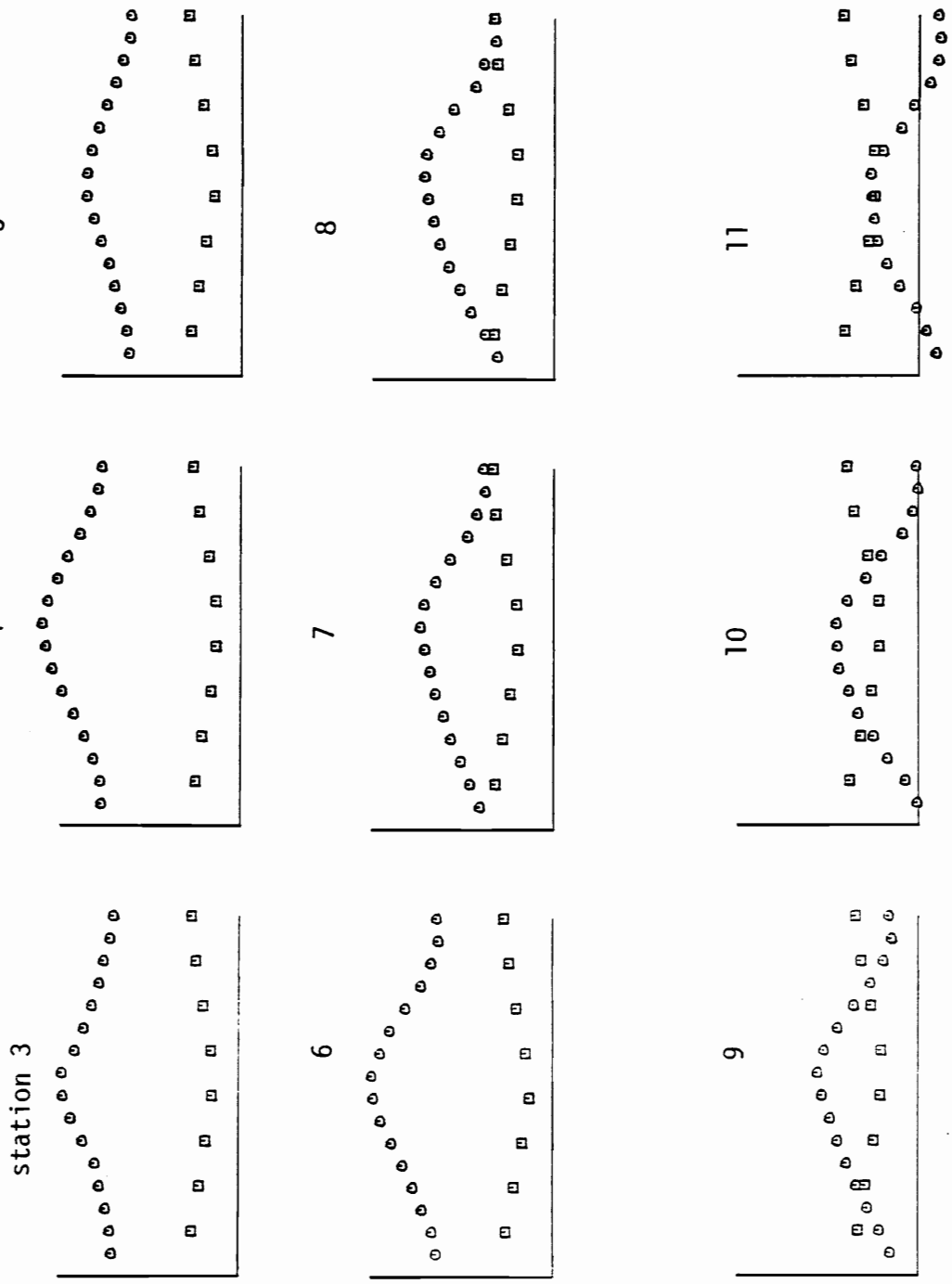

Fig. 3.1.20 Displacement thickness (δ^*/R) (▫) and wall shear $\frac{\partial u}{\partial y}\Big|_{y=0}$ (○) versus time at stations 3 to 11. The horizontal scale represents exactly one period.

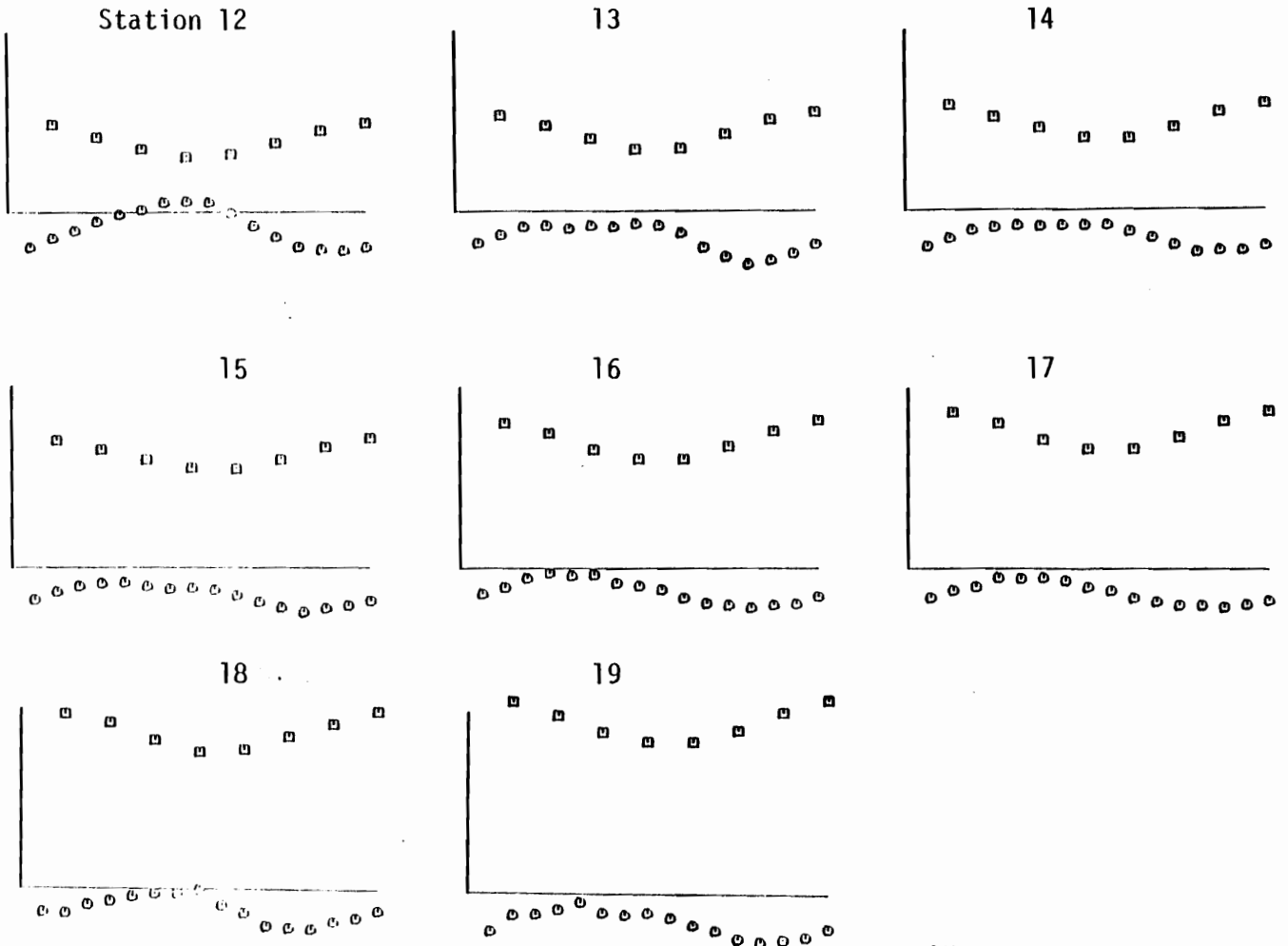

Fig. 3.1.21 Displacement thickness (δ^*/R) (▪) and wall shear $\frac{\partial u}{\partial y}|_{y=0}$ (○) versus time at stations 12 to 19.

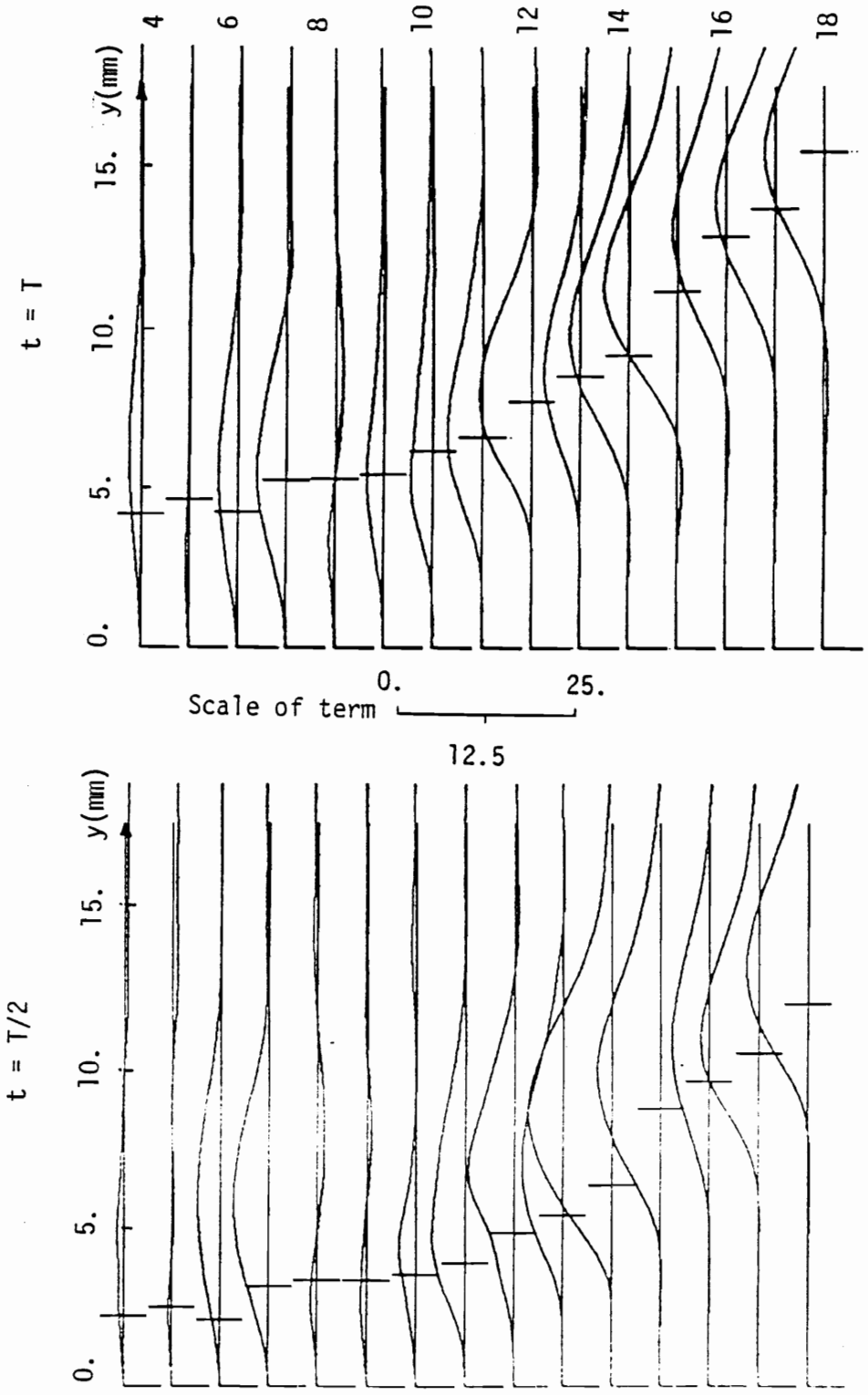

Fig. 3.1.22 Profiles of $\frac{u}{1+y}\frac{\partial u}{\partial x}$ of stations 4 ÷ 18 and t = T/2, T.

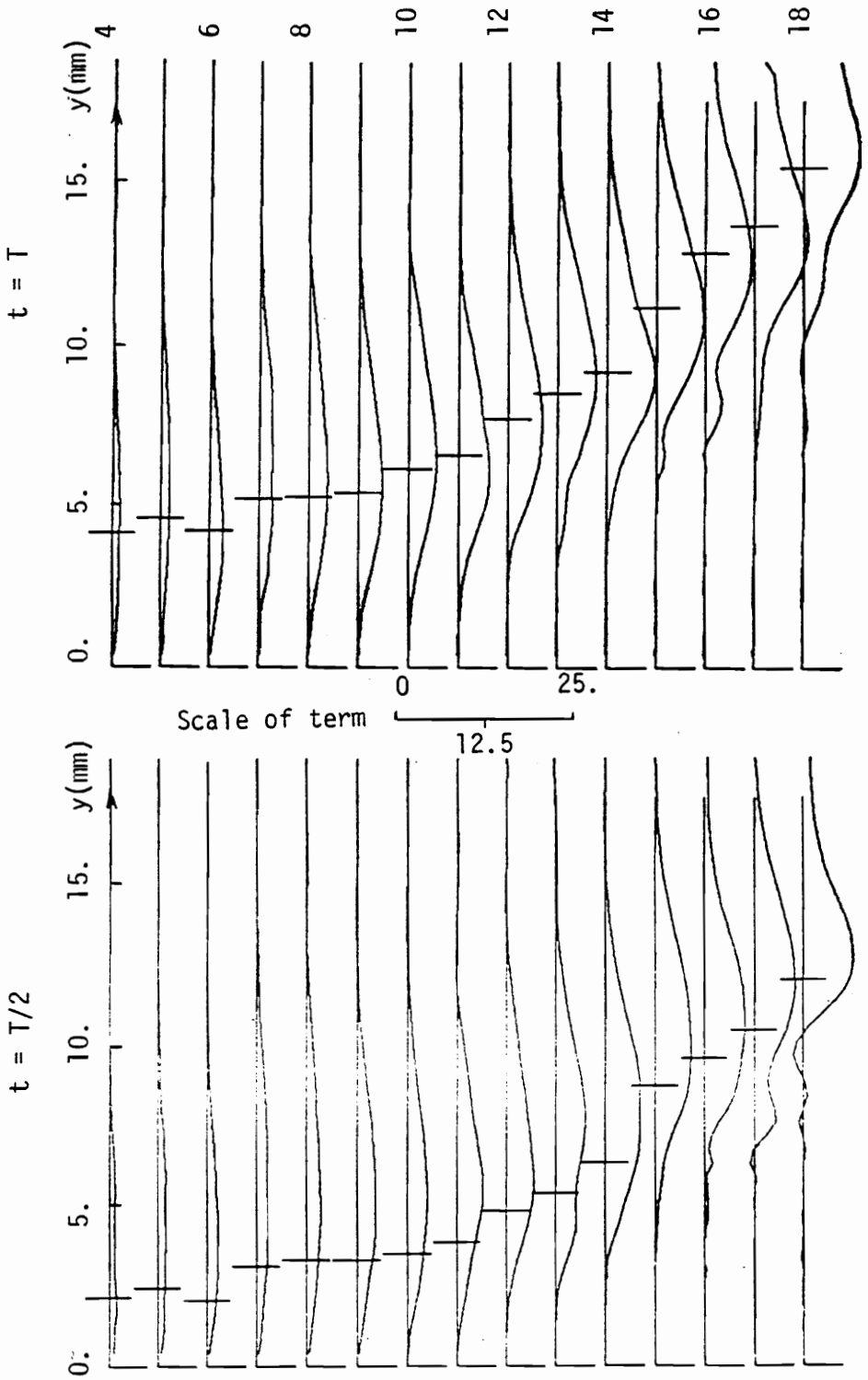

Fig. 3.1.23 Profiles of $\nu \frac{\partial u}{\partial y}$ at stations 4 ∶ 18 and t = T/2, T.

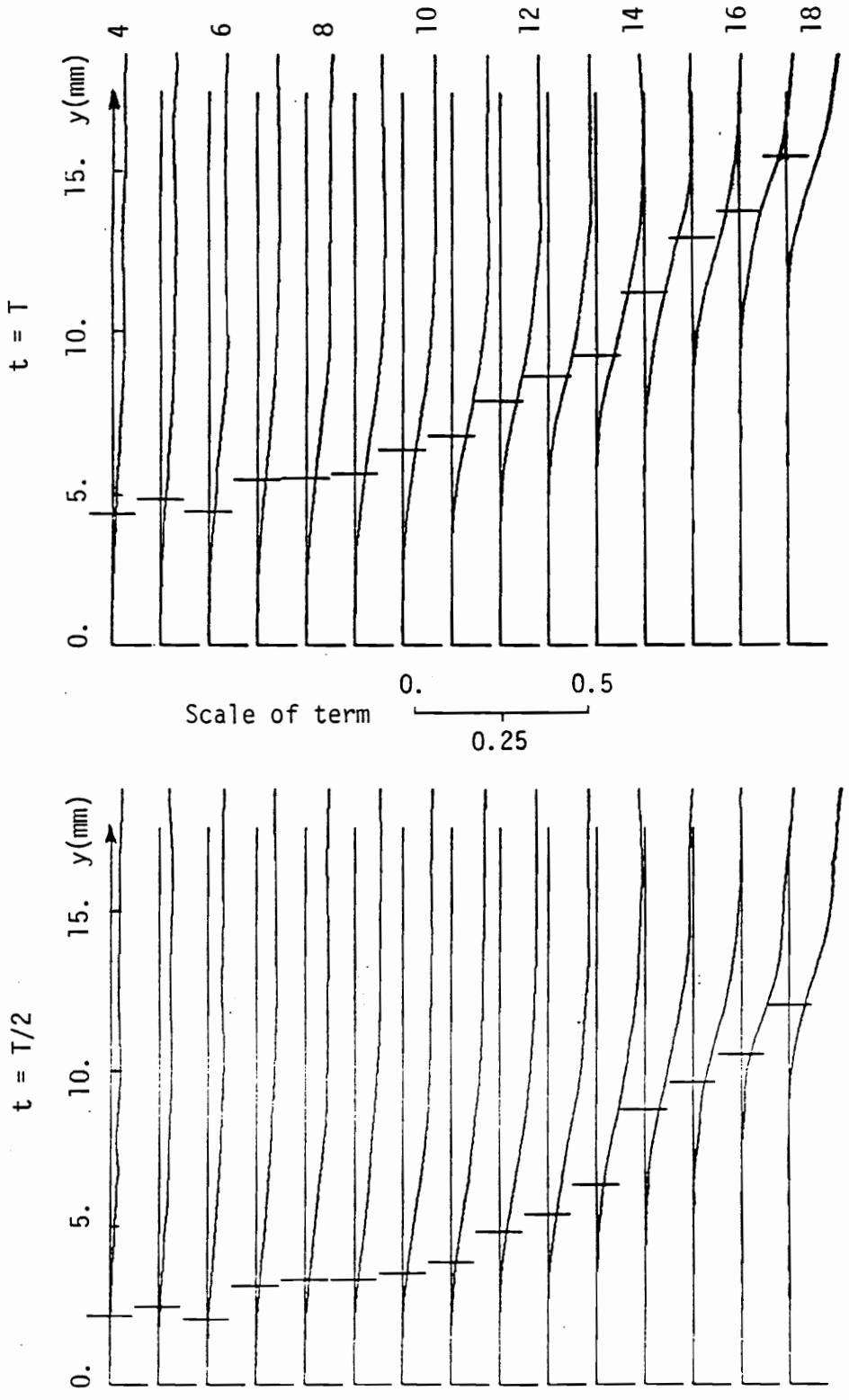

Fig. 3.1.24 Profiles of $\frac{uv}{1+y}$ at stations 4 ÷ 18 and t = T/2, T.

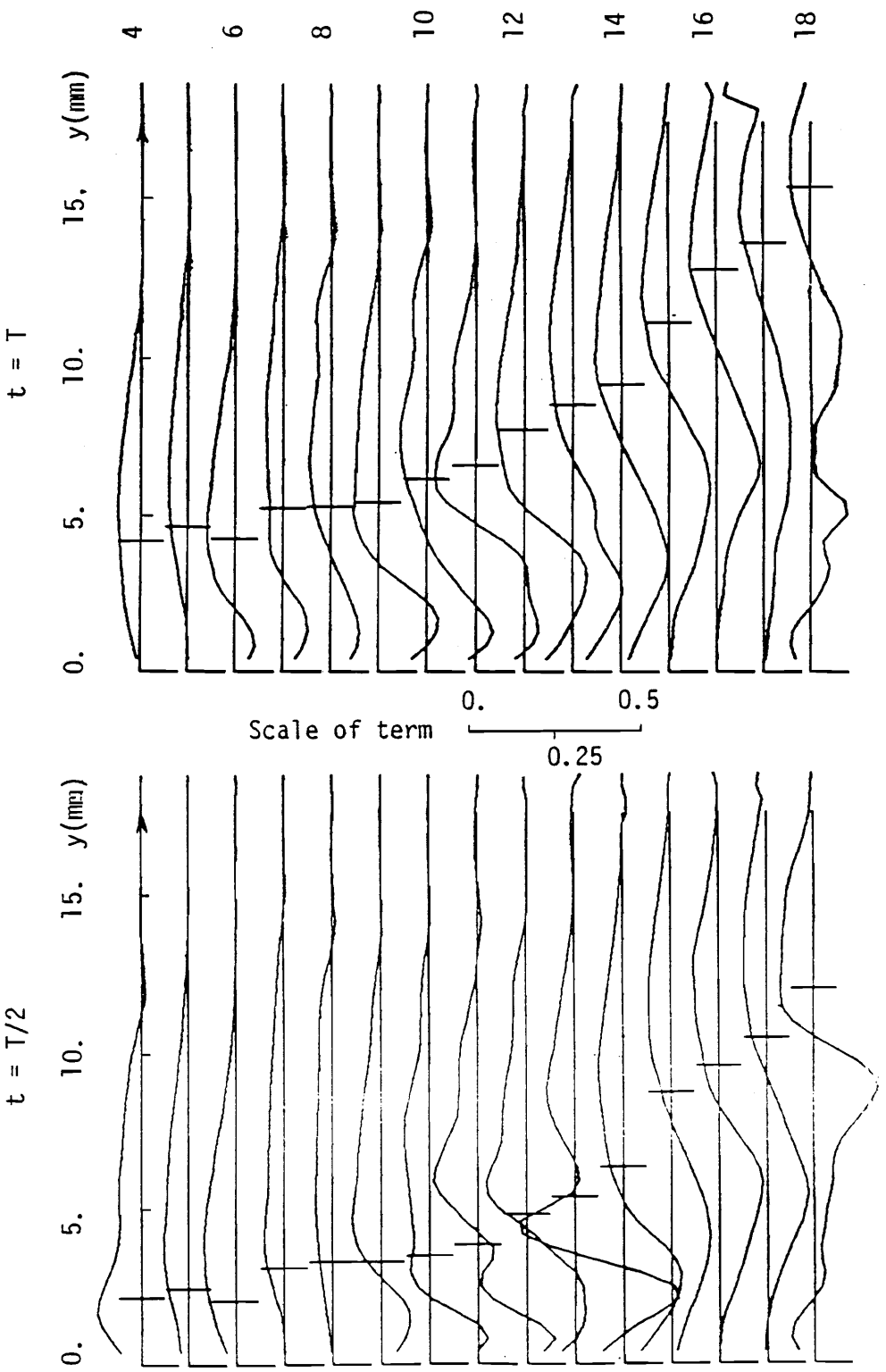

Fig. 3.1.25 Profiles of $\frac{1}{Re}\frac{\partial^2 u}{\partial y^2}$ at stations 4 ÷ 18 and t = T/2, T.

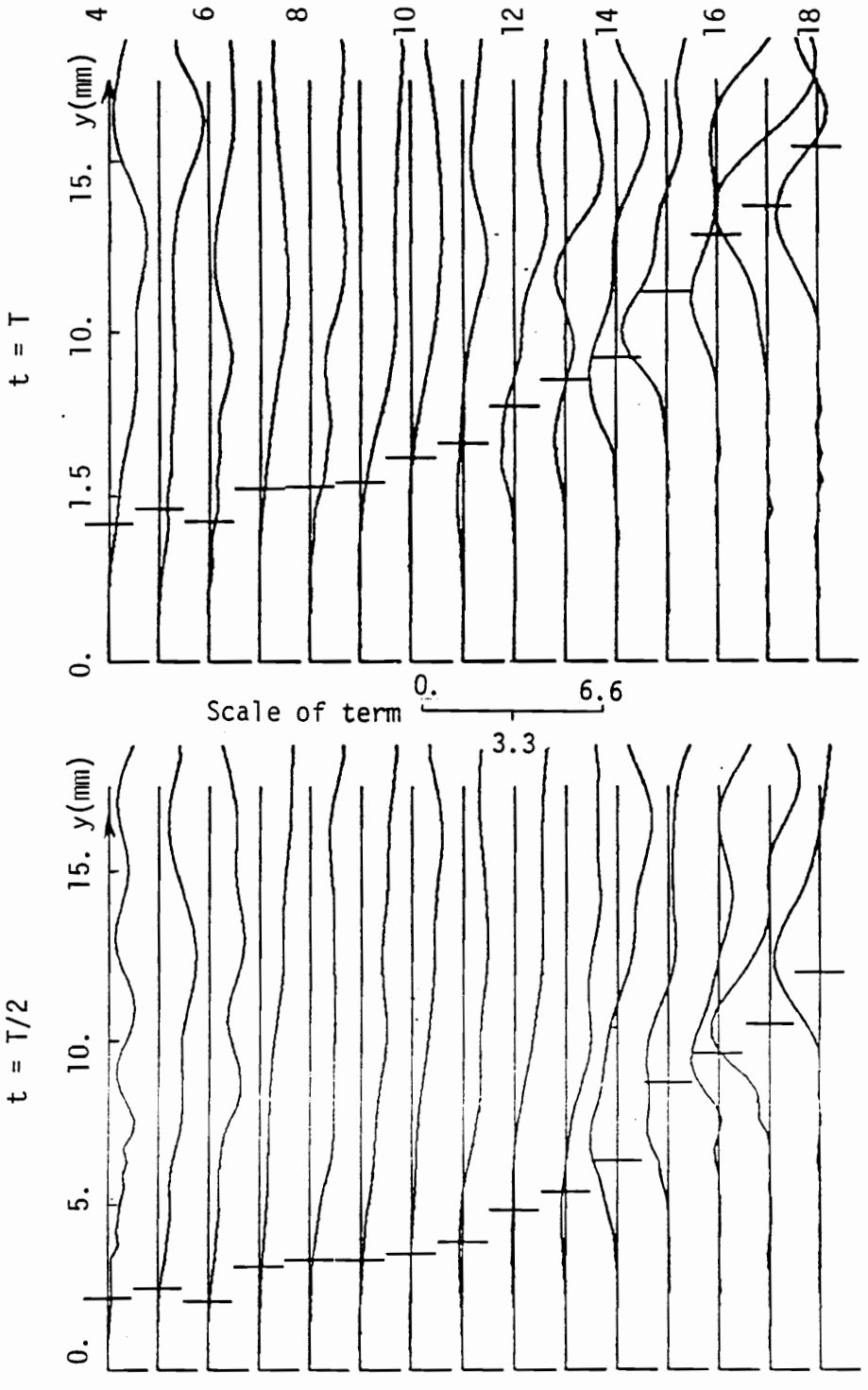

Fig. 3.1.26 Profiles of $\frac{u}{1+y}\,\partial v/\partial x$ at stations 4 ÷ 18 and t = T/2, T.

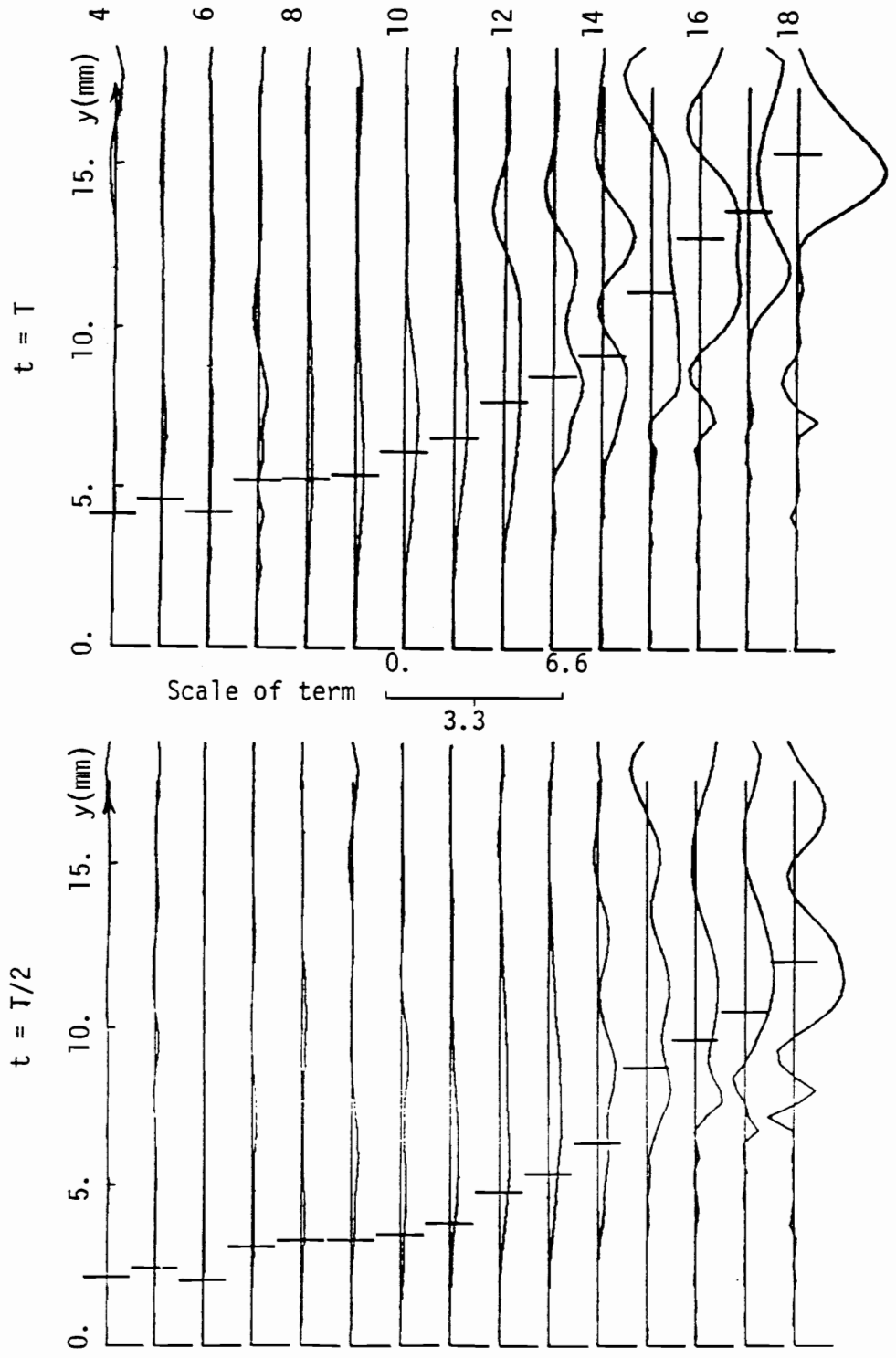

Fig. 3.1.27 Profiles of $v\partial v/\partial y$ at stations 4 ÷ 18 and t = T/2, T.

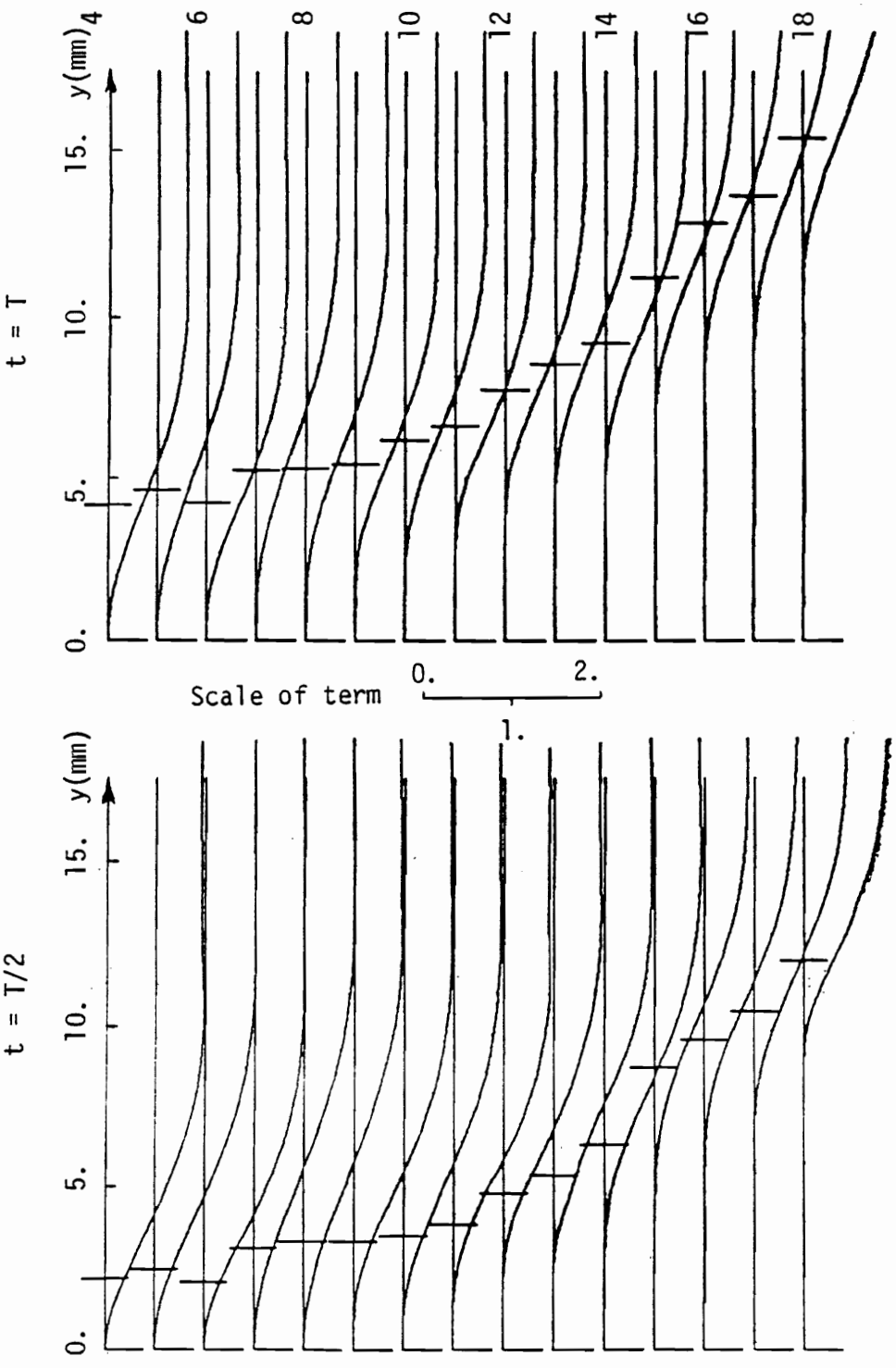

Fig. 3.1.28 Profiles of $u^2/(1+y)$ at stations 4 ÷ 18 and t = T/2, T.

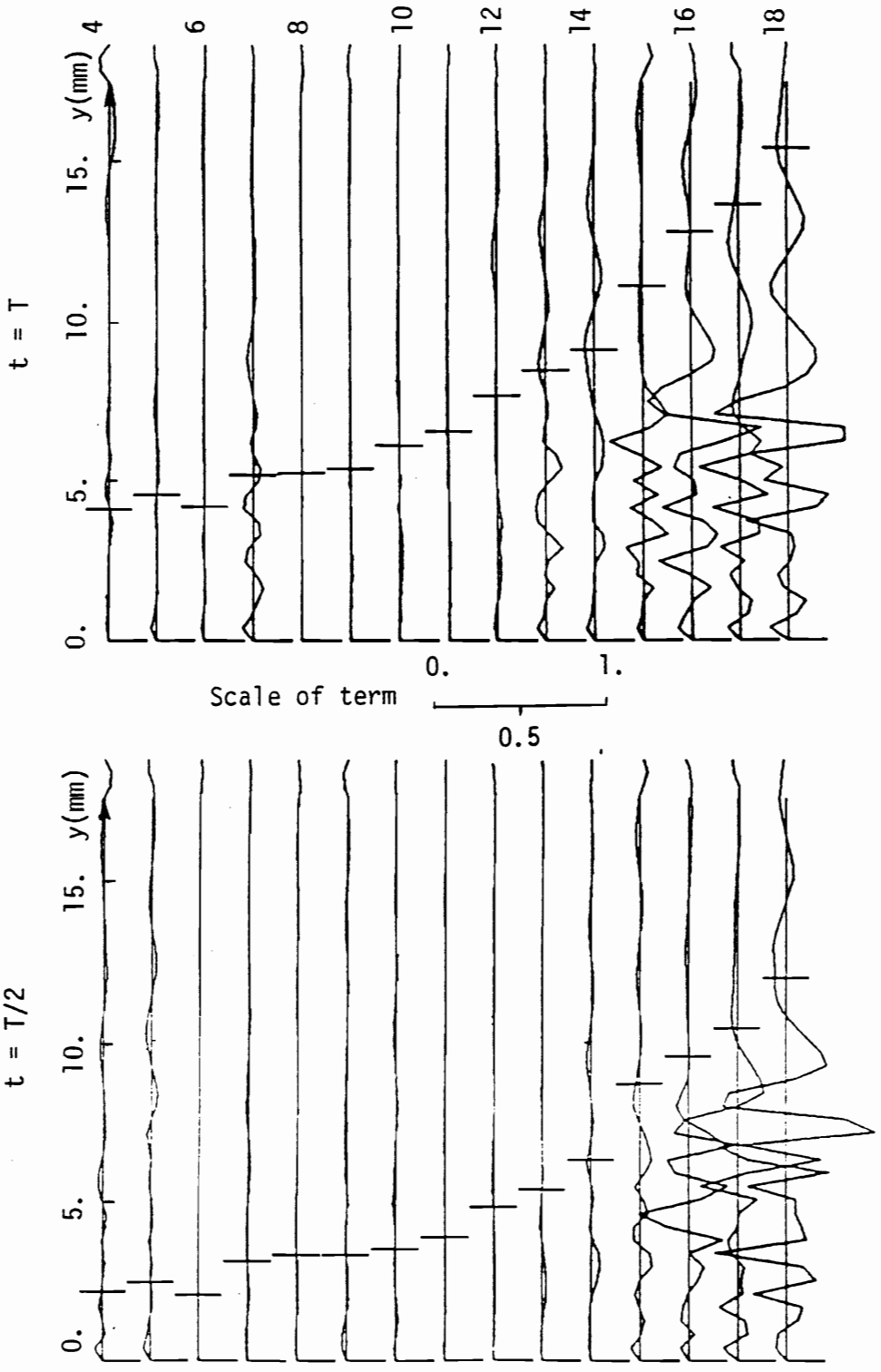

Fig. 3.1.29 Profiles of $\frac{1}{R_e}(\partial^2 v/\partial y^2)$ at stations 4 ÷ 18 and t = T/2, T.

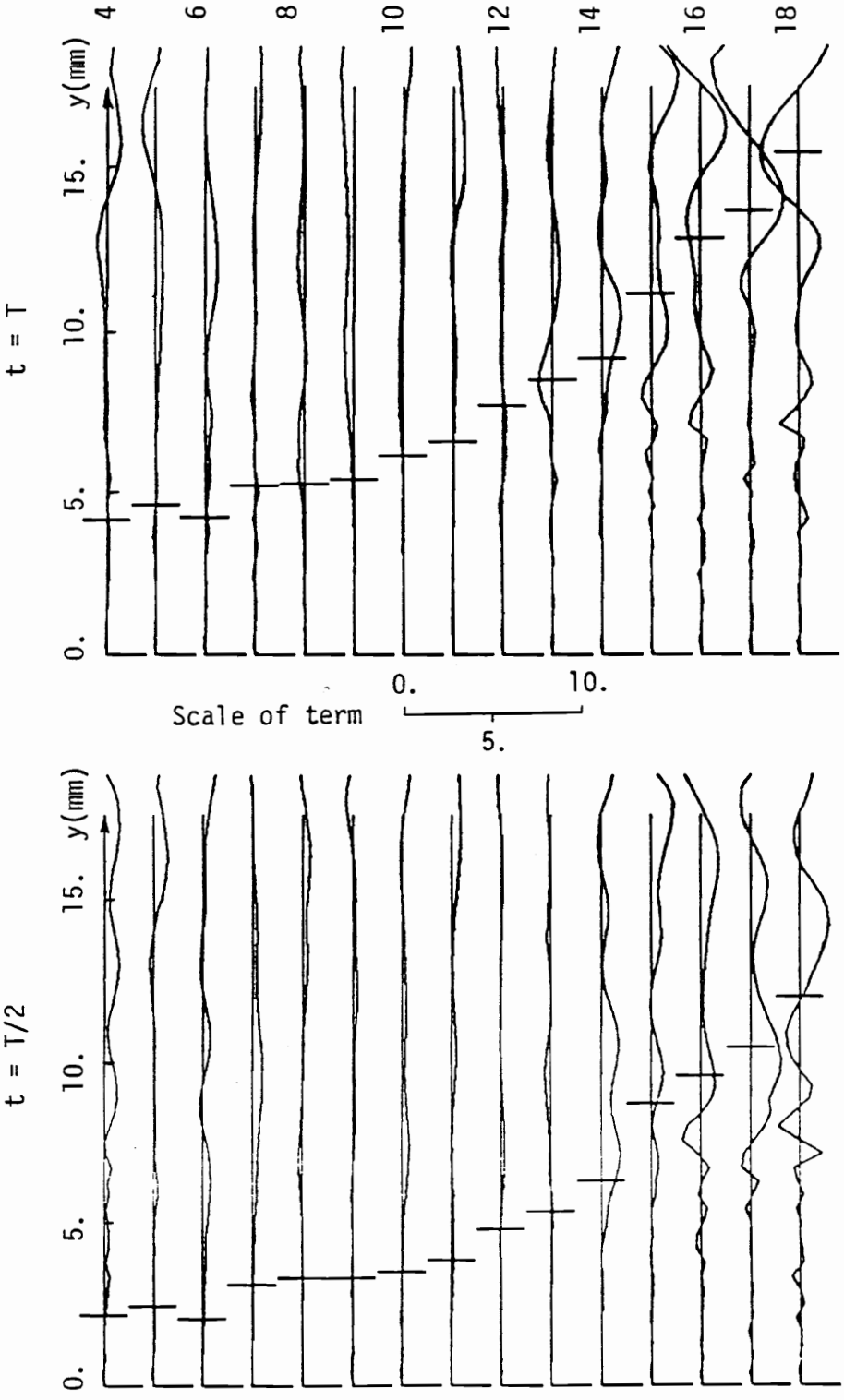

Fig. 3.1.30 Profiles of ∂P/∂y at station 4 ~ 18 and t = T/2, T.

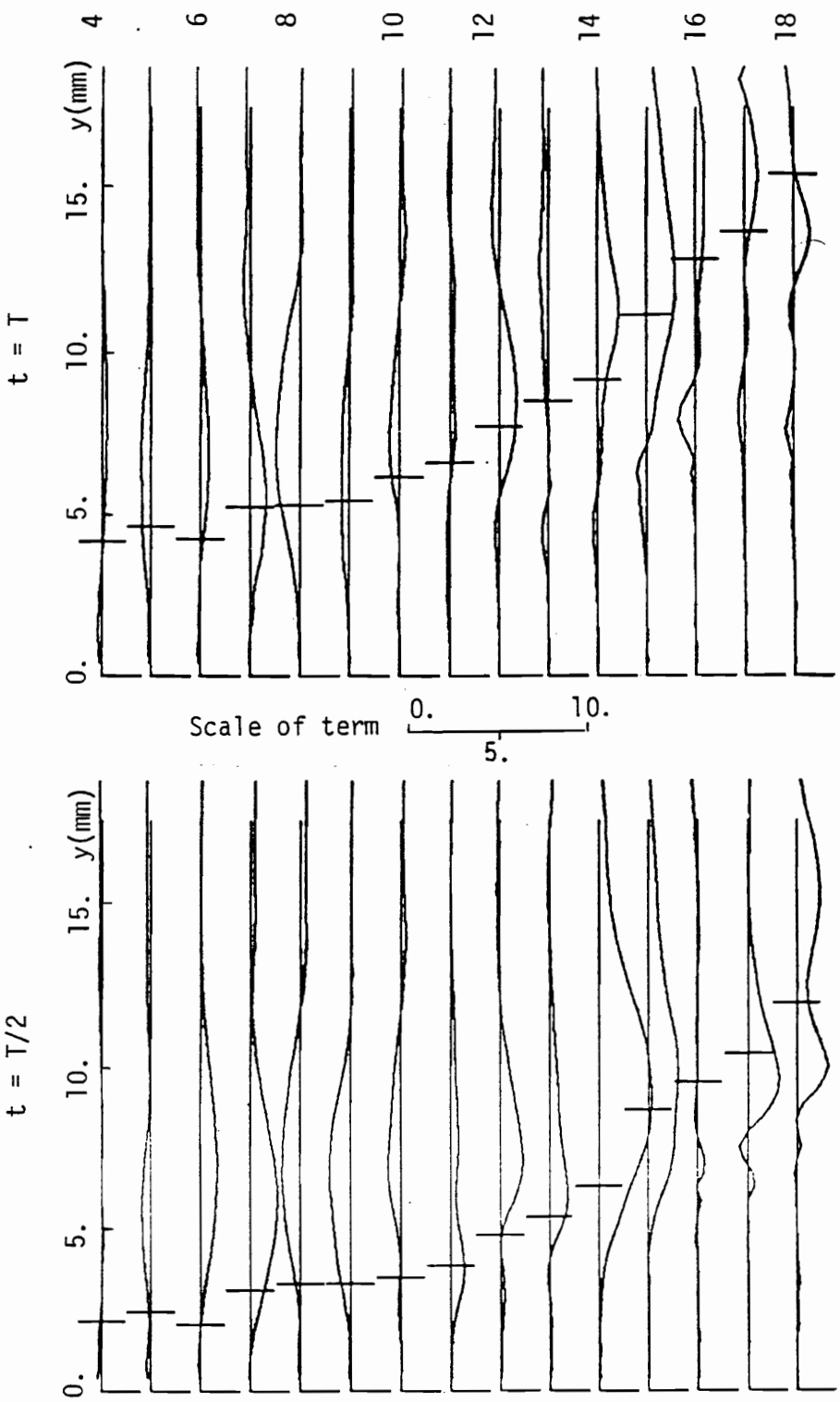

Fig. 3.1.31 Profiles of $\partial P/\partial x$ at stations 4 ÷ 18 and t = T/2, T.

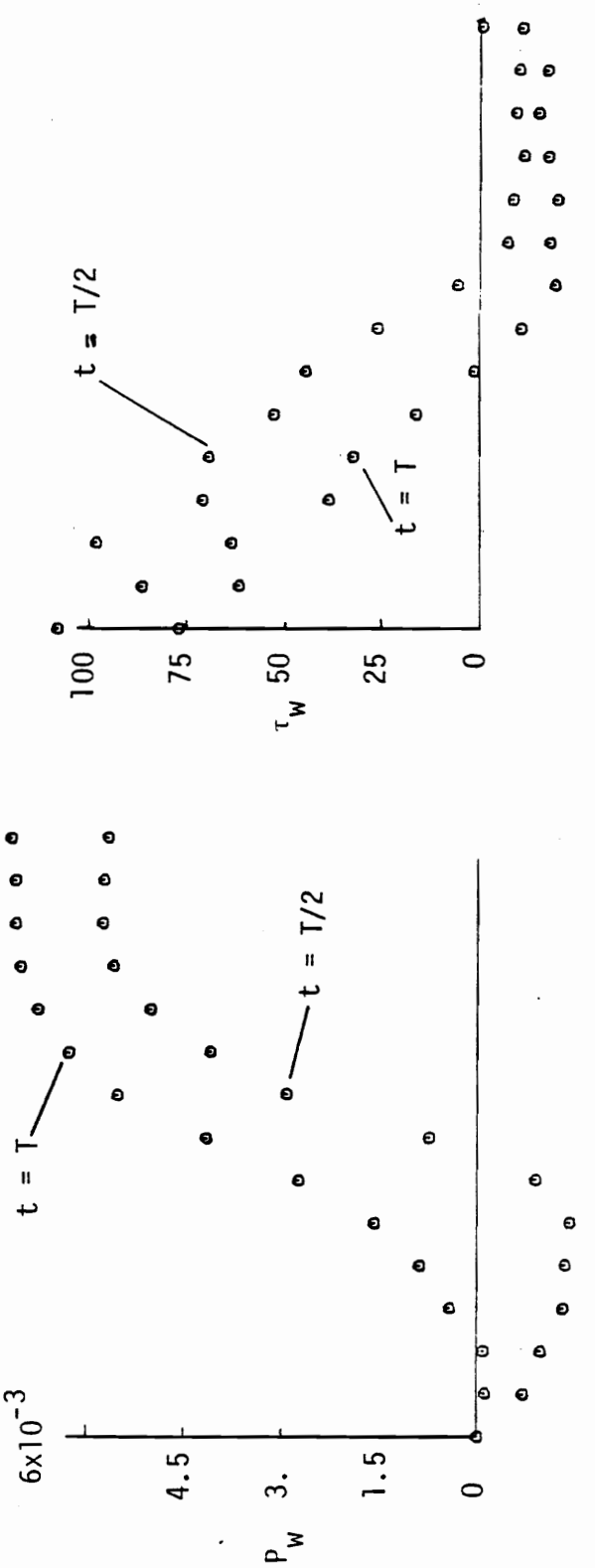

Fig. 3.1.32 Wall pressure P_w and wall shear, $\tau_w = \left|\frac{\partial u}{\partial y}\right|_{y=0}$ at t = T/2, T (stations, 3 ÷ 17).

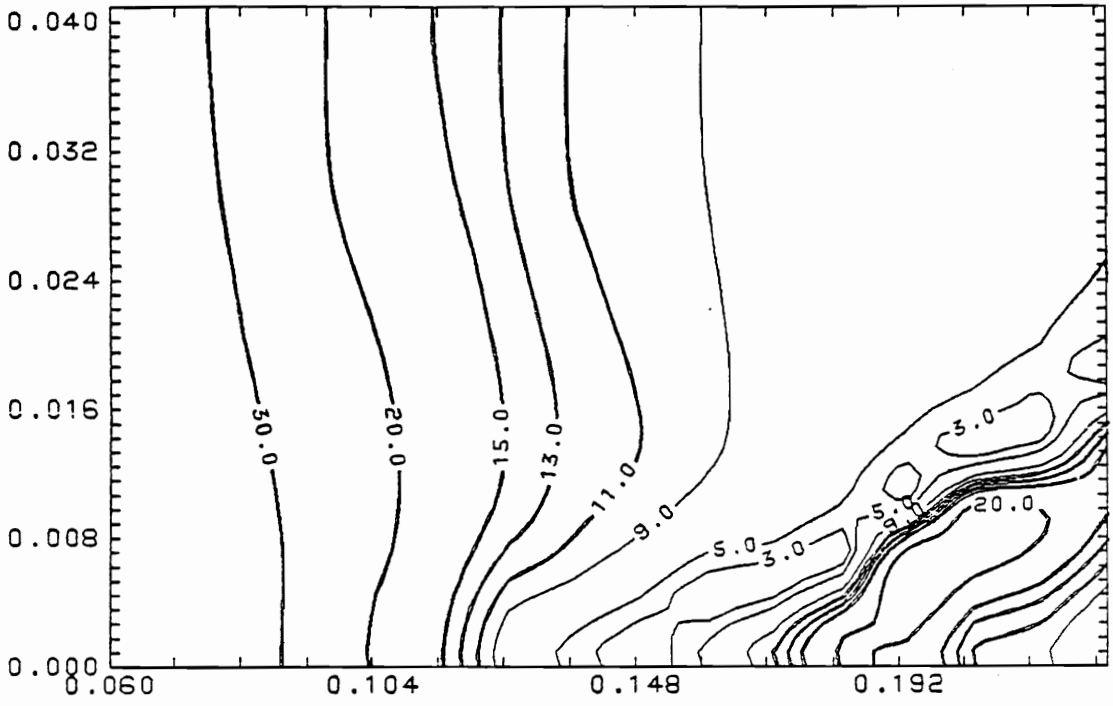

Fig. 3.1.33a Contours of u_m/v_m, with respect to a polar system.

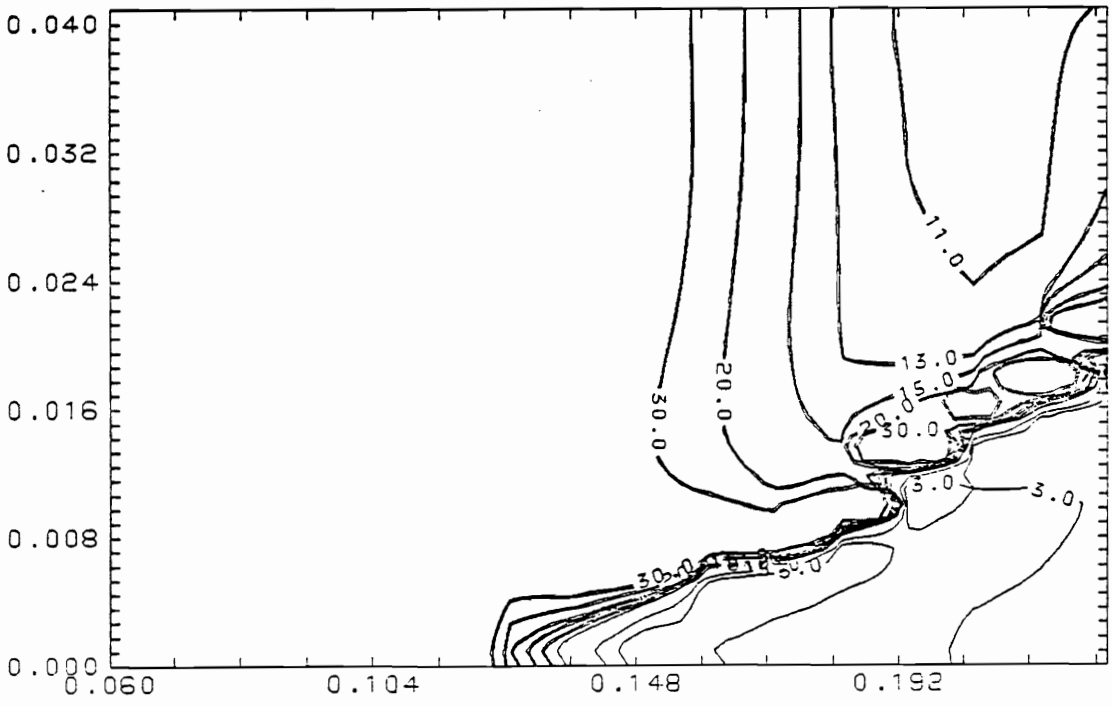

Fig. 3.1.33b Contours of u_m/v_m,w/R to a system aligned with the center of vorticity curve. In above figures, vertical scale is y/R.

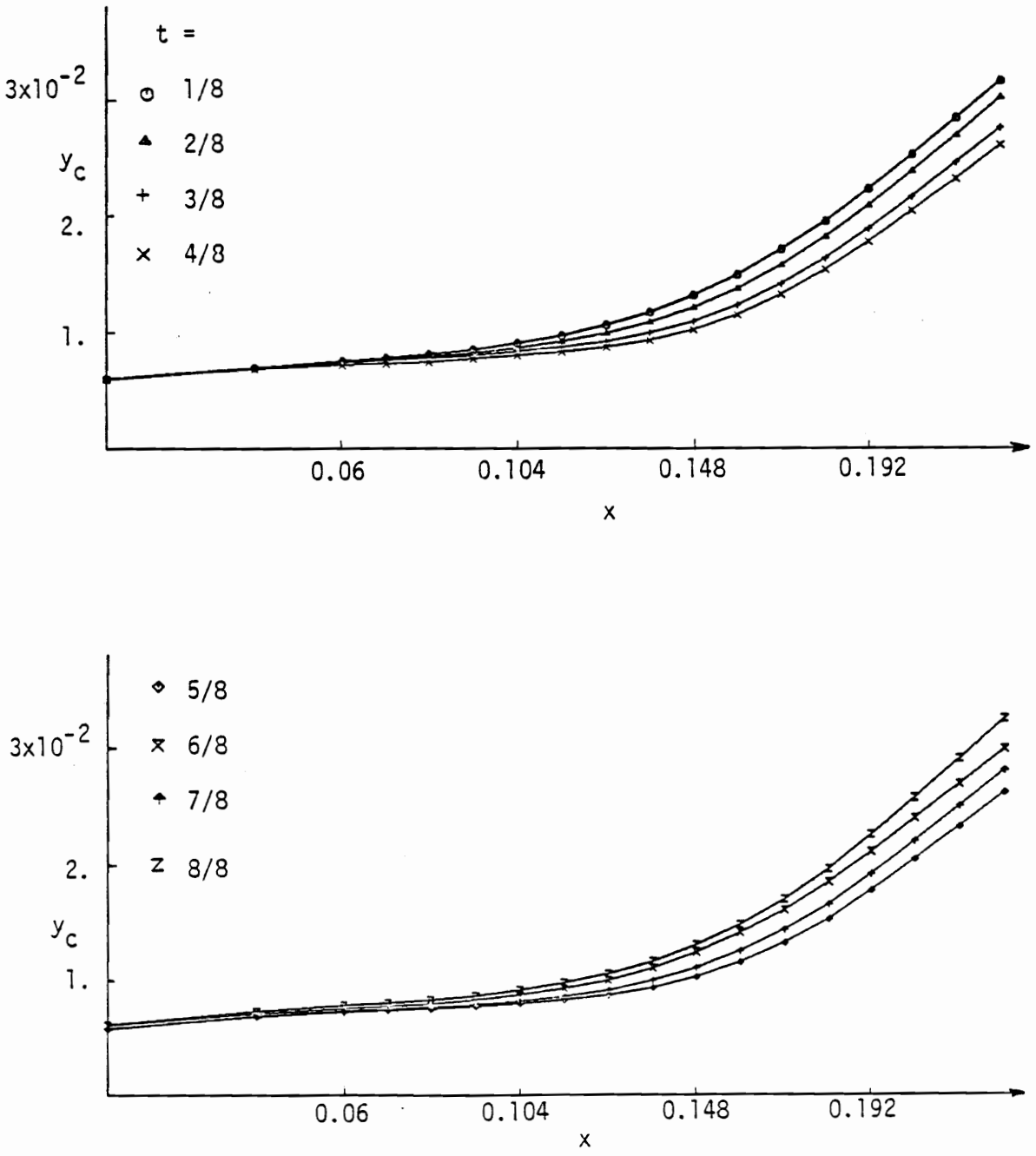

Fig. 3.1.34 Center of vorticity versus x and t (stations 1 ÷ 18)

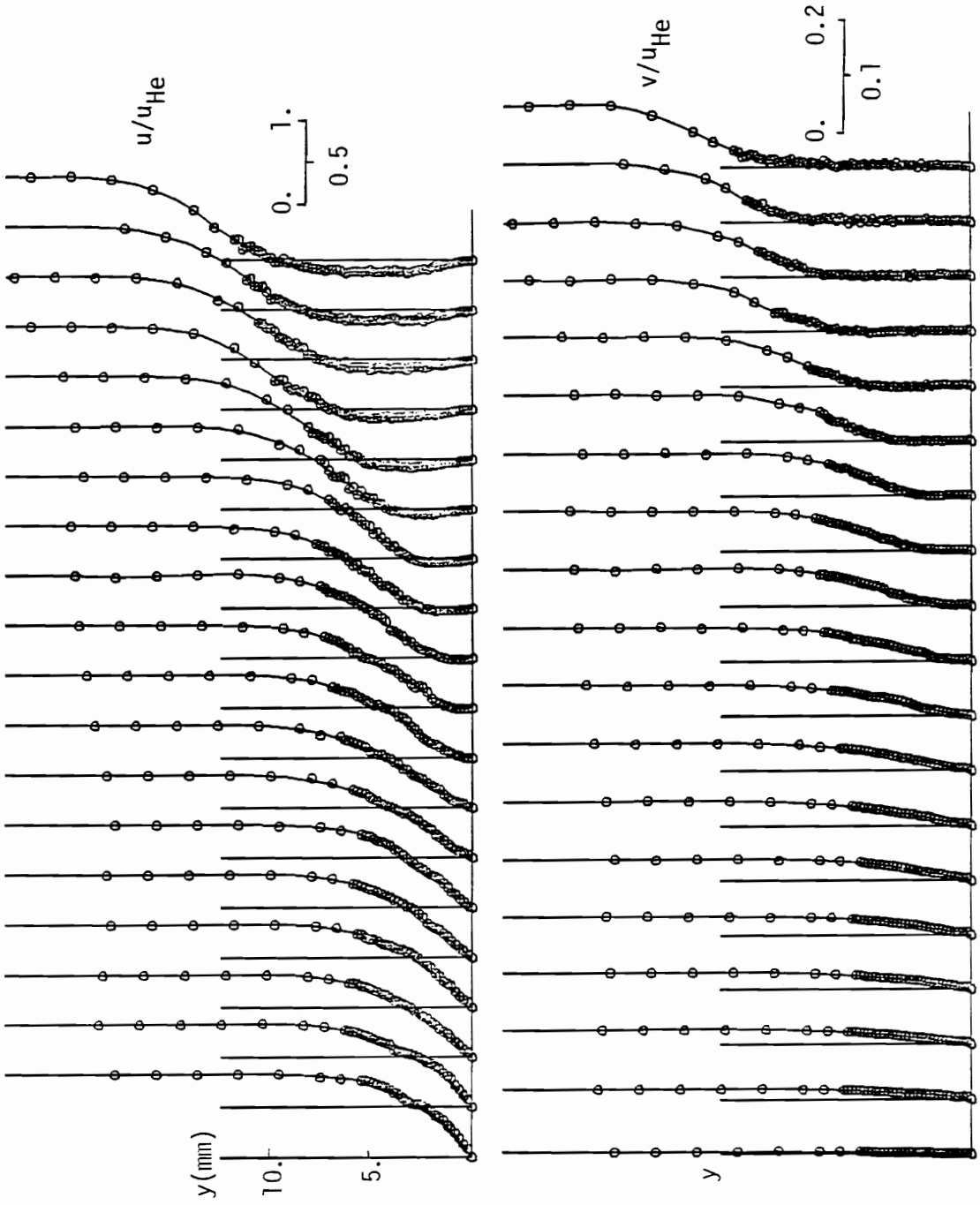

Fig. 3.1.35 Velocity profiles for steady free-stream

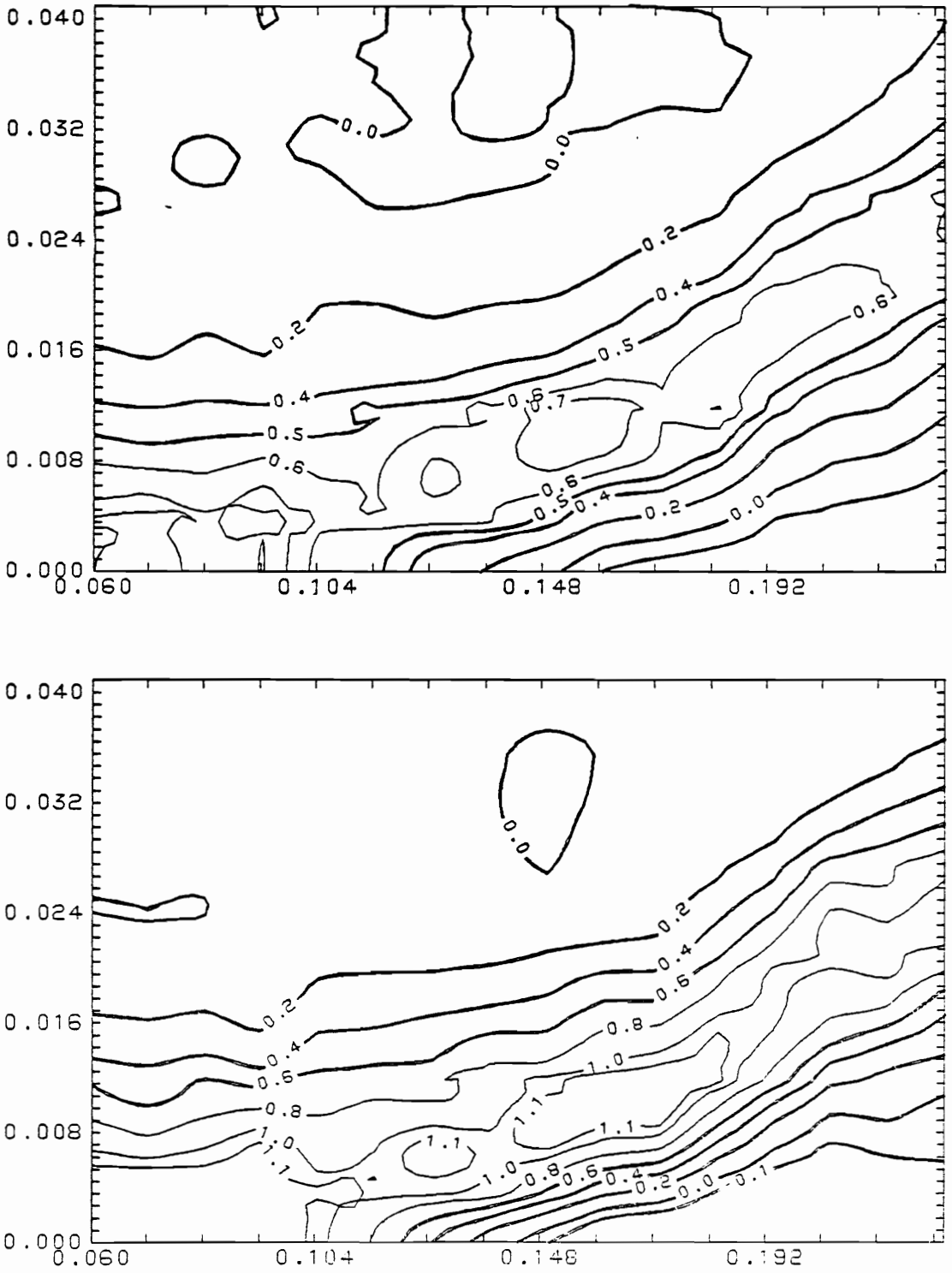

Fig. 3.1.36 Vorticity contours for time-mean (top) and steady (bottom). Horizontal and vertical scales are x/R, y/R respectively.

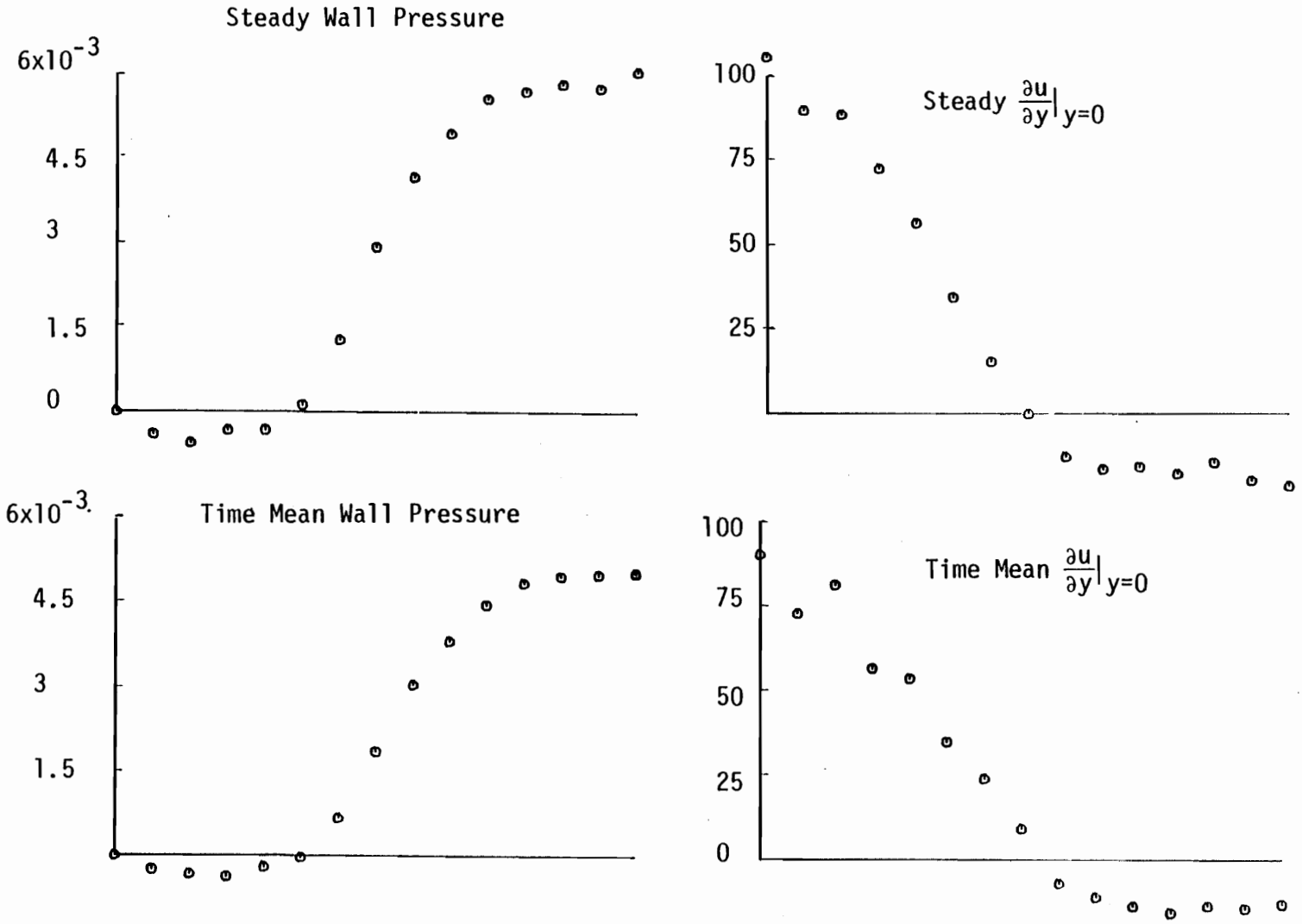

Fig. 3.1.37 Wall Pressure and $\frac{\partial u}{\partial y}|_{y=0}$ versus x for steady and time mean flow fields (stations 3 ÷ 17).

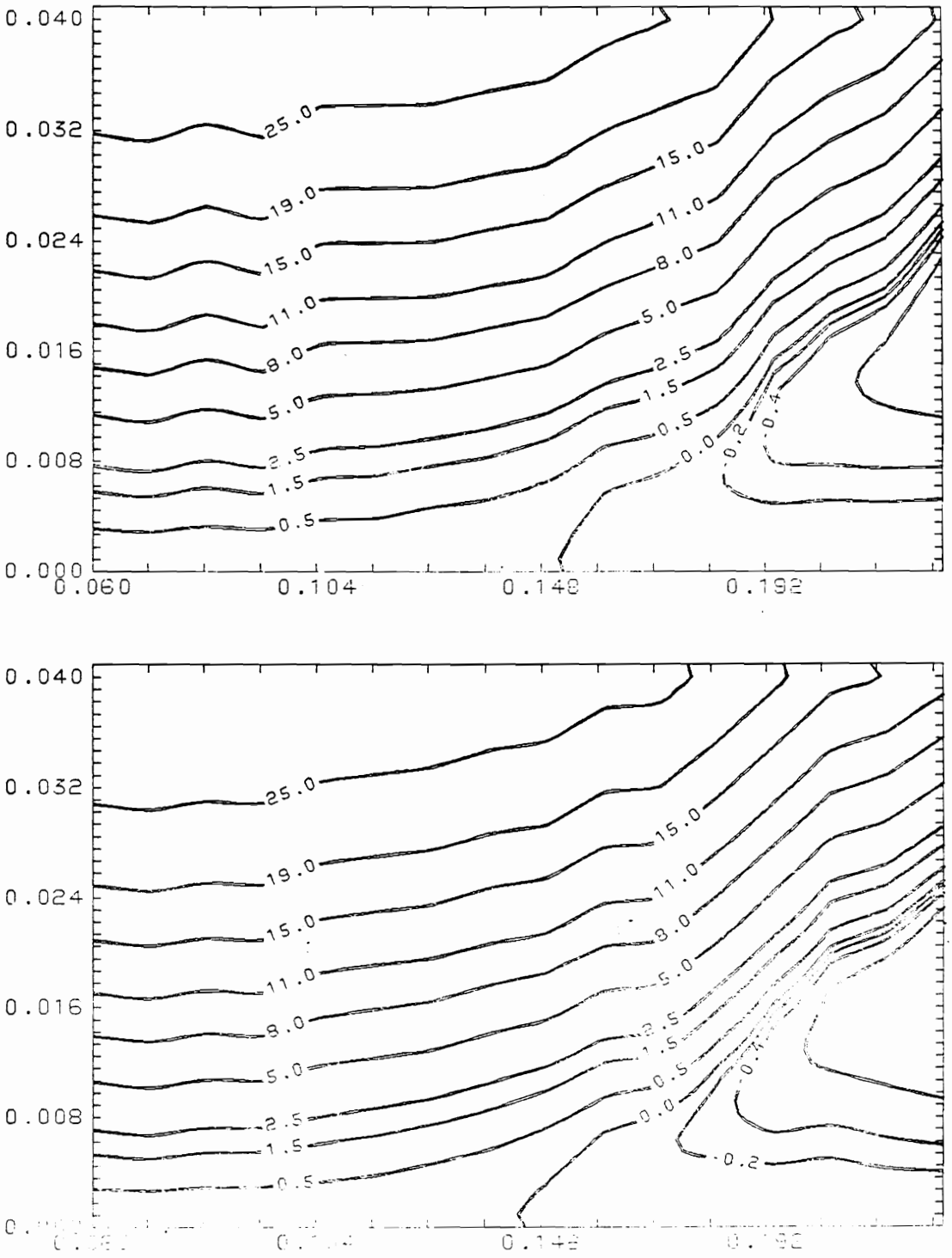

Fig. 3.1.38 Streamlines for time-mean (top) and steady (bottom). Horizontal and vertical scales are x/R, y/R respectively.

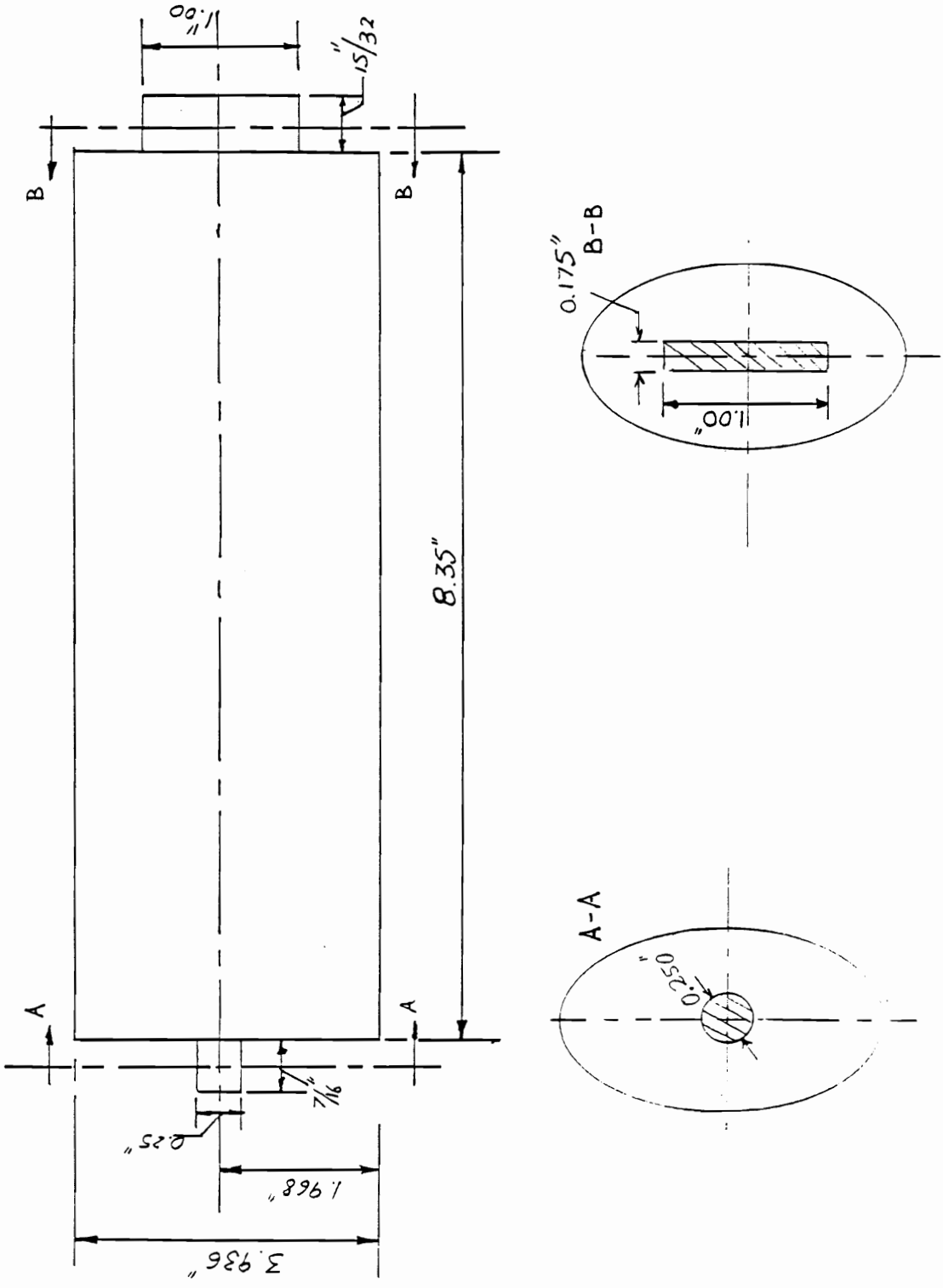

Fig. 3.2.1 Details of the model of the elliptic cylinder.

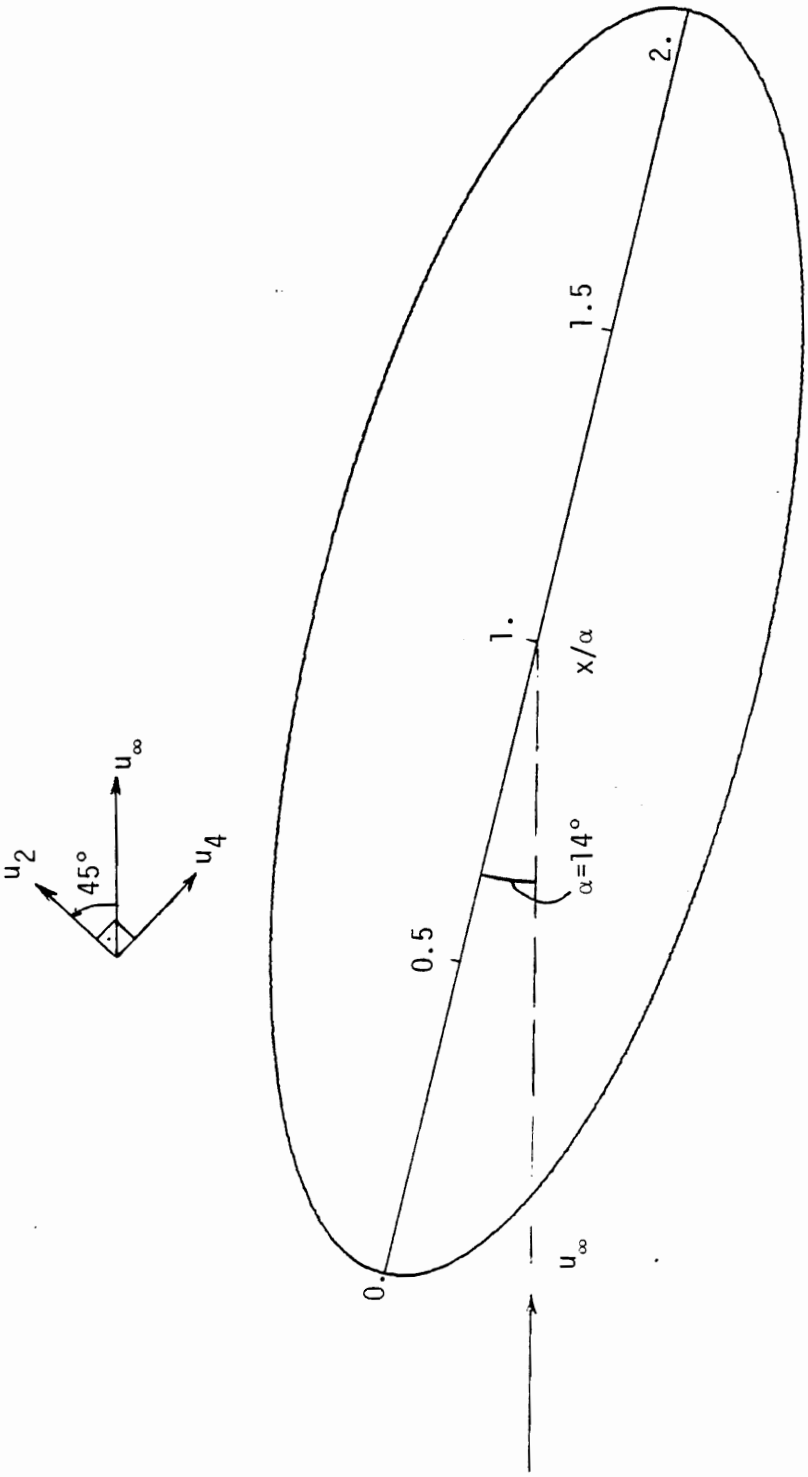

Fig. 3.2.2 Velocity components (u_2,u_4) obtained by the LDV in the region around the ellipse (the stagnation region is excluded).

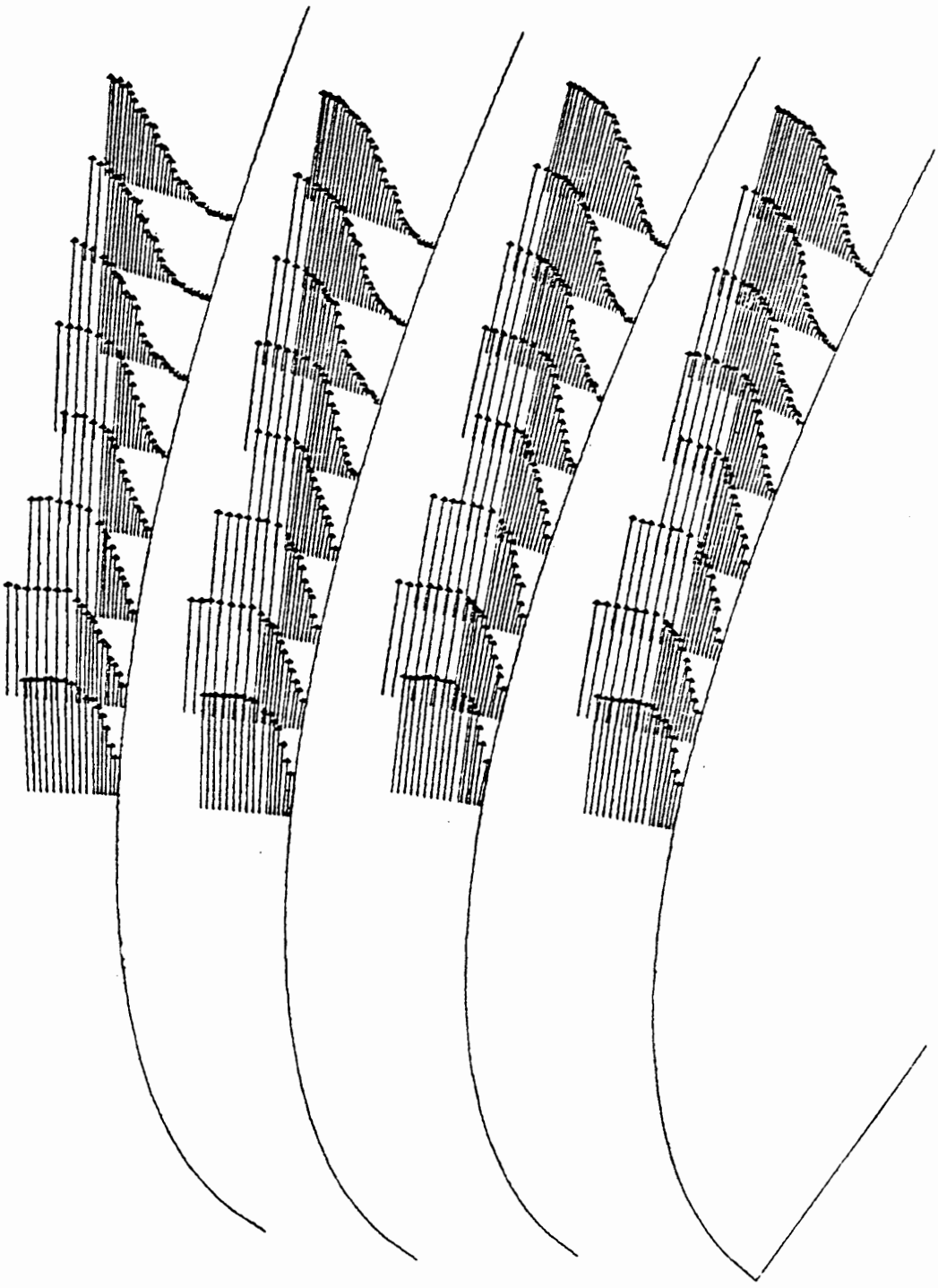

Fig. 3.2.3 Suction side separation region. Velocity vectors at stations x/a = 0.2, 0.25, 0.3, 0.35, 0.4, 0.45, 0.5, 0.55 and at t = KT/8, k = 1 ÷ 4 (top to bottom) scale 5:1.

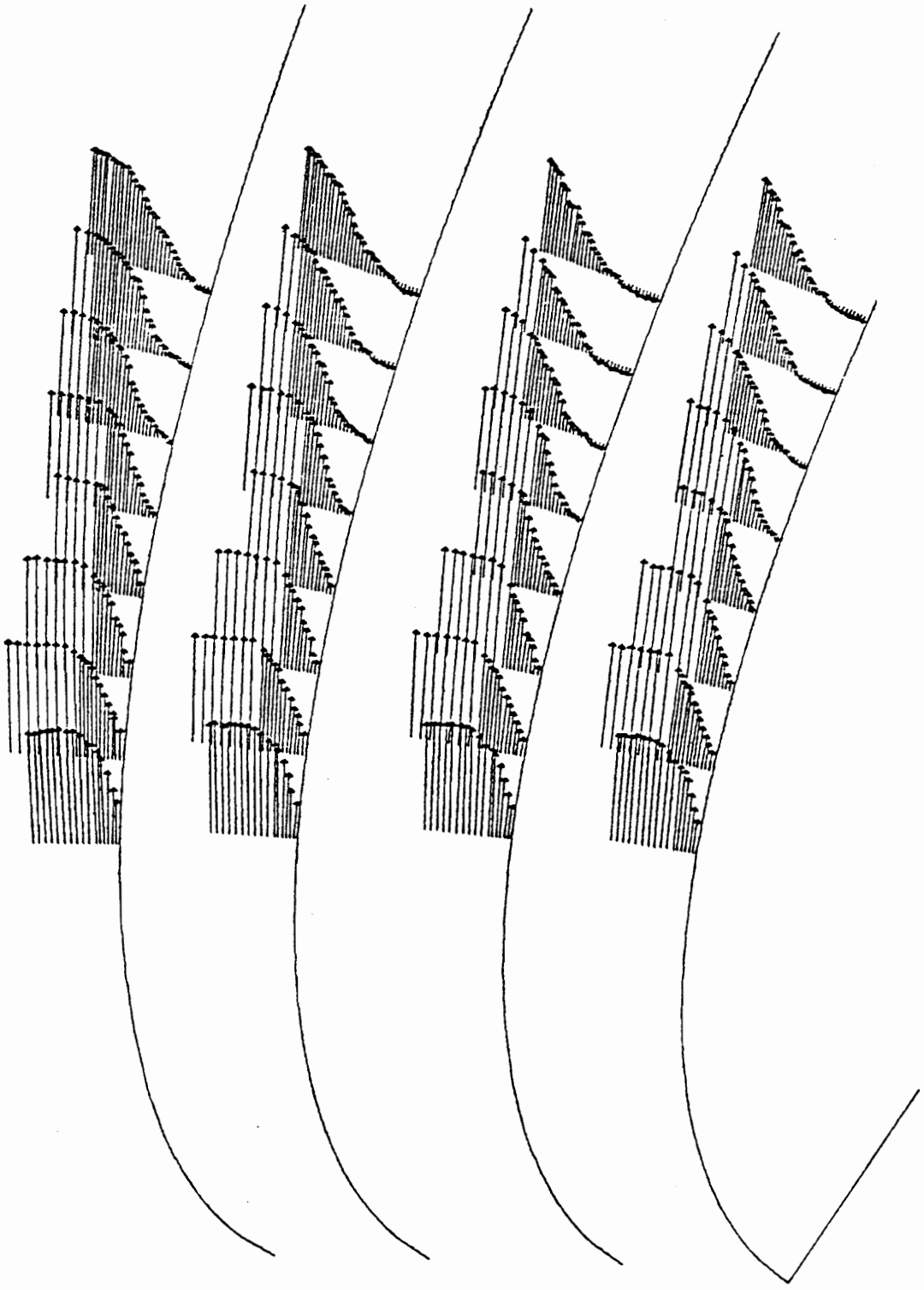

Fig. 3.2.4 Suction side separation region. Velocity vectors at stations x/a = 0.2, 0.25, 0.3, 0.35, 0.4, 0.45, 0.5, 0.55 and at t = KT/8, K = 5 ÷ 8 (top o bottom) Scale 5:1

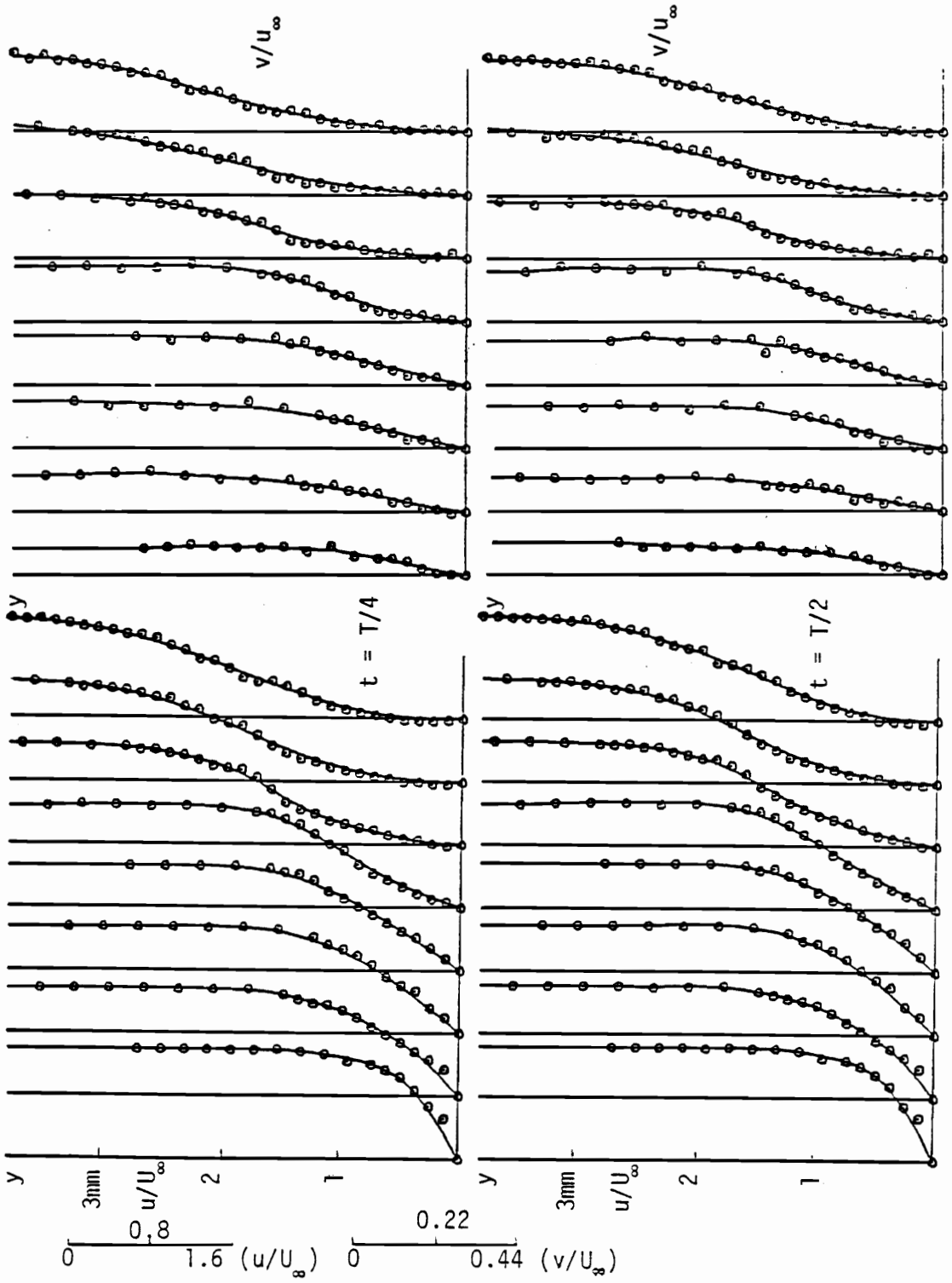

Fig. 3.2.5 Velocity profiles (u-v) at suction side separation region and t = T/4, T/2.

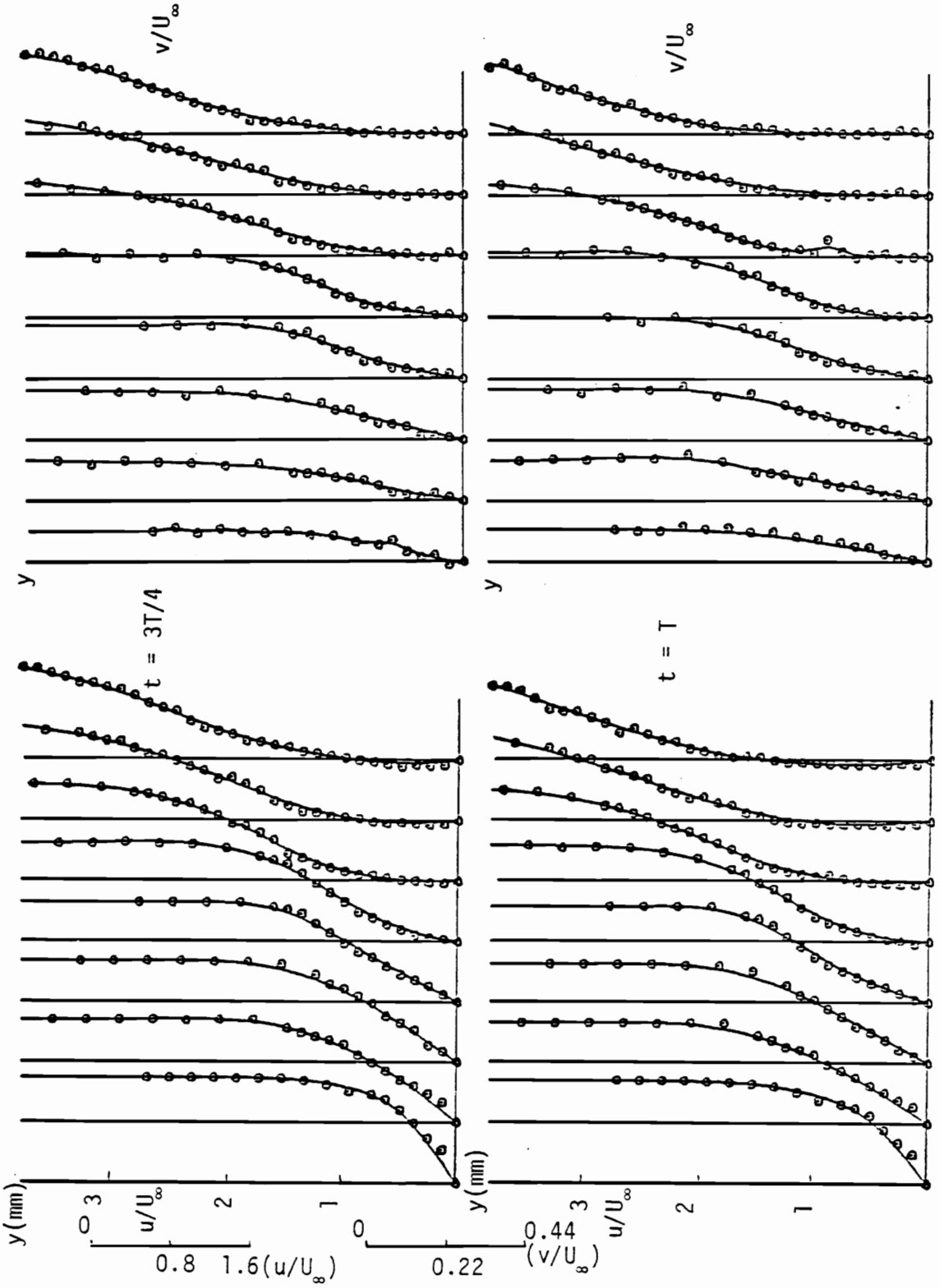

Fig. 3.2.6 Velocity profiles (u-v) at suction side separation region and t = 3T/4,T.

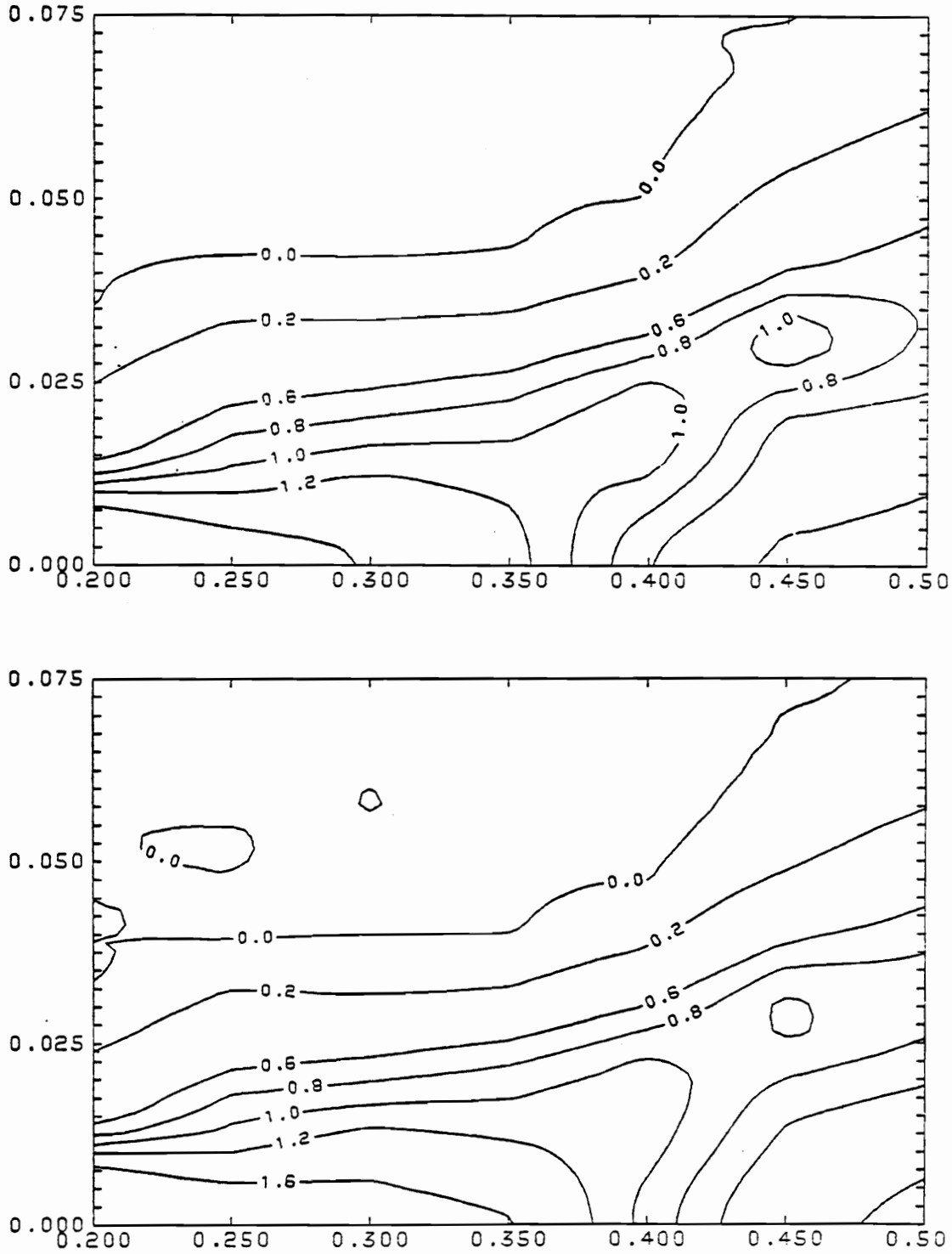

Fig. 3.2.7 Vorticity contours at suction side separation region and t = T/4, T/2 (top to bottom). Horizontal and vertical scales are x/a, y/a respectively.

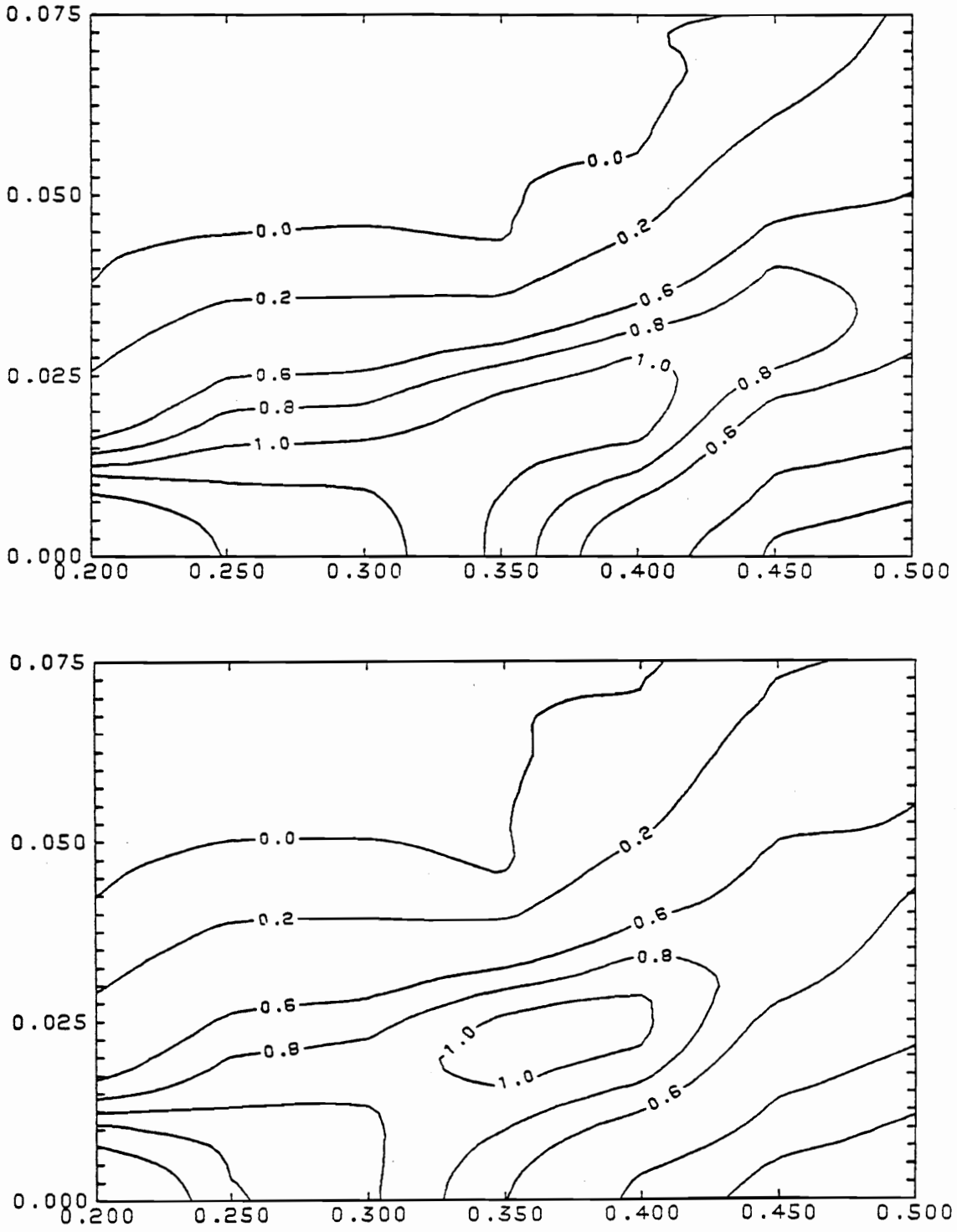

Fig. 3.2.8 Vorticity contours at suction side separation region and t = 3T/4, T (top to bottom). Horizontal and vertical scales a x/a, y/a respectively.

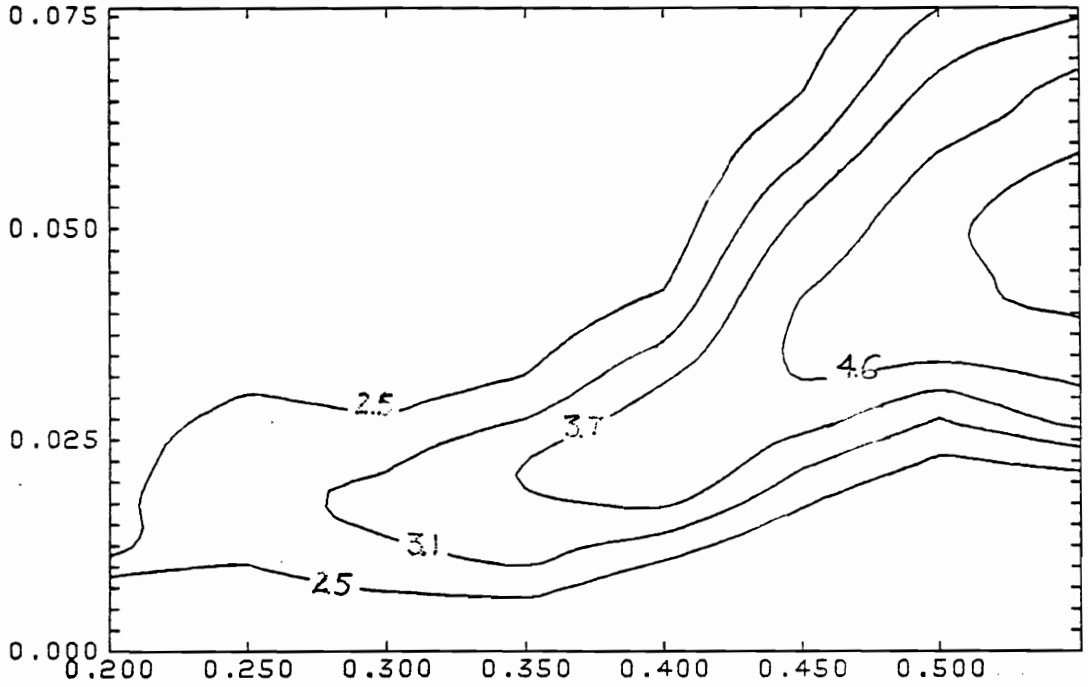

Fig. 3.2.9a Amplitude contours at suction side separation region.

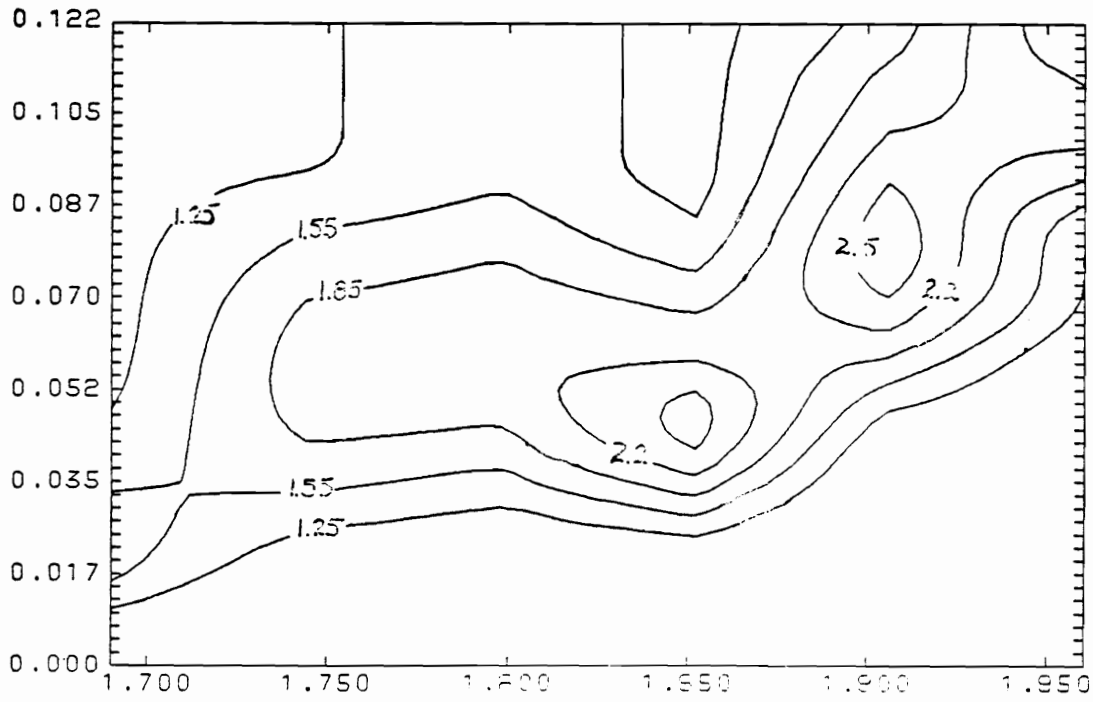

Fig. 3.2.9b Amplitude contours at pressure side separation region. Horizontal and vertical scales are x/a, y/a respectively.

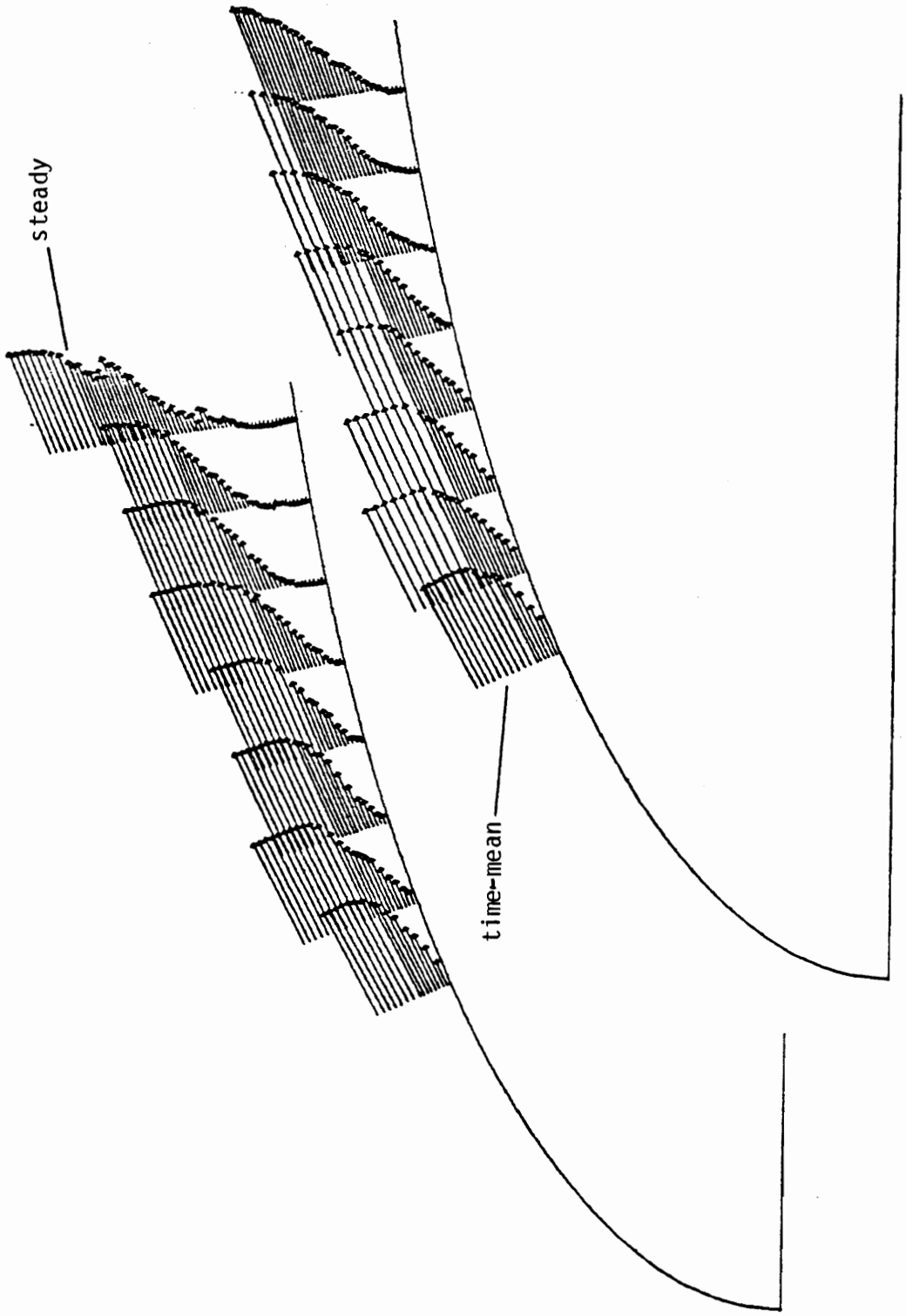

Fig. 3.2.10 Steady and time-mean velocity vectors at suction side separation region. Scale 5:1

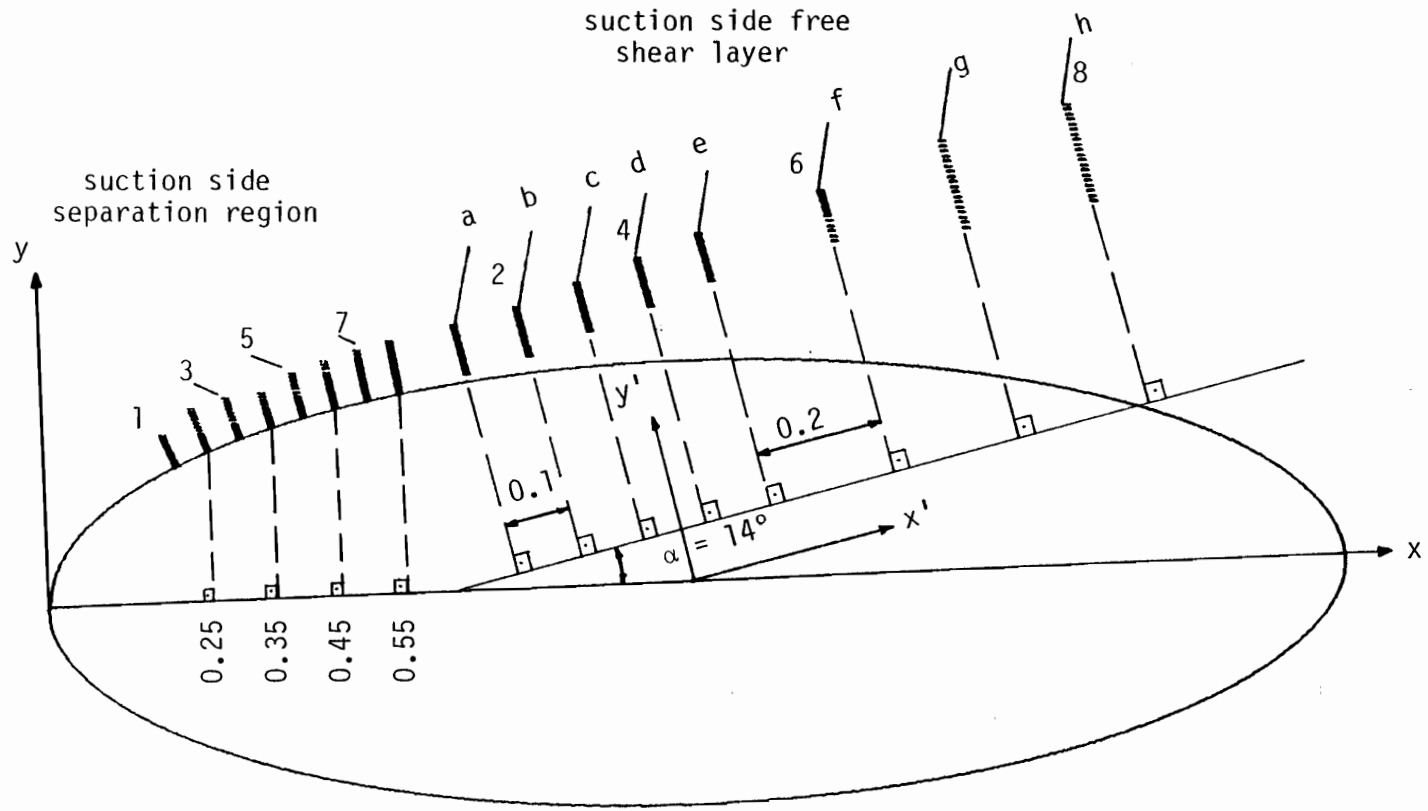

Fig. 3.2.11 Stations at suction side separation point and free shear layer. Scale 1.7:1. The x'-y' coordinates of the points a, b, c, d, e, f, g, h are given in Table 3.2.1, for the steady and unsteady free-stream experiments.

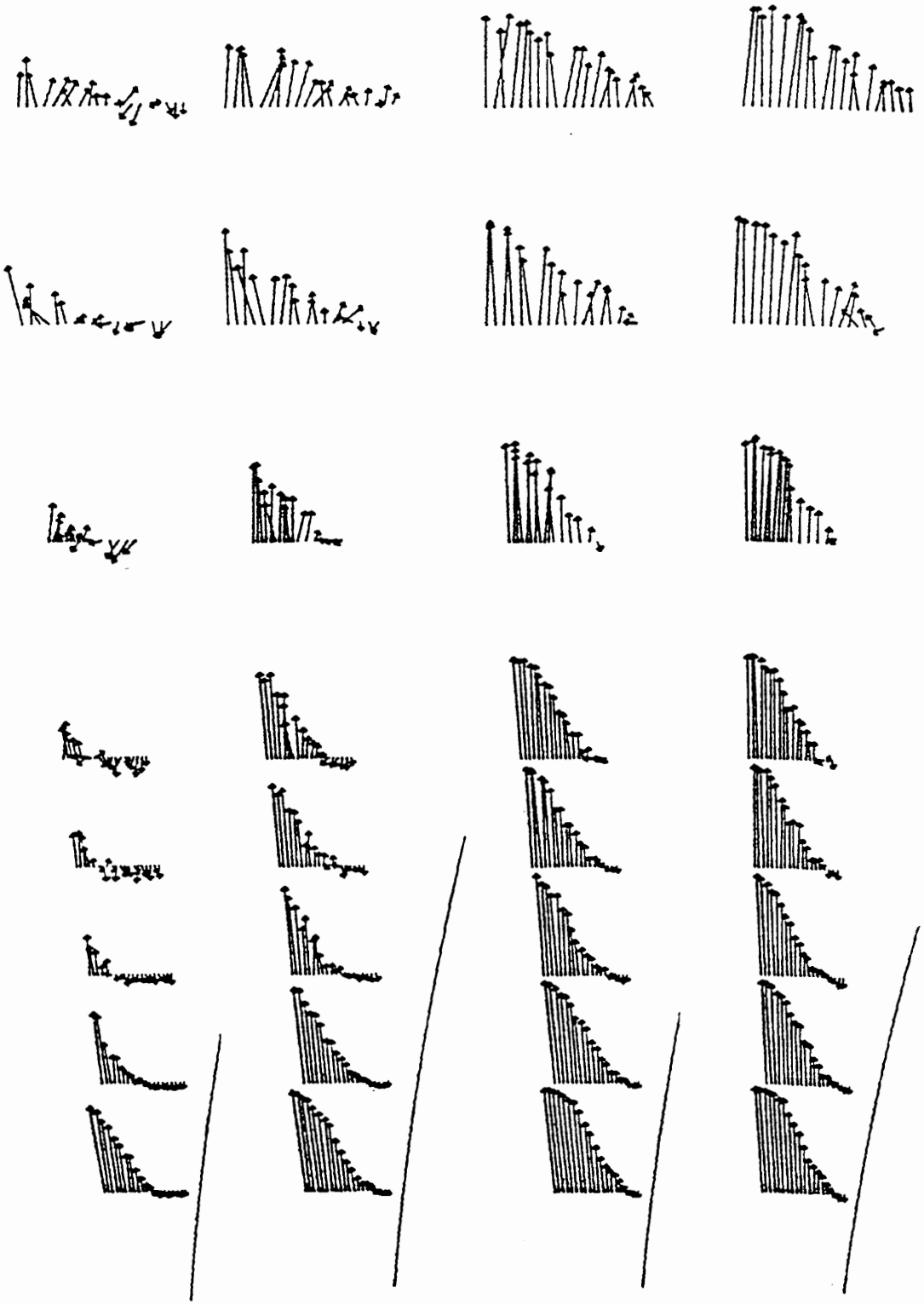

Fig. 3.2.12 Velocity vectors at suction side free shear layer and t = kT/8, k = 1 ÷ 4 (top to bottom). Scale 3.5:1

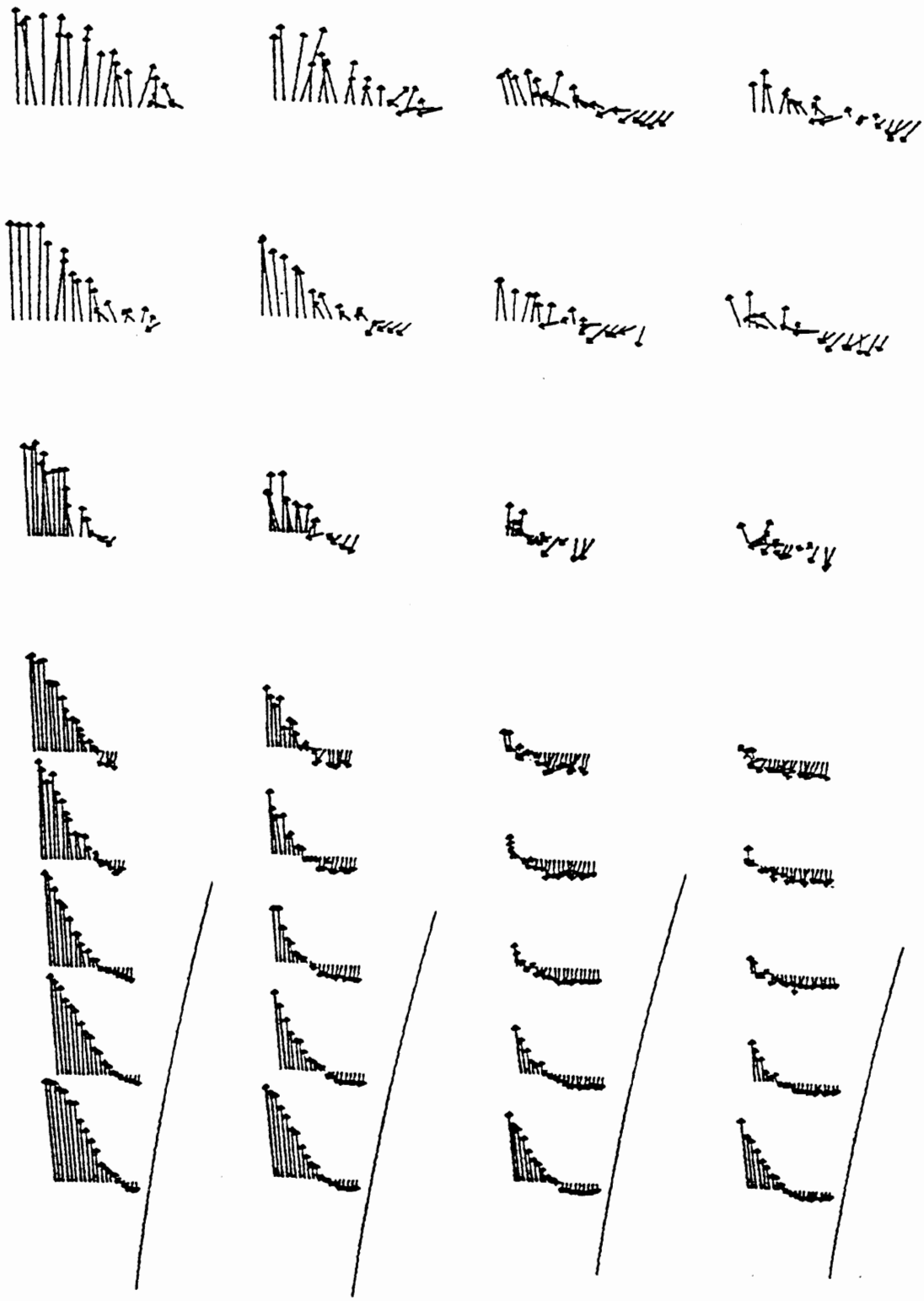

Fig. 3.2.13 Velocity vectors at suction side free shear layer and t = kT/8, k = 5 ÷ 8 (top to bottom) Scale 3.5:1

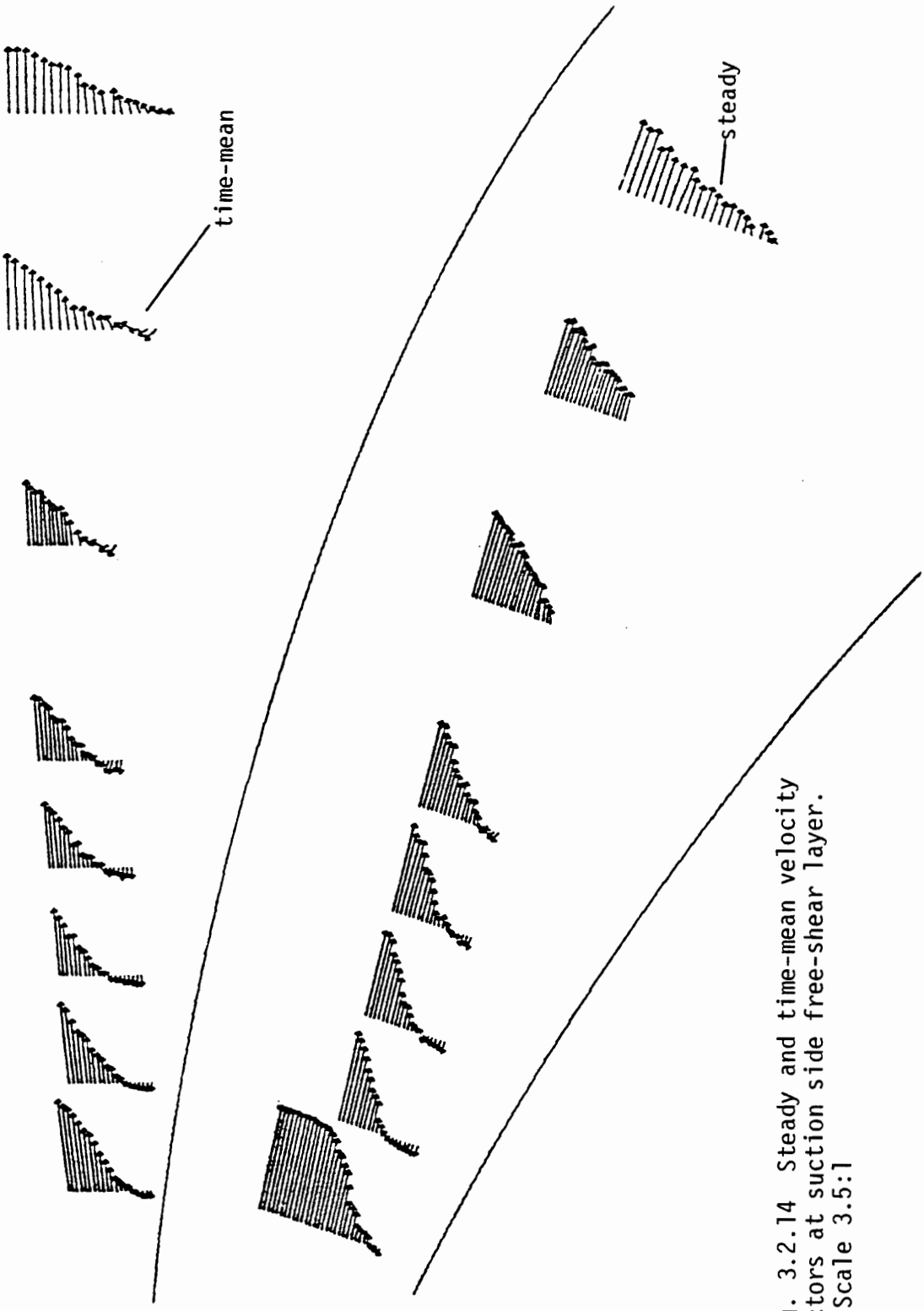

Fig. 3.2.14 Steady and time-mean velocity vectors at suction side free-shear layer.
Scale 3.5:1

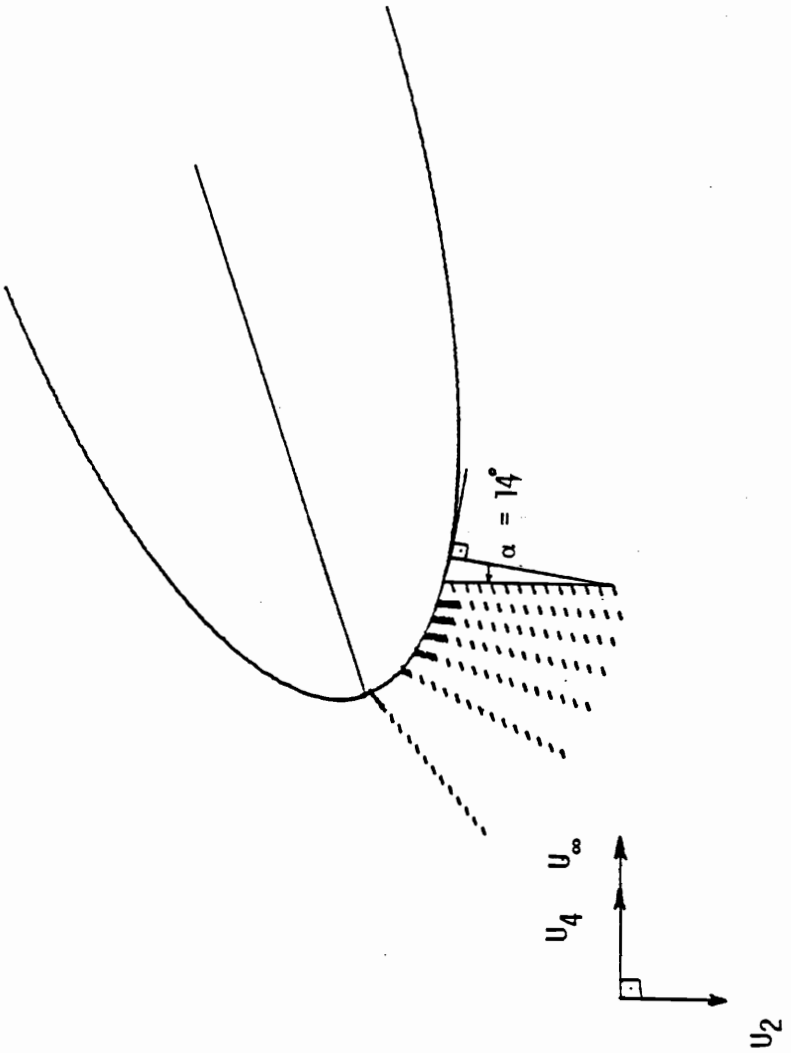

Fig. 3.2.15 Stagnation region

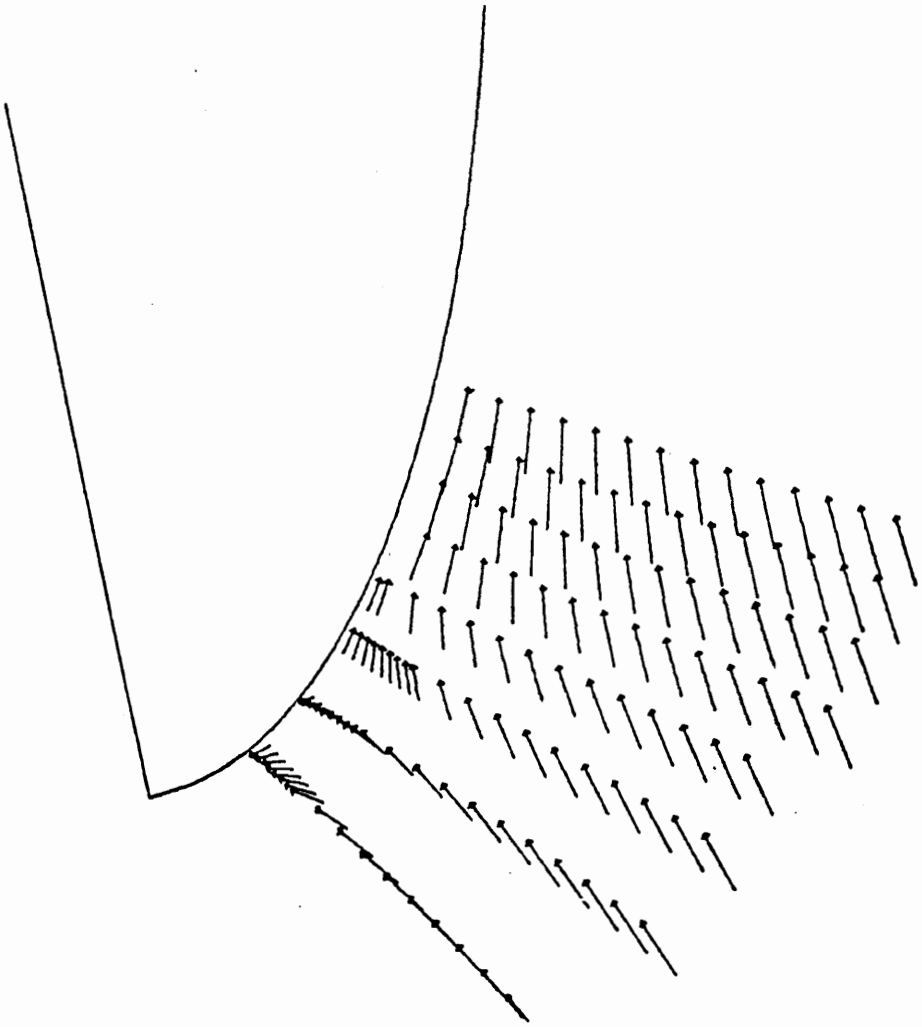

Fig. 3.2.16 Steady velocity vectors at stagnation point. Scale 5:1

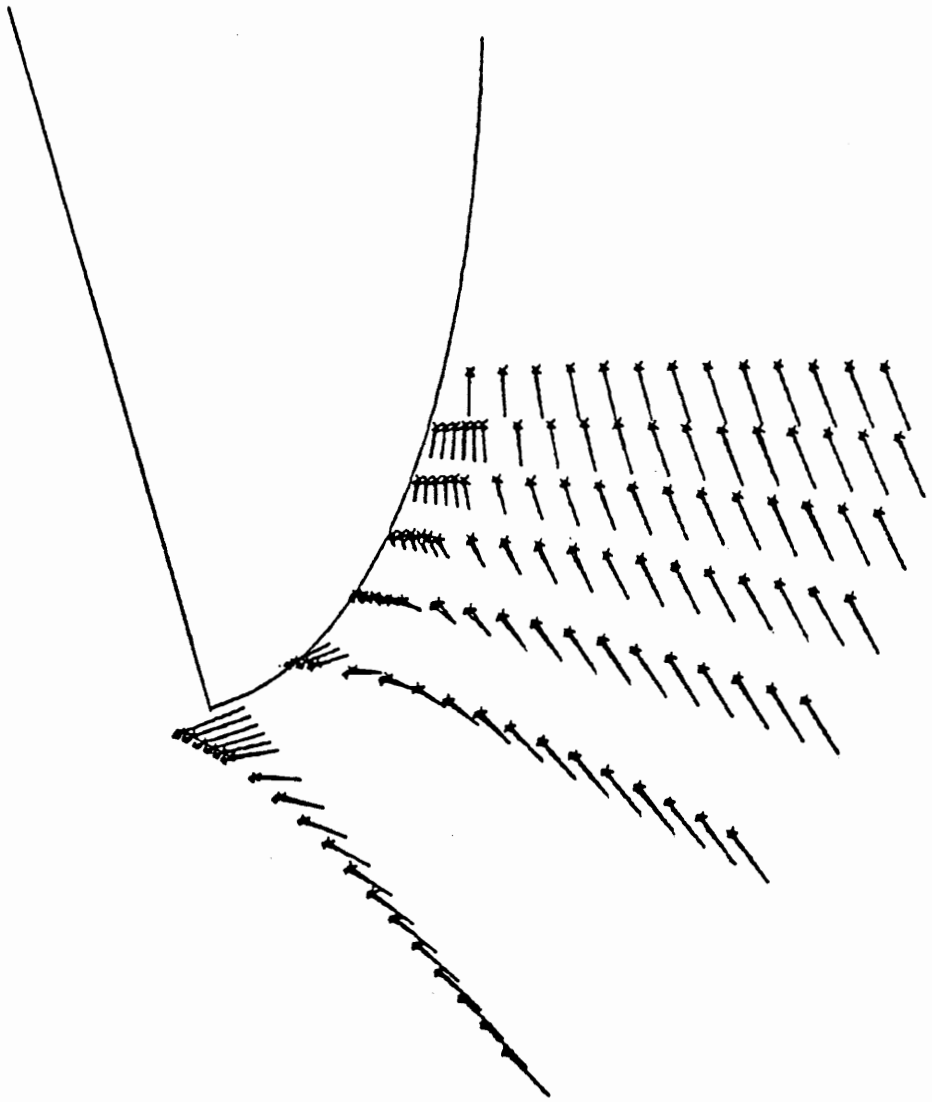

Fig. 3.2.17 Unsteady velocity vectors at stagnation point, t = T/2, T.
Symbol x: t = T
Δ: t = T/2
Scale 5:1

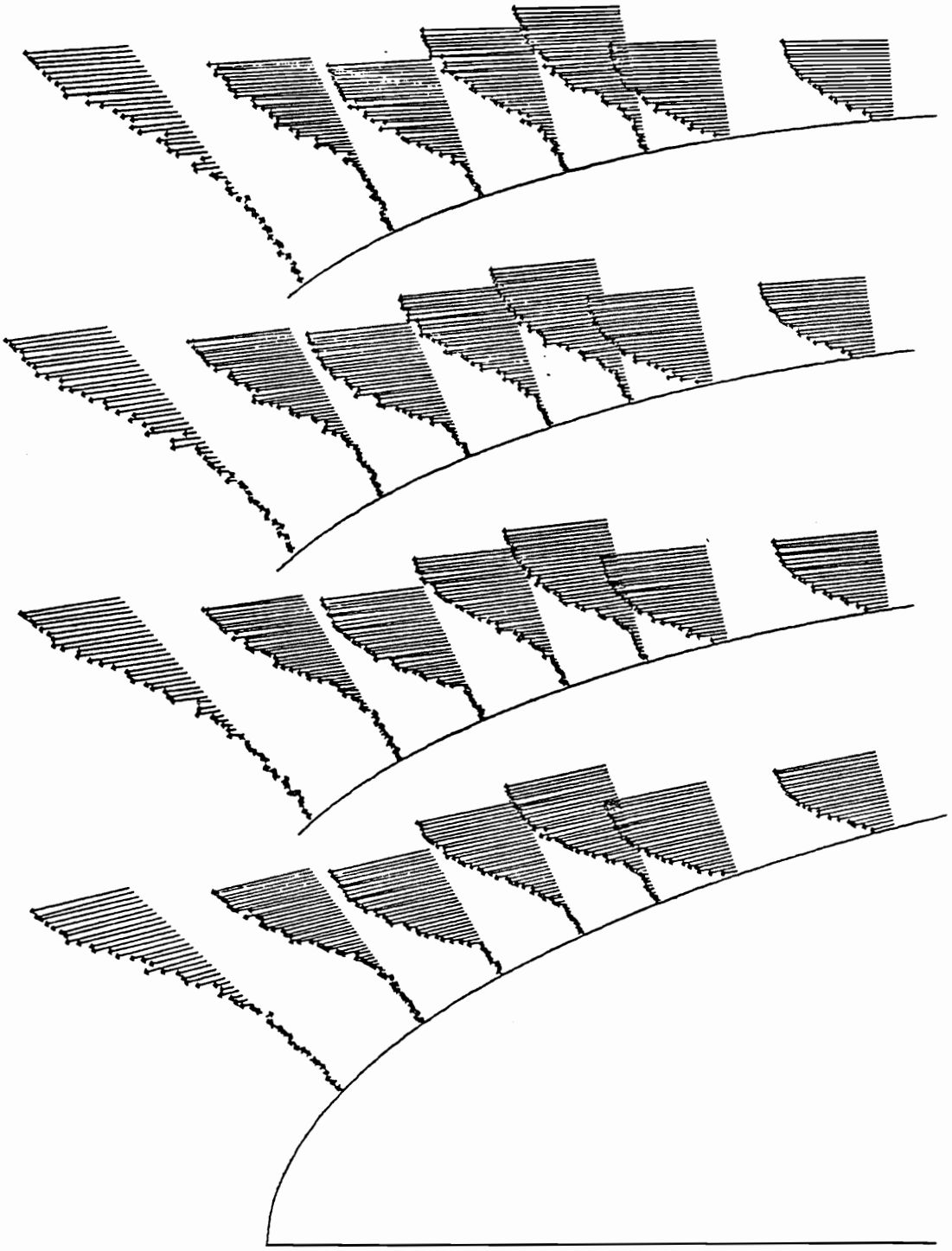

Fig. 3.2.18 Velocity vectors at pressure side separation region t = kT/8, k = 1 ÷ 4. Scale 5:1

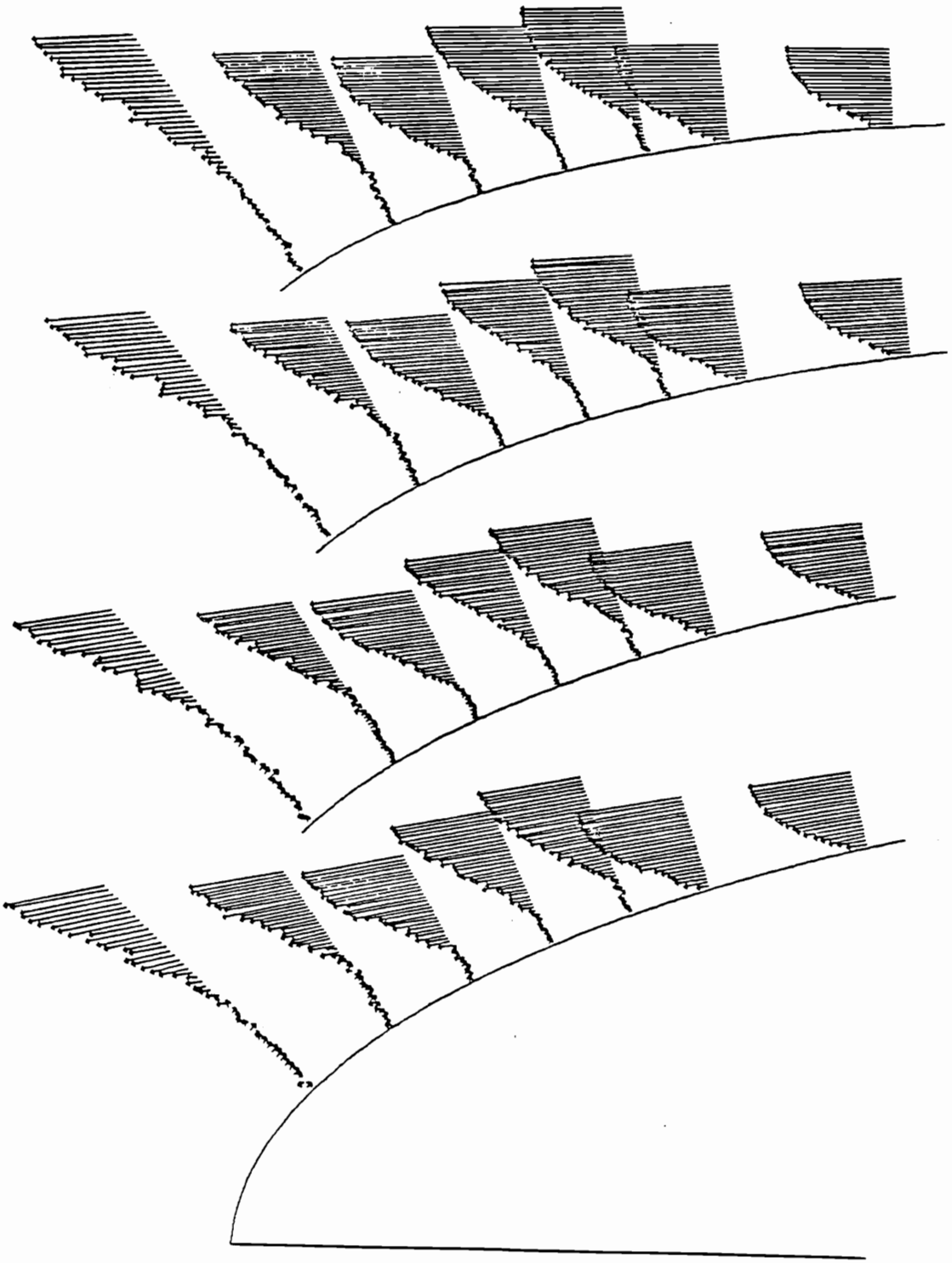

Fig. 3.2.19 Velocity vectors at pressure side separation region t = kT/8, k = 5 ÷ 8. Scale 5:1.

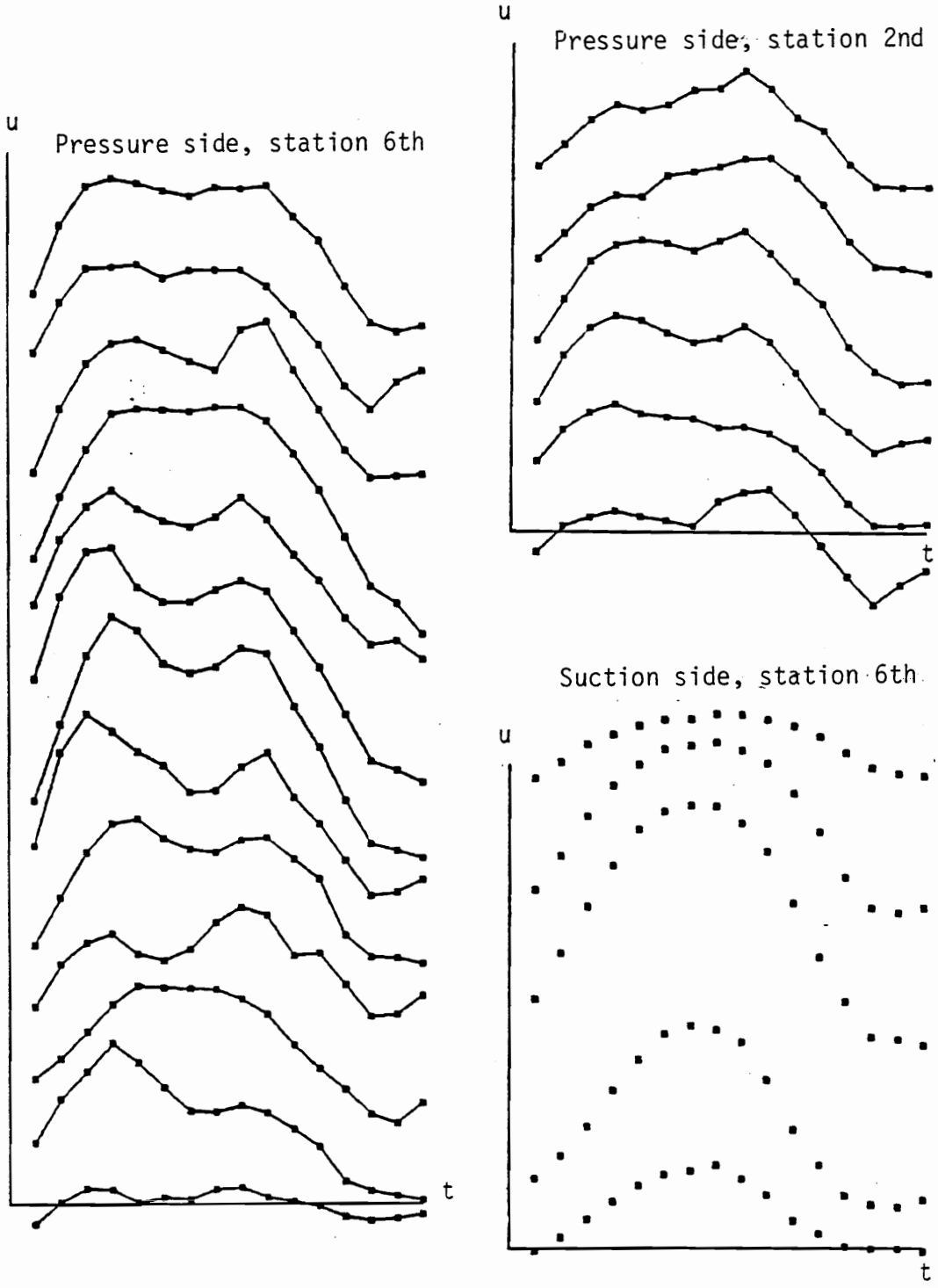

Fig. 3.2.20 Time records of u component at suction and pressure side separation regions, and at various locations far from the surface.

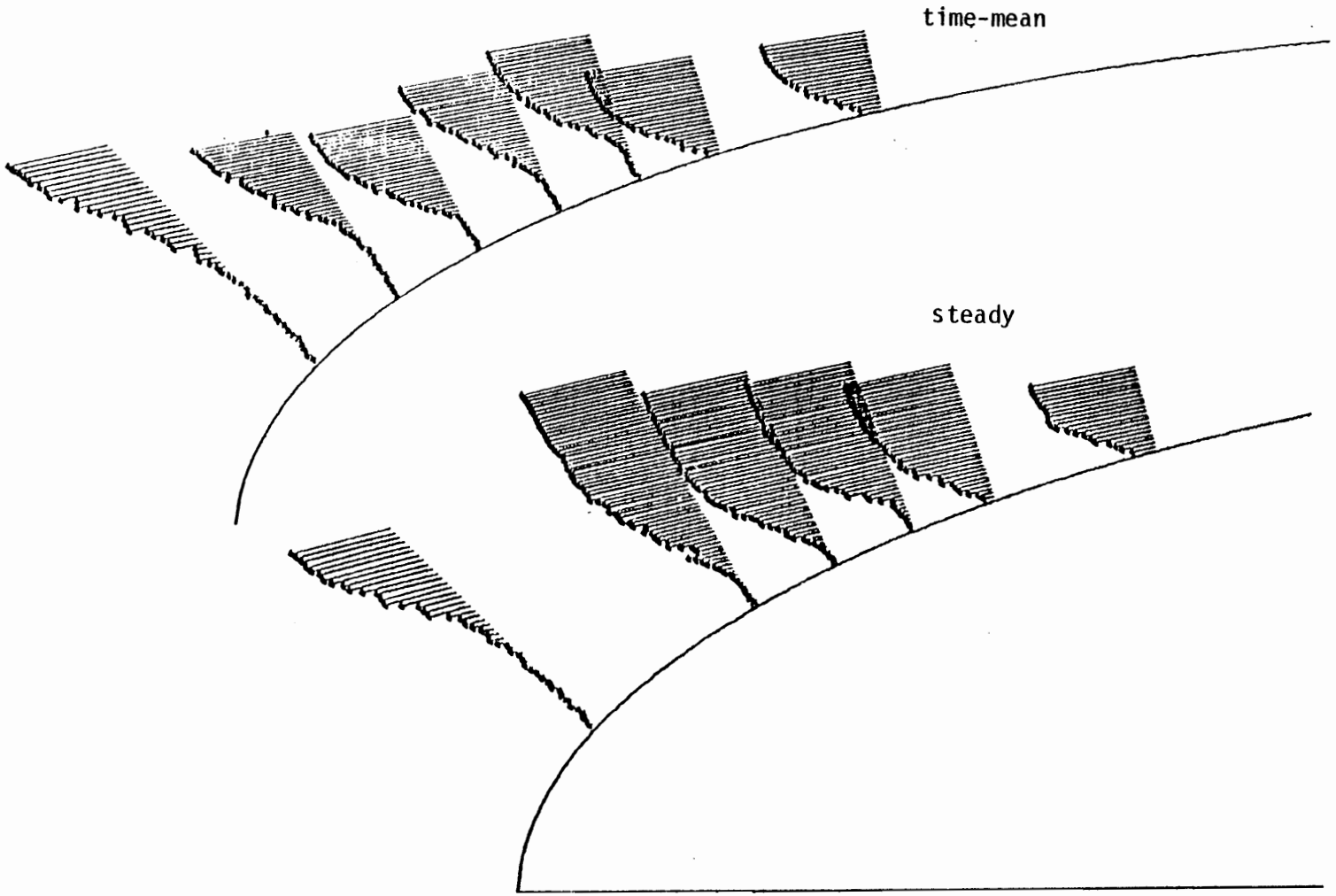

Fig. 3.2.21 Steady and time mean velocity vectors at pressure side separation region. Scale 5:1.

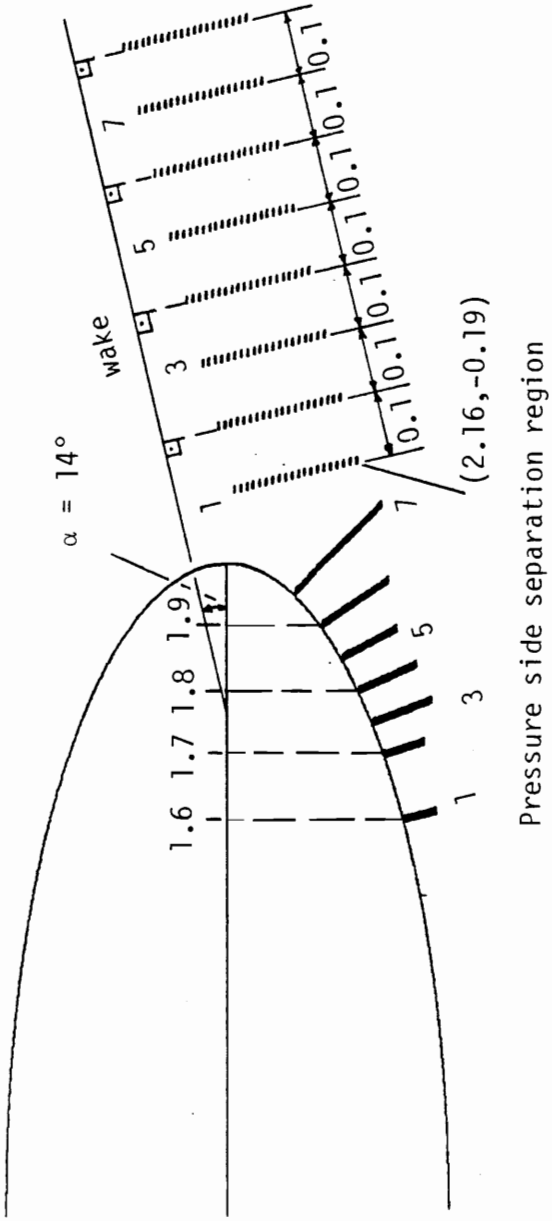

Fig. 3.2.22 Stations at pressure side separation region and the wake.

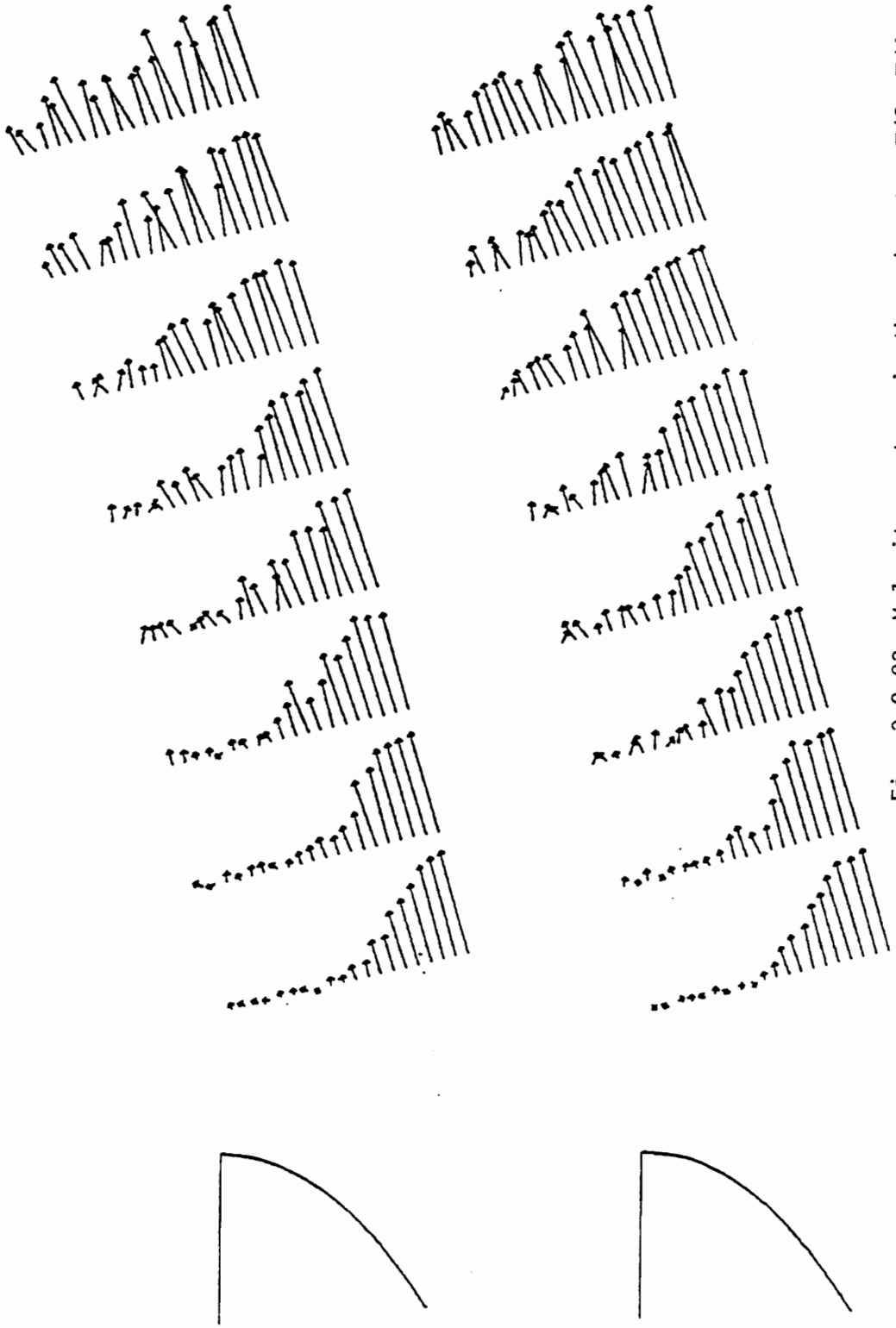

Fig. 3.2.23 Velocity vectors in the wake, t = T/8, T/4.
Scale 4:1

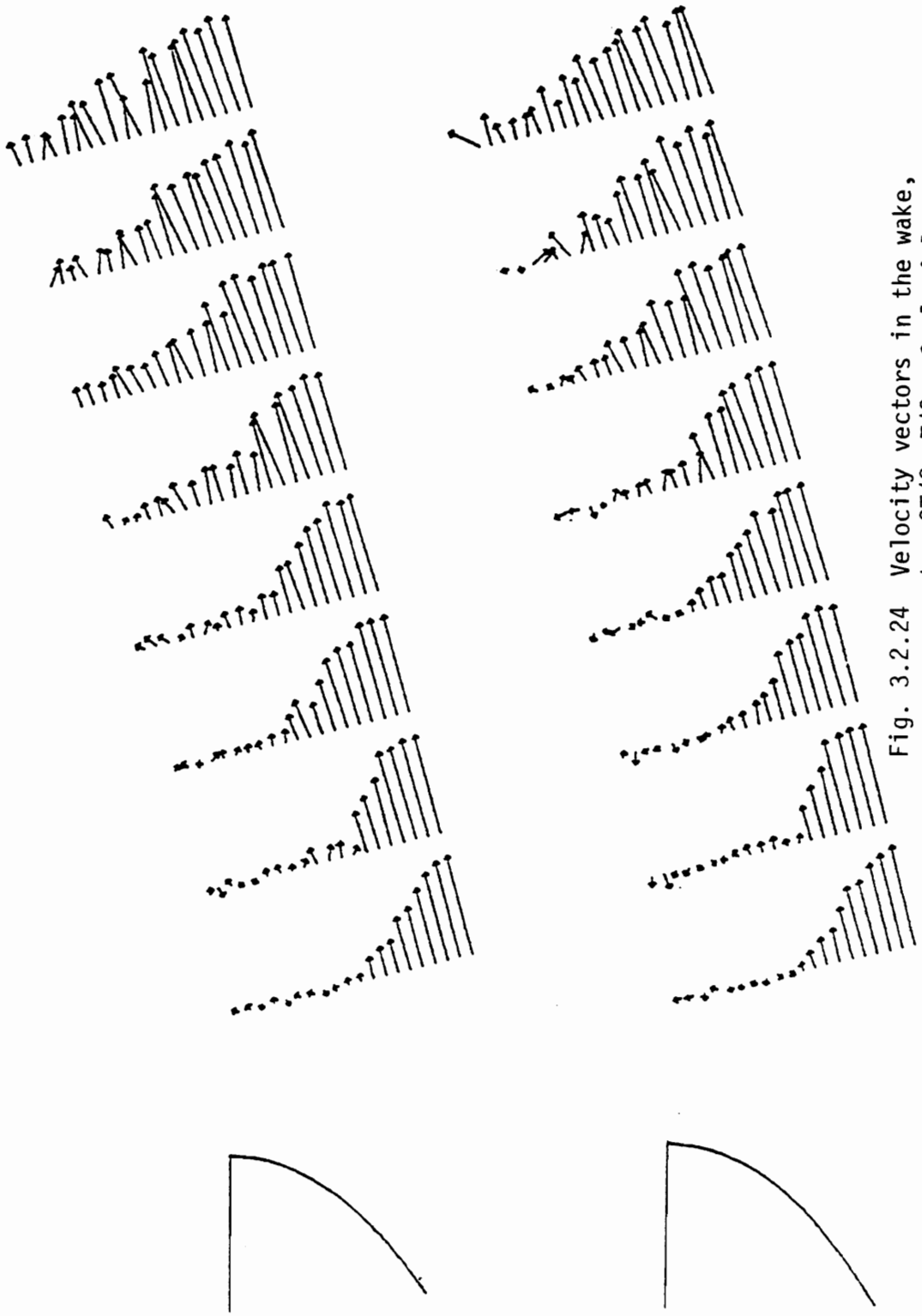

Fig. 3.2.24 Velocity vectors in the wake, t = 3T/8, T/2. Scale 4:1

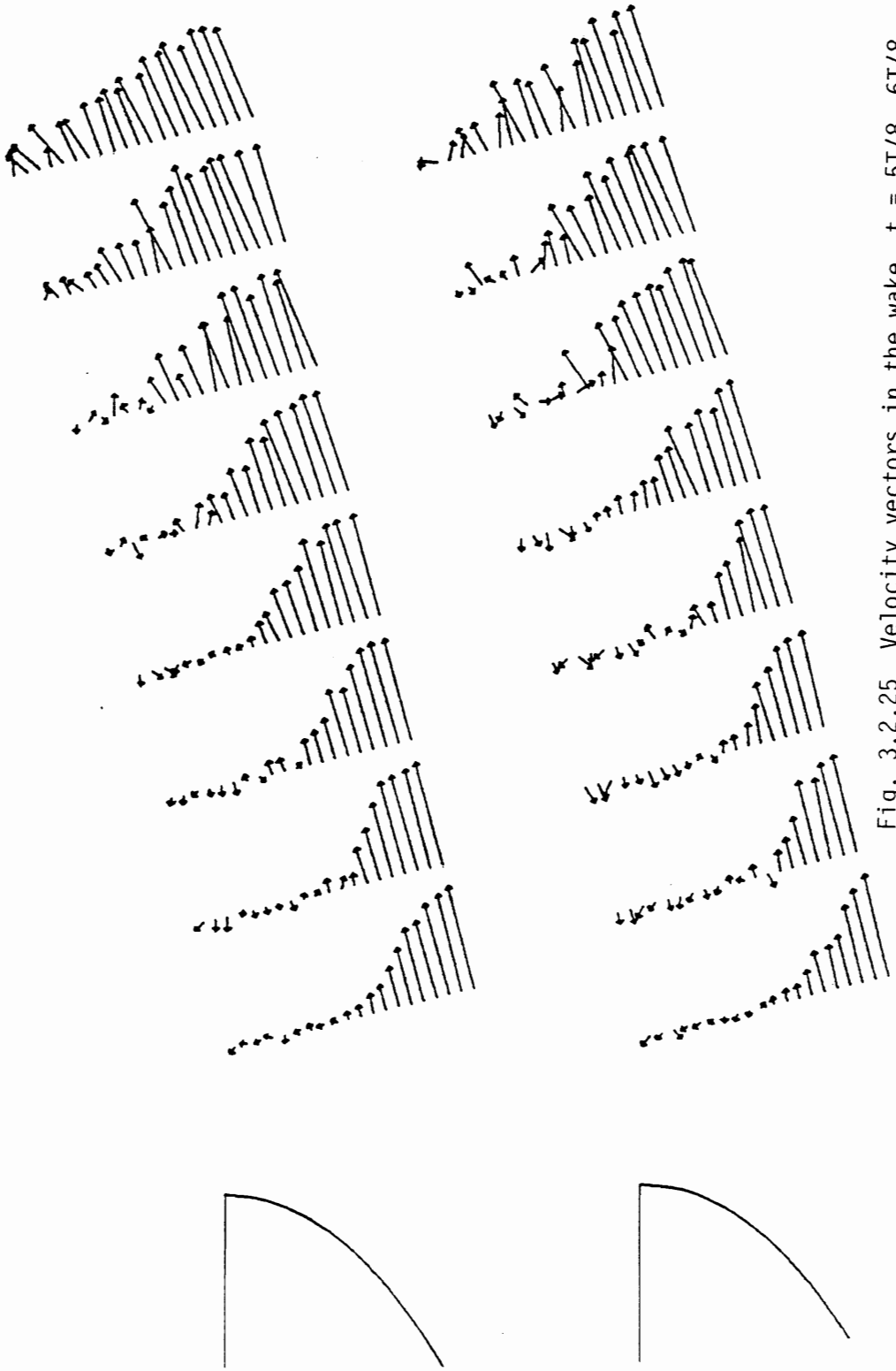

Fig. 3.2.25 Velocity vectors in the wake, t = 5T/8, 6T/8.
Scale 4:1

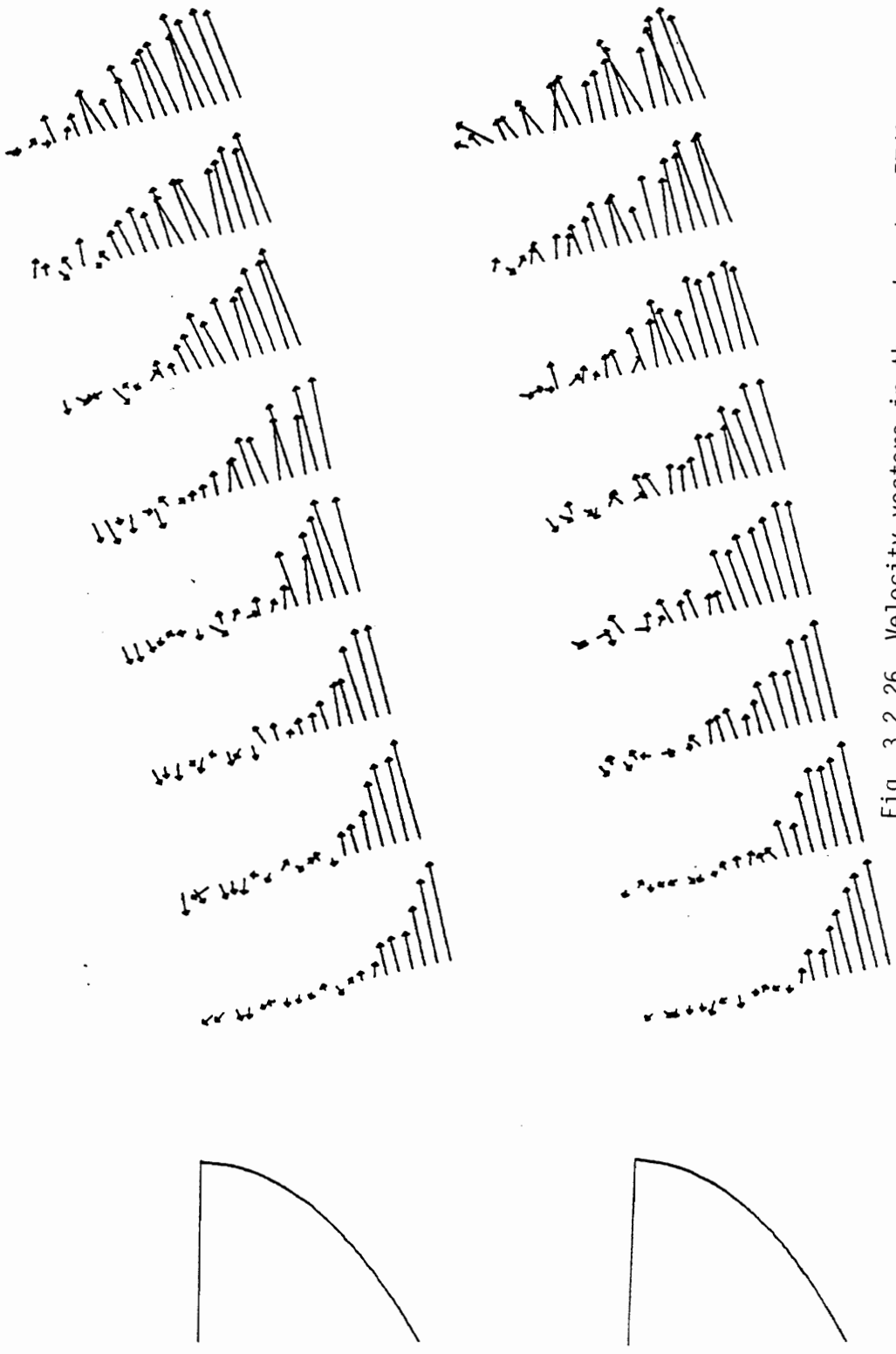

Fig. 3.2.26 Velocity vectors in the wake, t = 7T/8, 8T/8. Scale 4:1

Fig. 3.2.27 Steady and time-mean velocity vectors in the wake region. Scale 4:1

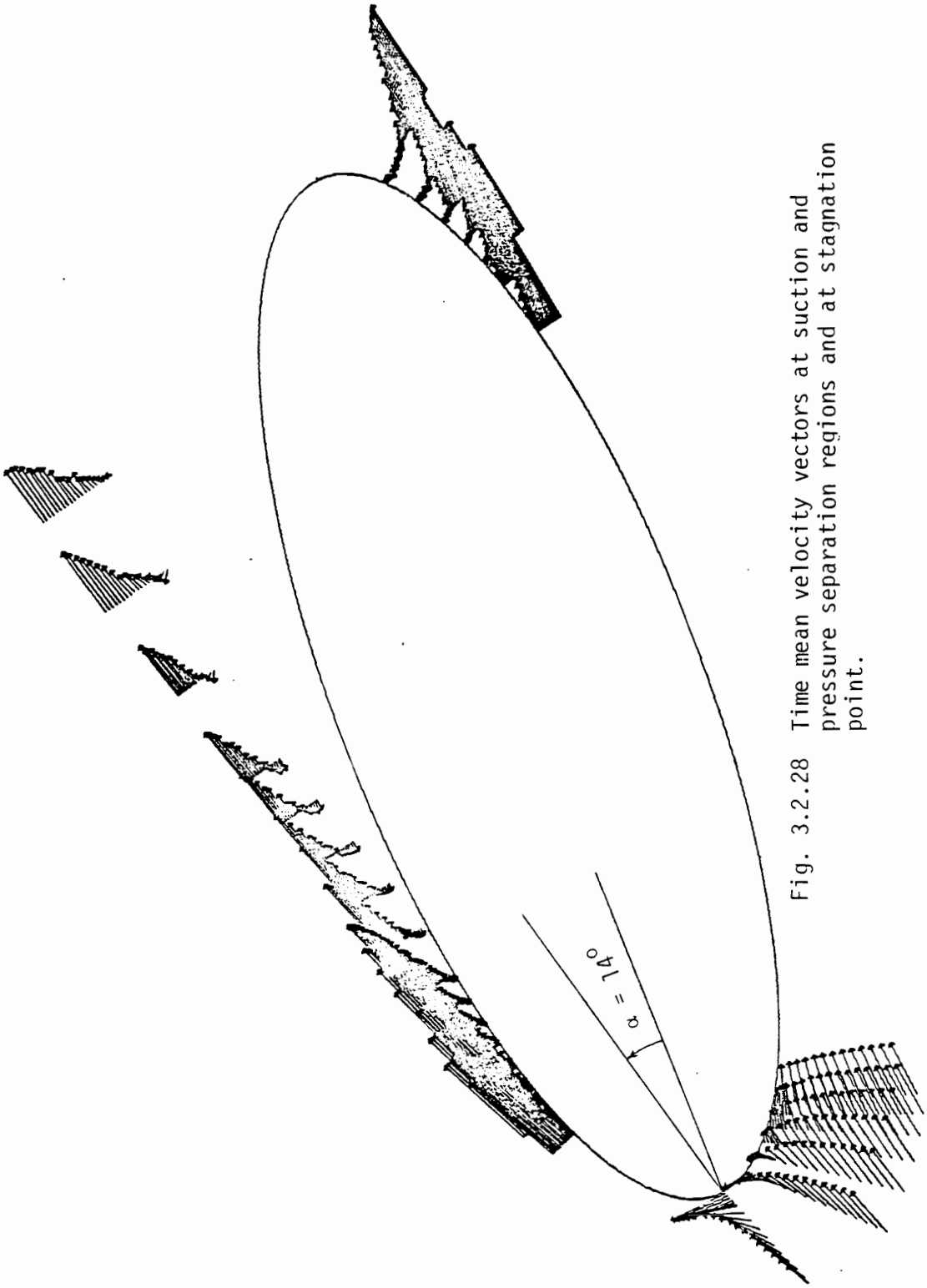

Fig. 3.2.28 Time mean velocity vectors at suction and pressure separation regions and at stagnation point.

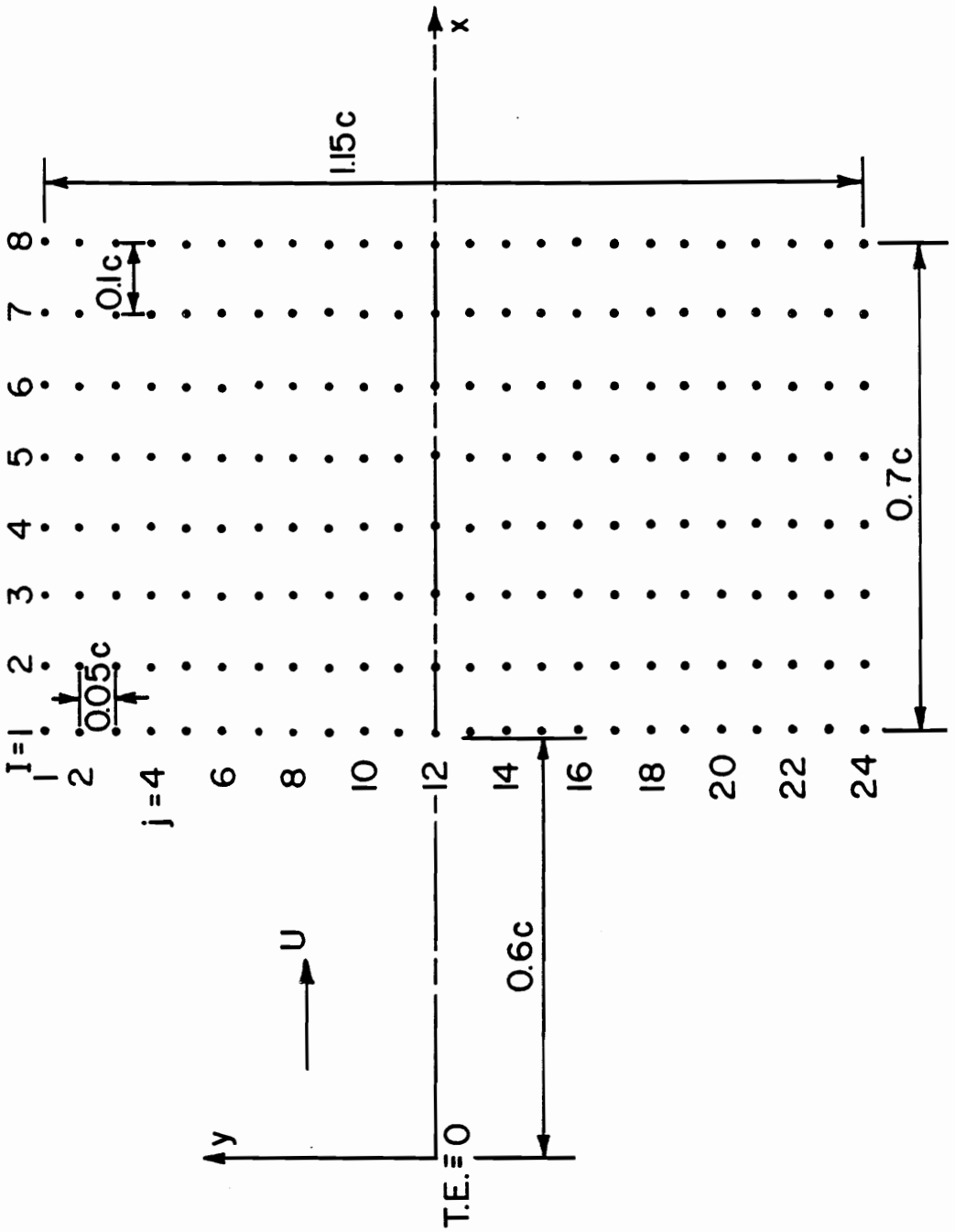

Fig. 3.3.1 Measuring grid downstream of a pitching airfoil NACA 0012. The trailing edge (T.E.) is located at x = 0.

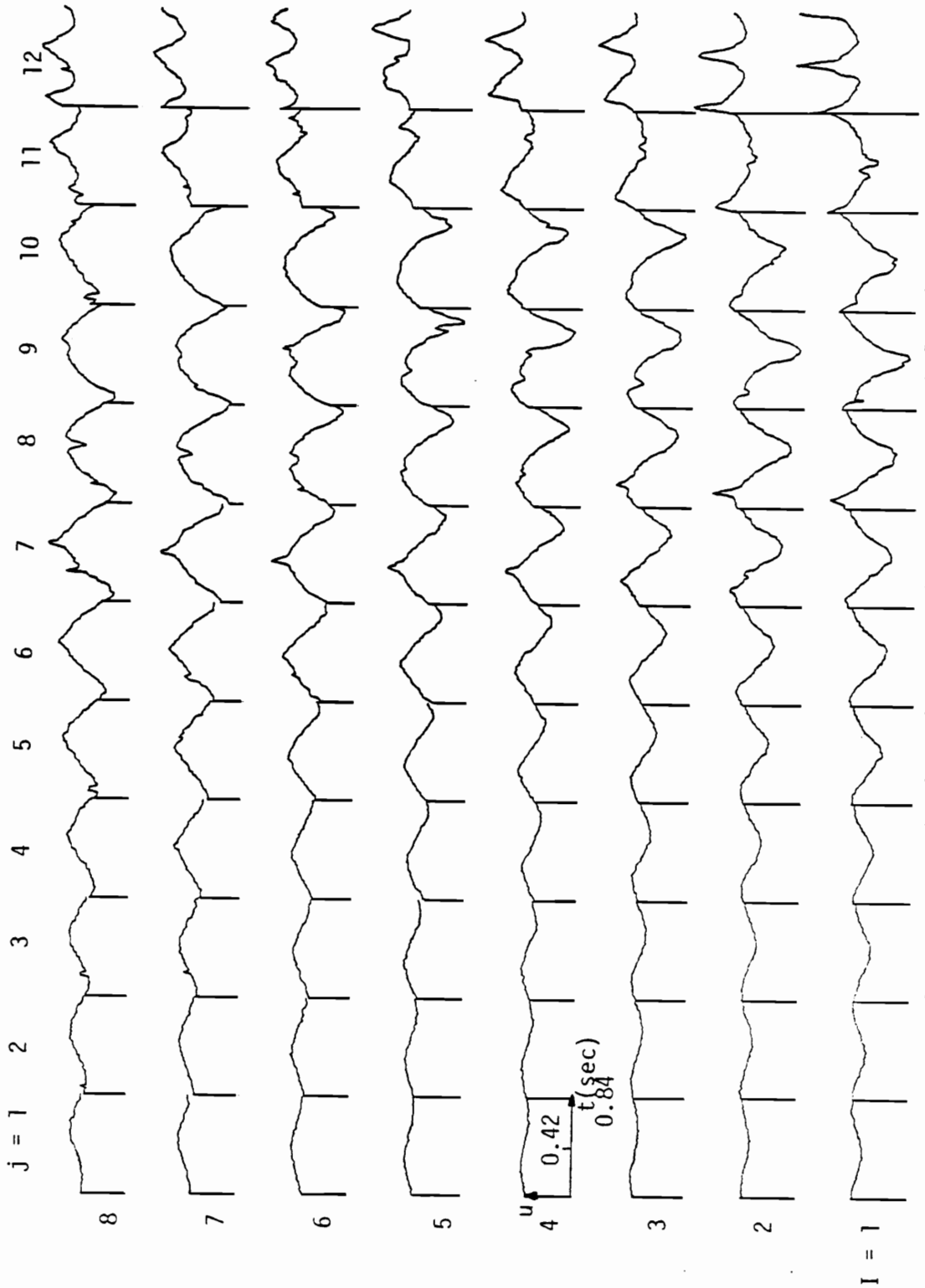

Fig. 3.3.2 Velocity time records at the upper half of measuring grid (j = 1, 12)

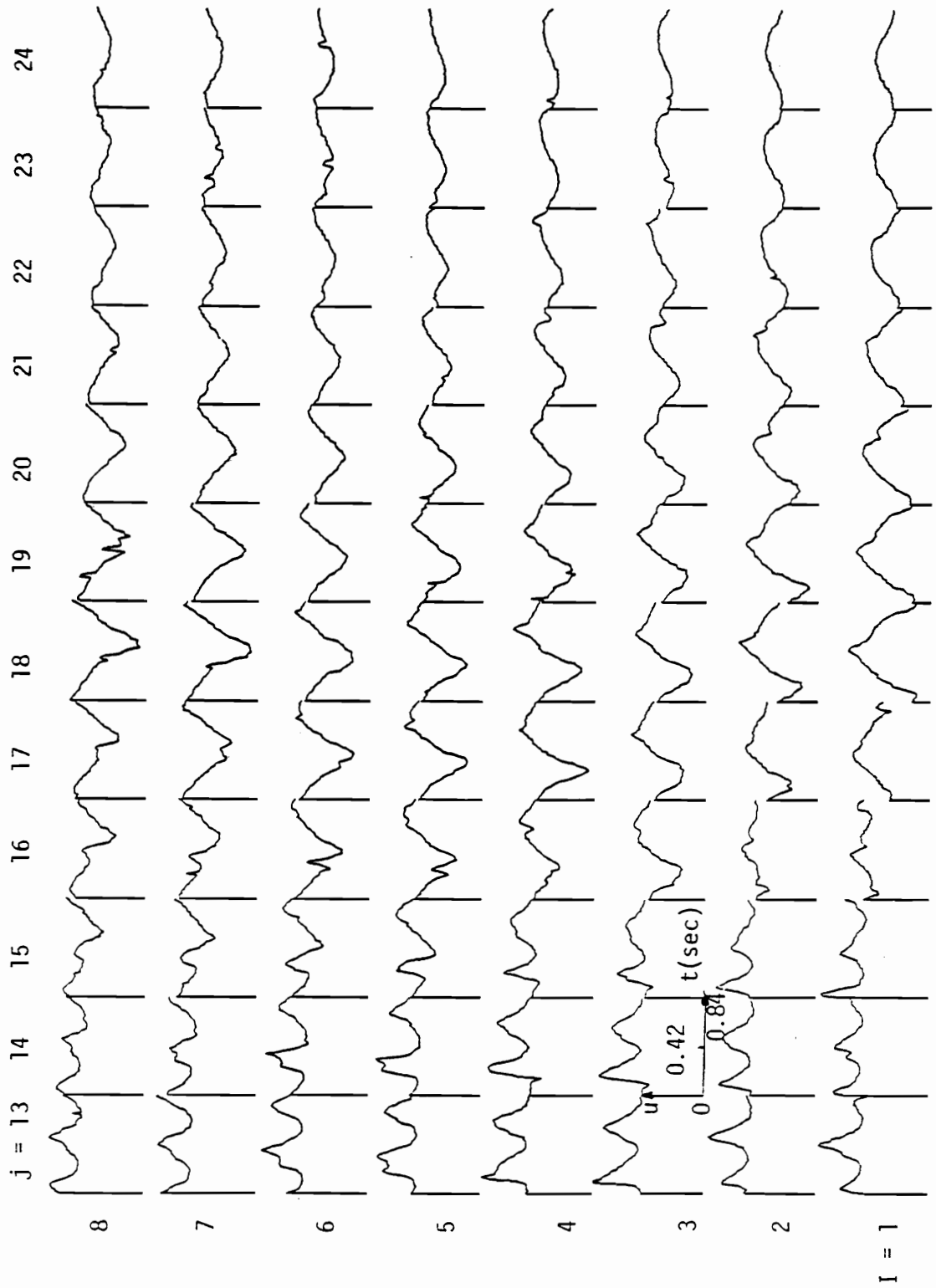

Fig. 3.3.3 Velocity time records at the lower half of measuring grid (j = 13, 24)

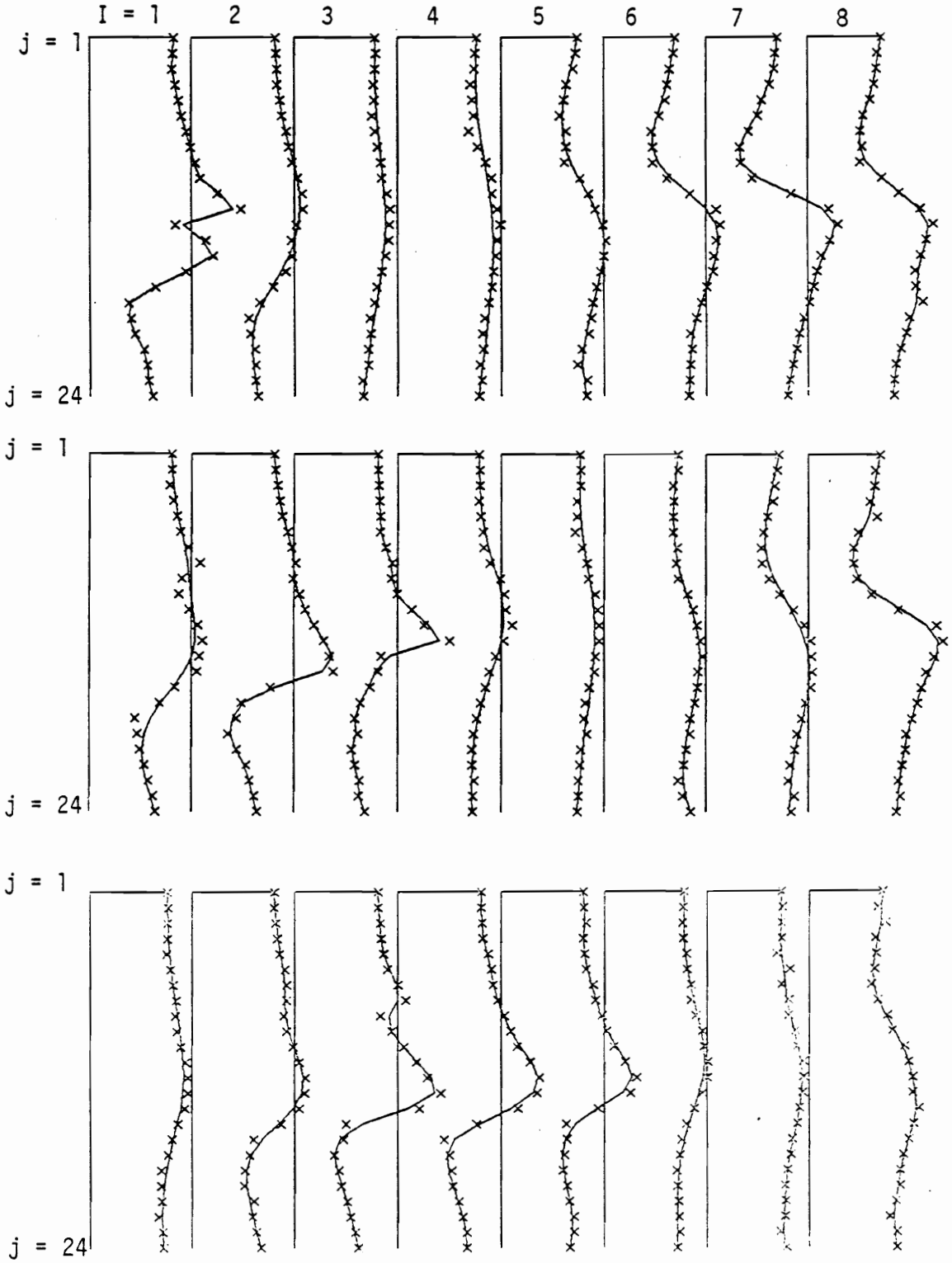

Fig. 3.3.4 Velocity profiles at t = t_1, t_2, t_3 (From top to bottom)

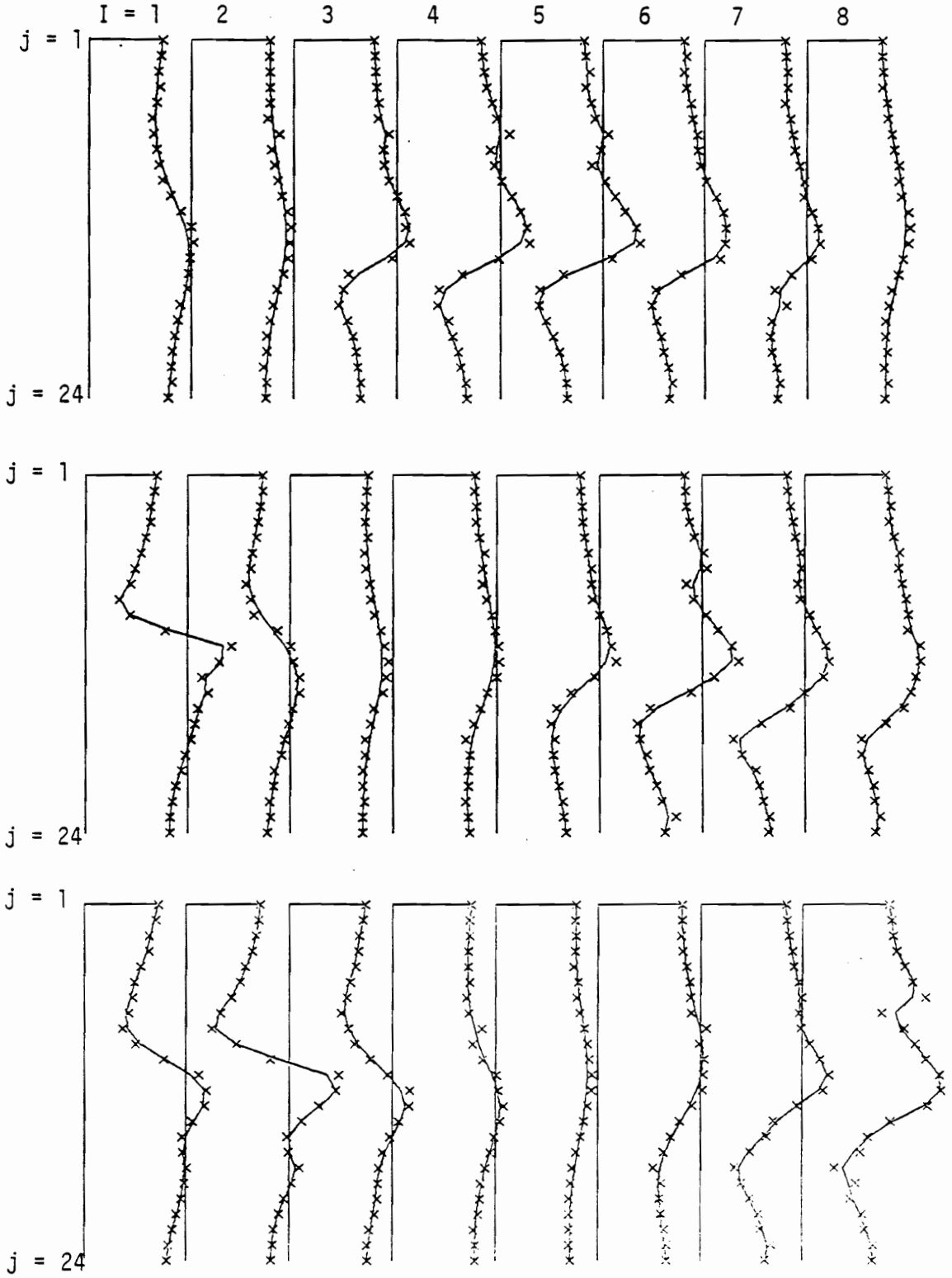

Fig. 3.3.5 Velocity profiles at t = t_4, t_5, t_6 (From top to bottom)

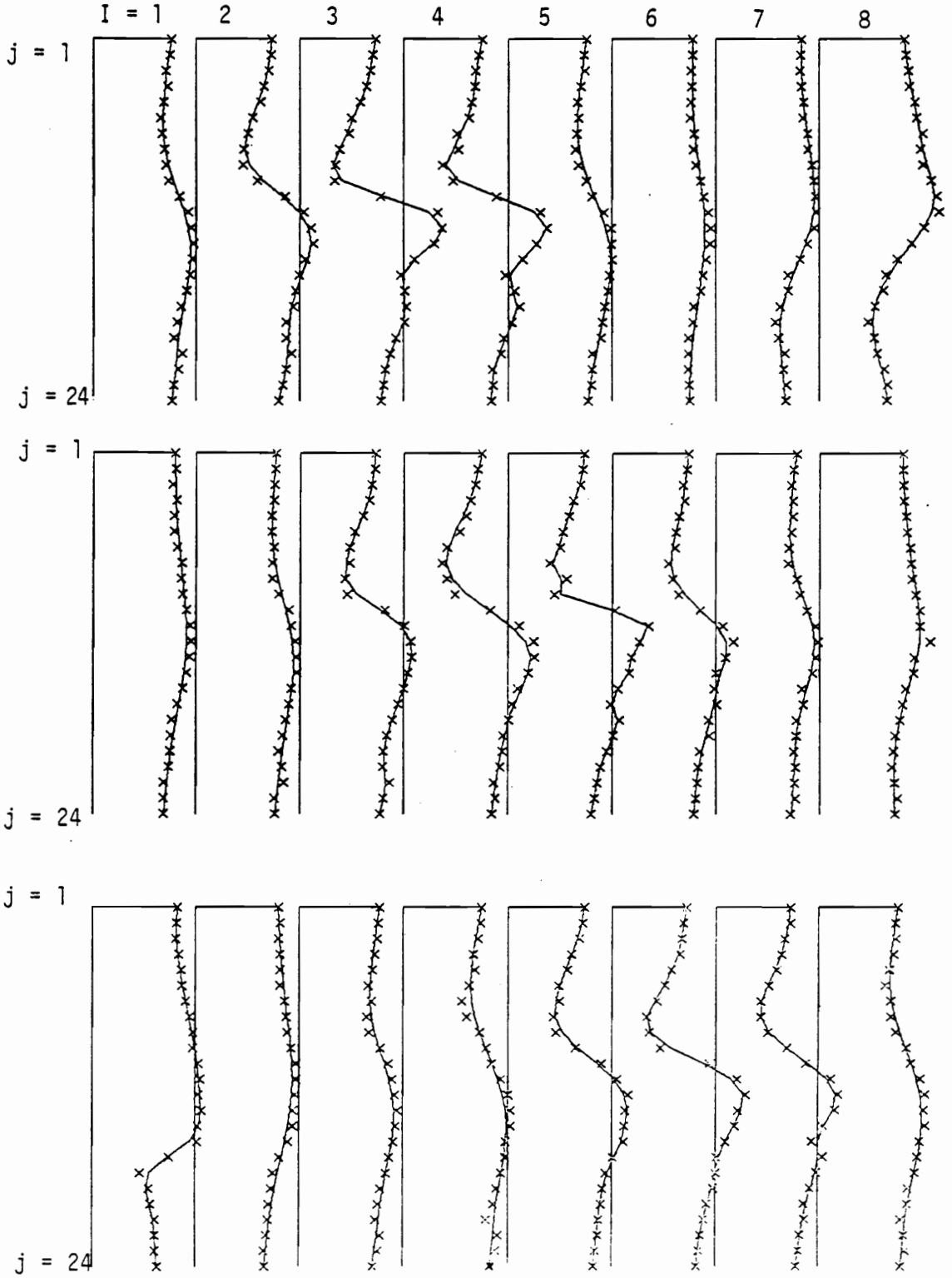

Fig. 3.3.6 Velocity profiles at t = t_7, t_8, t_9 (From top to bottom)

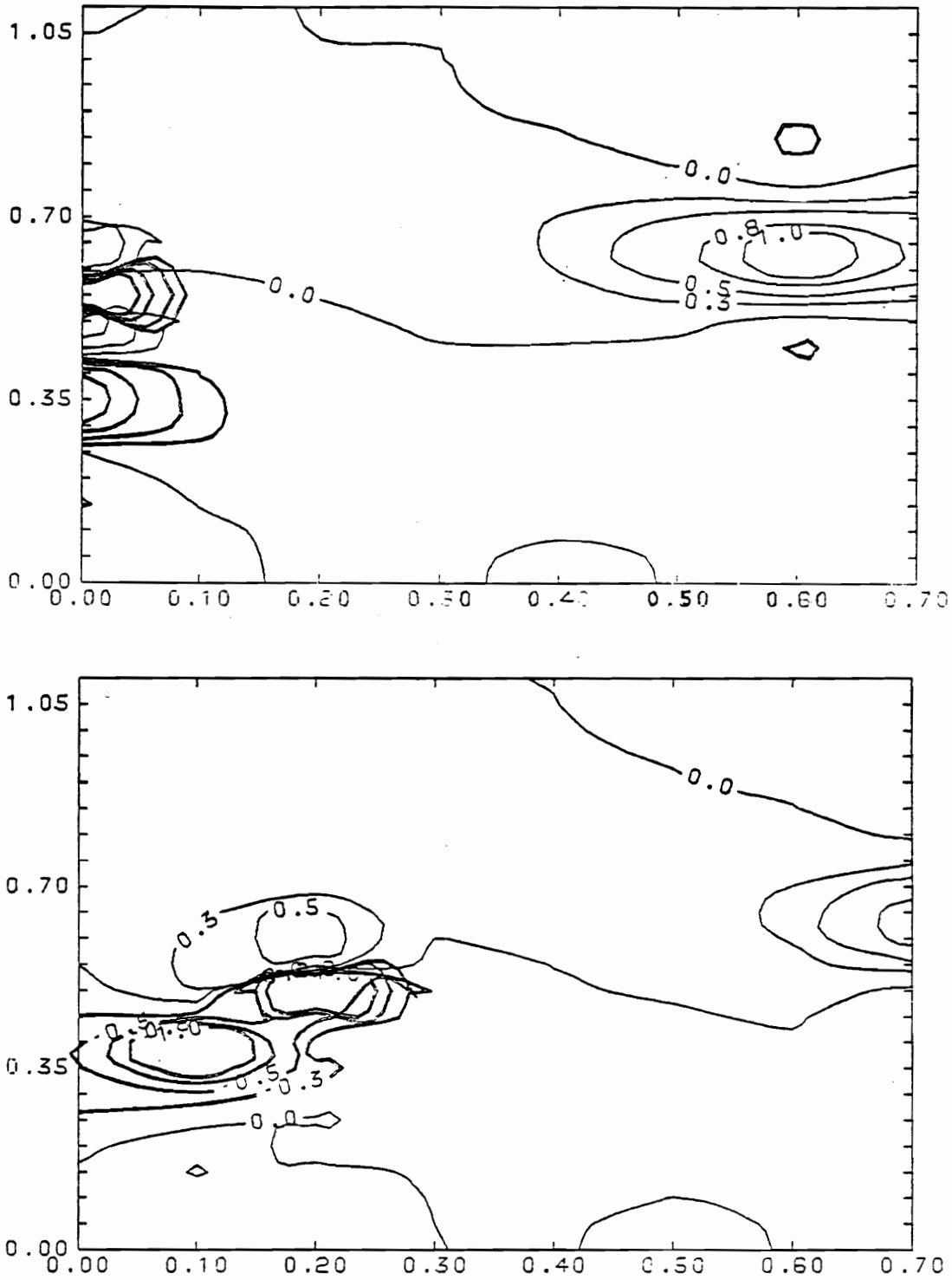

Fig. 3.3.7 Contours of $-du/dy$ at $t = t_1, t_2$ (From top to bottom). The horizontal and vertical scales are x/c, y/c respectively.

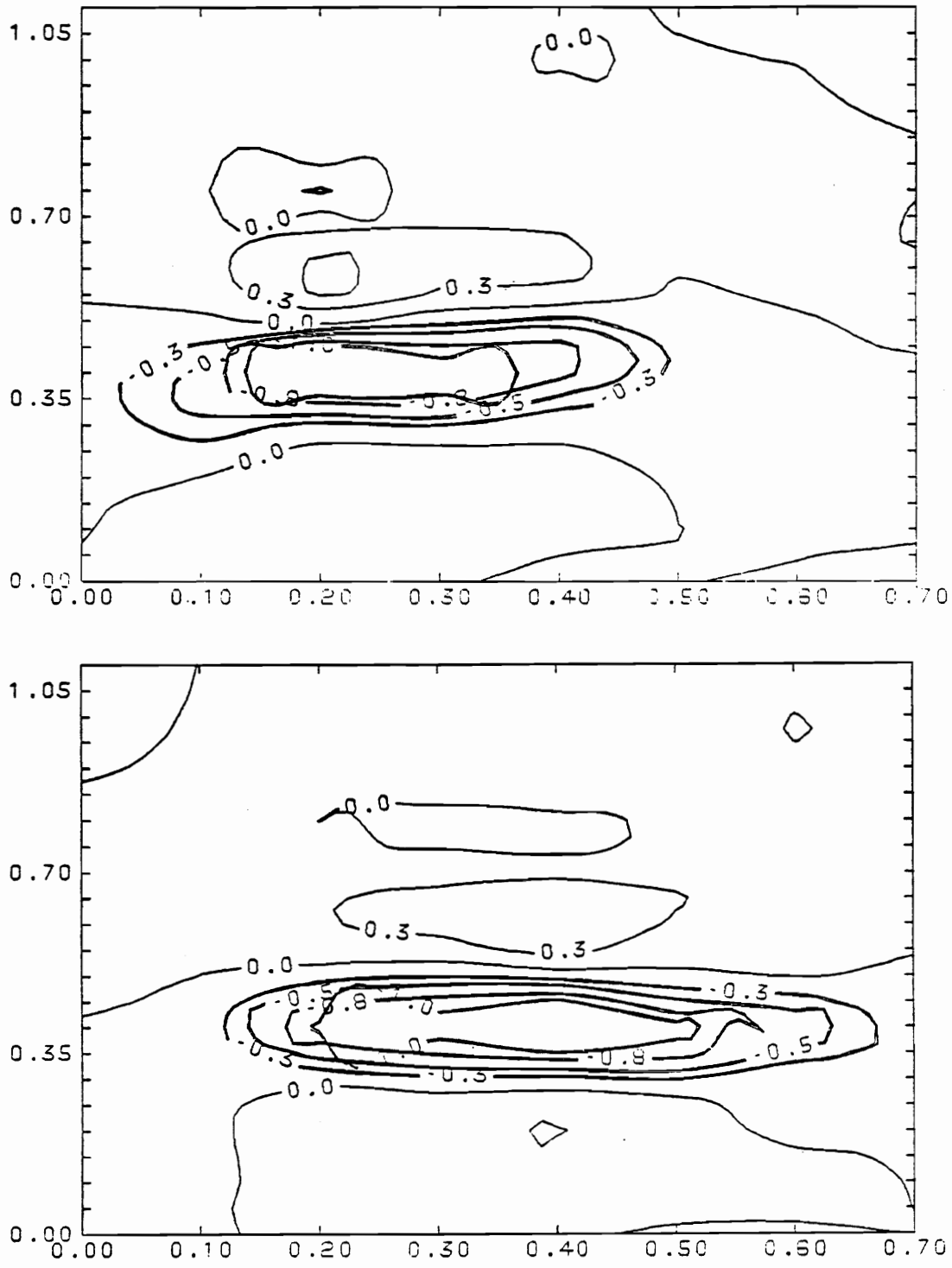

Fig. 3.3.8 Contours of $-du/_{dy}$ at $t = t_3, t_4$ (From top to bottom). The horizontal and vertical scales are x/c, y/c respectively.

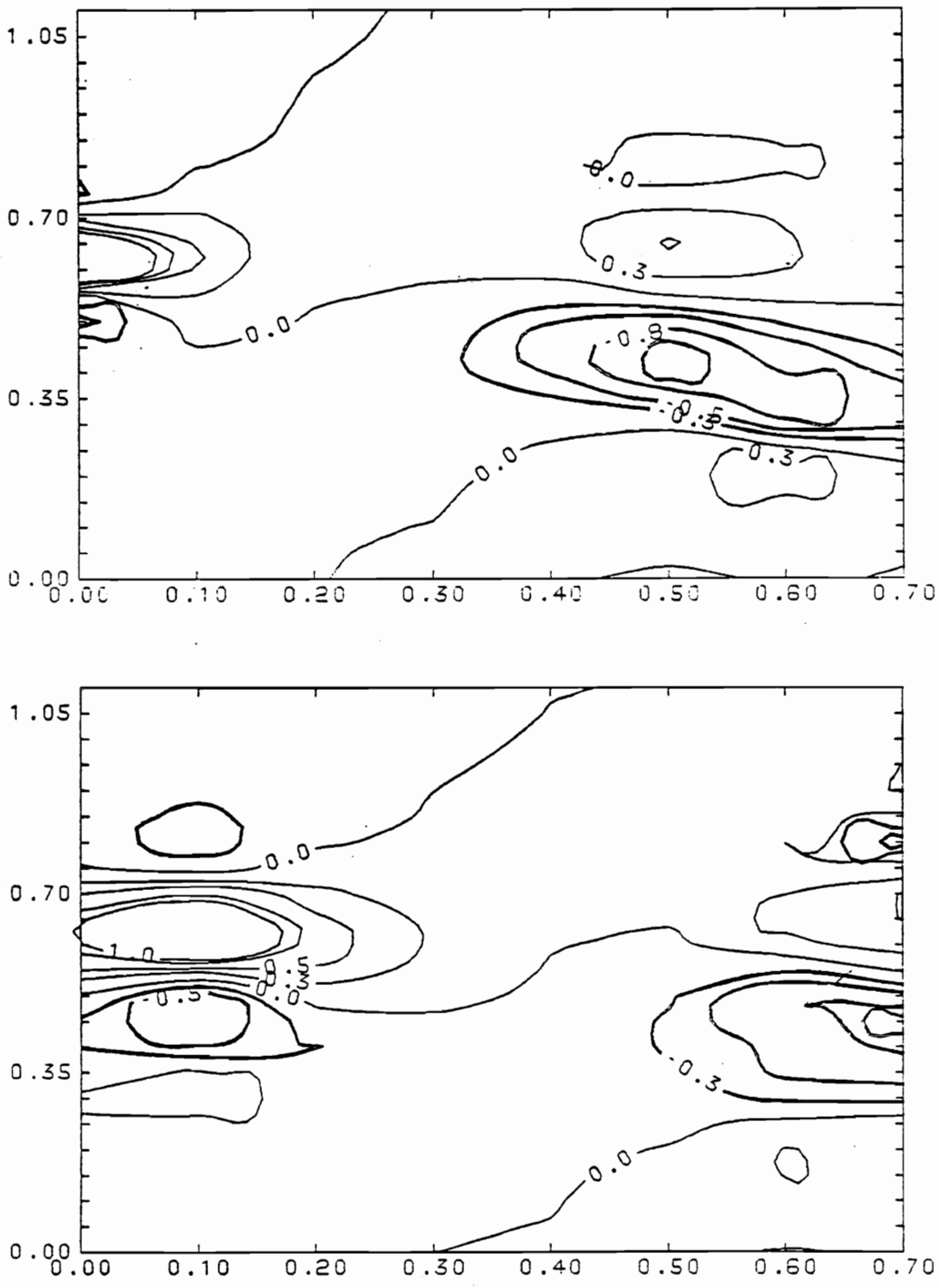

Fig. 3.3.9 Contours of $-du/dy$ at $t = t_5, t_6$ (From top to bottom). The horizontal and vertical scales are x/c, y/c respectively.

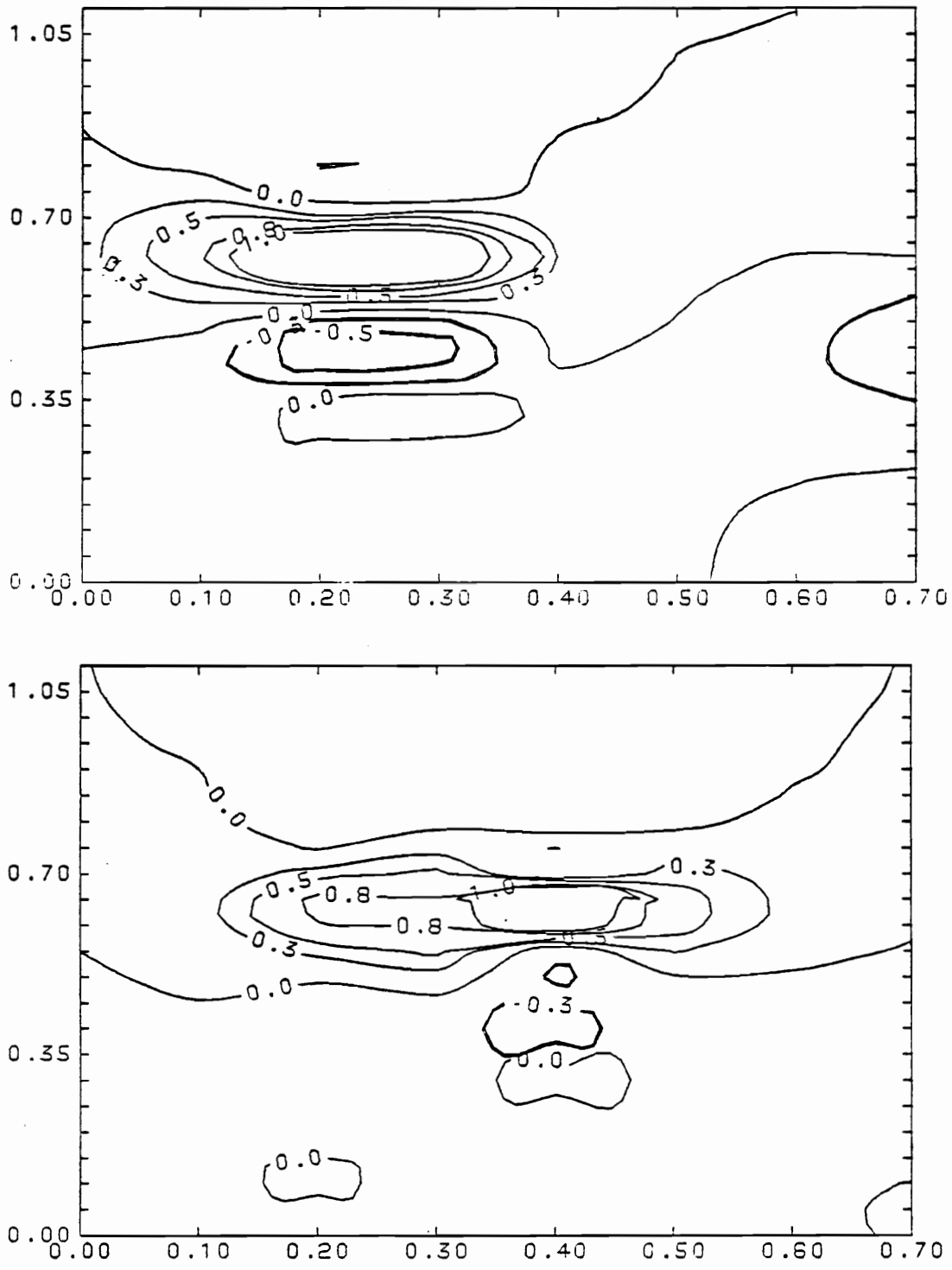

Fig. 3.3.10 Contours of $-du/_{dy}$ at $t = t_7, t_8$ (From top to bottom). The horizontal and vertical scales are x/c, y/c respectively.

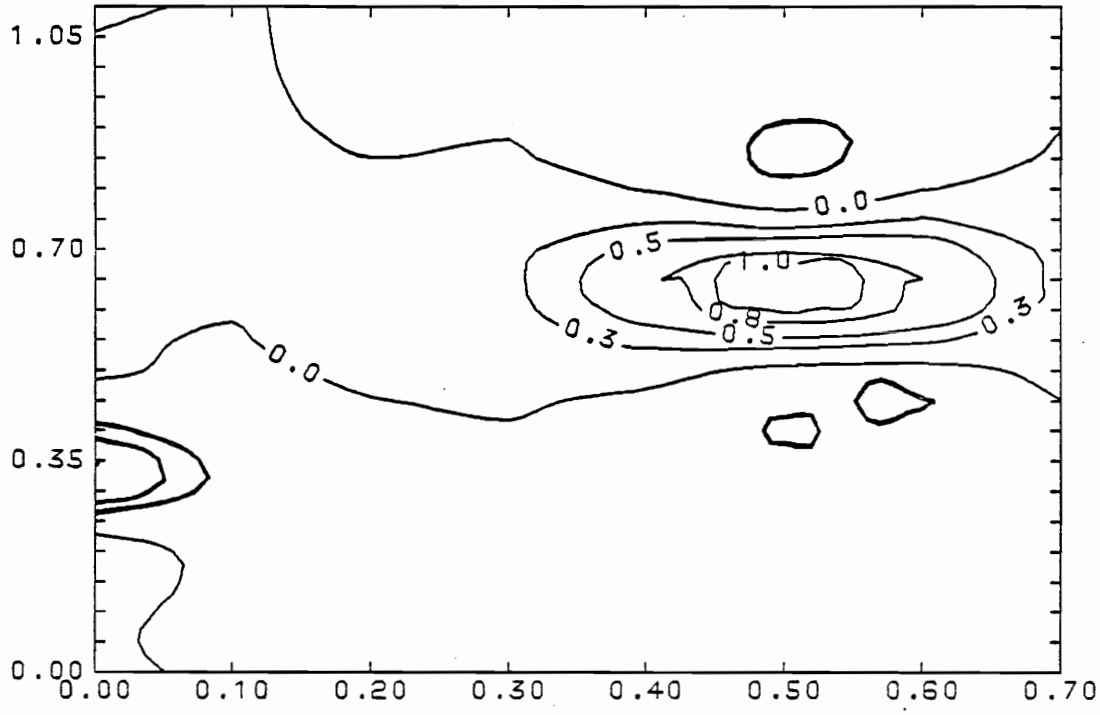

Fig. 3.3.11 Contours of $-du/_{dy}$ at $t = t_g$. The horizontal and vertical scales are x/c, y/c respectively.

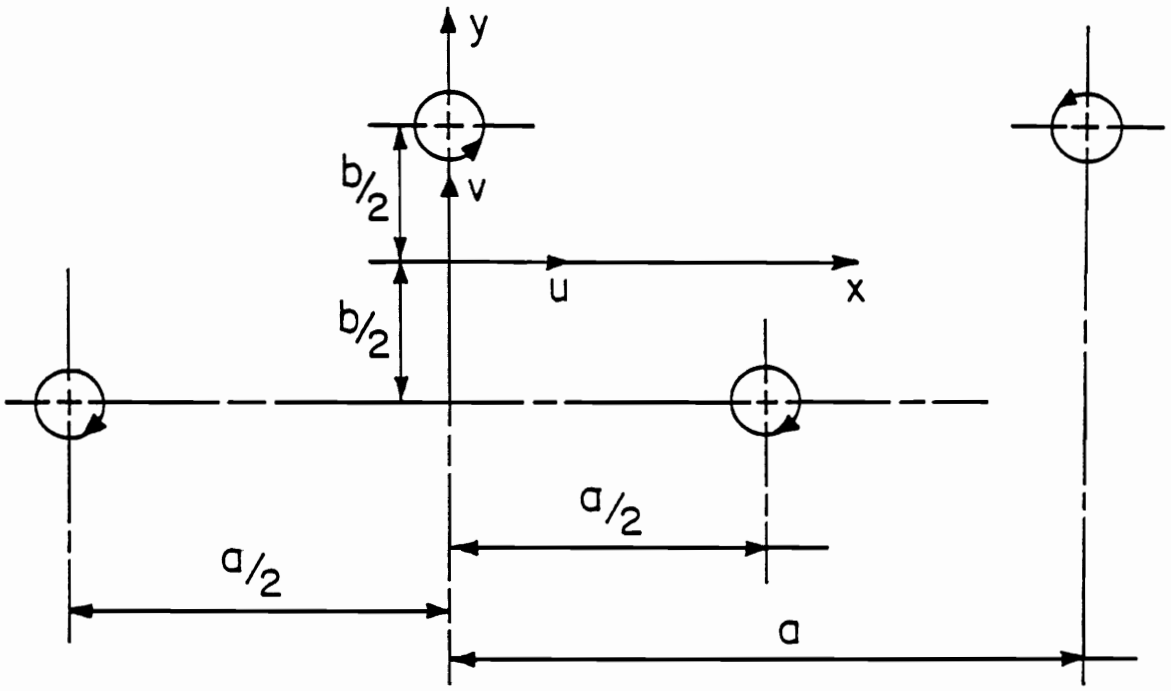

Fig. 3.3.12 Kármán Street

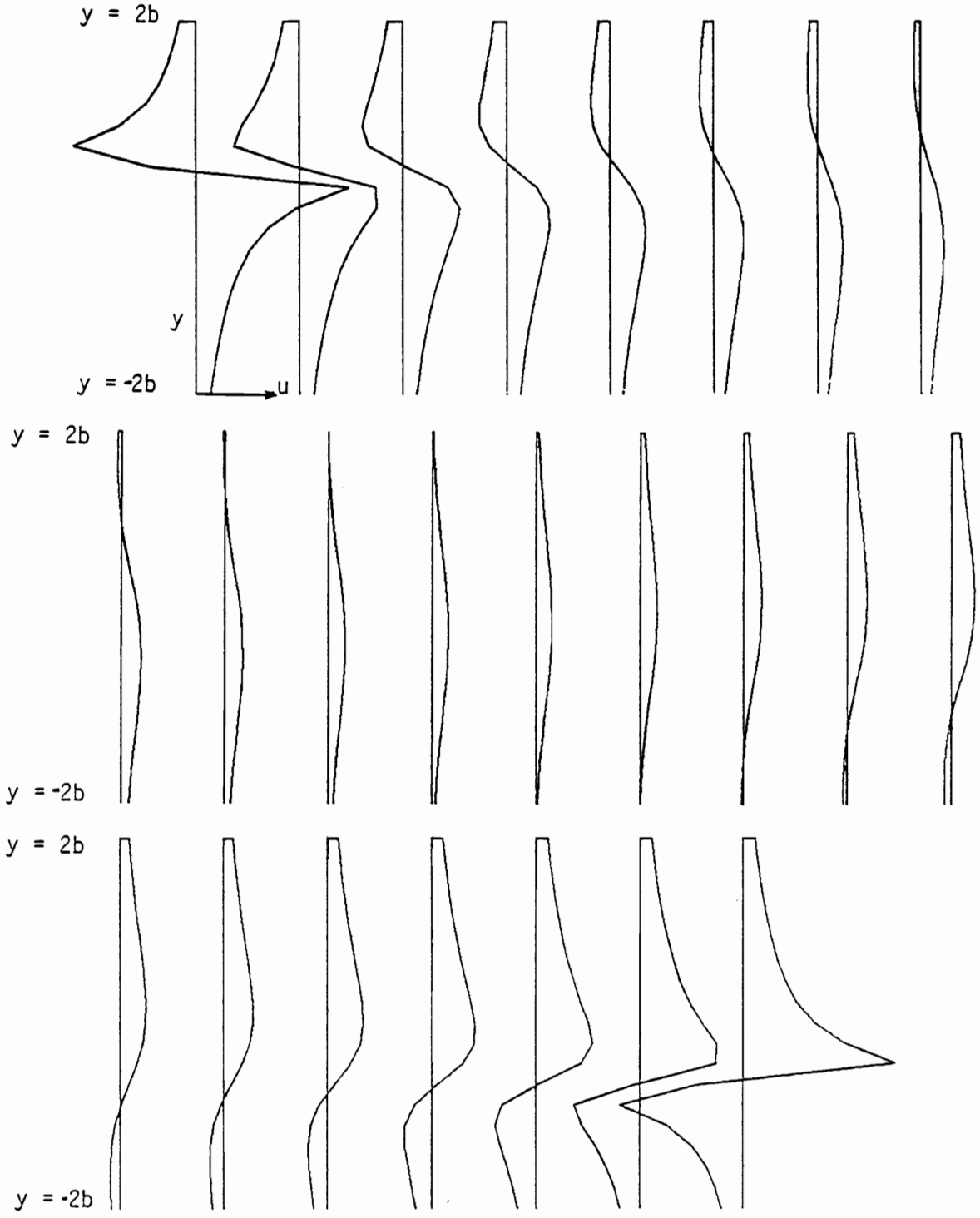

Fig. 3.3.13 Velocity profiles u(y), in the region between two ideal vortices of opposite sign.

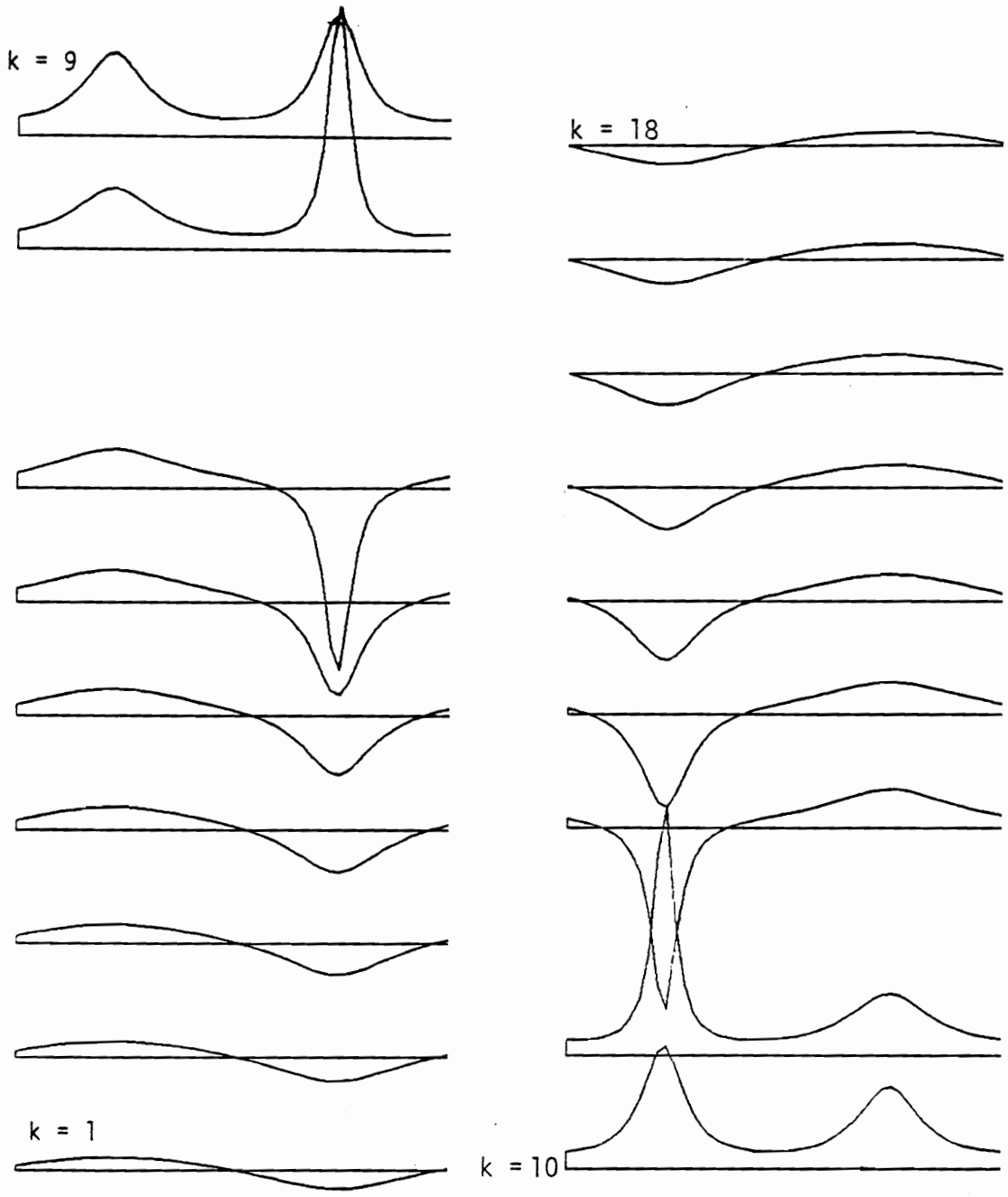

Fig. 3.3.14 Theoretical time records corresponding to station i = 3.

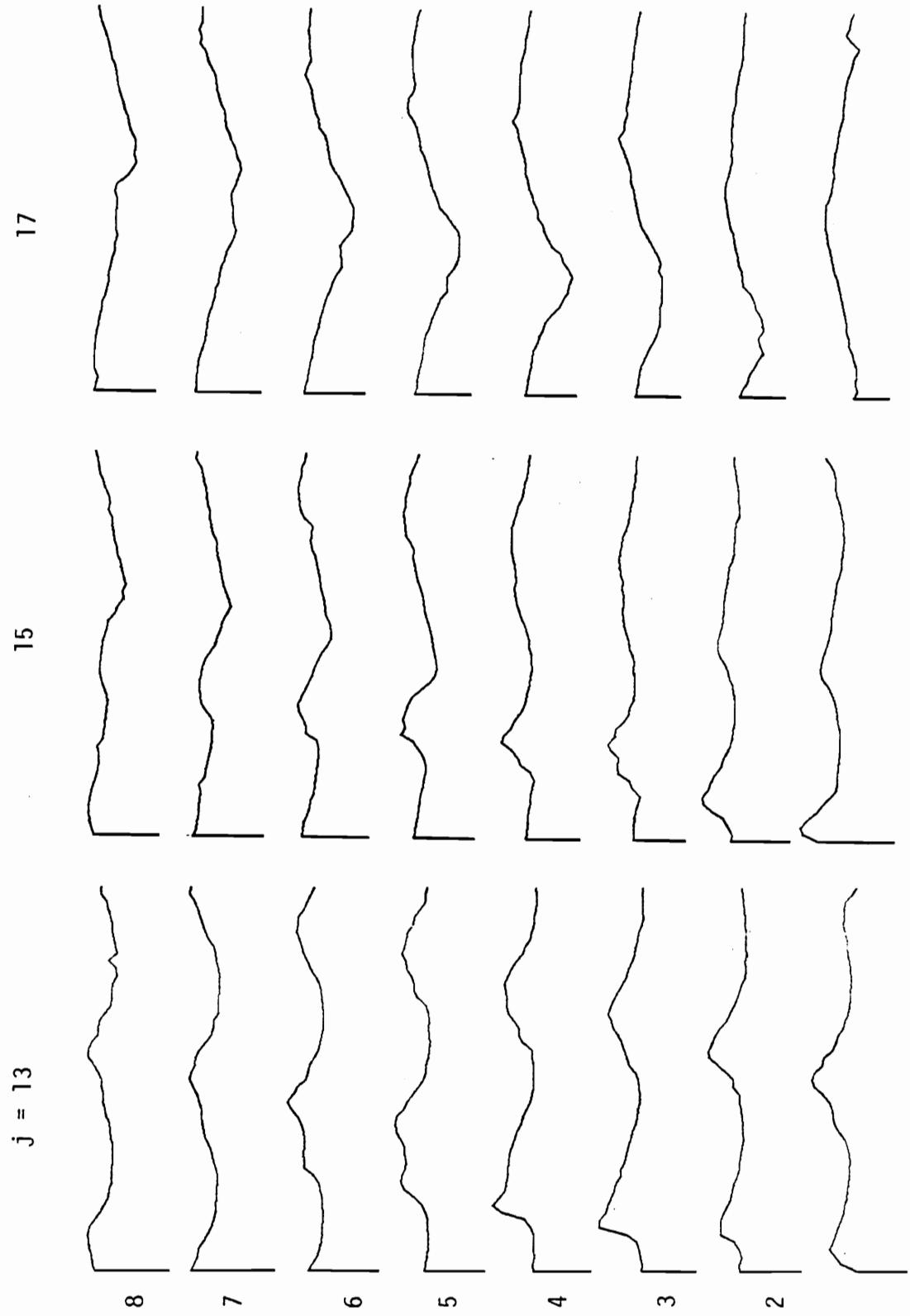

Fig. 3.3.15 Velocity time records at stations j = 13, 15, 17.

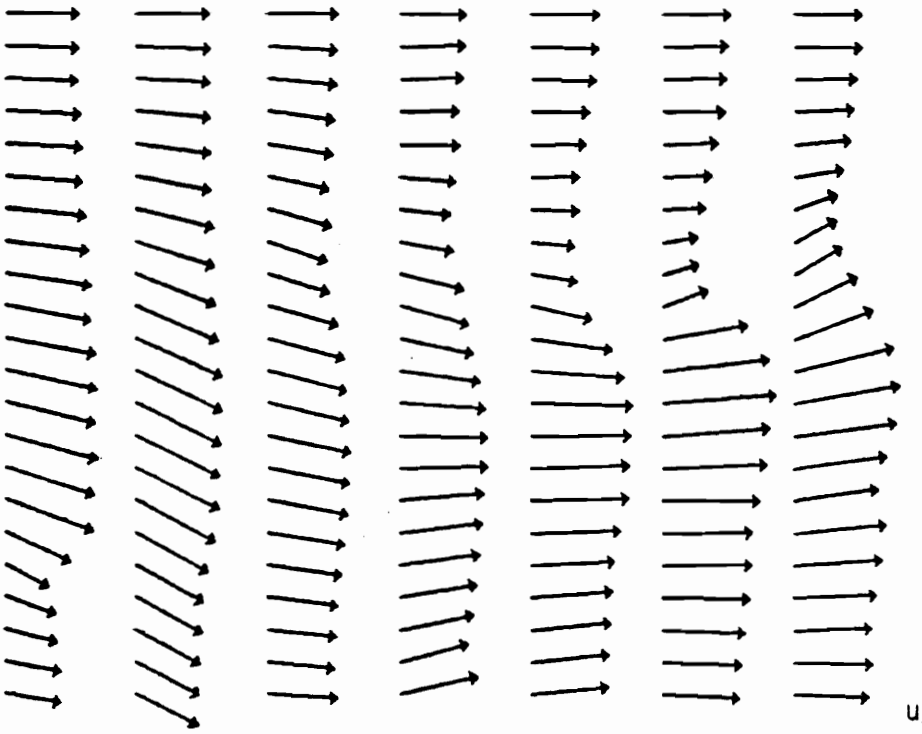

Fig. 3.3.16 Experimental velocity field at $t = t_g$.

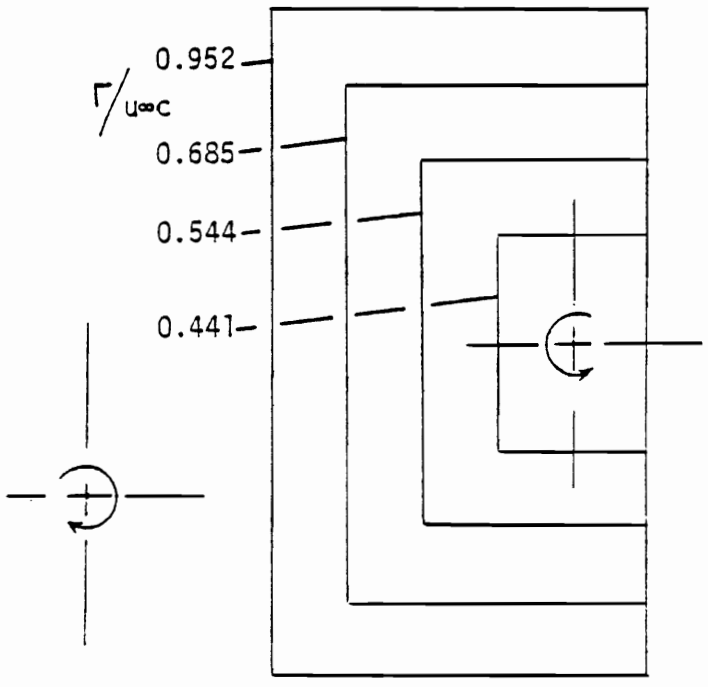

Fig. 3.3.17 Four different loops about an A.C.W. vortex. Scale 1:1.

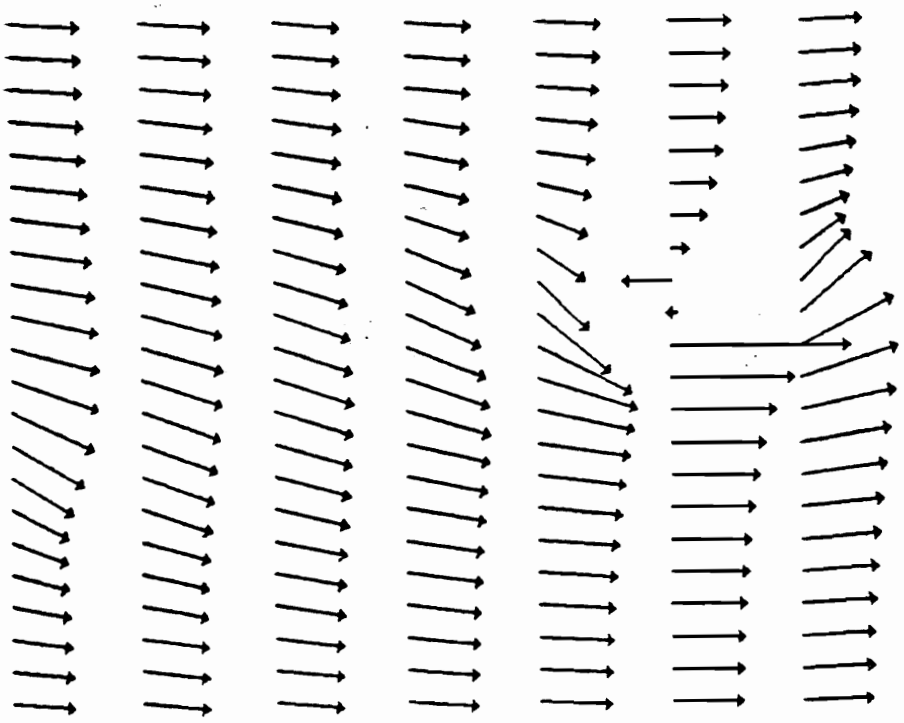

Fig. 3.3.18 Theoretical velocity field at $t = t_g$.

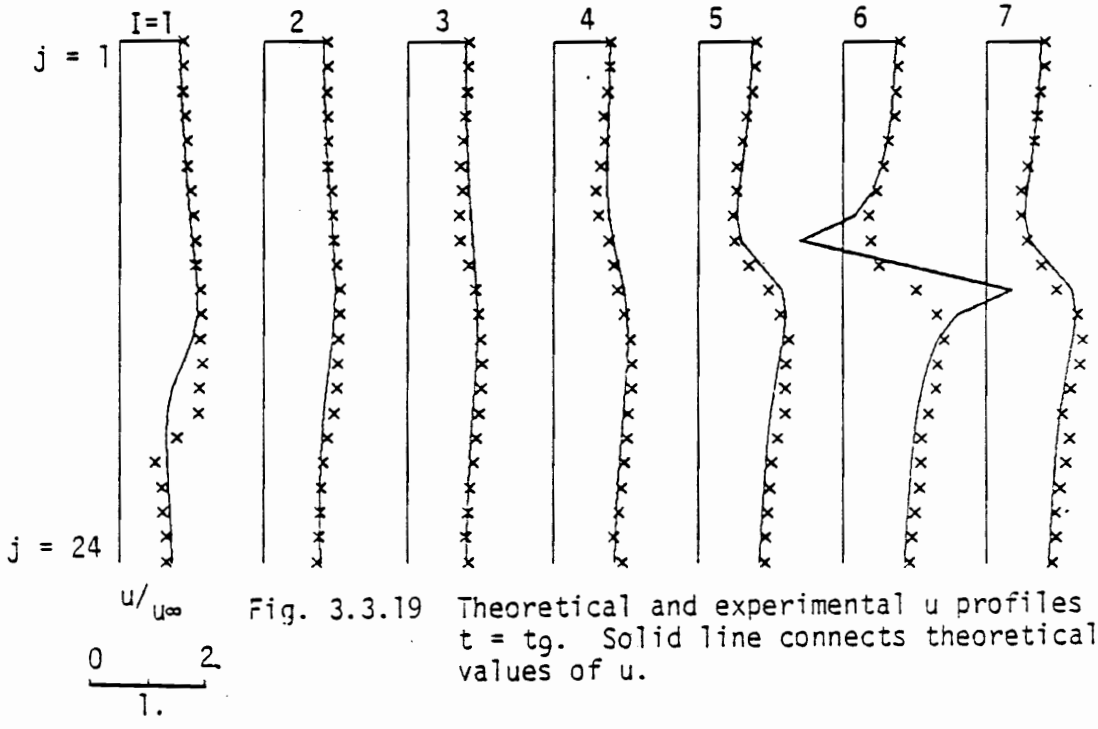

Fig. 3.3.19 Theoretical and experimental u profiles at $t = t_g$. Solid line connects theoretical values of u.

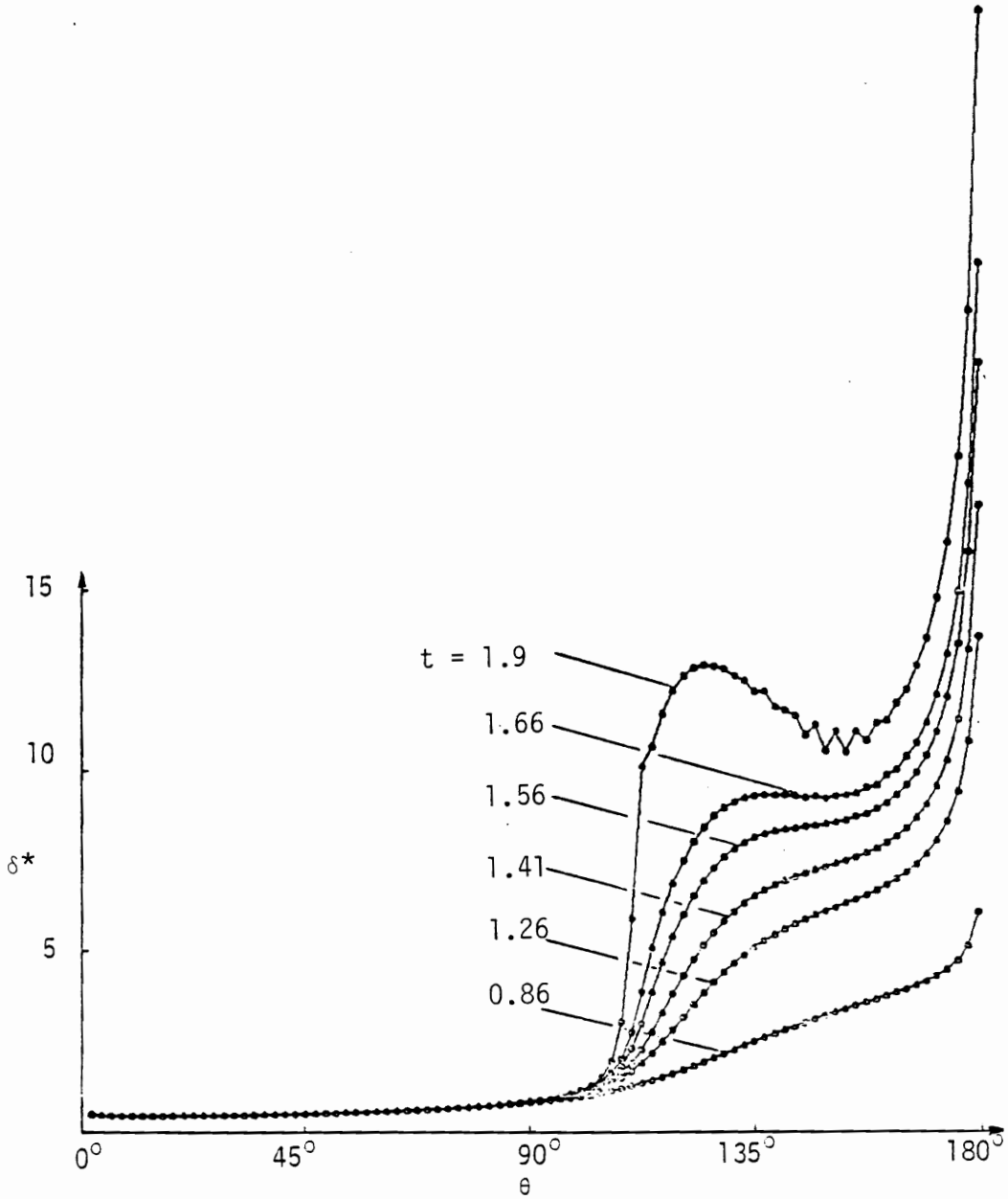

Fig. 4.3.1 Displacement thickness over a circular cylinder at various time instants.

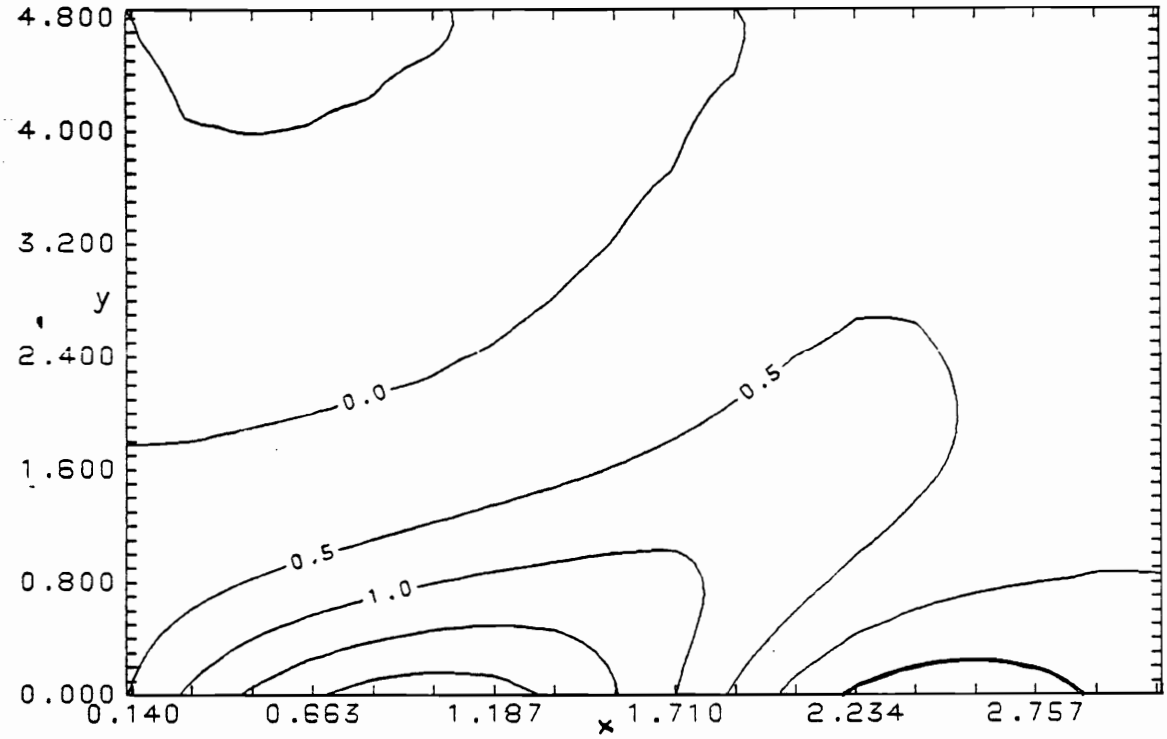

Fig. 4.3.2 Vorticity controus at t = 0.86

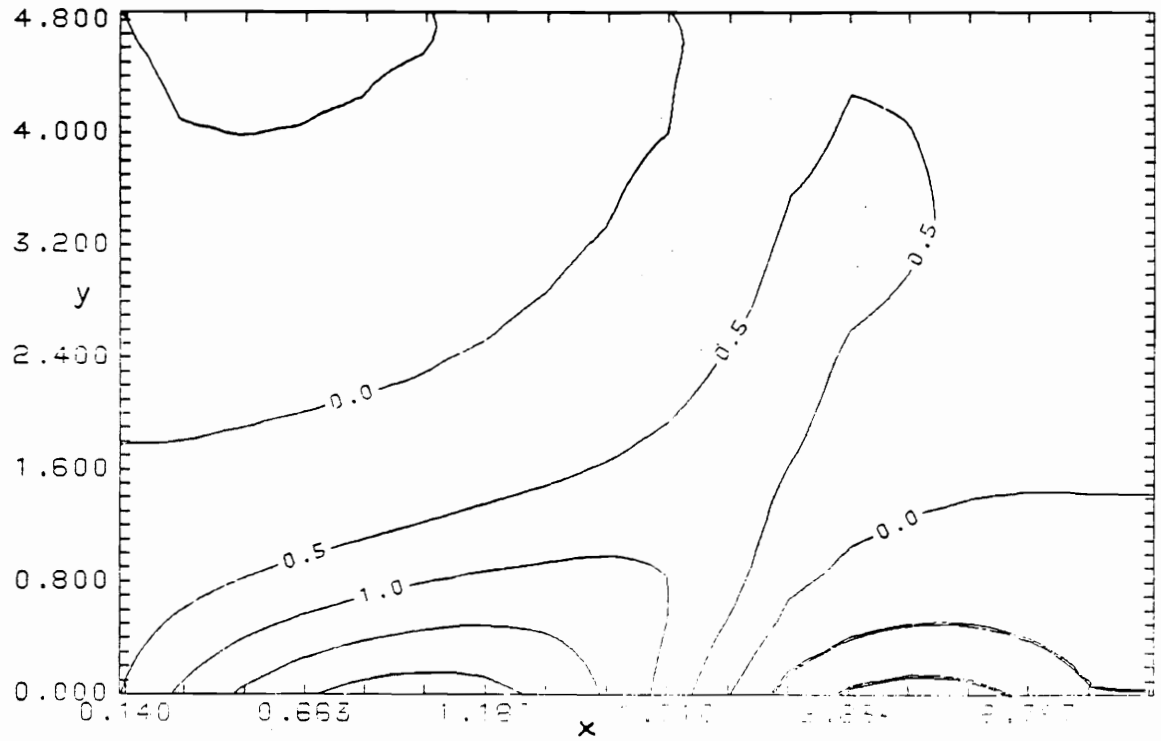

Fig. 4.3.3 Vorticity controus at t = 1.26

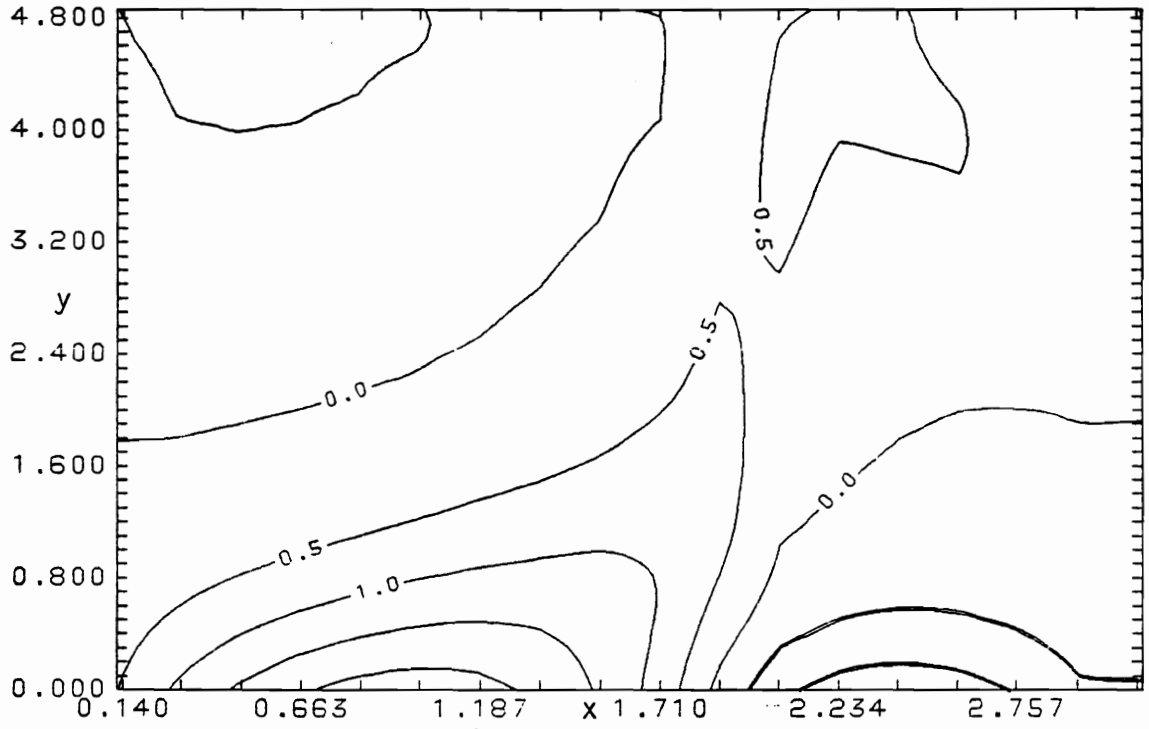

Fig. 4.3.4 Vorticity controus at t= 1.46

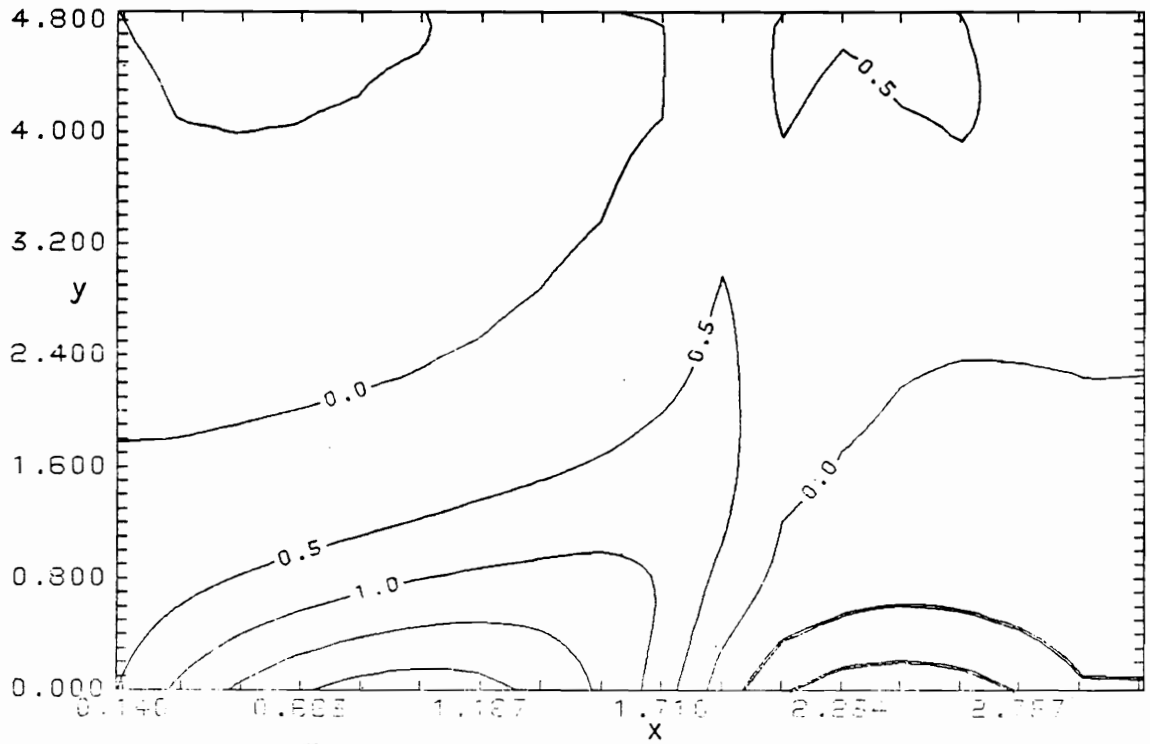

Fig. 4.3.5 Vorticity controus at t = 1.56

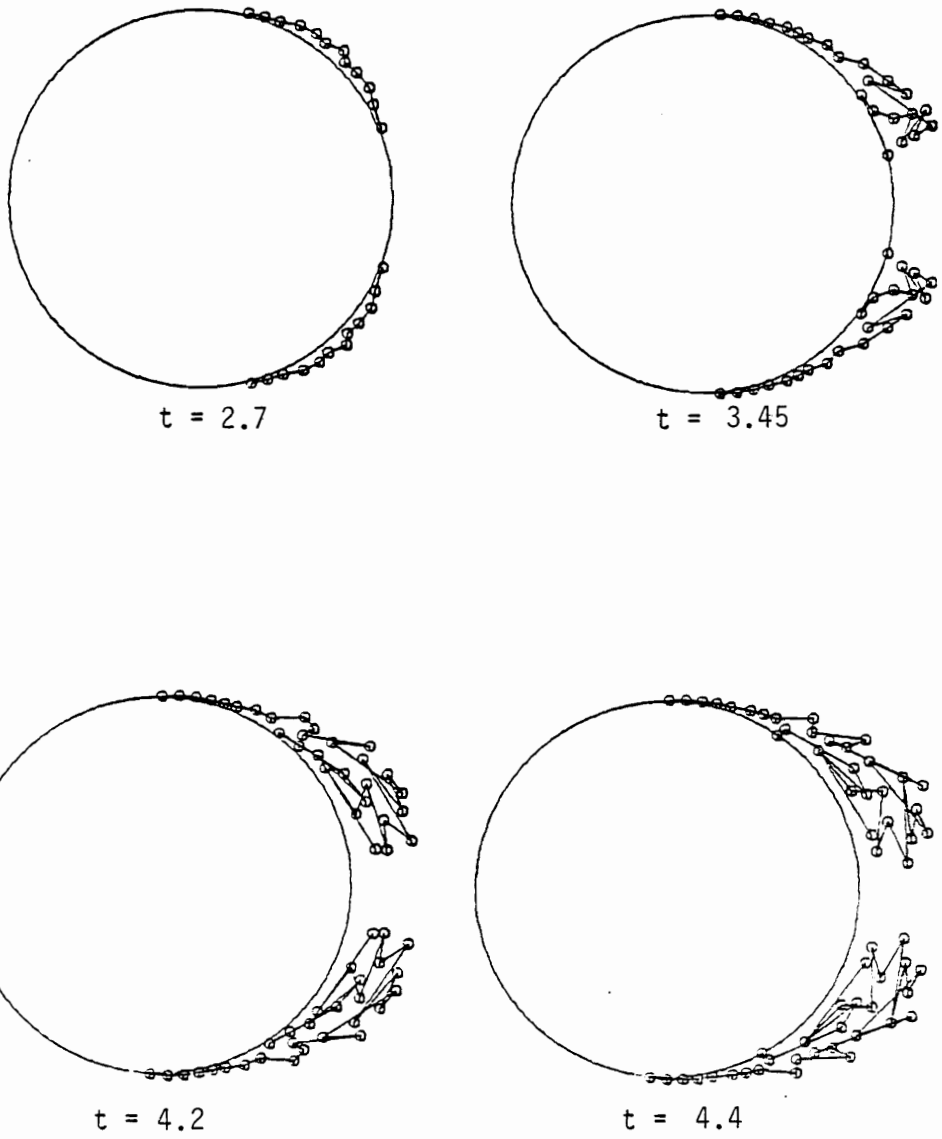

Fig. 4.4.2 Time development of cylinder's free shear layer

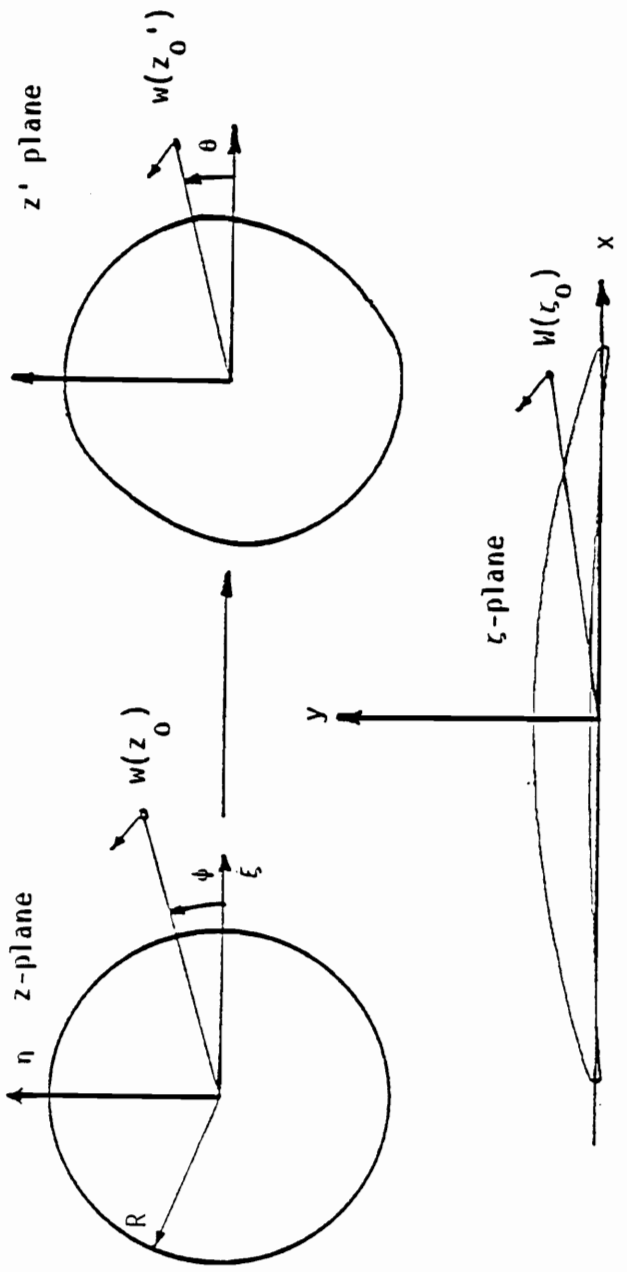

Fig.5.2.1 Conformal mapping.

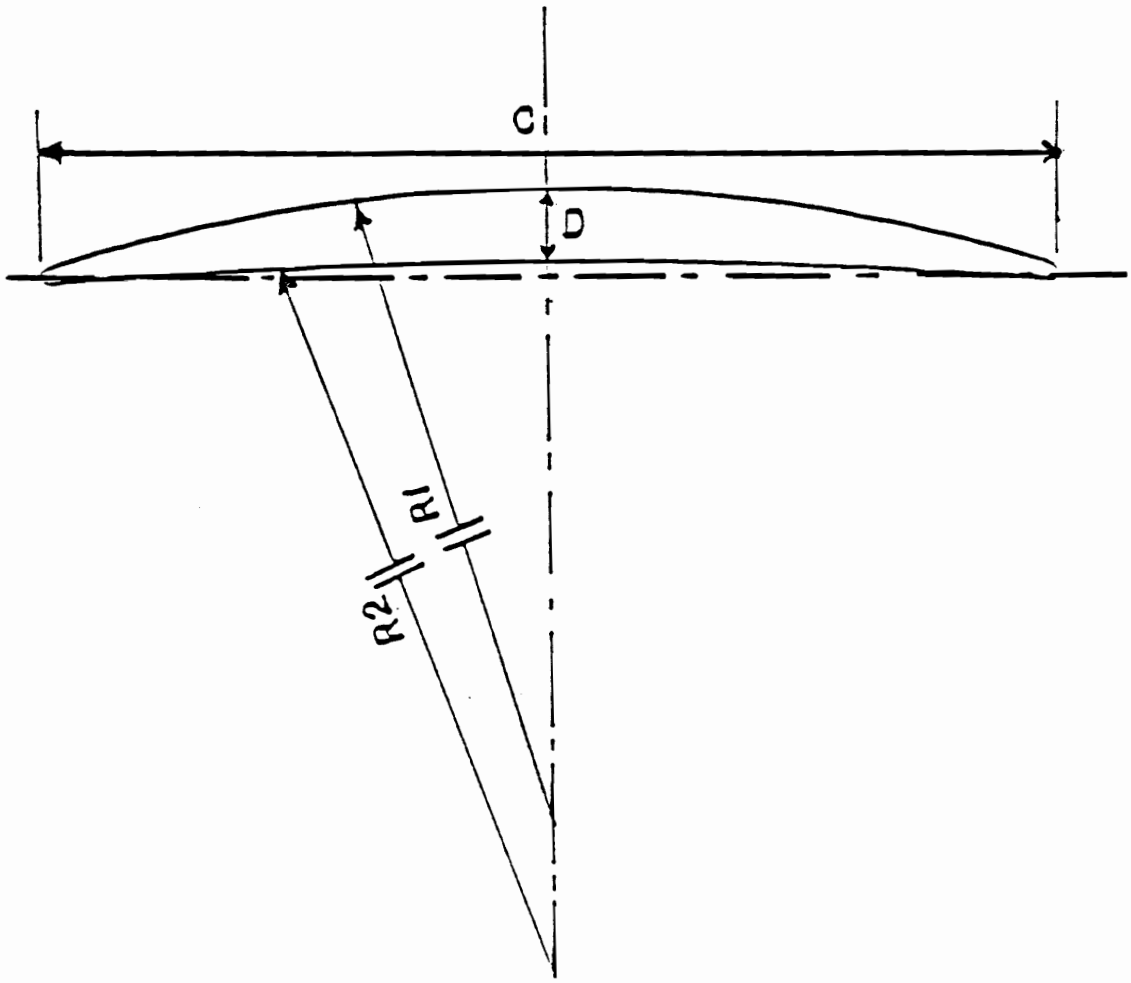

R_1 = 103.61 mm

R_2 = 361.06 mm

C = 65.53 mm

D = 5 mm

Fig. 5.2.2 Cross section of compressor blade.

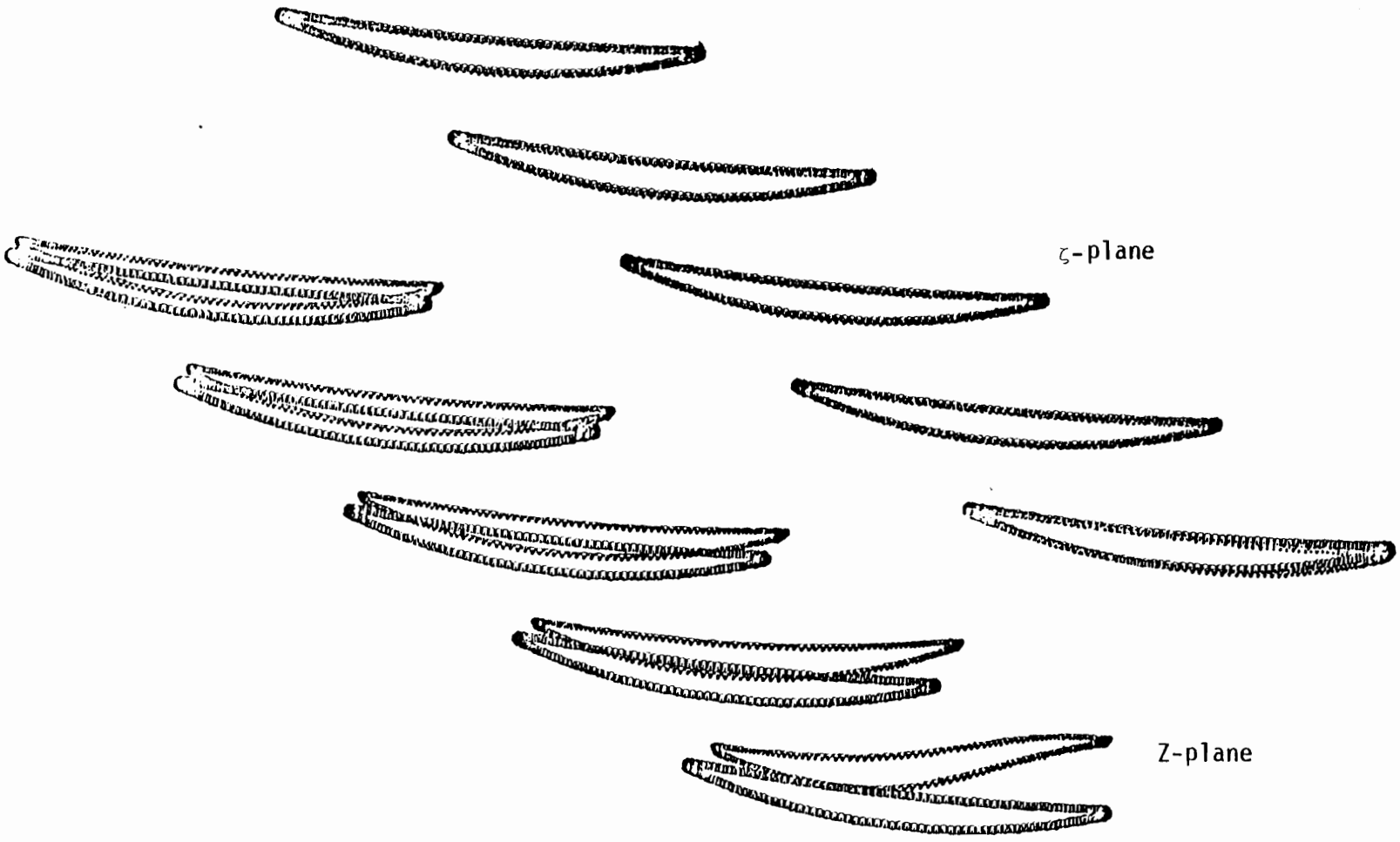

Fig. 5.2.3 The approximate blade row in ζ-plane as well as their images in Z-plane are represented by the symbol Δ, while the exact blade row by ʘ.

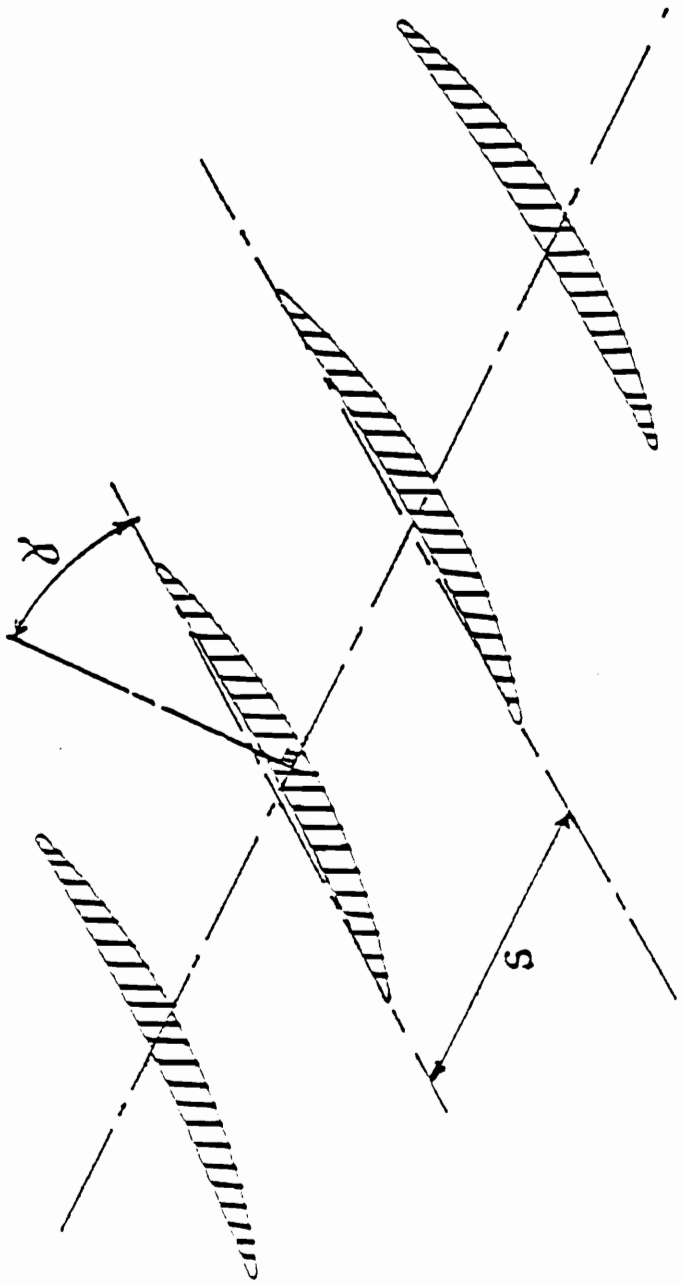

Fig. 5.3.1 Cascade notation

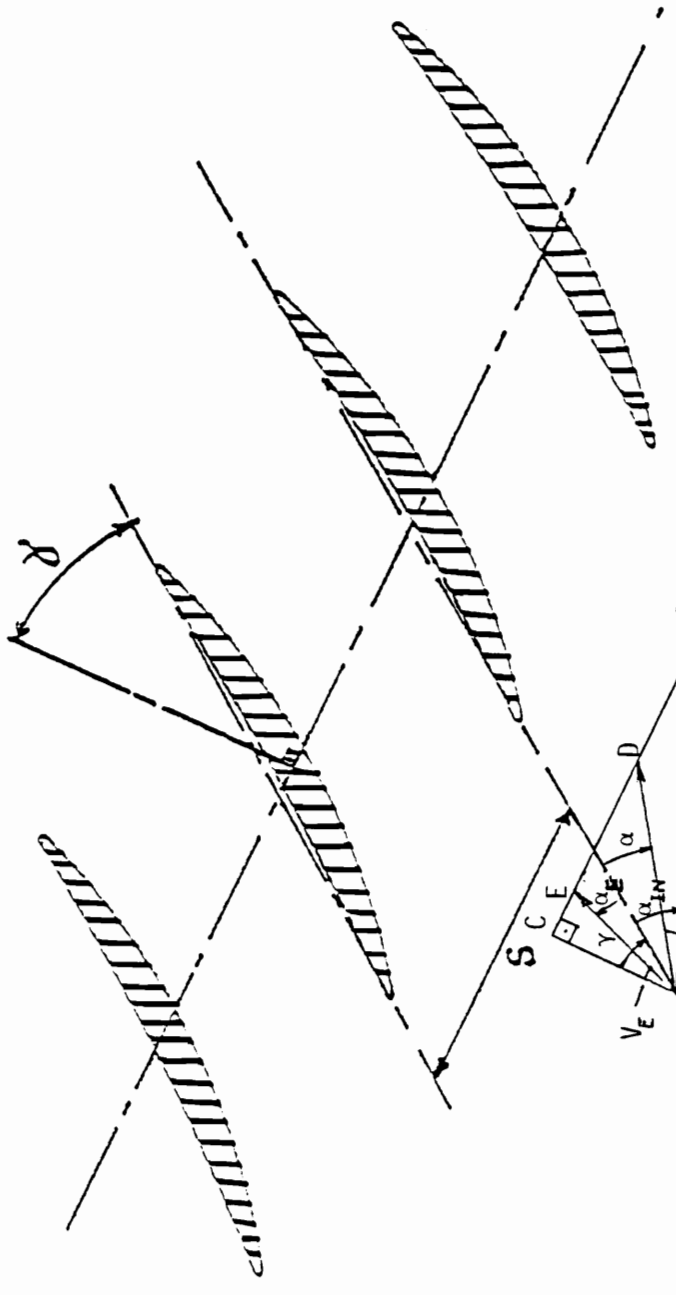

Fig. 5.3.2 Inlet, exit and average flow vectors V_{1N}, V_E, U_∞ respectively.

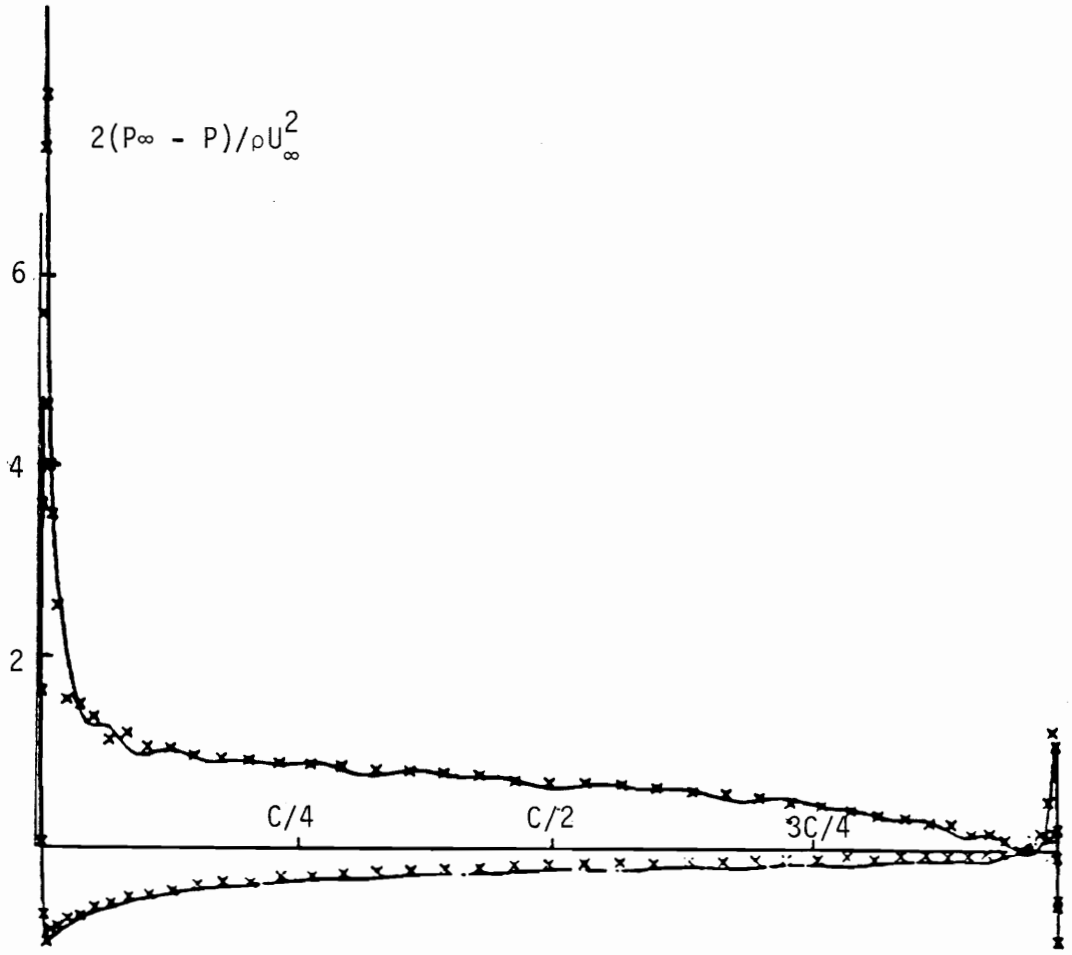

Fig. 5.3.3 The pressure coefficient for a mean angle of attack $\alpha = 8.41°$, an inlet angle $\alpha_{in} = 25°$ and stagger angle $\phi = 0$. x, Yokum (1981); ___, present method.

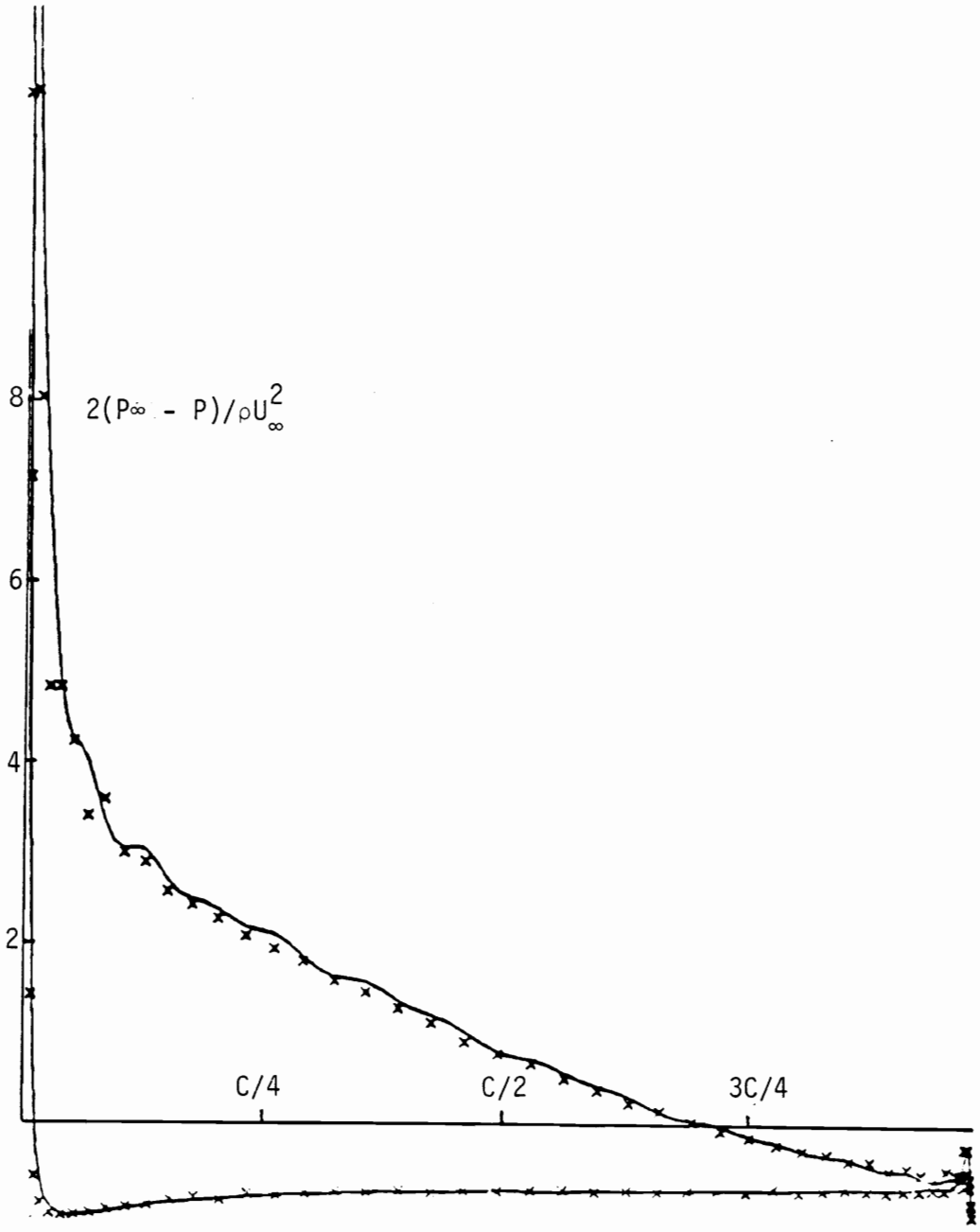

Fig. 5.3.4 The pressure coefficient for a mean angle of attack $\alpha = 17.54°$, an inlet angle $\alpha_{in} = 25°$ and a stagger angle $\phi = -50°$. x, Yokum (1981); __, present method.

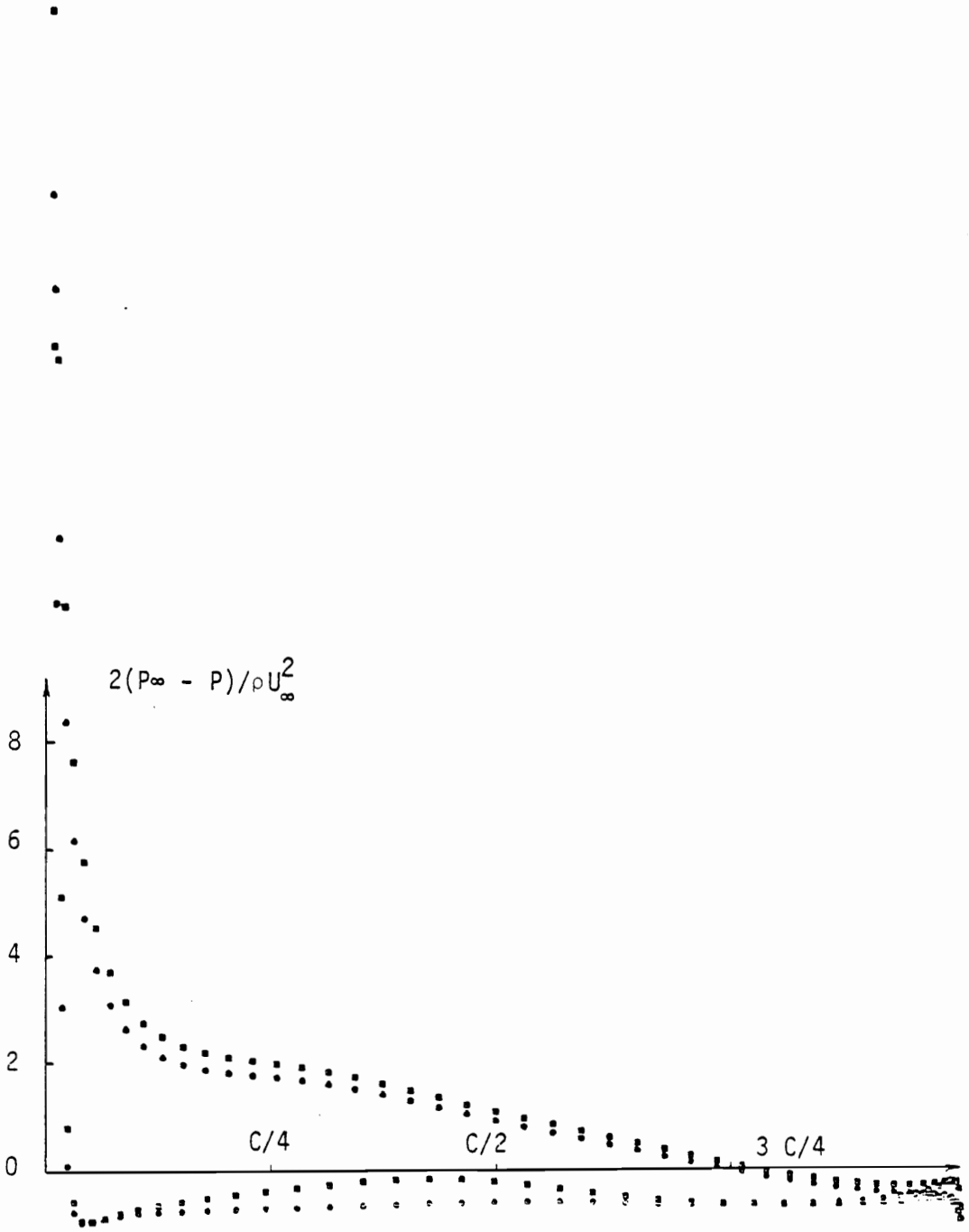

Fig. 5.5.1 Pressure distribution over adjacent blade (k = 1)
⊙ ; t = 0.6, ⊡ t = 6.

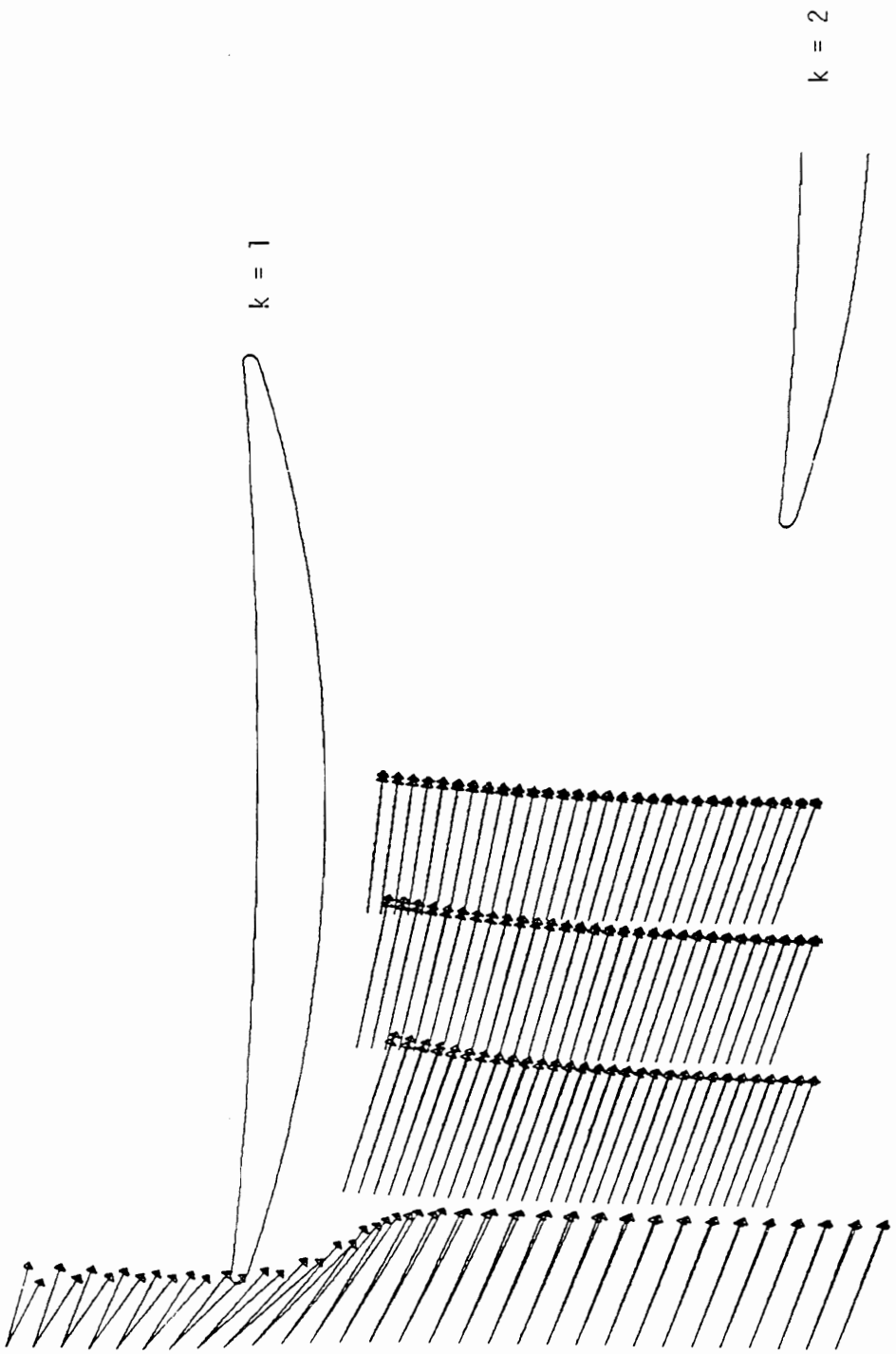

Fig. 5.5.2 Velocity field about adjacent blade (k = 1), at t = 6.

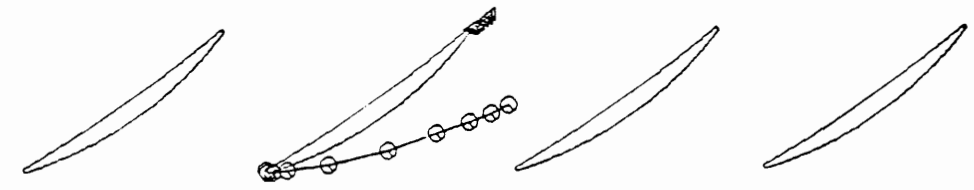

t = 3.

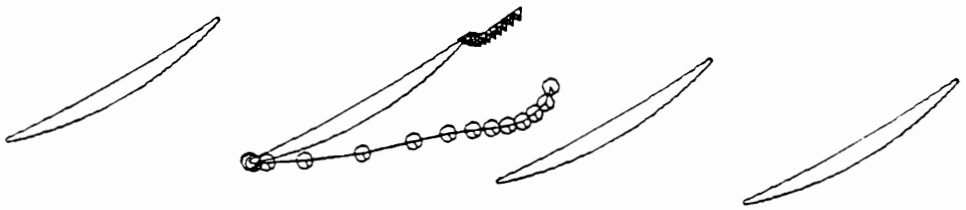

t = 4.5

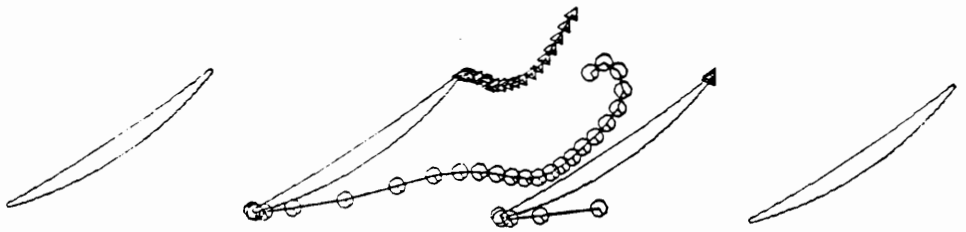

t = 7.5

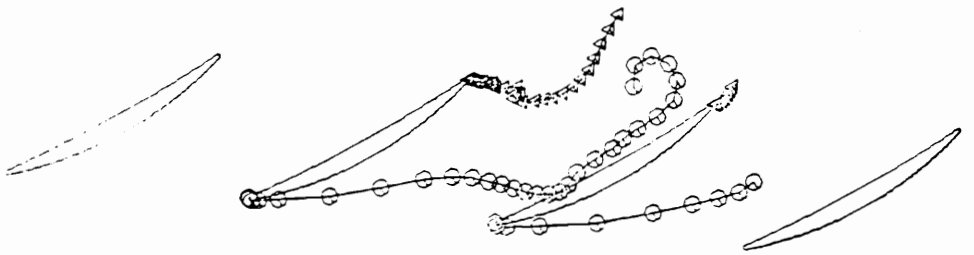

t = 9.

Fig. 5.5.3 Wake development downstream of blades k = 0, k = 1, at t = 3, 4.5, 7.5, 9.

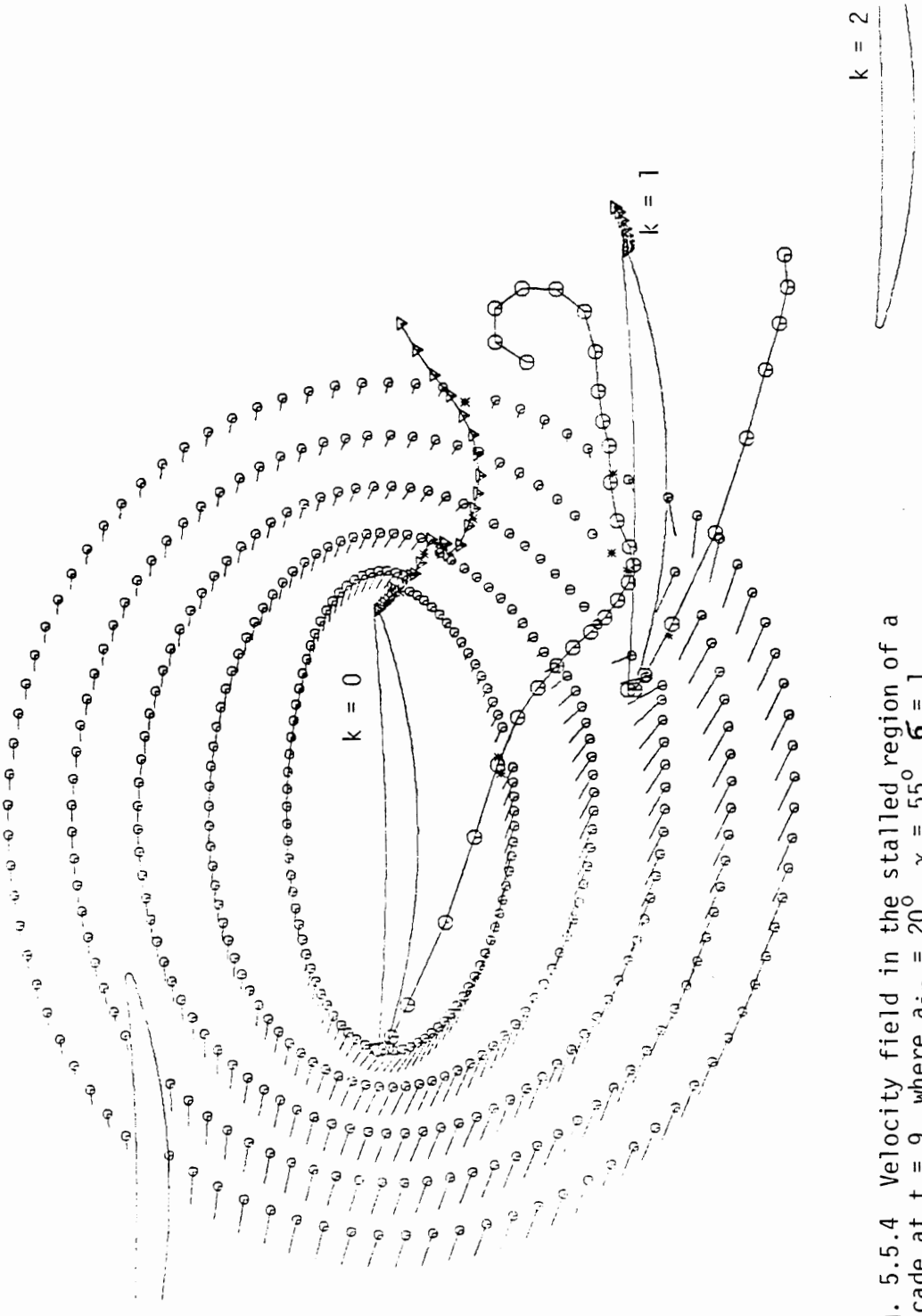

Fig. 5.5.4 Velocity field in the stalled region of a cascade at t = 9, where $a_{in} = 20^{o}$, $\gamma = 55^{o}$, $\bar{\sigma} = 1$.

Table 2.2.1

driving RPM	Valve B Closed f_0 (kHz)	RMS* (mV)	TU* (%)	ΔU/U (%)	Valve B at 2 f_0 (kHz)	RMS (mV)	TU (%)	ΔU/U (%)	Valve B at 4 f_0 (kHz)	RMS (mV)	TU (%)	ΔU/U (%)	Valve B Open f_0 (kHz)	RMS (mV)	TU (%)	ΔU/U (%)
4	96	35	0.54	18.75	80.25			16.87	52.5	18	0.52	14.28	45.3	15	0.49	11.58
9	96.4	35	0.54	8.56	80.10	26	0.48	8.2	52	19	0.54	5.7	50	17	0.55	5.5
15	92	32	0.50	4.7	79.8	25	0.44	5.6	52.65	20	0.57	5.7	48	15	0.5	5

Table 2.2.1 Amplitude Response with Turbulence Manipulators

* The filters were allowing only frequencies in the bandwidth 1 ± 300 Hz, so that the driving frequencies as well as high frequencies were filtered.

Table 2.2.2

Speed of Pump	By Pass Closed fo (kHz)	RMS (mV)	TU (%)	By Pass at 2 fo (kHz)	RMS (mV)	TU %	By Pass at 4 fo (kHz)	RMS (mV)	TU (%)	By Pass Open fo (kHz)	RMS (mV)	TU (%)
0.5	107	12	0.16[a]	94	25	0.39	64	35	0.82	55	30	0.81
0.5*	115	6	0.07	104	12	0.17	70	40	0.85	60	35	0.87
1	145	17	0.62	122	17	0.69	83	80	1.44	72	48	1
2	220	30	0.68	180	25	0.69	130	25	0.96	115	20	0.26[c]
3	290	40	0.68	255	38	0.76	180	35	1.028	160		
4	350	8[d]	0.11[e]	290	35	0.6	212	50	1.17	195	55	1.41
4*	360	7	0.09	310	20	0.32	230	50	1.08	210	60	1.42
5	420	15	0.53	360	7	0.09	260	50	0.96	225	60	1.33
5*	410	2[f]	0.015[g]	350	9	0.12	250	60	1.2	230	60	1.30

Table 2.2.2: The effect of the bypass system and the tunnel speed on the turbulence level. The speed of the tunnel is represented by the speed of the driving pump in control system values which correspond here roughly to speeds of up to 1.6m/sec. In the vertical columns f_U is the mean Doppler frequency, RMS is the root mean square of the signal and TU is the turbulence level. The by-pass opening is also marked in values of the control system. The starred rows correspond to tests with no extra honeycomb at the entrance of the test section. Data were obtained with a DISA tracker. This instrument displays large discrepancies if the reading is not within a narrow band of the scale. The readings marked by a letter were repeated with a different scale and resulted in the following values of the turbulence level: (a) TU = 0.56%, (b) RMS = 25 mV, (c) TU = 1.08%, (d) RMS = 12 mV, (e) TU = 0.5%, (f) RMS = 15 mV, (g) TU = 0.53%.

Table 2.2.3

Speed of Pump	By Pass Closed fo (kHz)	RMS (mV)	TU %	By Pass at 2 fo (kHz)	RMS (mV)	TU T	By Pass at 4 fo (kHz)	RMS (mV)	TU %	By Pass Open fo (kHz)	RMS (mV)	TU %
	(n=9) (v=2.94)			(n=9) (v=2.362)			(n=9) (v=1.611)			(n=9) (v=1.442)		
0.5	90	14	0.47	72	12	0.50	49	15	0.93	44	15	1.04
	(n=8) (v=2.219)			(n=8) (v=1.85)			(n=8) (v=1.244)			(n=8) (v=1.104)		
1	135	14	0.63	112	14	0.75	76	16	1.2	67	15	1.35
	(n=8) (v=3.342)			(n=8) (v=2.709)			(n=8) (v=1.887)			(n=8) (v=1.734)		
2	203	26	0.77	165	20	0.74	115	25	1.32	109	19	1.09
	(n=8) (v=4.41)			(n=8) (v=3.79)			(n=8) (v=2.67)			(n=8) (v=1.734)		
3	260	26	0.56	231	28	0.73	163	30	1.12	144	35	1.48
	(n=8) (v=5.53)			(n=8) (v=4.62)			(n=8) (v=3.26)			(n=8) (v=2.99)		
4	337	30	0.54	282	30	0.65	199	40	1.22	182	50	1.67
	(n=8) (v=6.63)			(n=8) (v=5.63)			(n=8) (v=4.04)			(n=8) (v=3.65)		
5	404	36	0.54	343	36	0.64	246	50	1.23	223	55	1.5

Table 2.2.3: Same as Table 2.2.2 except that data were obtained by a TSI counter. In all cases, a honeycomb was positioned at the entrance of the test section.

Table 3.2.1

	Steady case		Unsteady case	
	x'	y'	x'	y'
a	-0.25	0.55	-0.25	0.48
b	-0.15	0.51	-0.15	0.48
c	-0.05	0.52	-0.05	0.49
d	0.05	0.53	0.05	0.50
e	0.15	0.54	0.15	0.51
f	0.35	0.56	0.35	0.52
g	0.55	0.56	0.55	0.54
h	0.75	0.56	0.75	0.54
i	0.95	0.56		

Table 3.2.1 Coordinates of the stations in the suction side free shear layer.

Table 4.3.1

=	180°	166°	146°	138°	124°	110°
Collins & Dennis (1973a)	0.322	0.331	0.39	0.43	0.589	0.90
Collins & Dennis (1973b)	0.322	0.33	0.39	0.42	0.59	1.10
Telionis & Tsahalis (1974a)	0.35	0.36	0.40	0.45	0.60	1.11
Bar-Lev & Yang (1975)	0.322	0.33	0.389	0.438	0.602	1.089
Cebeci (1979)	0.32	0.33	0.39	0.436	0.596	1.10
Wang (1979)	0.32	0.358	0.421	0.472	0.646	1.186
Present calculations (1984)	0.32	0.33	0.39	0.44	0.60	1.10

Table 4.3.1 Upstream motion of the point of zero skin friction in the aft region of a circular cylinder impulsively started from rest.

VITA

The author was born in Kifissia, Athens, Greece, in October 1956. In 1974, he entered the National Technical University of Athens from where he graduated in October 1979, receiving a diploma in Mechanical Engineering. After his graduation, he worked for six months as an apprentice engineer in a commercial ship. In July 1980 he became a member of the Technical Chamber of Greece and having successfully passed the proper examination he was registered as a professional engineer. In September 1980 he enrolled in the Department of Engineering Science and Mechanics at Virginia Polytechnic Institute and State University, where he received his M.S. in June 1982.